NEAR-WALL TURBULENCE AND UTILISATION OF THE NONLINEAR DYNAMICS TOWARDS CONTROL OF TURBULENT FLOWS

BY

ANUBHAV KUSHWAHA

A dissertation submitted in partial fulfillment of the

requirements for the degree of

Doctor of Philosophy

(Chemical Engineering)

at the

UNIVERSITY OF WISCONSIN–MADISON

2017

Date of final oral examination: 26 June 2017

The dissertation is approved by the following members of the Final Oral Committee:

Michael D Graham, Professor, Chemical Engineering

Nicholas L Abbott, Professor, Chemical Engineering

Daniel J Klingenberg, Professor, Chemical Engineering

James B Rawlings, Professor, Chemical Engineering

Saverio E Spagnolie, Assistant Professor, Mathematics

To

Saumya Singh

Acknowledgments

Thanks to my advisor, Prof Michael D Graham, for introducing me to the amazing topic of turbulence. I had a penchant for fluid dynamics when I came to Madison, but I had very little knowledge of turbulent flows or turbulence in general. From Prof Graham I learnt about the research topic, the course material for the courses I took with him, as well as things outside of research, and I value this education a lot. It is his motivation that kept me moving forward during all these years.

Many thanks to Prof Abbott, Prof Klingenberg, Prof Rawlings and Prof Spagnolie for serving on my final oral exam committee.

I want to thank our collaborators, Prof Robert J Poole (University of Liverpool) and Prof Richard D Whalley (Newcastle University and University of Liverpool) for sharing their views and ideas on the topic as physical experimentalists.

Prof Li Xi, a former student of Prof Graham, now a faculty member at McMaster University, helped me in getting started with the DNS code when I joined the group. Thanks to him.

Working in the Graham group has been a great experience. I have learnt something from every former and current group member and other office-mates. We had helpful discussions and fun times that we enjoyed together. Amit Kumar, Jae Sung Park, Anaram Shahravan, Sarit Dutta, Kushal Sinha, Rafael Gustavo Henríquez Rivera, Benjamin Wilson, Sung-Ning Wang, Joshua Duncan, Frank Nguyen, Xiao Xhang, Ashwin Shekar and Sandy Chen have all been great to work with. I did get a chance to have fruitful interactions with Pratik Pranay and Friedemann Hahn.

Finally, I am grateful to my family and friends for their encouragement and endless support they provided me during all these years.

The work has been supported by the National Science Foundation through grants CBET-1066223

and CBET-1510291 (Fluid Dynamics Program), and the Air Force Office of Scientific Research through grants FA9550-11-1-0094 and FA9550-15-1-0062 (Flow Interactions and Control Program). The direct numerical simulation (DNS) code, ChannelFlow [Gibson, 2009], used in Part I of the dissertation, was developed and distributed by Prof John F Gibson at the University of New Hampshire. Computations in Part II, Part III and Appendix A are performed with the help of Portable, Extensible Toolkit for Scientific Computation (PETSc) [Balay et al., 2011]. The Newtonian code, originally written for boundary layer flows over a flat surface and modified by us to be used for simulating flows in a wall-bounded channel, was provided by Prof Sang Lee from the University of New Mexico and Prof Jae Sung Park from the University of Nebraska–Lincoln.

Abstract

Direct numerical simulations (DNS) of plane Poiseuille flow are performed in an extended domain at friction Reynolds numbers ranging from 70 to 100. In minimal domains, turbulence in this Reynolds number range displays substantial intermittency that is associated with chaotic movement of turbulent trajectories between lower and upper branch invariant solutions known as exact coherent states (ECS). Part of the present work aims to address the relationship between temporal dynamics in minimal channels and spatiotemporal dynamics in extended domains. Both temporal and spatial analyses of the turbulent velocity fields are performed, the latter using image analysis methods. These analyses partition the flow characteristics into low-, intermediate- and high-drag classes; we present the differences between flows fields in these classes in terms of simple quantities like mean velocity, wall shear stress and flow structures. The temporal and spatial analysis methods, although completely independent of one another, yield very similar results for both low and high drag regions. In particular, the conditional mean profiles in regions of low drag closely resemble those found in low drag temporal intervals in the minimal channel. Finally, we address the possibility of similarities between turbulence and exact coherent states in two ways: (1) comparing wall shear stress in localised patches the size of minimal channels in large domains with those in actual minimal channel; and (2) comparing conditional mean velocity profiles during low drag events with mean profiles from lower branch ECS. These analyses show that both the local near-wall flow structure in the low drag patches of the large domain and the conditional mean profiles in the region $y^+ \lesssim 30$ resemble those of a lower branch minimal domain ECS. In summary, the results presented here suggest that spatiotemporal intermittency in transitional channel flow turbulence is related to temporal intermittency, and by extension to the state space structure, in the minimal channel.

Lower and upper branch ECS from one particular family of solutions are imprinted separately on a turbulent flow field in the minimal channel at Reynolds number close to transition. Specifically, the spatial patterns of their wall shear stress are imprinted on the channel wall, and the phase of the pattern keeps changing dynamically in accordance with the wave speed of the ECS solution from with the imprinted pattern is derived. The motion of the wall results in a travelling wave of wall deformation in streamwise or spanwise direction. Boundary conditions on the moving wall are satisfied using immersed boundary methods. Imposition of any pattern changes the dynamics of the flow near the wall. When a lower branch ECS is imprinted, drag-reduction is observed for most of the cases, and a maximum drag reduction of just over 15% is achieved. The resultant flow field shows characteristics of a flow with lesser drag: mean velocity profile is elevated, Reynolds shear stress and velocity fluctuations are reduced, and the streaks appear more streamwise aligned with less fluctuations. The flow trajectories also pass through the vicinity of the imprinted lower branch ECS in the state space. On the other hand, when an upper branch is imprinted on the flow, the drag increases. In such cases, the trajectories remain in the high-drag region of the state space. These results indicate that flow can be driven toward a desired state — a low drag state in our case — by manipulating the near-wall dynamics using information from that state. This opens many avenues for the development of new flow control strategies.

Contents

List of Tables

List of Figures

Chapter 1

Overview

The problem of understanding the nature of fluid flow over a rigid surface, which from this point onward we will refer to as *wall*, or in a wall-bounded domain, for example, a channel or a pipe, remains one of the oldest problems in fluid mechanics. Even though the equations of motion that govern the flow of a fluid are known — they are the celebrated Navier–Stokes equations, and even though in this time when researchers have state-of-the-art experimental equipment and immense computational resources, the challenge lies in understanding and rationalising the information extracted from such experiments or computations. A classical example of such a problem is the problem of transition: what is it that makes the flow go from a highly ordered *laminar* state in space and time to a highly disordered *turbulent* state in both space and time as the flow rate increases [Reynolds, 1883]?

One idea that may help us understand transition to turbulence emerges from the dynamical systems theory — it is the use of invariant solutions to the Navier–Stokes equations. These solutions, sometimes known as the building blocks of turbulence, may help us understand complicated flows occurring both spatially and temporally. Some of these nonlinear solutions lie on or near the edge of the basin boundary, i.e., the boundary between laminar and turbulent regions in the state space. These solutions have been found in a variety of shear flows, and it has been observed both numerically and experimentally that the chaotically moving turbulent trajectories visit some of these solutions in the state space [Park and Graham, 2015; Suri et al., 2017].

We are interested in flows of incompressible Newtonian fluids in rectangular, wall-bounded do-

mains, i.e., channels. An incompressible flow is one in which the material density of an element of the fluid, at a given temperature, remains constant both spatially and temporally as the fluid element flows with some velocity. Mathematically, an incompressible flow implies that the divergence of the fluid at a given temperature is zero. A Newtonian fluid is a fluid in which the local viscous stresses arising due to the flow are linearly proportional to the local strain rate, i.e., the rate of change of its deformation. The region close to the surface on which fluid flows, or the *near-wall* region, is dominated by viscosity, and the stress exerted by the fluid at the wall is the measure of the skin-friction drag. For Newtonian fluids, inertia drives the nonlinear behaviours in the flow, the magnitude of which depends on a single dimensionless parameter, the Reynolds number (Re) [Bird et al., 2007] — it the ratio of inertial forces to viscous forces. It can also be thought of as the ratio of viscous time scale to inertial time scale. Significant nonlinear behaviours can only be expected for $\mathrm{Re} > \mathcal{O}(1)$: the flow is smooth and orderly at low Reynolds number and with the increasing Reynolds number, fluctuations increase and eventually the flow becomes fully turbulent. Reynolds number has a major effect on the length and time scales of the flow. This results in variation in a number of flow properties with changing Reynolds number, including the flow structures.

Organised structures play a very important role in all turbulent shear flows. Being able to visualise flow structures, either in experiments or in simulations, is important: it helps not only in understanding transition to turbulence by giving qualitative and/or quantitative information about the flow but also in developing flow control techniques via direct interference with these deterministic events. Most of the structural information on the wall-bounded flows available in the literature come from rather low-Reynolds-number experiments and simulations. This is because flow becomes increasingly unstable at high Reynolds number, resulting in more breakdown of structures. The reduced length scales of flow structures, that can range anywhere from 1 µm to 1 mm at high Reynolds numbers, coupled with high frequencies of the flow, usually up to 100 kHz [Kasagi et al., 2009b], make taking accurate measurements very difficult. Simulating high Reynolds number flows requires very fine spatial and temporal resolutions in order to capture each and every flow structure. This in turn increases the computational costs. The focus of this study is on flows at Reynolds numbers close to transition.

At low Reynolds numbers, organised structures appear to be similar in all shear flows, e.g.,

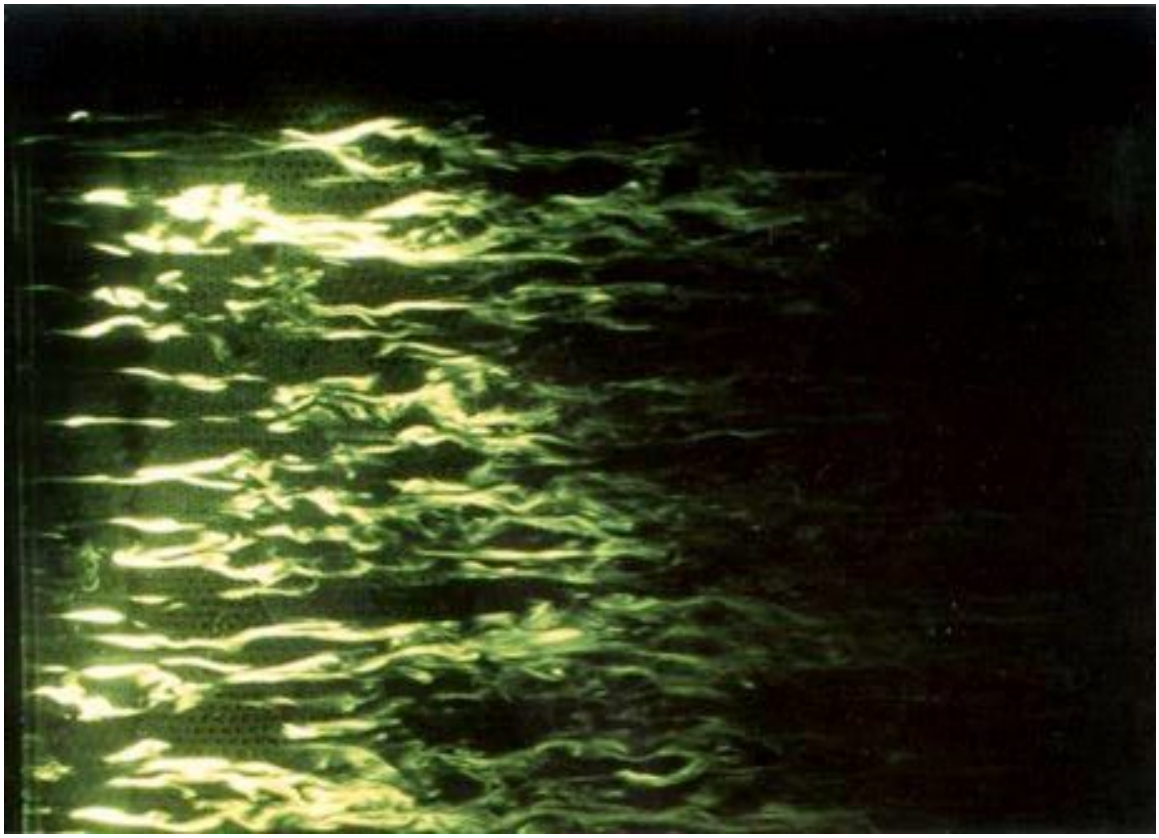

Figure 1.1: Top view of a turbulent boundary layer on a flat plate at a low Reynolds number ($\mathrm{Re}_\theta = 725$). Low-speed streaks are visualised using a sheet of laser and fluorescent dye (after Gad-El-Hak et al. [1984]).

channel flow, pipe flow or turbulent boundary layer flow *only* in the near-wall region or the inner layer. In the outer layer, the flow is vastly different — the outer region of a turbulent boundary layer is, by construction, different from the core region of a pipe or a channel flow. In addition to the near-wall structures, some of the mean mean statistics for different shear flows are also very similar. For example, the mean velocity profile, i.e., flow velocity (U^+) as a function of distance from the wall (y^+), when scaled with the wall variables (hence the + in the superscript) and plotted, follow a characteristic *log law* that is independent of Reynolds number. The profiles follow the log law for a range of y^+ that increases with Re, and deviate from the log law near the channel's mid-plane/pipe centre/top of the boundary layer. The current work is focussed purely on channel flows but an example of coherent structures visualised by Gad-El-Hak et al. [1984] in a laboratory scale boundary layer flow on a plate is depicted in Figure 1.1. In the figure, the view is from the top

and the flow is from left to right. The Reynolds number based on the momentum thickness (Re_θ) is 725. Fluorescent dye and a thin sheet of laser are used for illumination. The laser sheet is parallel to and almost touching the wall. Due to the vortical motion near the wall, fluid is transferred both towards and away from the wall. This results in variation of flow speeds at a fixed distance from the wall. This is depicted as bright and dark regions elongated in the flow direction in the figure. The bright structures are the slow moving fluid, known as *low-speed* streaks whereas the dark regions are regions of fluid moving with high speed, or *high-speed* streaks. Similar flow features are observed in channel flows, and a more detailed explanation on these structures is given below.

Our focus is on incompressible, Newtonian, pressure-driven turbulent flows in a wall-bounded domain. As noted above, physical and numerical experiments have shown the presence of organised flow structures near the wall and that most of the turbulent energy production (about 80%) takes place in the this region [Lumley and Blossey, 1998]. Prandtl postulated that at high Reynolds numbers, the mean velocity profile very close to the wall is determined by the viscous scales, independent of the flow away from the wall. If y denotes the distance from the wall, the region $y^+ \leq 5$, known as viscous sublayer, is where the viscosity dominates. The outer part of the inner layer ($y^+ \geq 30$) has negligible effect of viscosity and is known as the log-law layer. The region between the viscous sublayer and the log-law layer is known as the buffer layer and it is the transition region between the viscosity-dominated and the turbulence-dominated parts of the flow. The superscript + indicates flow variables normalised by the friction velocity, u_τ, and the kinematic viscosity of the fluid, ν.

Reynolds stress, that arises from the momentum transfer by the fluctuating velocity field [Pope, 2000], accounts for turbulence in fluid flow. Velocity at any position $\boldsymbol{x}$ and any given time t, $\boldsymbol{U}(\boldsymbol{x}, t)$, can be decomposed into its mean, $\langle \boldsymbol{U}(\boldsymbol{x}, t) \rangle$, and the fluctuation, $\boldsymbol{u}'(\boldsymbol{x}, t)$. Here $\boldsymbol{U} = (U\ V\ W)^{\mathrm{T}}$: U, V and W are the three components of the velocity along the streamwise (x), wall-normal (y) and spanwise (z) directions, respectively, and $\boldsymbol{x}$ is the position vector. Thus, the velocity fluctuations in the three directions can be written as: $u' = U - \langle U \rangle$, $v' = V - \langle V \rangle$ and $w' = W - \langle W \rangle$. The fluctuating velocity field gives rise to near-wall quasi-streamwise vortices (QSVs), which are responsible for high skin-friction drag in turbulent boundary layers/channel flows [Choi et al., 1994]. The streamwise vortices, consisting of wall-normal and spanwise velocities, independent of the streamwise direction, interact with the mean shear, $\mathrm{d}U/\mathrm{d}y$, and create a spanwise dependence in the streamwise velocity

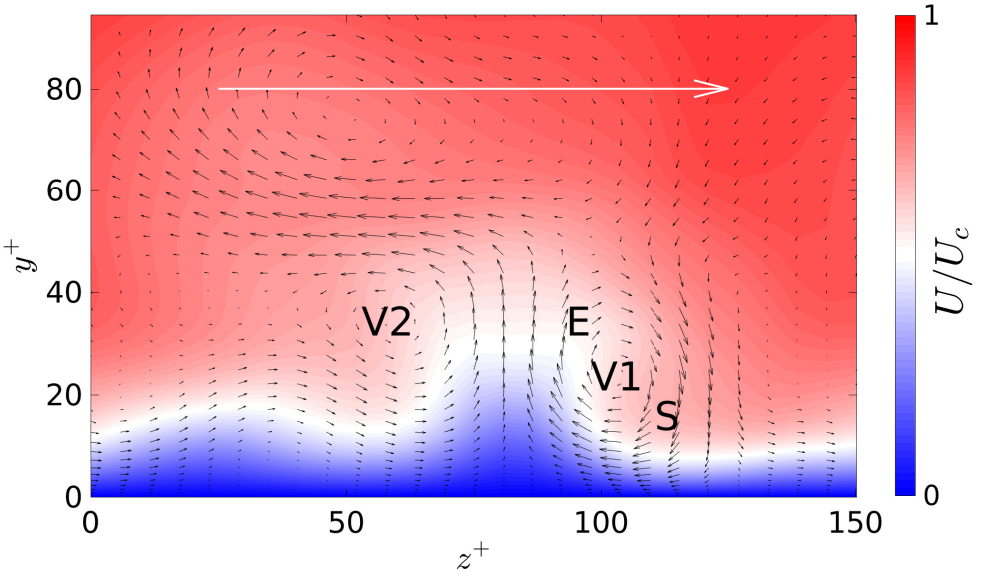

Figure 1.2: An instantaneous snapshot of flow velocities in the y-z plane in the lower half of the channel in a plane Poiseuille flow at $\mathrm{Re}_\tau = 94.5$. The flow is into the plane of paper. Box dimensions are $(L_x, L_y, L_z) = (4.24\ l, 2\ l, 1.65\ l)$, where l is the half-height of the channel. The streamwise velocity component is shown by contours and the wall-normal and spanwise components by black arrows. They are scaled by the laminar centreline velocity, U_c. Two vortices, V1 and V2, and their effect on the mean flow, i.e., formation of streaks are shown. The white horizontal arrow at the top represents the reference vector and has a length U_c.

(main flow) near the wall. These structures, known as streaks, are unstable because of the spanwise gradient of the streamwise velocity. They migrate slowly away from the wall, known as streak lifting or ejection, and when in the buffer layer, they exhibit rapid oscillations followed by a breakdown, known as turbulent burst. The finer-scale motions created again lead to the formation of more vortices [Pope, 2000]. This process is self-sustaining [Waleffe, 1997; Jiménez and Pinelli, 1999; Waleffe, 2003] and is unaffected by the outer part of the boundary layer at low Reynolds number [Kim, 2011; Jiménez and Pinelli, 1999]. Note that an ejection event is the transfer of low-momentum fluid away from the wall, i.e., $u' < 0$ and $v' > 0$, although an event that satisfies these conditions is not necessarily an ejection. Ejections are accompanied by sweep events, when high-momentum fluids are induced towards the wall, i.e., $u' > 0$ and $v' < 0$, creating regions of high wall shear stress. Majority of turbulence production takes place in the buffer region during sweep and ejection events [Pope, 2000]. Reynolds stress, given by $-\langle u'v' \rangle$, increases when the product $u'v'$ is negative. Thus both ejection and sweep events produce turbulent energy. Figure 1.2 shows the velocity

distributions in the wall-normal and spanwise directions (y-z plane). The colour contours are that of the streamwise velocity component (U) while vectors represent the wall-normal (V) and spanwise (W) velocity components. Two streamwise vortices (approximate centres at V1 and V2) are shown. Vortex V1 is bringing high-momentum fluid from the bulk flow towards the wall (sweep event S) and at the same time lifting low-momentum fluid away from the wall (ejection event E). A low-speed streak is formed in the process. Regions of local wall shear stress, that are highly correlated with vortical structures, are created. Specifically, high skin-friction zones are created under the sweep events and low skin-friction zones under the ejection events.

From the control point of view, an intuitive strategy to attenuate and control turbulence in the near-wall region would be to suppress the sweep and ejection events by manipulating the interactions between these streamwise vortices and the wall. Suppressing sweeps and ejections makes the flow orderly and fluctuations in the flow are greatly reduced. There have been various approaches in the past to reduce the turbulent motions near the wall by suppressing the coherent structures, and significant progress has been made, both numerically and experimentally, to provide a better understanding of the physics of turbulence and its control.

The dissertation is organised as follows. An in-depth discussion on the structures and statistics of regions of varying levels of turbulence, occurring spatially and temporally, is presented in Part I. It includes discussion on detection and sampling of events of interest, conditional averaging, and comparison of channel flow turbulence with the invariant solutions to the Navier–Stokes equations. A detailed literature review on the development of immersed boundary methods (IBM) and the usage of IBM in order to implement channel wall deformation for manipulating the near-wall flow dynamics is presented in Part II. In Part III, I have reviewed existing drag-reduction methods, their benefits and limitations, and various types of wall motions with the aim of achieving reduction in skin-friction drag along with the results. Finally, numerical details of a finite-volume Navier–Stokes solver for direct numerical simulation (DNS) of incompressible flows is discussed in Appendix A.

Part I

Statistics and structures of low- and high- drag events in turbulent channel flow

Chapter 2

Introduction

The past 20 years or so have seen rapid advances in understanding transition to turbulence [Hof et al., 2004; Kerswell, 2005; Eckhardt et al., 2007; Willis et al., 2008; Kawahara et al., 2012]. These advances build on the mathematical foundation of dynamical systems theory and the discovery of nontrivial invariant solutions to the Navier–Stokes equations (NSE) for the canonical shear flows: plane Couette flow [Nagata, 1990; Clever and Busse, 1997; Nagata, 1997; Viswanath, 2007; Gibson et al., 2008, 2009; Halcrow et al., 2009; Itano and Generalis, 2009; Schneider et al., 2010; Deguchi et al., 2013; Blackburn et al., 2013; Nagata, 2013], plane Poiseuille flow [Waleffe, 1998, 2001, 2003; Toh and Itano, 2003; Nagata and Deguchi, 2013] and pipe flow [Faisst and Eckhardt, 2003; Wedin and Kerswell, 2004; Kerswell, 2005; Kerswell and Tutty, 2007; Pringle and Kerswell, 2007; Eckhardt et al., 2007; Duguet et al., 2008]. These solutions, sometimes called exact coherent states (ECS) [Waleffe, 1998], take the form of steady states, nonlinear travelling waves, relative periodic orbits and edge states (these are solutions that live on the boundary in state space of the basins of attraction of the laminar and turbulent states, respectively). Most of these states have been found in so-called "minimal flow units" (MFU) or "minimal channel" geometries: i.e. they are spatially periodic in the unbounded dimensions of the domain with periods that roughly correspond to the smallest length scales at which turbulence can persist in the domain of interest. The spatial structure of these solutions qualitatively matches that of near-wall turbulence: a mean shear flow with streamwise-modulated streamwise vortices that generate low- and high-speed streaks. Additionally,

direct numerical simulations of turbulence in MFUs indicates that at low (transitional) Reynolds numbers, the turbulent trajectories in these geometries are organised at least in part around the ECS [Gibson et al., 2008; Kawahara et al., 2012; Park and Graham, 2015]. It is important to note that some highly localised invariant solutions, which display nontrivial flow only over a small region of an extended flow domain, while the remainder of the domain remains laminar, have been found as well [Brand and Gibson, 2014; Chantry et al., 2014; Zammert and Eckhardt, 2014]. These solutions are highly reminiscent of the turbulent spots or puffs that are a common feature of turbulence near transition [Avila et al., 2013].

More broadly, the spatiotemporal dynamics of turbulence in extended domains contains many open issues even in the transitional Reynolds number regime. One of these is the extent to which dynamics in extended domains is related to dynamics in minimal ones. Aiming to shed some light on these issues, the present work focuses on the plane channel flow geometry, using direct numerical simulations and temporal and spatial sampling techniques to characterise intervals and regions of high and low turbulence activity. Specifically, our results are consistent with the hypothesis that temporal intermittency observed in minimal channels becomes spatiotemporal in extended domains and that main features of the ECS and minimal channel turbulence results are found in localised regions in the extended domain.

A number of research groups have computed exact coherent states for the channel flow geometry [Waleffe, 2001; Itano and Toh, 2001; Waleffe, 2003; Nagata and Deguchi, 2013; Park and Graham, 2015; Rawat et al., 2016]. For the most part, these solutions arise in pairs at saddle-node bifurcations; the "upper-branch" solution of each pair has larger velocity fluctuations and higher drag compared to the "lower branch" solution. Park and Graham [2015] found a family of channel flow ECS in the minimal channel geometry, which they denoted "P4", that has particularly intriguing behaviour. The mean velocity profile of the upper branch state approaches the Prandtl-von Kármán log-law while that of the lower branch approaches a form generally associated with turbulence in viscoelastic polymer solutions, the so-called Virk profile [Virk, 1975]. This profile is a good approximation of experimental and computational observations in the so-called "maximum drag reduction" (MDR) regime. This ECS result adds to the set of observations in which mean velocity profiles close to the Virk profile are found in Newtonian flow [Kerswell et al., 2003; Bandyopadhyay, 2006; Xi and

Graham, 2010a,b; Dubief et al., 2010; Xi and Graham, 2012a,b]. Notwithstanding this intriguing similarity to MDR, the present work addresses only Newtonian flow. The flow structures of the upper and lower branch solutions are very different — the upper branch has strong streamwise vortices and wavy streaks representing strong fluctuations while the lower branch has weak vortices and almost streamwise-invariant streaks.

Direct numerical simulations (DNS) of turbulence in the same minimal geometry at Reynolds numbers near transition have been found by a number of researchers [Jiménez and Moin, 1991; Xi and Graham, 2010a, 2012b] to exhibit temporal intermittency between high- and low- drag intervals: Xi and Graham [2010a] denoted these as "active" and "hibernating", respectively. Park and Graham [2015] found that this behaviour is a reflection of the organisation of the turbulent dynamics around the P4 solution family. Specifically, as illustrated in Figure 2.1(a), at friction Reynolds number $\mathrm{Re}_\tau = 85$ the trajectory spends most of its time orbiting in the vicinity of the upper branch solution, displaying relatively high drag and a mean profile near the von Kármán profile, but occasionally takes excursions that approach the lower branch solutions (there are actually two of these because the lower branch turns back on itself) and thus exhibit low drag. Over part of the Reynolds number regime the lower branch states lie on the basin boundary between the laminar and turbulent attractors in the minimal domain, so the approach of the turbulent dynamics to these states implies an approach to the laminar-turbulent basin boundary. At higher Reynolds number, these excursions become increasingly rare as we describe below. Mean velocity profiles of some upper and lower branch travelling wave solutions from the P4 family are plotted in Figure 2.1(b). As noted above, the upper branch velocity profiles nearly collapse with the classical Newtonian (von Kármán) profile, while the lower branch velocity profiles approach the Virk MDR. Park and Graham [2015] showed that near the wall ($y^+ \lesssim 30$), instantaneous velocity profiles from minimal channel DNS are very nearly bracketed between the UB and LB solutions, while deviations from these solutions are observed near the centre of the channel. Thus, the P4 travelling waves appear to form an approximate envelope for the DNS mean velocity profiles for $y^+ \lesssim 30$. This is important as these similarities in the near-wall behaviour suggest that the turbulent dynamics in minimal channels is organised at least in part around these travelling wave solutions.

A natural question is how closely these minimal channel observations are related to the phe-

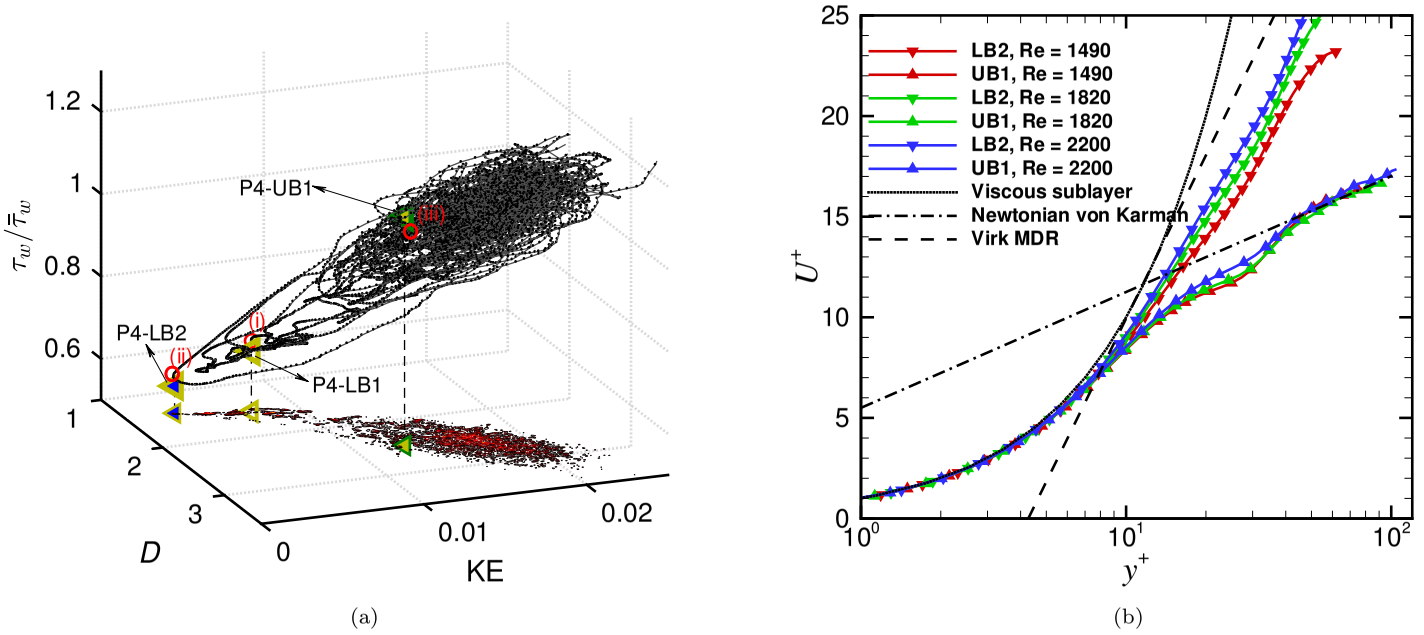

(a) (b)

Figure 2.1: (a) State-space visualisation of DNS trajectories in a minimal channel turbulent flow ($L_x \times L_y \times L_z = \pi \times 2 \times \pi/2$, $\mathrm{Re}_c = 1800$ ($\mathrm{Re}_\tau = 85$), constant mass flux), projected onto three dimensions: disturbance kinetic energy (KE), energy dissipation rate (D), and normalised instantaneous wall shear stress ($\tau_w/\bar{\tau}_w$) [Park and Graham, 2015]. The grey line indicates the turbulent trajectory, to which black dots are attached at intervals of 1 l/U_c. The joint probability density of KE and D is shown at the bottom of the figure. The labelled symbols ($\triangleleft$) are P4 solutions. Points (i), (ii), and (iii) are the closest approaches to P4-LB, P4-LB2, and P4-UB, respectively. All quantities are calculated only for the bottom half of the channel. (b) Mean velocity profiles of lower (LB) and upper branch (UB) travelling waves of the P4 family. These solutions are also being used for comparison with DNS (Chapter 4.2.2).

nomenon of "laminar-turbulent intermittency" in the transitional Reynolds number regime for spatially extended flows (i.e. experimentally realised flows where no artificial periodicities are present). Manneville [2015] provides an excellent overview of this phenomenon; the basic observation is that the transitional Reynolds number regime, at a given point in the domain the flow alternates randomly between states with weak and strong fluctuations. Pipe flow is the most well-studied case. Here laminar-turbulent intermittency is first observed as localised turbulent patches, known as puffs, surrounded by laminar flow upstream and downstream of it [Wygnanski and Champagne, 1973; Wygnanski et al., 1975]. These puffs have complex behaviour, involving growth and splitting [Eckhardt et al., 2007; Avila et al., 2011], and many aspects of the transition regime can be captured using reaction-diffusion-advection models involving evolving fronts that separate spatial regions of turbulent and laminar motions [Barkley, 2011; Barkley et al., 2015; Graham, 2015], with the turbulent regions taking over the whole domain once the Reynolds number is sufficiently high. Nevertheless, even at Reynolds numbers traditionally regarded as above the transition regime, substantial spatiotemporal fluctuations in turbulence activity persist [Avila and Hof, 2013]. In the case of boundary layer flows, turbulent spots are surrounded by laminar flow [Wygnanski et al., 1976]. These spots spread in all directions as they convect downstream [Emmons, 1951; Nolan and Zaki, 2013], culminating in a fully turbulent boundary layer. In channel flow, the focus of the present work, experimental studies by Carlson et al. [1982] reveal the presence of arrowhead shaped turbulent spots with streamwise streaks trailing from the rear of the spot. The front of the spot moves faster than the rear end, resulting in the expansion of the spot before it eventually splits into two. Within a spot, strong turbulent fluctuations occur, which are preceded by oblique waves that surround the spot. Other studies [Duguet and Schlatter, 2013; Lemoult et al., 2012, 2013, 2014; Hashimoto et al., 2009; Rolland, 2015; Tuckerman et al., 2014; Barkley and Tuckerman, 2005] observed elongated near-wall streaks forming stripe patterns. These patterns are oriented obliquely relative to the main flow direction. Flow is highly turbulent near the centre region of the stripes, and around the stripes are regions of streamwise streaks that are relatively less turbulent. As the Reynolds number is increased, the fluctuation intensity in the less turbulent regions increases along both streamwise and spanwise directions, the stripiness in the flow structures start to vanish and eventually, the flow becomes uniformly turbulent, i.e., any apparent large-scale structures are absent.

To differentiate between regions of turbulent flow from nonturbulent flow, conditional sampling techniques have been used by many researchers. Volino et al. [2003] conducted transitional boundary layer experiments in a wind tunnel and measured velocities at several locations in the streamwise and wall-normal directions. They calculated intermittency factors using flow quantities such as streamwise velocity and Reynolds shear stress, and found that the mean velocity profiles differed significantly between the turbulent and nonturbulent regimes. They also showed that the wall-normal velocity fluctuations and Reynolds shear stress in the turbulent spots are significantly higher and the skin friction was 70% higher within the turbulent zone compared to the nonturbulent zone. However, no data on the flow structures in the turbulent and nonturbulent zones were reported. Hutchins et al. [2011] identified conditional structures during low or high skin-friction events in a turbulent boundary layer flow. They defined a low skin-friction event as an event during which the instantaneous skin-friction fluctuation is negative, and vice-versa, and found that the mean velocity profile during low skin-friction events lie well above the velocity profiles during high skin-friction events, which is same as the findings of Volino et al. [2003]. In addition, the conditional flow fields reveal the presence of an elongated low-speed structure aligned in the flow direction flanked on either side by a pair of counter-rotating vortices [Hutchins and Marusic, 2007; del Álamo et al., 2006].

A conceptually simple technique of conditionally partitioning data sets such as flow fields into distinct groups or *clusters* such that properties in the same cluster are more similar to each other than those in other clusters is k-means clustering. Kaiser et al. [2014] used this method to partition snapshots from a mixing layer flow into k distinct clusters. The mean or *centroid* of each cluster is determined iteratively by minimising the sum of squares of distances between individual snapshots of a cluster and the centroid of that cluster. This results in the formation of k different clusters such that properties are similar within a cluster but vary from one cluster to the other. Another approach to partitioning large data sets is *thresholding*. Nolan and Zaki [2013] performed numerical studies for boundary layer flows and developed a thresholding technique to discriminate laminar spots from turbulent spots. An input signal, which is a time series of flow properties, e.g., velocity fluctuations, is carefully thresholded using Otsu's method [Otsu, 1979] — an image-processing technique used to automatically perform image segmentation by determining threshold(s) between distinct regions such that each region shares certain characteristics. Otsu's method picks out the optimum threshold(s)

by minimising the *intra-class* variance, or maximising the *inter-class* variance. It can also be used for multilevel thresholding; in general, the number of classes is one more than the number of thresholds. Although the k-means and Otsu algorithms are different, it can be shown that they both extremise the same objective function [Liu and Yu, 2009]. Nolan and Zaki identified laminar and turbulent regions in boundary layer flows and computed conditional averages for those distinct regions. They observed that the laminar-conditioned velocity profiles have a characteristic laminar shape whereas the turbulent-conditioned profiles follow the law of the wall. We use Otsu's method below.

Many other methods for discriminating turbulent areas from nonturbulent regions in a flow field have been employed where thresholds are set for various flow properties. For example, instantaneous wall-normal and spanwise velocities, instantaneous turbulent dissipation and vortex identification (λ_2 and Q criteria) are thresholded by Rehill et al. [2012] in a boundary layer flow over a flat plate. They found that the Q criterion and the dissipation methods show the least sensitivity to changes in the threshold level and hence are the best input signals that can be used for identifying turbulent spots. Baltzer et al. [2013] examined and characterised the spatial arrangements of very large-scale motions in a pipe flow at high Reynolds number. Regions at a distance of $y/R = 0.15$ from the pipe wall where the streamwise velocity fluctuations were stronger than the threshold value u'_{thr} of $-0.10U_{bulk}$ were extracted — these are the low-speed regions in the flow field. A conditional average of many such low-speed events reveals the presence of an elongated low-speed streak with counter-rotating vortices on either side of it. Similar thresholding techniques to extract features from turbulent flow fields in pipe, channel or boundary layer flows, although for large-scale motions, have been adopted by Dennis and Nickels [2011]; Lee and Sung [2011]; Lee et al. [2014, 2015a].

For the most part, the work just described does not address the question introduced above regarding the relationship between temporal intermittency in minimal domains and spatiotemporal intermittency in extended ones. Indeed very little study has been made of the dynamics of the "laminar" intervals in laminar-turbulent transition, although the dynamics in these regions can be nontrivial and according to Avila et al. [2010] persist into the fully turbulent regime. Evidence for the existence of a spatiotemporal relationship between minimal channels and full turbulent flows has been presented by Jiménez et al. [2005]; Flores and Jiménez [2010]; Jiménez [2013]. They have shown that the variability in temporal statistics during bursting events in minimal boxes agrees well

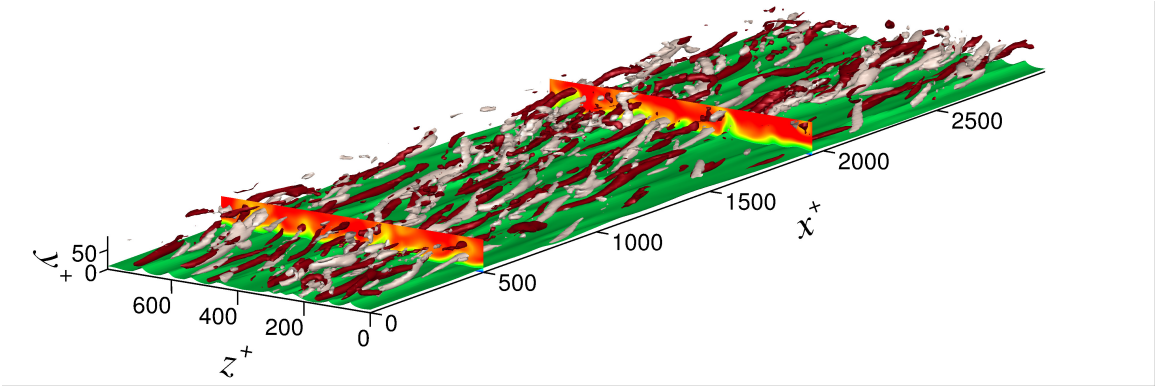

(a) View from an angle

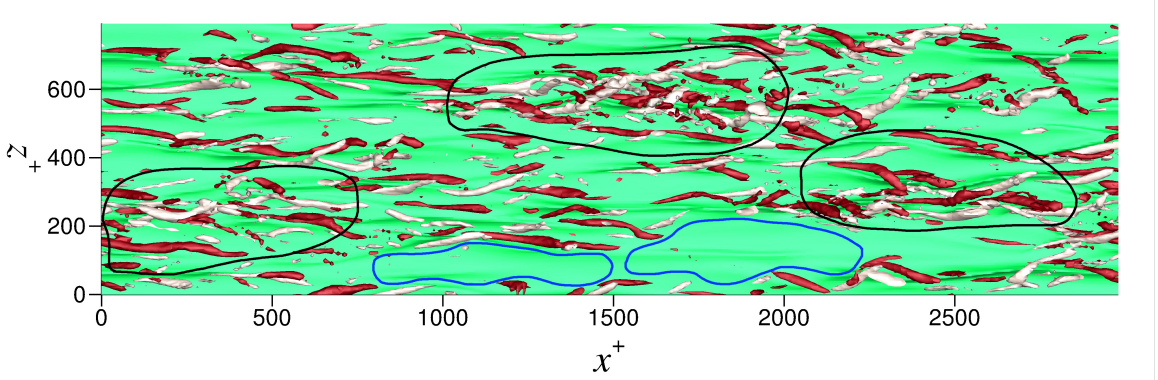

(b) View from top

Figure 2.2: Flow structures of a typical snapshot from channel flow DNS ($\mathrm{Re}_\tau = 85$, $L_x^+ \approx 3000$, $L_z^+ \approx 800$). Flow is in the x-direction. Only the lower half of the channel is shown. The green sheet is the isosurface of streamwise velocity $U = 0.35$; cross-planes in the first panel at $x^+ = 500$ and 1950 show contours of streamwise velocity; tubular structures are isosurfaces of $Q_{2D} = 0.05$ [Xi and Graham, 2010b] colour-coded by the streamwise vorticity at the same location: red represents positive vorticity and white represents negative vorticity. Sample regions showing weak and strong fluctuations are shown enclosed by blue and black boundaries, respectively, in the second panel.

with the variability in spatial statistics in sub-boxes of similar sizes in large domains suggesting that the flow dynamics in minimal channels are also part of full size turbulent flows. Figure 2.2 shows a snapshot from a channel flow DNS in which we have arbitrarily circled regions of intense or weak turbulence activity (regions of "active" and "hibernating" turbulence in the nomenclature introduced in Xi and Graham [2010a]). The aim of the present work is to systematically characterise the dynamics and structure in these regions and examine their relationship to minimal channel and ECS results.

Part I is organised as follows. A brief discussion on formulation of the system and simulation parameters are presented in Chapter 3. Sampling methodology of intermittent low and high drag events based on pointwise sampling of wall shear stress and conditional averaging of these events are discussed in Chapter 4.1.1. In Chapter 4.1.2 we quantify this temporal intermittency. The mean velocity profiles of low and high drag intervals are presented in Chapter 4.1.3 and the underlying flow structures during these events have been illustrated in Chapter 4.1.4. Chapter 4.2.1 presents a discussion on the identification of spatial intermittency and a comparison of temporal statistics in a large domain with the spatial statistics and finally in Chapter 4.2.2 we compare DNS results with nonlinear travelling wave solutions and find connections between the two. A summary of main results and conclusions of Part I is presented in Chapter 5.

Chapter 3

Formulation

We consider pressure driven flow of an incompressible Newtonian fluid in a rectangular, wall-bounded domain (channel) maintained at constant mass flux, a schematic of which is shown in Figure 3.1. The x, y and z axes correspond to the streamwise, wall-normal and spanwise directions, respectively. No-slip boundary conditions are applied at the top and bottom walls and periodic boundary conditions are adopted in the streamwise and spanwise directions. The periods are L_x and L_z in these directions, respectively. The half-channel height, $l = L_y/2$ is chosen as the characteristic length scale for nondimensionalisation of all the lengths in the geometry. Velocities are scaled with the laminar centreline velocity U_c for the given mass flux. Time t is scaled with l/U_c and pressure p with ρU_c^2, where ρ is the fluid density. The nondimensionalised Navier–Stokes equations are then given as:

$$\frac{\partial \boldsymbol{u}}{\partial t} + \boldsymbol{u} \cdot \boldsymbol{\nabla} \boldsymbol{u} = -\boldsymbol{\nabla} p + \frac{1}{\mathrm{Re}} \nabla^2 \boldsymbol{u} \tag{3.1}$$

$$\boldsymbol{\nabla} \cdot \boldsymbol{u} = 0 \tag{3.2}$$

The Reynolds number is given as $\mathrm{Re} \equiv l U_c/\nu$, where ν is the kinematic viscosity of the fluid. The friction Reynolds number is defined as $\mathrm{Re}_\tau \equiv l u_\tau/\nu$, where $u_\tau \equiv \sqrt{\overline{\tau_w}/\rho}$ is the friction velocity; $\overline{\tau_w}$ is the time- and area-averaged (mean) wall shear stress.

This study focusses on results for three Reynolds numbers, $\mathrm{Re} = 1490, 1820$ and 2200 (corre-

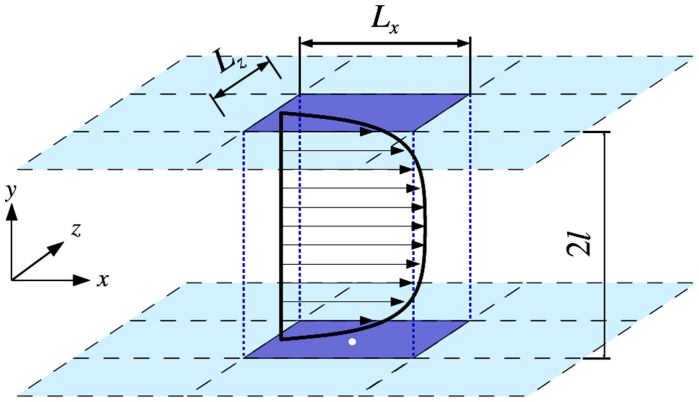

Figure 3.1: Schematic of the plane Poiseuille flow geometry: the actual simulation box is highlighted with dark-coloured walls in the centre, surrounded by its periodic images. The white dot on the bottom wall represents a sampling point $\boldsymbol{x}_s$ where we measure the instantaneous wall shear stress in Chapter 4.1.

sponding to friction Reynolds numbers, $\mathrm{Re}_\tau = 70, 85$ and 100, respectively). The streamwise and spanwise periods in outer units are $42.86\ l \times 11.43\ l$ at $\mathrm{Re}_\tau = 70$, $35.36\ l \times 9.43\ l$ at $\mathrm{Re}_\tau = 85$ and $30.00\ l \times 8.00\ l$ at $\mathrm{Re}_\tau = 100$. These dimensions correspond to a domain size of $L_x^+ \approx 3000, L_z^+ \approx 800$ in wall units at all values of Re_τ: 70, 85 and 100. Here, the superscript '+' indicates normalisation with the viscous length scale, $\delta_\nu = \nu/u_\tau$.

Simulations are performed using *ChannelFlow*, a direct numerical simulator for incompressible Newtonian fluid flow in a periodic, rectangular, wall-bounded domain, developed and maintained by Gibson [2009]. The system of coupled Equations (3.1) and (3.2) is integrated in time with a third-order semi-implicit scheme: a third-order implicit backward differentiation method is used to update the linear terms while the nonlinear terms are integrated with an explicit third-order Adams–Bashforth method [Peyret, 2002]. Fourier-Chebyshev-Fourier spatial discretisation is applied in all variables and nonlinear terms are calculated with the collocation method. We use $(N_x, N_y, N_z) = (196, 73, 164)$ grid points for $\mathrm{Re}_\tau = 70$, $(160, 73, 120)$ grid points for $\mathrm{Re}_\tau = 85$ and $(160, 85, 120)$ grid points for $\mathrm{Re}_\tau = 100$ in the streamwise, wall-normal and spanwise directions, respectively. The numerical grid spacings in streamwise and spanwise directions are $\delta_x^+ \approx 15$ and $\delta_z^+ \approx 5$, respectively, for all the cases. Nonuniform Chebyshev spacing in the wall-normal direction gives $\delta_{y,min}^+ \approx 0.07$ at the wall and $\delta_{y,max}^+ \approx 3$ at the centre of the channel. A constant time step, $\delta t = 0.02$, which satisfies the CFL stability condition, is used in all simulations. The spatial and temporal resolutions are at the same level as those reported in previous studies [Alfonsi, 2011]. A convergence check

was also done — spatial resolution was increased and all the quantities reported in the dissertation were recalculated, yielding negligible changes from the results reported here. Each simulation run is sufficiently long (more than 25 Re $\approx 6 \times 10^4$ l/U_c time units) to ensure meaningful statistical averages.

Chapter 4

Results and discussion for Part I

The results are organised as follows. In Chapter 4.1 we characterise events based on temporal behaviour — the fundamental "measurement" we consider here is the time series of shear stress at a point on the wall. Based on behaviour, specifically low- and high-drag events at that point, we focus on the time series of flow properties at a point on a wall and at various discrete distances above the wall, flow properties are sampled conditionally based on when an event happens in time and conditional averages are presented. In Chapter 4.2 we characterise events based on space. Instead of focussing just at a point, we examine the entire domain at the same time. Spatial regions or patches showing similar characteristics are identified and put together in order to get spatially conditional averages. Finally, we compare temporal and spatial dynamics of large-domain DNS with minimal channel ECS.

4.1 Temporal intermittency

4.1.1 Time series of wall shear stress — unconditional and conditional

We first describe our method of characterisation of events with varying amounts of drag relative to the mean. To detect and sample such events happening locally with time, we measure the instantaneous wall shear stress at a sampling point $\boldsymbol{x}_s$ on a wall. A point $\boldsymbol{x}_s$ is shown as a white dot on the bottom wall in Figure 3.1. In fact, to get better statistics we choose nine measurement

locations on the wall of the large domain in a way that the shear stress at each location is not correlated with the other locations: any two adjacent points are 1.67×2.67 correlation lengths apart. Our criteria for an event is that the wall shear stress (τ_w) at $\boldsymbol{x}_s$ must pass through a threshold value and stay on the same side of the threshold for a specified minimum time duration. Specifically, for a "hibernation" event, characterised by low drag, the wall shear stress must fall below the specified threshold and remain below it for a specified time duration, and likewise for a high-drag "hyperactive" event where τ_w must exceed a threshold value for a specified duration. We measure this time duration in units of $t^* = tu_\tau/l$, i.e., eddy turnover times, and our base case is to set this duration to $t^* = 3$ — we address below the issue of sensitivity to the chosen value while for the moment we note that this value was chosen based on observations from prior work. Jiménez and Moin [1991] have observed that the peak-to-peak distance in the time series of wall-shear deviations from the mean in turbulence in a minimal channel is about $t^* \approx 4$. Similar observations were made in MFUs by Webber et al. [1997]. Xi and Graham [2010a] defined hibernation in minimal channels as events when the area-averaged wall shear stress is below 90% of its mean value for more than 1.18 t^*. In a later study [Xi and Graham, 2012b] in which hibernation was defined differently, they showed that the average duration of hibernation events was $t^* \approx 4.5$. The default threshold values chosen for the current study are 90% of the mean wall shear stress ($\overline{\tau_w}$) for a hibernation event, and 110% of $\overline{\tau_w}$ for a hyperactive event. For $\mathrm{Re}_\tau = 70, 85, 100$, $t^* > 3$ corresponds to $tU_c/l > 63.5, 64.5, 65.3$, respectively, in outer units and $tu_\tau^2/\nu > 211.1, 254.1, 303.1$, respectively, in inner units. Again, sensitivity to the threshold value is addressed with the presentation of the results.

Figure 4.1 shows time series of shear stress measured at a point $\boldsymbol{x}_s$ at $\mathrm{Re}_\tau = 70$, 85 and 100. By the criteria above, the flow is in hibernation during the intervals bounded by the vertical orange lines: the instantaneous wall shear stress (grey line) is significantly lower than the time averaged value ($\overline{\tau_w}$) shown as a dashed line for 3 or more l/u_τ. These are examples of low-drag events in turbulence and this intermittent behaviour is observed at all the Reynolds numbers considered. Figure 4.2 shows some instantaneous snapshots of wall shear stress fluctuations before and during hibernation events at friction Reynolds numbers 70, 85 and 100. The white dot in the centre of the domain represents the location where the wall shear stress shown in Figure 4.1 is measured. The flow structures are significantly three-dimensional at all the Reynolds numbers considered and fluctuations can be seen

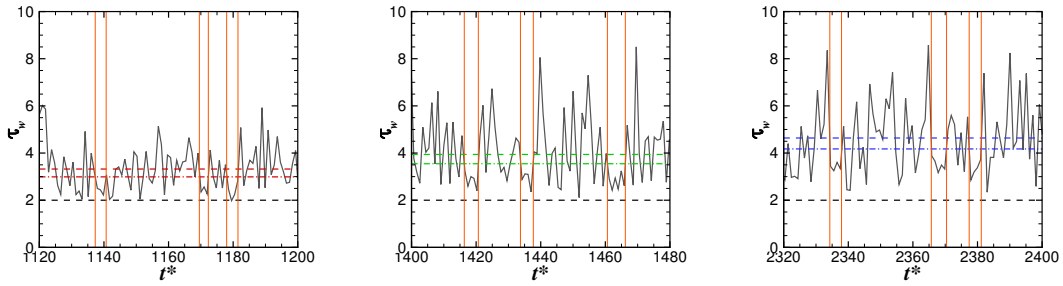

(a) $\mathrm{Re}_\tau = 70$ (b) $\mathrm{Re}_\tau = 85$ (c) $\mathrm{Re}_\tau = 100$

Figure 4.1: Time series of the wall shear stress at different friction Reynolds numbers. Grey = instantaneous; black dashed = laminar; colour dashed = time averaged; colour dashed-dotted = threshold.

throughout the domain: the intermittency observed is purely *within* turbulence. It is interesting to note that at $\mathrm{Re}_\tau = 70$, which is the lowest Re_τ we consider, a large-scale stucture of weak and strong turbulent fluctuations appears in the form of stripes that are oriented obliquely relative to the mean flow. Similar stripy patterns have also been observed experimentally in channel flow by Hashimoto et al. [2009] as well as in Couette flow computations (e.g. Barkley and Tuckerman [2005]). The stripes we see here are oriented at $20° \sim 30°$ relative to the mean flow which is in excellent agreement with the orientation angle reported in experiments [Hashimoto et al., 2009]. As the Reynolds number increases, the stripiness start to disappear (see Figure 4.2 (c)-(f)) and eventually the turbulence becomes uniform. Further, it can be observed that in the "before hibernation" figures (left column), the wall shear stress at and near the measurement point is high (red), whereas it is low (blue) in the "after hibernation" figures (right column).

In Figure 4.3(a), we show time series of 639 temporal hibernation events measured at $\mathrm{Re}_\tau = 85$. The beginning of each event is shifted to $t^* = 0$. The ensemble average of all the instantaneous hibernation events is shown as a thick green line. On average the wall shear stress during hibernation falls to a plateau in the time interval $0.7 \leq t^* \leq 3.0$ and is preceded by a sharp peak in the wall shear stress (higher than the mean) during $-0.8 \leq t^* \leq 0$. Figure 4.3(b) shows instances that satisfy the "hyperactivity" criterion. Before hyperactivity begins, a brief drop in the wall shear stress is observed and it becomes higher than the mean for $t^* \approx 0.7 - 3.0$. The frequency of occurrence of hibernation and hyperactive events has been quantified and the results are presented in Chapter

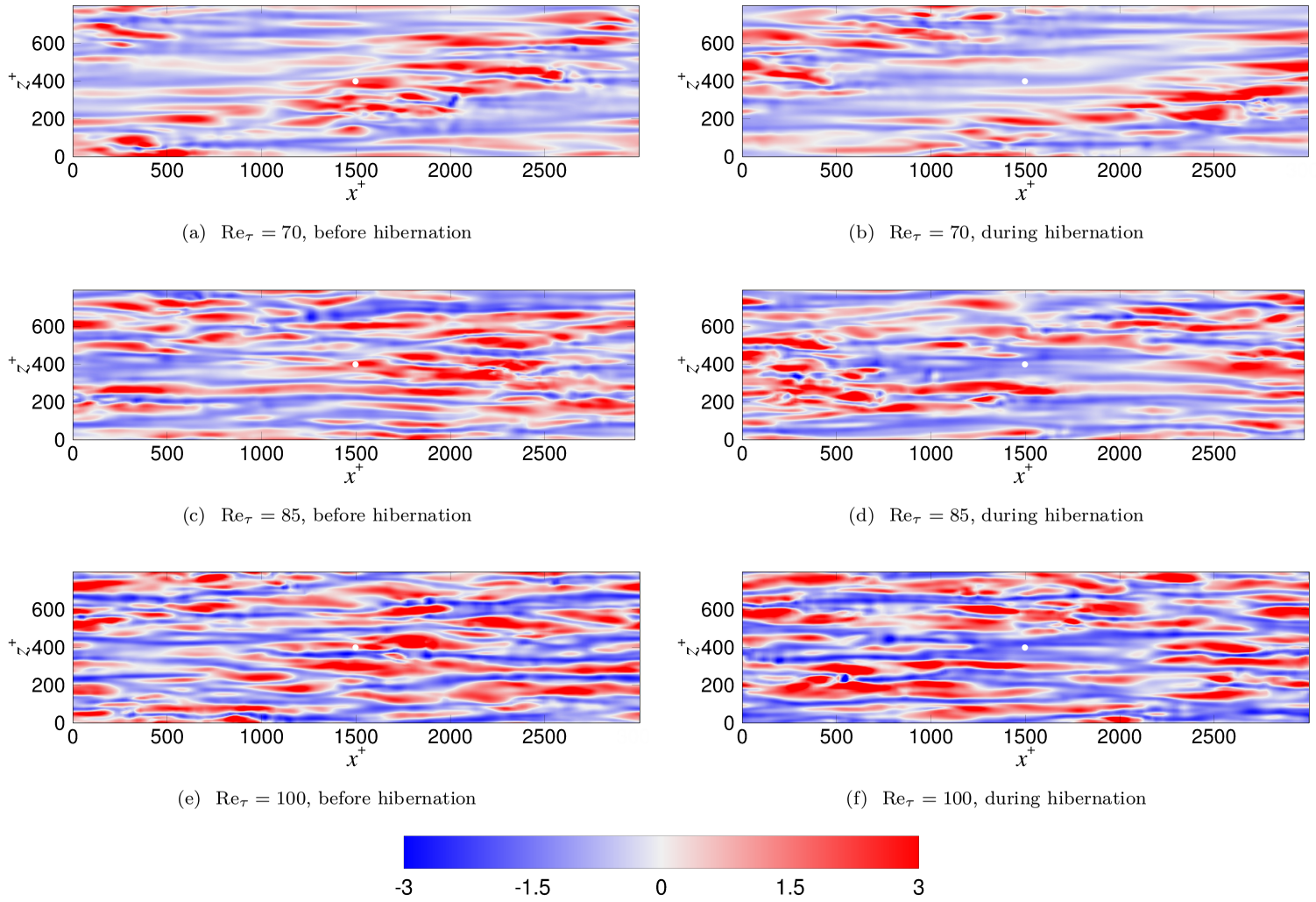

(a) $\mathrm{Re}_\tau = 70$, before hibernation

(b) $\mathrm{Re}_\tau = 70$, during hibernation

(c) $\mathrm{Re}_\tau = 85$, before hibernation

(d) $\mathrm{Re}_\tau = 85$, during hibernation

(e) $\mathrm{Re}_\tau = 100$, before hibernation

(f) $\mathrm{Re}_\tau = 100$, during hibernation

Figure 4.2: Spatial patterns of instantaneous wall shear stress fluctuations in the x-z plane of a turbulent channel flow at ((a), (b)) $\mathrm{Re}_\tau = 70$, ((c), (d)) 85 and ((e), (f)) 100. Figures in the left column show patterns before hibernation, and figures in the right column depict patterns during hibernation.

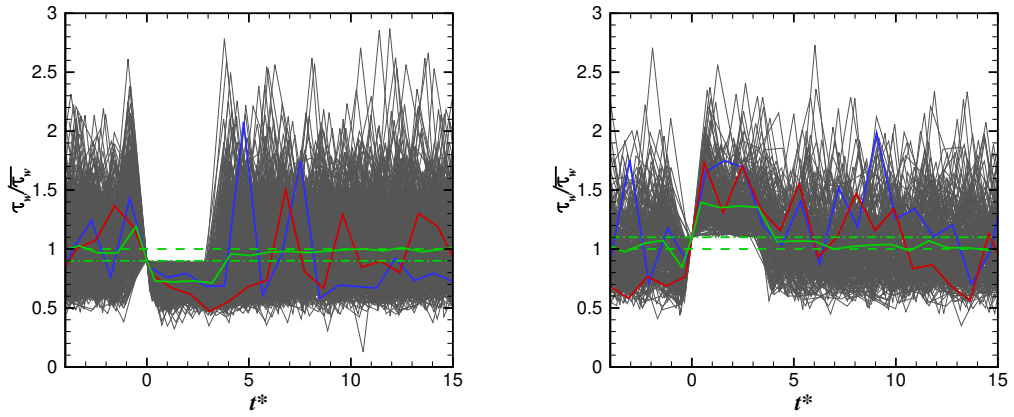

(a) Hibernating turbulence (b) Hyperactive turbulence

Figure 4.3: Instantaneous (thin grey lines) and ensemble-averaged (thick green solid line) wall shear stress before, during and after the intervals of hibernation and hyperactivity at $\mathrm{Re}_\tau = 85$. The thick blue and red lines highlight specific individual instantaneous events with a duration of 4 and 6 eddy turnover times, respectively. The mean wall shear stress is represented by the green dashed line and the threshold by the green dashed-dotted line. All the events are shifted along the time-axis such that $t^* = 0$ represents their beginning.

4.1.2. We do not yet have a physical explanation as to why there is a spike in wall shear stress before hibernation or a dip before hyperactivity.

The abovementioned characteristics of hibernation and hyperactivity are observed for a range of Reynolds numbers studied ($\mathrm{Re}_\tau = 70, 85, 100$). Figure 4.4(a) shows ensemble-averaged wall shear stress before, during and after hibernation for three different Reynolds numbers. Error bars representing standard error of the data at their respective Reynolds number are also shown. The error bars are small, especially within the low drag events.

As the Reynolds number is increased, keeping the threshold the same, the decrease in wall shear stress during hibernation events becomes larger. This claim is supported by the observation that the standard error during hibernation events is smaller than the variation in the wall shear stress observed with increasing Re_τ. On the other hand, the effect of Reynolds number on the strength of hyperactive turbulence is not very clear as shown in Figure 4.4(b), although a drop in wall shear stress before the start of hyperactivity is still observed for all the cases.

Figure 4.5 illustrates what happens to the wall shear stress as flow leaves hibernation. Here, data from Figure 4.3(a) and Figure 4.4(a) are replotted with the time axis shifted such that $t^* = 0$

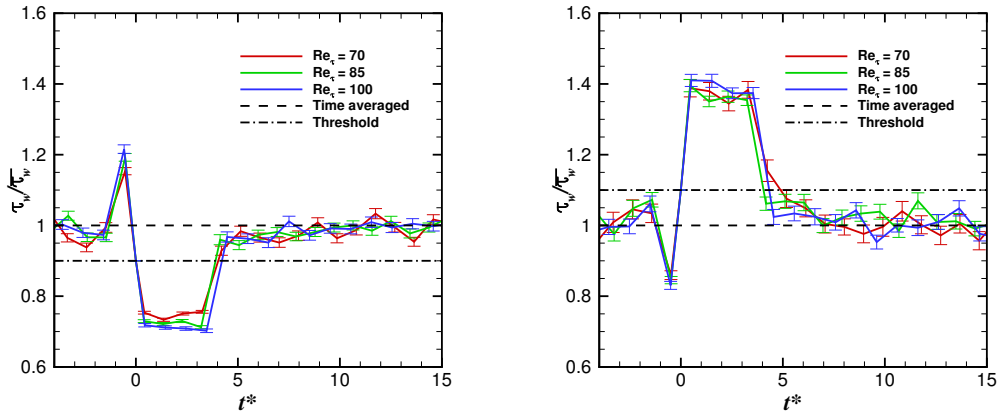

(a) Threshold $\tau_w/\overline{\tau_w} \leq 90\%$ (b) Threshold $\tau_w/\overline{\tau_w} \geq 110\%$

Figure 4.4: Ensemble-averaged wall shear stress before, during and after hibernation and hyperactivity at different Reynolds numbers along with the mean and sampling threshold values. Error bars indicate standard error. Here $t^* = 0$ corresponds to the beginning of an event.

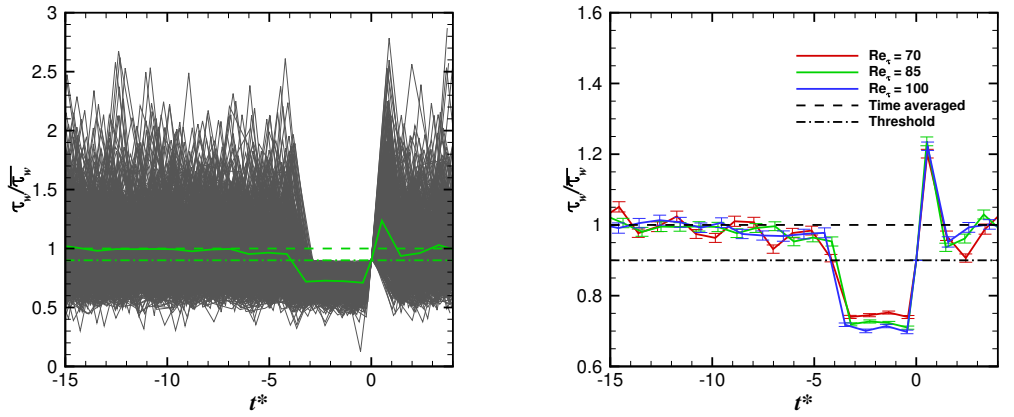

(a) (b)

Figure 4.5: (a) Instantaneous and ensemble-averaged wall shear stress at $\mathrm{Re}_\tau = 85$, and (b) Ensemble-averaged wall shear stress at different Reynolds numbers as the flow leaves hibernation. Error bars indicate standard error. Here $t^* = 0$ corresponds to the end of an event.

represents the *end* of a hibernation event. We observe that on average, as the flow leaves hibernation, there is a brief spike in the wall shear stress. This effect is observed at all Reynolds numbers considered. As seen earlier in Figure 4.4(a), the strength of hibernation increases with Reynolds

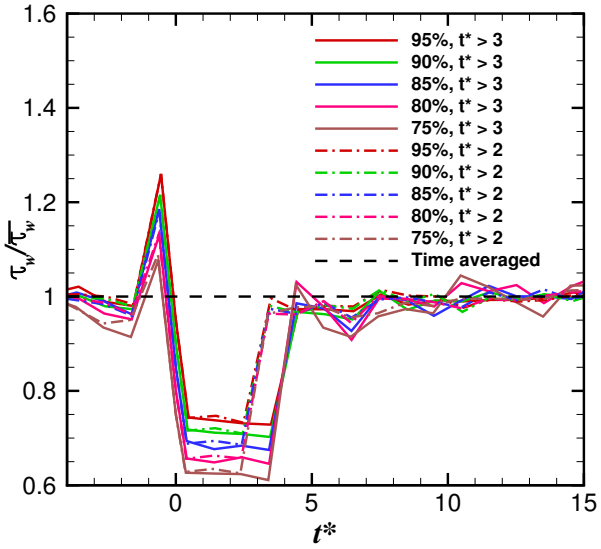

Figure 4.6: Conditional wall shear stress for start of hibernation at $\mathrm{Re}_\tau = 100$. Results are presented for various threshold criteria (95%, 90%, 85%, 80%, 75% — increasing hibernation strictness in that order) and time durations ($t^* > 3$ and $t^* > 2$). Error bars are not shown to avoid overcrowding. Here $t^* = 0$ corresponds to the beginning of a hibernation event.

number.

A detailed sensitivity analysis at $\mathrm{Re}_\tau = 100$, showing the effect of both threshold and time duration criteria on the stress plateau just after the beginning of hibernation, is presented in Figure 4.6. It is observed in Figure 4.6 that as the threshold criterion for hibernation is made more stringent, i.e., going from 95% to 75% of the mean stress, the stress during hibernation becomes smaller, but for a constant threshold, the stress plateau remains the same for both the durations, indicating that the cut-off duration has no effect on the strength of hibernation. Results for the exit from hibernation as well as for hyperactivity are analogous, as are those at $\mathrm{Re}_\tau = 70$ and 85. Thus, for brevity, they are omitted.

4.1.2 Statistics of temporal events

In this chapter we quantify the duration and frequency of occurrence of hibernating and hyperactive turbulence and their dependence on Reynolds number. The statistics reported in this chapter are obtained from simulation runs over a duration of 60000 l/U_c (more than 25 Re) for all the cases.

The average duration of hibernating events is calculated as:

$$\overline{t_H} = \frac{\sum_{n=1}^{N_H} t_{H,n}}{N_H} \tag{4.1}$$

where $t_{H,n}$ is the duration of the nth hibernating interval and N_H is the total number of hibernating intervals identified in the data set. On similar lines, we can define temporal intermittency factors for hibernation and hyperactivity, specifically, the fraction of time flow spends in hibernation and hyperactivity, respectively. These intermittency factors are calculated as:

$$F_H = \frac{\sum_{n=1}^{N_H} t_{H,n}}{T} \tag{4.2}$$

$$F_{HA} = \frac{\sum_{n=1}^{N_{HA}} t_{HA,n}}{T} \tag{4.3}$$

Here, F_H and F_{HA} are temporal intermittency factors for hibernation and hyperactivity, respectively, $t_{HA,n}$ is the duration of the nth hyperactive interval and T is the total duration of the simulation. Note that $F_H + F_{HA} < 1$ because for the major part of the total time the flow is neither in hibernation nor in hyperactivity. The quantities calculated from above equations are plotted in Figure 4.7 illustrating their dependence on Reynolds number.

We observe that the fraction of time spent in hibernation, F_H, decreases with increase in Reynolds number. In contrast, the average duration of hibernating intervals remains almost invariant with the change in Re_τ: it is a bit higher than the cut-off duration chosen for the identification of hibernating or hyperactive events, i.e., $t^* = 3$. The average duration of hyperactive events, $\overline{t_{HA}}$, was also calculated using an expression analogous to Equation (4.1) and it was found to be very similar to $\overline{t_H}$ (hence not plotted to avoid overcrowding). Since 3 is the minimum duration for hibernation and hyperactivity, their average duration must be larger than 3. The fraction of time spent in hyperactivity, F_{HA}, increases with increasing Re_τ. With the average duration of hibernation and hyperactivity remaining almost invariant with Reynolds number, and the corresponding time-fraction decreasing and increasing, respectively, the following inferences can be drawn for hibernating and hyperactive

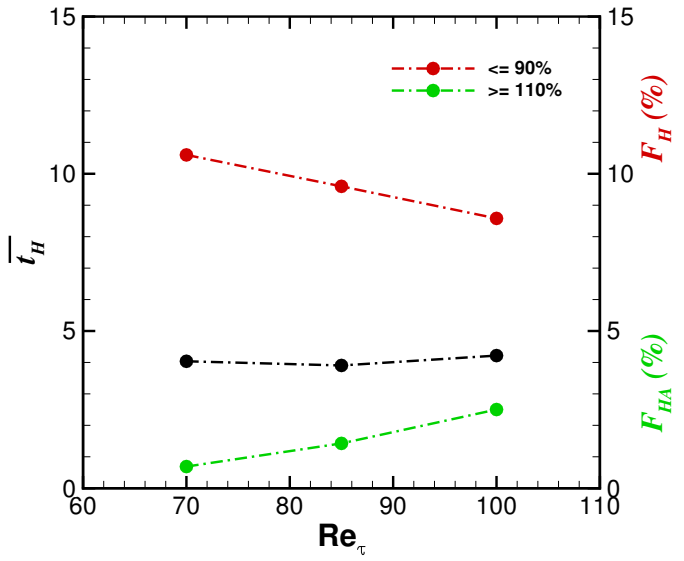

Figure 4.7: Average duration of hibernating turbulence (left ordinate) and the fraction of time spent in hibernation and hyperactivity, F_H and F_{HA}, respectively, (right ordinate) as functions of friction Reynolds number.

turbulence. Increasing the Reynolds number and/or the strictness of the threshold criterion makes hibernation happen less frequently. Secondly, the frequency of occurrence of hyperactive turbulence decreases with the threshold whereas it increases with the Reynolds number.

It is important to note that the abovementioned quantities, $\overline{t_H}$, F_H, $\overline{t_{HA}}$ and F_{HA}, should be interpreted in terms of their behaviour and trend with respect to Re_τ and the threshold; their specific values will definitely depend on the choice of the cut-off duration for a hibernating/hyperactive event. For example, if we choose $t^* = 2.5$ as the criterion for a hibernating/hyperactive event, $\overline{t_H}$ and $\overline{t_{HA}}$ decrease and F_H and F_{HA} increase. Nevertheless, the overall trends remain similar to the $t^* = 3$ case. It is also worth noting that the occurrence of hyperactive events is in general very infrequent — all the cases reported are less than 5%, and they become extremely rare at low Reynolds numbers ($< 1\%$).

It is worth mentioning that the finite box size does seem to have some effect on intermittency factors: we calculated the same quantities for a box 1.7 times bigger in both streamwise and spanwise directions and found that both F_H and F_{HA} have reduced. Their trend as a function of Re_τ remains the same, however. On the other hand, it should also be noted that the *conditional* quantities

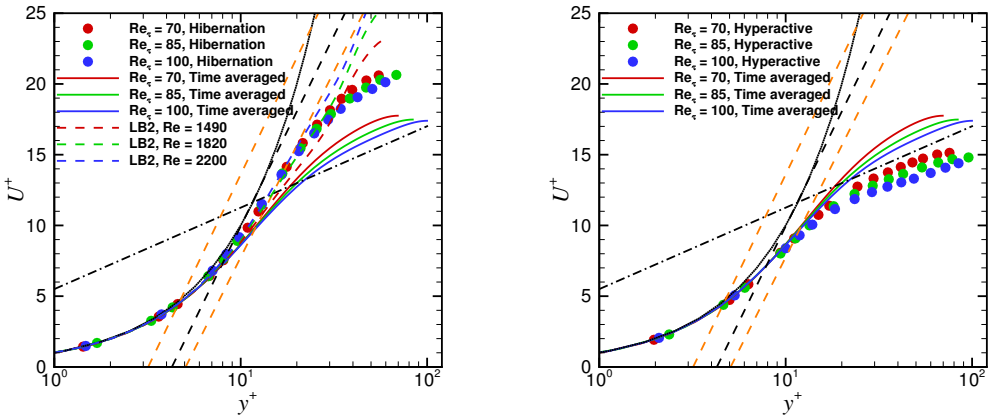

(a) Threshold $\tau_w/\overline{\tau_w} \leq 90\%$ (b) Threshold $\tau_w/\overline{\tau_w} \geq 110\%$

Figure 4.8: Unconditional (solid lines) and conditional (filled circles) ensemble-averaged streamwise mean-velocity profiles at different Reynolds numbers. The black dotted line is the viscous sublayer, $U^+ = y^+$; black dashed-dotted line is the Prandtl-von Kármán log-law, $U^+ = 2.5 \ln y^+ + 5.5$ and the black dashed line is the Virk MDR log-law, $U^+ = 11.7 \ln y^+ - 17.0$. The orange dashed lines show the lower and upper 95% confidence intervals to the MDR asymptote Virk et al. [1970]; Graham [2014].

including wall shear stress (including the precursor peak and plateau), mean velocity and flow structures, are insensitive to a further increase in box size.

4.1.3 Conditional mean velocity profiles

Figure 4.8 shows the streamwise unconditional time averaged velocity profiles at different Reynolds numbers with solid lines. These all lie slightly above the Prandtl-von Kármán log-law and are in good agreement with experimental and other numerical values reported in the literature at similar Reynolds number [Patel and Head, 1969; Kasagi and Shikazono, 1995; Tsukahara et al., 2005]. In Figure 4.8(a) we also present in solid circles the conditional mean velocity profiles during hibernation events at the same Reynolds numbers, evaluated on a line extending from the measurement point $\boldsymbol{x}_s$ vertically into the fluid. These profiles are calculated by first determining the ensemble-averaged streamwise velocity for several hibernation events, averaging it over the plateau region $t^* = 0.7 - 3.0$, and finally scaling it with the hibernating wall shear stress determined during the same time interval. For reference, also shown on the same plot is the 95% confidence interval to the MDR asymptote within which velocity profiles in the MDR regime from a number of representative computational

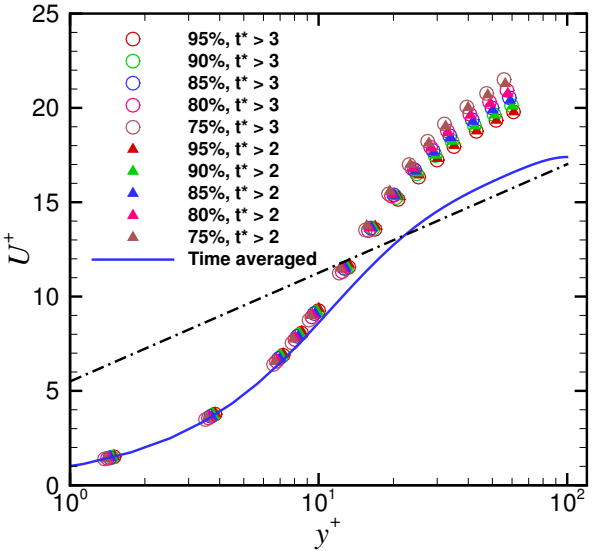

Figure 4.9: Unconditional (line) and conditional (symbols) mean velocities for hibernation at $\mathrm{Re}_\tau = 100$. Results are presented for various threshold criteria ($95\%, 90\%, 85\%, 80\%, 75\%$ — increasing hibernation strictness in that order) and time durations ($t^* > 3$ and $t^* > 2$).

and experimental studies lie [Graham, 2014] — close to the wall, data for polymer solutions lies close to the lower end of the interval, while farther from the wall it approaches the upper end. The hibernating profiles lie well above the Prandtl-von Kármán log-law, and in fact brush against the lower end of the MDR confidence interval. Figure 4.8(a) also shows mean velocity profiles of lower branch ECS. It is observed that in the region $y^+ \lesssim 30$ the conditional and ECS velocity profiles are very similar while close to the centreline the conditional turbulent mean deviates downward from the ECS profile. Even in the low drag intervals the turbulence has fluctuations in the core of the flow that are absent from the P4 lower branch solutions. Only a weak dependence of conditional profiles on Re_τ is observed.

Mean velocity profiles during hyperactive turbulence are illustrated in Figure 4.8(b), alongside the unconditional profiles at the same Reynolds numbers. It is observed that as the Reynolds number is increased keeping the threshold criterion fixed, the mean velocity profile of the hyperactive event moves down, away from the Prandtl-von Kármán log-law.

A detailed sensitivity analysis at $\mathrm{Re}_\tau = 100$, showing the effect of both threshold and time duration criteria on the velocity profiles, is presented in Figure 4.9. Increasing the strictness of

the stress threshold (different coloured curves) results in the lowering of the plateau stress during hibernation (Figure 4.6), which then results in the elevation of velocity profile in the region $y^+ \gtrsim 20$ as shown in Figure 4.9. Note that here also, and in all the future chapters, each velocity profile is scaled with the corresponding mean wall shear stress, unconditional or conditional as the case may be. On the other hand, the velocity profiles are insensitive to the the time duration (circles and triangles) — this result is consistent with with insensitivity of the the stress plateau during hibernation on the duration threshold. The same trends are obtained for $\mathrm{Re}_\tau = 70$ and 85.

4.1.4 Spatial variation of wall shear stress and flow structures during temporal hibernation events

In this chapter we look at the spatial patterns of wall shear stress and velocities observed before and during hibernation intervals. In particular, flow behaviour at and away from the measurement location and its relation to hibernation and hyperactivity are discussed. Figures 4.10(a) and 4.10(b) show the spatial structure of ensemble-averaged wall shear stress fluctuations at $\mathrm{Re}_\tau = 85$ before ($t^* = -0.52$) and during ($t^* = 0.41$) the hibernation event as observed at the white dot at the wall at $(x^+, z^+) = (1500, 400)$. They are generated by identifying several instantaneous hibernation events at the centre of the domain (white dot) based on the set criteria, $\tau_w/\overline{\tau_w} \leq 90\%$ for a duration of $t^* > 3$ for this case, shifting the time-axis so that $t^* = 0$ corresponds to the time of the onset of hibernation, i.e., when the wall shear stress starts to fall below the threshold, and finally ensemble-averaging all the conditionally-sampled instantaneous wall shear stress-fluctuations fields, $\tau'_w(x, z, t)$, corresponding to the given time. Here, the fluctuating field is given as $\tau'_w = \tau_w - \overline{\tau_w}$. Ensemble-averaged results at $\mathrm{Re}_\tau = 70$ and 100 are qualitatively similar and hence not shown. The "before" picture (Figure 4.10(a)) shows a region of higher-than-mean wall shear stress (red colour) that corresponds to the precursor peak in the local wall shear stress as observed in Figure 4.3(a). It also shows a region of lower-than-mean wall shear stress (blue colour) trailing behind the red region. This blue region has fully developed in the "after" picture (Figure 4.10(b)) and it corresponds to the plateau in the local wall shear stress in Figure 4.3(a), depicting the low wall shear stress nature of hibernating turbulence, for example, an elongated low-speed streak spanning a length of approximately 1500 and 50 viscous wall units in the streamwise and spanwise directions, respectively. This low-speed streak

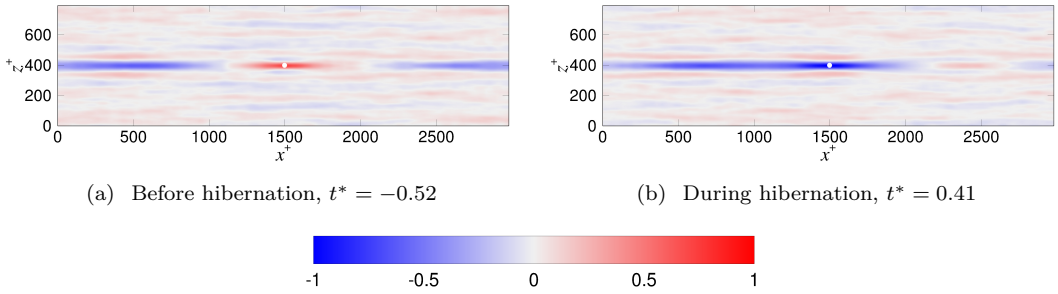

(a) Before hibernation, $t^* = -0.52$ (b) During hibernation, $t^* = 0.41$

Figure 4.10: Spatial patterns of ensemble-averaged conditionally-sampled ($\tau_w/\overline{\tau_w} \leq 90\%$) wall shear stress fluctuations at $\mathrm{Re}_\tau = 85$ before and during hibernation.

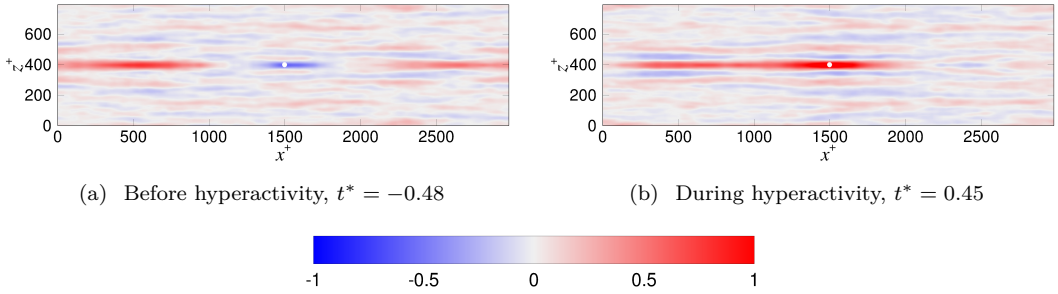

(a) Before hyperactivity, $t^* = -0.48$ (b) During hyperactivity, $t^* = 0.45$

Figure 4.11: Spatial patterns of ensemble-averaged conditionally-sampled ($\tau_w/\overline{\tau_w} \geq 110\%$) wall shear stress fluctuations at $\mathrm{Re}_\tau = 85$ before and during hyperactivity.

is a result of a low wall shear stress region and corresponds to a localised pair of counter-rotating vortices. The structures of these vortex pairs is discussed below. Sample instantaneous wall shear stress-fluctuations fields before and during hibernation are shown in Figure 4.2. In all the "before" pictures (left column) we can see high wall shear stress at the measurement location while in the "after" pictures (right column), a low wall shear stress is seen at the same location.

We use the method described above to generate the ensemble-averaged spatial patterns of the wall shear stress before and during hyperactivity. The light blue colour in the centre of Figure 4.11(a) corresponds to the very brief drop in the wall shear stress before the start of hyperactivity, for example, see Figure 4.3(b). The red region trailing behind it which is fully developed in the channel centre (Figure 4.11(b)) corresponds to the higher-than-mean wall shear stress during hyperactivity. As discussed in Chapter 4.1.2, the frequency of occurrence of hyperactive events is very low — only

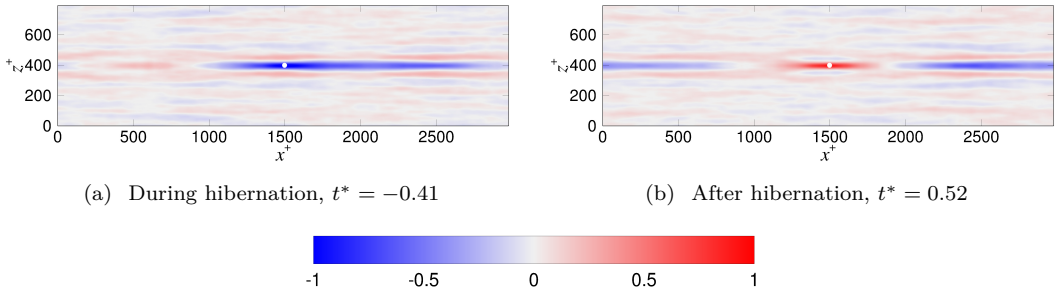

(a) During hibernation, $t^* = -0.41$ (b) After hibernation, $t^* = 0.52$

Figure 4.12: Spatial patterns of ensemble-averaged conditionally-sampled ($\tau_w/\overline{\tau_w} \leq 90\%$) wall shear stress fluctuations at $\mathrm{Re}_\tau = 85$ during and after hibernation.

about 2% of the total time is spent in hyperactivity for the case plotted. Thus, averaging in even very long trajectories does not give good statistics. This effect can in fact be observed at points far from the measurement location in Figure 4.11 where the wall shear stress does not revert as smoothly as in the case of low-drag events back to the overall mean value.

We now look at the spatial patterns at $\mathrm{Re}_\tau = 85$ as the flow leaves hibernation. In Figure 4.5(a) we observed a brief spike in the wall shear stress just after the hibernation period. The plateau of low wall shear stress is illustrated by an elongated low-speed streak in Figure 4.12(a) and the spike that follows by a region of elevated wall shear stress at the measurement location in the centre in Figure 4.12(b).

In the spatial patterns presented above for the three cases: (1) before and during hibernation, (2) before and during hyperactivity, and (3) during and after hibernation, reflection symmetry was enforced in the spanwise direction. Therefore, we do not get any information about the orientation of an ensemble-averaged hibernation event with respect to the mean flow, i.e., whether it is symmetric or asymmetric. In order to determine the relative orientation of ensemble-averaged hibernation events, we introduce an additional condition while sampling them — the additional condition will determine whether the flow is toward the left or toward the right of the measurement location. This additional condition is described below. In addition to the hibernation criteria, we also measure the following flow quantities: (1) $\partial U/\partial z$ at $y^+ = 15$ above the wall shear stress measurement location, and (2) $\partial W/\partial y$ at the wall shear stress measurement location. While the first quantity tells if a streak is flowing straight ($\partial U/\partial z = 0$) or if it is meandering ($\partial U/\partial z \neq 0$), the second quantity

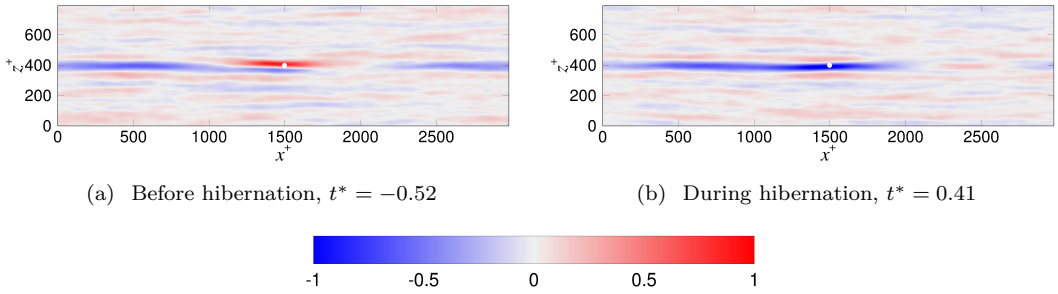

(a) Before hibernation, $t^* = -0.52$ (b) During hibernation, $t^* = 0.41$

Figure 4.13: Spatial patterns of ensemble-averaged conditionally-sampled ($\tau_w/\overline{\tau_w} \leq 90\%$ and $\partial U/\partial z|_{y^+=15} > 0$) wall shear stress fluctuations at $\mathrm{Re}_\tau = 85$ before and during hibernation.

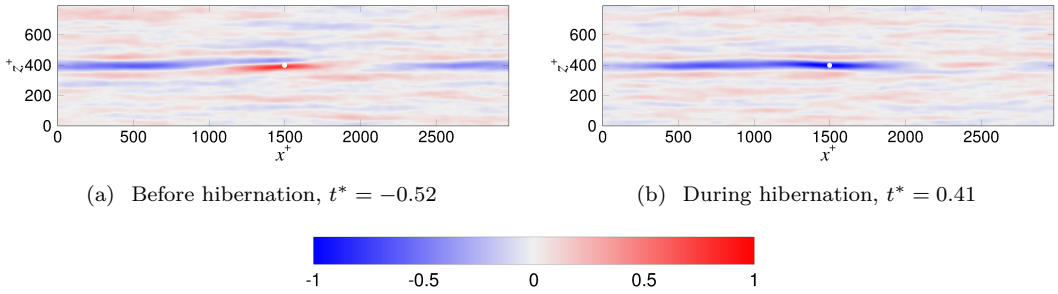

(a) Before hibernation, $t^* = -0.52$ (b) During hibernation, $t^* = 0.41$

Figure 4.14: Spatial patterns of ensemble-averaged conditionally-sampled ($\tau_w/\overline{\tau_w} \leq 90\%$ and $\partial W/\partial y > 0$) wall shear stress fluctuations at $\mathrm{Re}_\tau = 85$ before and during hibernation.

is simply the spanwise wall shear stress. Events that satisfy the hibernation criteria as well as the condition $\partial U/\partial z|_{y^+=15} > 0$ (or $\partial W/\partial y > 0$) are averaged. Hibernation events for which the quantity is < 0 are flipped in the spanwise direction and then the average is computed.

The spatial patterns of wall shear stress fluctuations before and during hibernation satisfying the additional asymmetry criterion are shown in Figure 4.13 (for $\partial U/\partial z|_{y^+=15} > 0$) and Figure 4.14 (for $\partial W/\partial y > 0$). It is observed that for both the cases, compared to the results shown in Figure 4.10, the "before" picture looks somewhat asymmetric whereas the structure during hibernation is very close to being symmetric.

We now look at the flow structures in the cross-flow plane as observed before and during hibernating intervals. In Figure 4.15 we show the ensemble-averaged y-z planes of the channel at $\mathrm{Re}_\tau = 85$ before ($t^* = -0.52$) the hibernation event. Figure 4.15(b) corresponds to the location

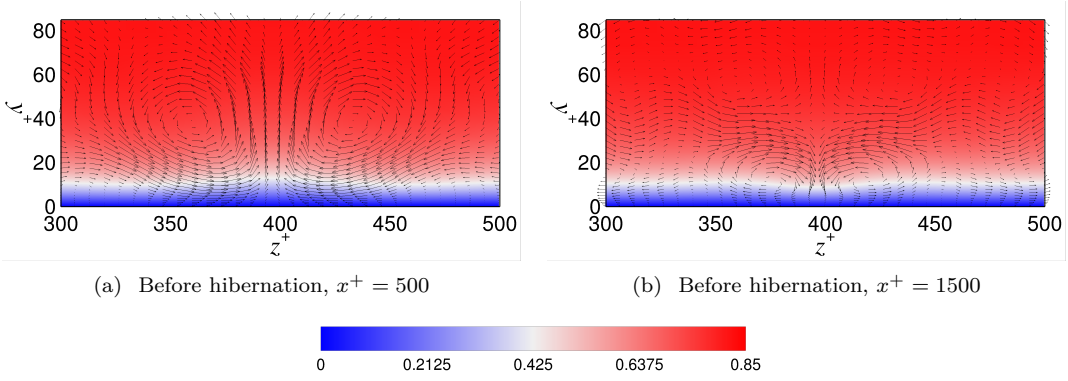

(a) Before hibernation, $x^+ = 500$ (b) Before hibernation, $x^+ = 1500$

Figure 4.15: Flow patterns of ensemble-averaged conditionally-sampled ($\tau_w/\overline{\tau_w} \leq 90\%$) velocities in the y-z plane of a turbulent channel flow at $\mathrm{Re}_\tau = 85$ *before* the hibernation event.

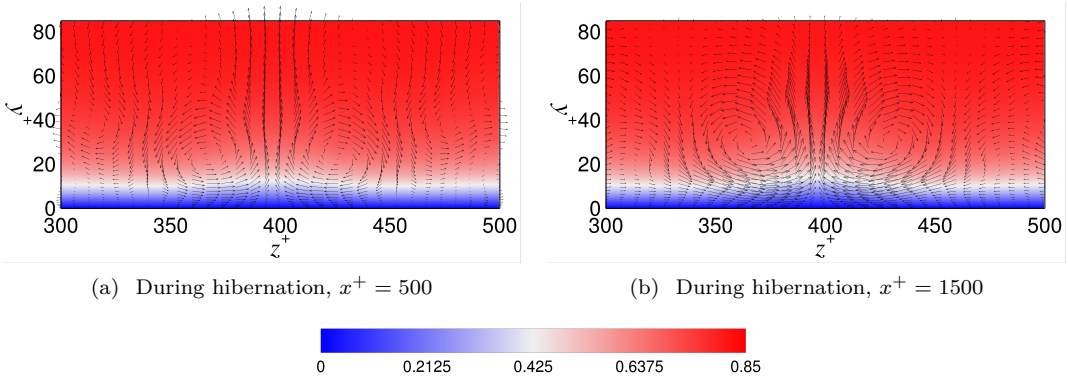

(a) During hibernation, $x^+ = 500$ (b) During hibernation, $x^+ = 1500$

Figure 4.16: Flow patterns of ensemble-averaged conditionally-sampled ($\tau_w/\overline{\tau_w} \leq 90\%$) velocities in the y-z plane of a turbulent channel flow at $\mathrm{Re}_\tau = 85$ *during* the hibernation event.

where measurements are taken, at $x^+ = 1500$, while Figure 4.15(a) corresponds to $x^+ = 500$, a region developing behind the measurement location. Flow is out of the plane. Contours represent the streamwise velocity whereas arrows represent the wall-normal and spanwise velocities. At the measurement location we observe a downward motion of fluid (indicated by downward-pointing arrows) and this momentum transfer toward the wall results in a region of high wall shear stress corresponding to the precursor peak in Figure 4.3(a) and 4.10(a). The low wall shear stress region that trails behind the high wall shear stress is formed due to the motion of fluid away from the wall. This region develops into a long low-speed streak as the flow enters hibernation. This is illustrated in Figure 4.16 for $\mathrm{Re}_\tau = 85$ at $t^* = 0.41$. At both the locations, i.e., measurement location at

$x^+ = 1500$ and trailing location at $x^+ = 500$, we observe transfer of momentum away from the wall which corresponds to counter-rotating streamwise vortex pairs that result in a long streamwise streak as observed earlier in Figure 4.10(b).

4.2 Spatial intermittency and connections to nonlinear travelling waves

4.2.1 Spatial distribution of hibernation and quantification of spatial intermittency

We now turn from temporal sampling to *spatial* sampling of the channel flow dynamics. To discriminate between spatially occurring high, intermediate and low drag regions and quantify the intermittency, we use a technique similar to what Nolan and Zaki [2013] used to discriminate laminar spots from turbulent spots. Specifically, we introduce a detector function that uses information from longitudinal and lateral variations of velocity, and compute this for each snapshot obtained from DNS. Simply using the wall shear stress as the detector function is not desirable because even in a region of high turbulence activity there will be low stress regions corresponding to low-speed streaks. We found that a better detector function combines the wall shear stress with the spanwise derivative of the streamwise velocity above the wall in the buffer layer:

$$D\left(x,z\right) \equiv \left|\frac{\partial U}{\partial y}\right|_w + \left|\frac{\partial U}{\partial z}\right|_{y^+=15}. \tag{4.4}$$

The first term on the right-hand side is simply the drag; the reasoning for choosing the second term is as follows. It is known that the streaks do not always flow straight in the streamwise direction — they meander in the spanwise direction as well. Johansson et al. [1991] showed that streaky structures asymmetric in the spanwise direction result in large turbulence production. To take this into account, we include the streamwise velocity gradient in the spanwise direction, $\partial U/\partial z$, in the buffer layer at the point of maximum variance, $y^+ = 15$, in our detector function. We did consider other detector functions, for example, $D = |\partial U/\partial y|_w + |\partial W/\partial y|_w$, where W is the spanwise velocity

— both gave very similar results. This function is lowpass-filtered by a Gaussian filter, the size of which is set according to correlation lengths: the characteristic streamwise length of the streak (600 wall units) and the characteristic stream spacing (100 wall units). We then apply Otsu's method independently to the D field for each snapshot [Otsu, 1979], which results in a demarcation between regions of varying levels of turbulence. We emphasise that there are no explicit thresholds of either time or stress level in Otsu's method — all we specify is the number of classes we want the data at each time instant to be classified into. Otsu's method picks out the optimum threshold by minimising the *intra-class* variance, or in other words, maximising the *inter-class* variance. We specify that three classes be sought (corresponding to low, intermediate and high values of D). The boundaries (or edges) between any two classes results in demarcation of weakly, intermediately and strongly fluctuating regions (hibernating, active and hyperactive).

An example of the result of the Otsu algorithm is shown in Figure 4.17. The contours in Figure 4.17(b) represent the wall shear stress patterns from an instantaneous flow-field at $\mathrm{Re}_\tau = 85$. Black solid and dashed lines correspond to the two thresholds obtained from the filtered detector function at the same time instant, the contours of which are shown in Figure 4.17(a). The solid line represents the demarcation line between high-drag and intermediate-drag regions and the dashed line separates the intermediate-drag areas from the low-drag areas. A distinct difference between the three regions is observed — areas enclosed by solid lines show high wall shear stress and strong fluctuations whereas the areas enclosed by dashed lines are smooth, local wall shear stress values are low and the variations are small. Regions between solid and dashed lines lie in the intermediate-drag regime.

Streamwise velocity profiles are sampled conditionally for the three intermittent spatial regimes — low, intermediate and high D — and averaged over those conditional areas for the entire time series. Note that we are treating all the spatially occurring low drag events equally — an event covering a large area is given equal weightage as two or more widely separated events covering the same area. Same is applicable to intermediate and high drag events. In Figure 4.18(a), 4.18(b) and 4.18(c) we compare conditionally-averaged mean velocity profiles from edge-detection scheme with the pointwise thresholding results discussed earlier in Chapter 4.1.3. We see a clear dependence of mean flow statistics on the spatially intermittent nature of near-wall turbulence — the conditional profiles in the low and high drag regions lie respectively, above and below, the intermediate drag

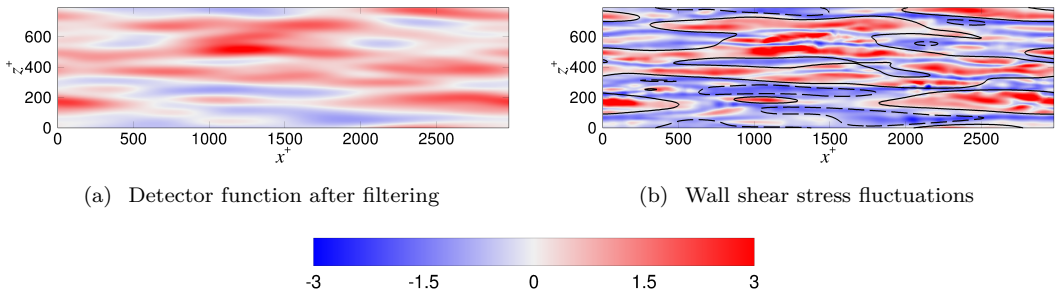

(a) Detector function after filtering (b) Wall shear stress fluctuations

Figure 4.17: Contours of (a) detector function after filtering and (b) spatial patterns of wall shear stress fluctuations from a single snapshot of DNS at $\mathrm{Re}_\tau = 85$, along with the thresholds (solid and dashed curves) obtained from application of Otsu's method to the field shown in (a).

conditional profile which lies almost over the unconditional time averaged velocity profile. This is observed at all the Reynolds numbers. We also find a very good agreement of velocity profiles of hibernating, active and hyperactive turbulence that were based on temporal analysis with those from spatial analysis, i.e., conditional low and high drag velocity profiles from temporal sampling show good correspondence with the conditional low and high drag profiles, respectively, from spatial analysis. It is important to emphasize that the temporal and spatial sampling techniques are completely different from one another (the temporal analysis requires thresholds on wall shear stress and time duration to be specified explicitly while there are no predetermined thresholds in the spatial analysis), so the quantitative similarity between the results is a reflection of the robustness of the intermittency phenomenon in these flows. Here also, the agreement between velocity profiles of lower branch ECS and low drag regions is good in the region $y^+ \lesssim 30$, especially for $\mathrm{Re}_\tau = 70$ and 85.

In the above results, we have illustrated the intermittent dynamics (both temporal and spatial) of transitional channel flow turbulence in an extended domain. In minimal channels, the intermittency is associated with the chaotic movement of turbulent trajectories between lower and upper branch ECS. In Figure 4.19, we compare conditional mean profiles from our analyses here to those in the minimal channel. Velocity profiles of ECS are also included for comparison. The mean velocity profile of low drag events in the minimal channel is determined using the log-law slope criterion developed by Xi and Graham [2012b]: the instantaneous log-law slope of the velocity profile (A^*_{20-30}) is obtained in the interval $y^* = 20 - 30$, and if $A^*_{20-30} > 7$, it is considered to be low drag (or hibernation). Here, the superscript '$*$' indicates normalisation with the instantaneous viscous length scale. It is

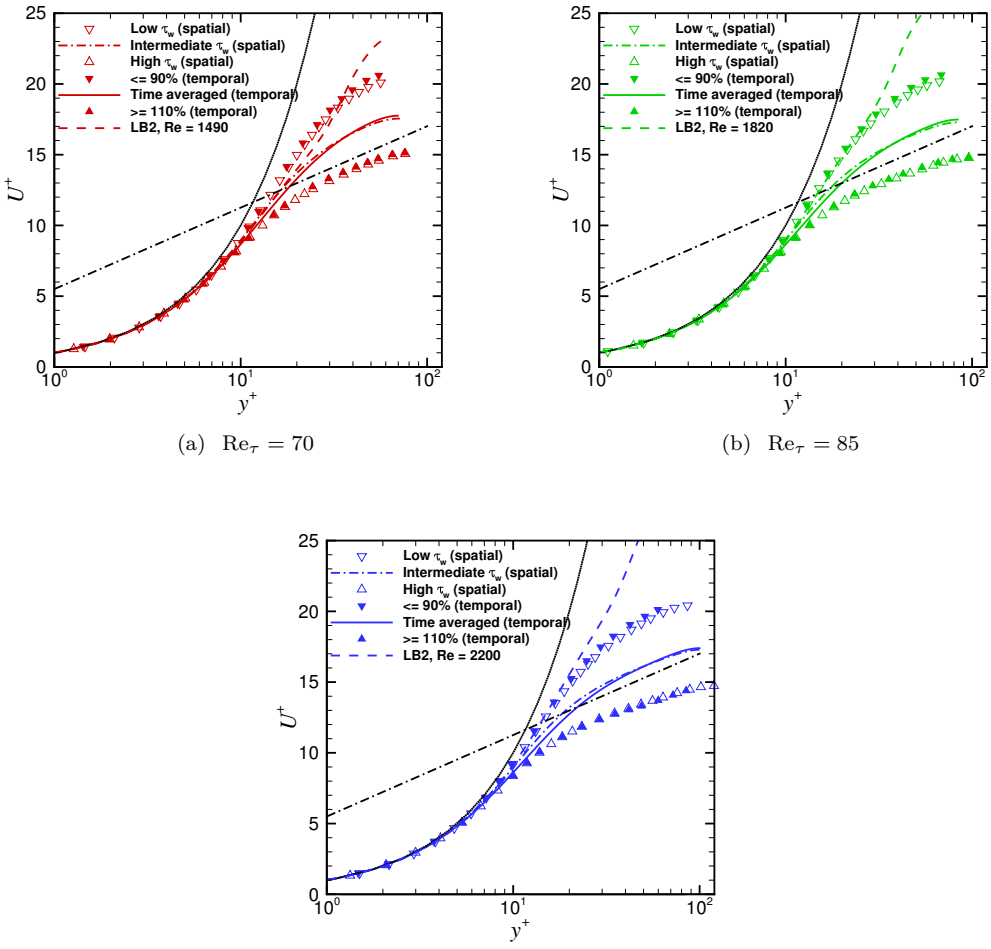

(a) $\mathrm{Re}_\tau = 70$ (b) $\mathrm{Re}_\tau = 85$

(c) $\mathrm{Re}_\tau = 100$

Figure 4.18: A comparison between conditionally-averaged streamwise velocity profiles based on time and space criteria at the corresponding Reynolds number.

observed that all the low drag velocity profiles — both minimal and large domain — show very good agreement. The agreement with lower branch ECS profile is also excellent in the region $y^+ \lesssim 30$.

Finally, we quantify the spatially intermittent nature of hibernation. Figure 4.20 shows intermittency factors for hibernation based on temporal and spatial sampling techniques: the red line from temporal sampling as one shown in Figure 4.7 and the green line is based on spatial sampling and

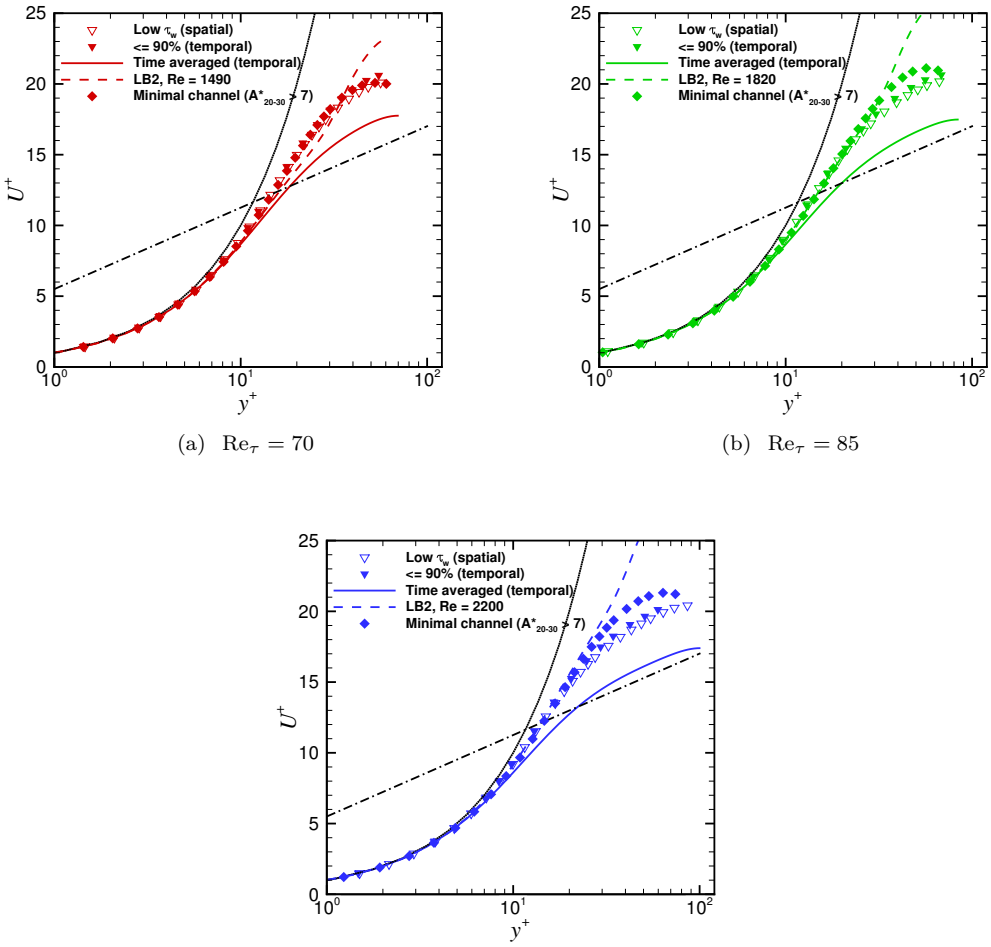

(a) $\mathrm{Re}_\tau = 70$ (b) $\mathrm{Re}_\tau = 85$

(c) $\mathrm{Re}_\tau = 100$

Figure 4.19: Comparison of low drag velocity profiles in minimal channel occurring temporally (when $A^*_{20-30} > 7$) with low drag velocity profiles in an extended domain occurring both temporally (when $\tau_w/\overline{\tau_w} \leq 90\%$ for $t^* > 3$) and spatially (regions of low values of $D(x,z)$). Velocity profiles of lower branch ECS are also plotted for comparison.

is calculated as:

$$F_H = \frac{\sum_{n=1}^{N_H} A_{H,n}}{A} \tag{4.5}$$

Here, $A_{H,n}$ is the area of the nth patch of the domain undergoing hibernation at any given time, N_H is the total number of patches in an instantaneous snapshot and A is the total surface area of the wall. It is observed that firstly, both temporal and spatial intermittency factors are very close

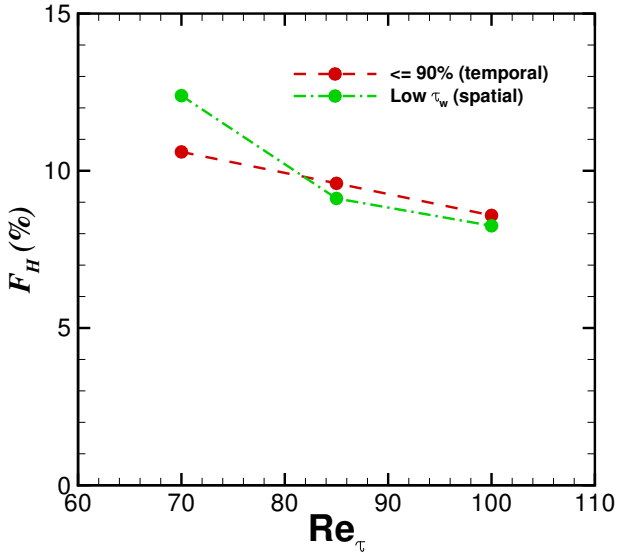

Figure 4.20: Intermittency factors for hibernation, both temporal and spatial, as a function of friction Reynolds number.

to each other for all the Reynolds numbers, and secondly, as the Reynolds number is increased, the occurrence of hibernation, both temporally and spatially, decreases. It is worth mentioning that, by construction, the spatial separation of hibernation patches is larger than the correlation lengths of the flow. The average separations between the centres of mass of hibernation patches in the streamwise and spanwise directions, respectively, in wall units, are 1131.54×288.14 for $\mathrm{Re}_\tau = 70$, 1108.87×282.32 for $\mathrm{Re}_\tau = 85$ and 1113.66×282.19 for $\mathrm{Re}_\tau = 100$. In other words, it is higher than the correlation lengths in the streamwise and spanwise directions, respectively, by a factor of 1.89×2.88 for $\mathrm{Re}_\tau = 70$, 1.85×2.82 for $\mathrm{Re}_\tau = 85$ and 1.86×2.82 for $\mathrm{Re}_\tau = 100$. There does not seem to be a clear dependence of the mean spatial separation between hibernation patches on Reynolds number, but the area of the region undergoing hibernation does depend on Reynolds number as already shown in Figure 4.20. It is noteworthy that we get nearly identical velocity profiles and intermittency factors from two completely independent thresholding criteria, one based on time, and the other based on space.

4.2.2 Connections to nonlinear travelling waves

Figure 4.21 illustrates a bifurcation diagram of average velocity versus friction Reynolds number for the "P4" family of minimal domain travelling wave (TW) solutions discussed in Chapter 2. These solutions have streamwise and spanwise periods of length π and $\pi/2$, respectively, in outer units. A solution with higher friction Reynolds number (Re_τ) is an upper branch (UB) solution corresponding to high drag, while that with lower Re_τ is a lower branch (LB) solution. Curves for the Prandtl-von Kármán and Virk MDR log law profiles are also shown. In this representation, also known as the Prandtl-von Kármán plot, the lower branch solutions lie above the upper branch solutions, because for the same wall shear stress, a lower branch solution has higher bulk velocity than the upper branch solution. We will make comparisons between extended-domain DNS results and minimal channel ECS at constant mass flux (laminar centreline velocity Re). The DNS at $\mathrm{Re}_\tau = 70$, 85 and 100 have Reynolds numbers based on the laminar centreline velocity (Re) of 1490, 1820 and 2200, respectively. The ECS used for comparison are represented on the plot as red, green and blue triangles, respectively. Triangles pointing upwards are upper branch solutions whereas triangles pointing downwards are lower branch solutions. For the P4 family, there are two lower-branch-solution branches, denoted as "LB1" and "LB2", and two upper-branch-solution branches, denoted as "UB1" and "UB2" [Park and Graham, 2015]. Lower branch solutions used for comparison with DNS that lie on the LB1 branch are represented as hollow triangles while the ones that lie on the LB2 branch are represented as filled triangles. Only the solutions that lie on the UB1 upper branch are used for comparison — the UB2 branch has not yet been successfully resolved for higher Re. Mean velocity profiles of these travelling wave solutions are illustrated in Figure 2.1(b). A subharmonic branch (SB) arises above the turning point of the LB solutions at $\mathrm{Re}_\tau = 88.7$, giving rise to spatiotemporal period doubling — this branch has doubled fundamental spatial periods in the streamwise and spanwise directions compared to the P4 solution family.

It should be kept in mind that the ECS used for comparison here come from one particular family (P4) at one particular domain size. An interesting feature of this family of solutions, as already mentioned earlier, is that the turbulent dynamics in the minimal channel is organised around these ECS. As illustrated in Figure 2.1(a), Park and Graham [2015] studied connections between travelling wave solutions and turbulent trajectories in a minimal domain, observing that while the

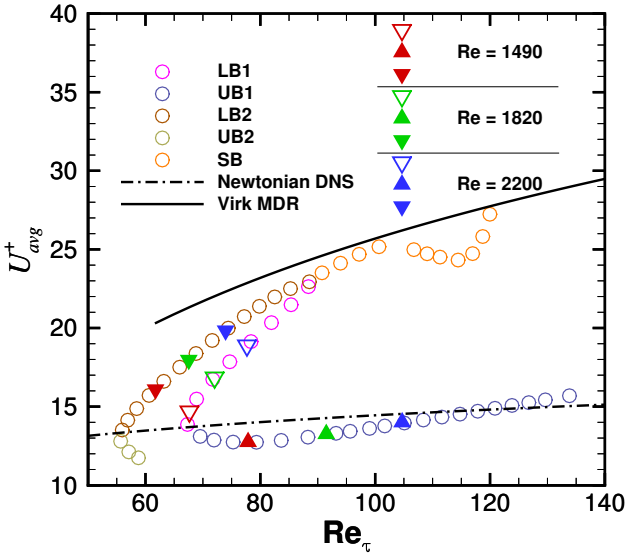

Figure 4.21: Prandtl-von Kármán plot of the bifurcation diagram for the "P4" family of ECS [Park and Graham, 2015]. The average velocities as a function of friction Reynolds number are shown. Corresponding curves for Newtonian turbulence and Virk MDR are also shown.

dynamical trajectory spends most of the time in one core region of the state space, fluctuating about the upper branch ECS UB1, it occasionally escapes the core region and passes through the vicinity of LB1 solutions, approaching LB2 very closely. In particular, LB2 is the closest approach of the trajectories to the laminar state and seems to form a lower bound of the turbulent trajectory with regard to flow properties like wall shear stress, energy dissipation rate and turbulent kinetic energy — see Figure 2.1(a). This observation is further illustrated in Figure 4.22 where we show time series of wall shear stress in minimal channel turbulence at laminar centreline Reynolds numbers of 1490, 1820 and 2200.

To address the relationship between large-box DNS with upper and lower branch ECS, we begin by comparing averages over patches the size of minimal channel ECS in the large domain with the actual ECS. In Figure 4.23 we show time series of wall shear stress measured over a patch the size of a minimal channel, $L_x^+ \approx 360, L_z^+ \approx 140$, and compare it with the wall shear stress of the exact coherent states at the same Re. Due to the saddle-node bifurcation shown in Figure 4.21, we observe that the wall shear stress of both LB1 and LB2 decreases as the Reynolds number is increased. The

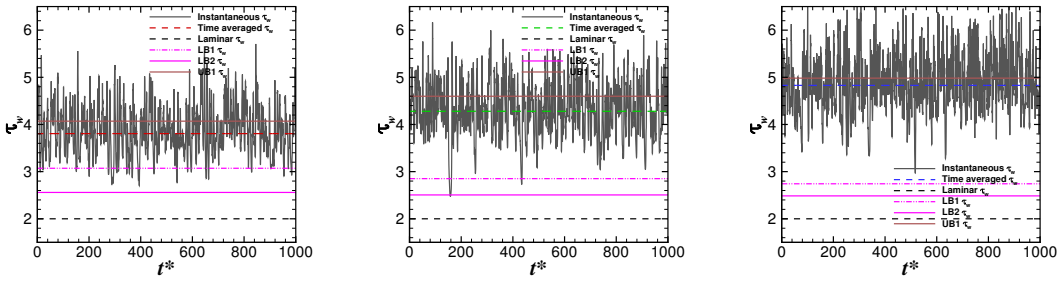

(a) Re = 1490 (b) Re = 1820 (c) Re = 2200

Figure 4.22: Time series of the wall shear stress measured in a minimal channel at different Reynolds numbers. Time averaged values and wall shear stress for upper and lower branch ECS are also shown for comparison.

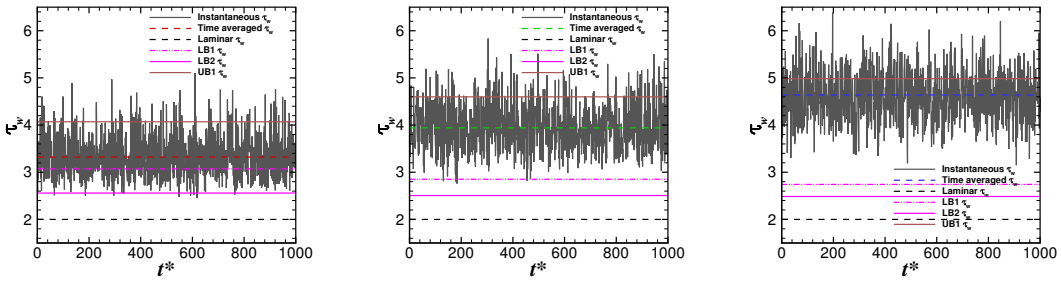

(a) Re = 1490 (b) Re = 1820 (c) Re = 2200

Figure 4.23: Time series of the wall shear stress measured over a minimal patch in a large channel at different Reynolds numbers. Time averaged values and wall shear stress for upper and lower branch ECS are also shown for comparison.

gap between the lower branch ECS and the DNS increases with increasing Reynolds number. The LB2 branch seems to form the lower bound to the wall shear stress for the corresponding large-box DNS; this bound is fairly sharp at low Re but becomes less so as Re increases. This result is important because the same trend has been observed in minimal channels. In fact, Figure 4.23 (minimal patches in the large box) is virtually indistinguishable from Figure 4.22 (minimal box). This suggests that localised regions in a large box approach the travelling wave solutions in a way similar to minimal channels.

To make a closer comparison of hibernating turbulence occurring spatially in a large domain with a lower-branch ECS, we consider the conditionally averaged velocity field around a point located in the centre of an instantaneous patch undergoing hibernation. For DNS at Re = 1820, a total

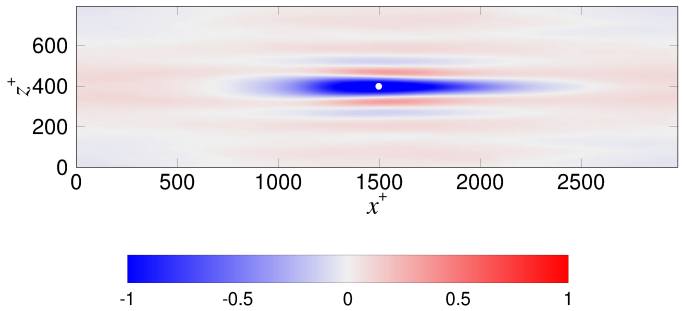

Figure 4.24: Spatial patterns of ensemble-averaged wall shear stress fluctuations at $\mathrm{Re}_\tau = 85$ ($\mathrm{Re} = 1820$). The white dot represents the location at which the centroids of individual low-drag patches were centred.

number of 26033 low-drag regions or patches are identified using the edge-detection scheme discussed in Chapter 4.2.1. This amounts to an average of 9 events occurring per field. The conditionally averaged flow field is determined by locating the centroids of all the low-drag patches, shifting the velocity fields such that all centroids coincide, and then averaging them. Reflection symmetry is enforced in the spanwise (neutral) direction. The spatial wall shear stress pattern of the resulting conditionally averaged flow field is shown in Figure 4.24. We observe a low-speed streak in the streamwise direction straddled by streamwise vortices. Qualitatively, the picture looks similar to the conditionally averaged wall shear stress patterns obtained by pointwise thresholding (see Figure 4.10(b)) except for a couple of differences. First, the spatially sampled streak is not as elongated as the temporally sampled one. Second, the spatially identified streak has a spanwise width a little bit higher than that from temporal sampling. This is because there is no time criterion in spatial sampling. To get an estimate of the size of the ensemble-averaged low-drag patch (e.g. Figure 4.24), we calculate the moments of inertia of individual patches and then take the average. The effective radius, or the radius of gyration (R_g), of the patch is a good representation of its size, and it is related to the moment of inertia (I) as:

$$I = mR_g^2 \tag{4.6}$$

where m is the "mass" of the patch. For our case, m would be the total wall shear stress of the

patch. The radius of gyration, $R_{g,xx}$ (or $R_{g,zz}$) can then be calculated as:

$$R_g = \sqrt{\frac{\int r^2 \mathrm{d}m}{\int \mathrm{d}m}} \tag{4.7}$$

where r is the distance of the area element of "mass" $\mathrm{d}m$ from the axis along the spanwise (or the streamwise) direction, passing through the centroid of the patch. To get a better indication of the simple size of the regions, we calculate the uniformly-weighted lengths, i.e., we assume that $\mathrm{d}m =$ constant. The moments of inertia about the streamwise direction (I_{xx}) and the spanwise direction (I_{zz}) give us the radii of gyration in the spanwise and streamwise directions, respectively. The uniformly-weighted average lengths of the low-drag patch in the streamwise and spanwise directions, i.e., $R_{g,xx}$ and $R_{g,zz}$, respectively, are 317.97×45.59 for $\mathrm{Re}_\tau = 70$, 287.65×31.76 for $\mathrm{Re}_\tau = 85$ and 277.70×29.11 for $\mathrm{Re}_\tau = 100$. This observation further corroborates the claim that the size of low-drag regions decreases as the Reynolds number is increased (see Figure 4.20).

Illustrated in Figure 4.25 are conditionally averaged mean velocity profiles at the centroid of hibernation regions occurring spatially. For example, the hibernation profile in Figure 4.25(b) corresponds to the streamwise velocity profile observed at the white dot in Figure 4.24. As we have done everywhere, each velocity profile plotted in Figure 4.25 is scaled with the corresponding mean wall shear stress, unconditional or conditional as the case may be. This is why they all collapse in the near-wall region. For all the three cases, we observe that the velocity profiles at the centroid of hibernation patches are elevated: they lie well above the unconditional time averaged profiles from DNS and very close to the lower branch ECS. In fact, in the region $y^+ \lesssim 30$, both the conditional and ECS velocity profiles are very similar, and become nearly indistinguishable as the Reynolds number is increased. However, the behaviour in the core (near the centreline) remains distinct. Similar observations were made while comparing lower branch ECS profiles with conditionally averaged (low drag) profiles from temporal and spatial sampling techniques (Figure 4.8(a) and Figure 4.18). This pattern is also observed by other researchers when comparing ECS to minimal channel turbulence [Park and Graham, 2015; Hwang et al., 2016] and localised relative periodic orbits (RPOs)/lower branch solution to turbulent puffs in pipe flows [Avila et al., 2013] — it seems that a single ECS is not capable of capturing both near-wall and core dynamics. The close similarity for $y^+ \lesssim 30$ again

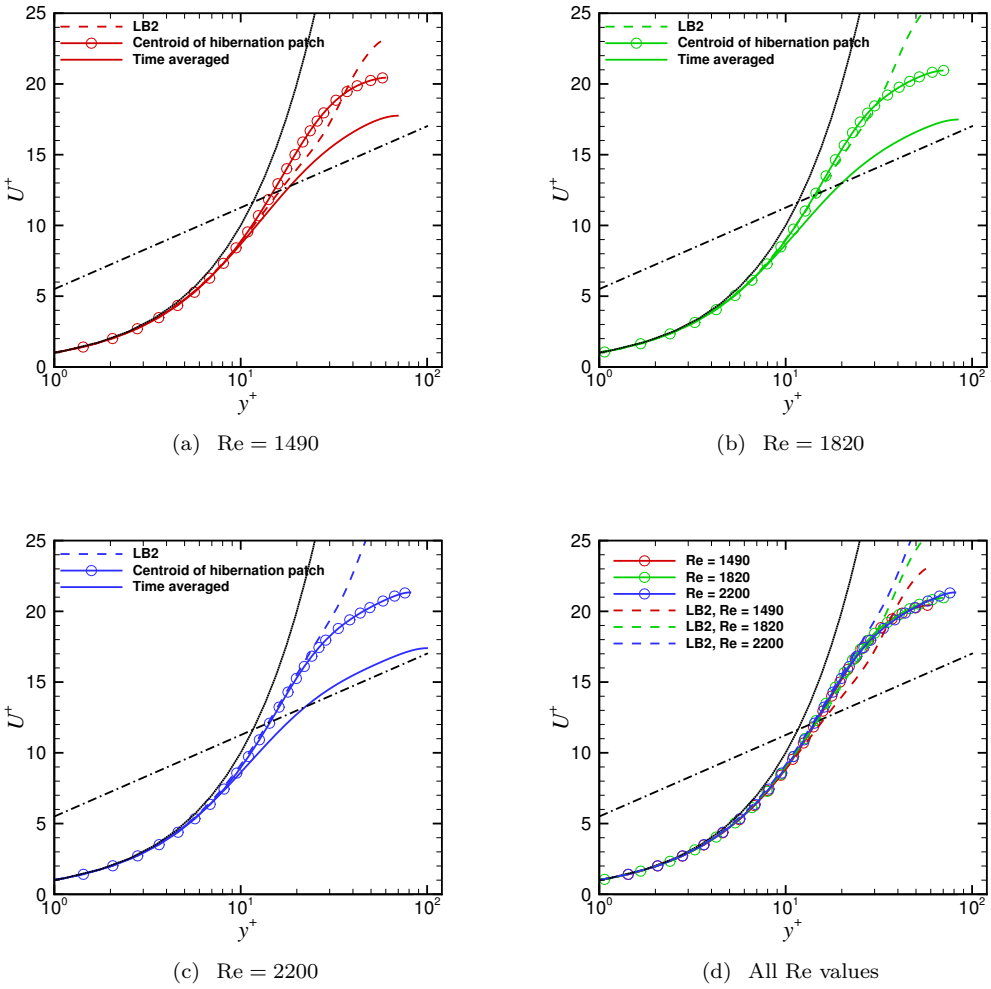

Figure 4.25: (a), (b), (c) Comparison of conditional mean velocity profiles at the centroid of hibernation patches in a large box with lower branch ECS at the same Reynolds number. (d) All the conditionally averaged velocity profiles at the centroids of hibernation patches at different Reynolds numbers.

suggests that a hibernation event in an extended domain is, at least with regard to mean velocity, a spatially local approach toward a lower branch ECS. In Figure 4.25(d), conditional streamwise velocity profiles observed at the centroid of hibernation regions are presented as a function of Reynolds number. There does not seem to exist an obvious dependence on Reynolds number.

We now propose a way of quantifying the "local closeness" of a DNS to lower and upper branch exact coherent states. We consider instantaneous snapshots of spatial patterns of wall shear stress.

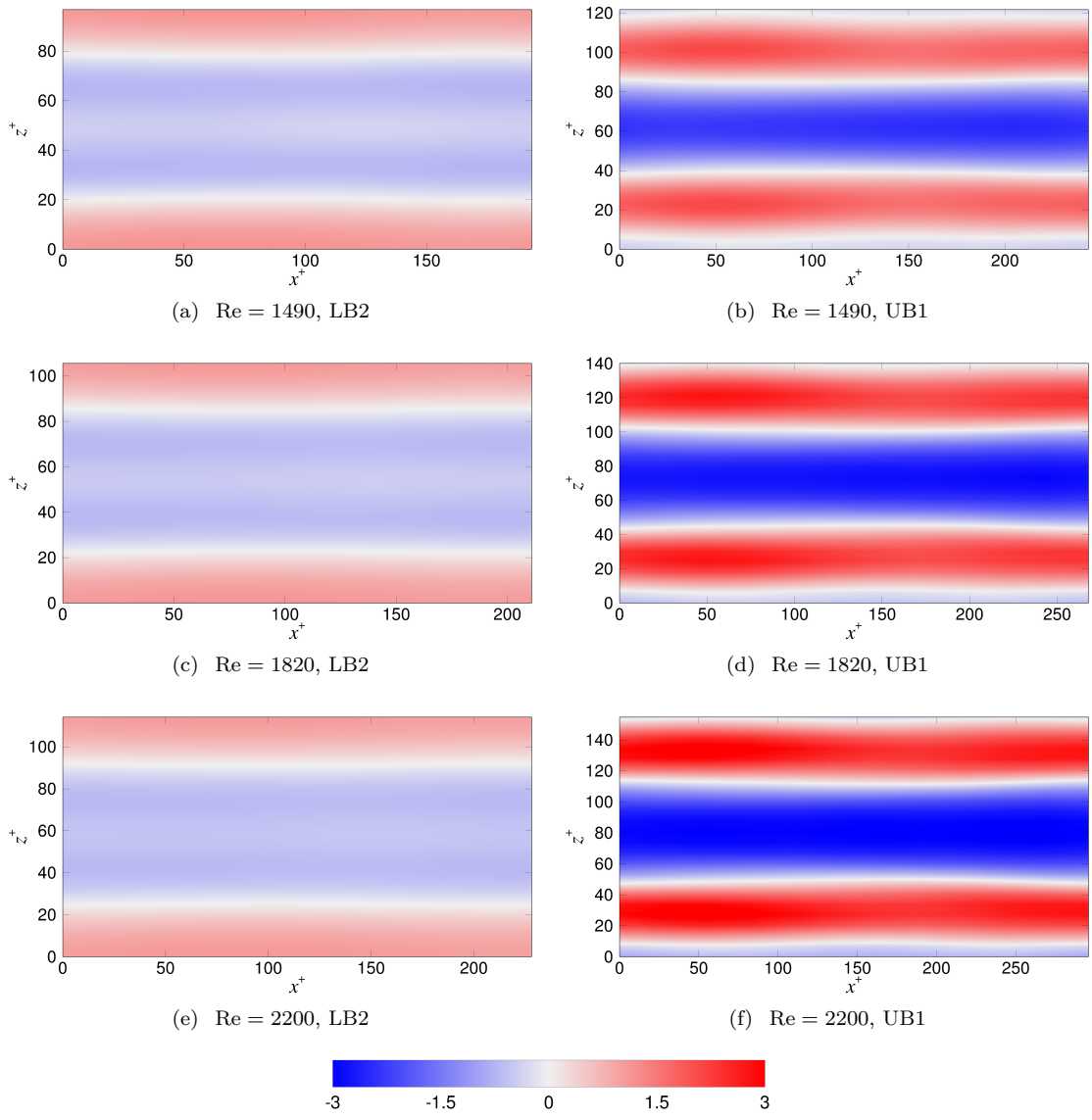

Figure 4.26: Spatial patterns of wall shear stress fluctuations of P4 lower and upper branch travelling wave solutions.

See Figure 4.2 for some examples of snapshots at $\mathrm{Re}_\tau = 70$, 85 and 100; here we will be using the snapshots from the right column to make comparisons with the travelling wave solutions (plotted again in Figure 4.27 (a), (d), (g)). We calculate how closely a localised coherent structure from a DNS snapshot resembles the chosen ECS based on the wall shear stress measurements. In particular,

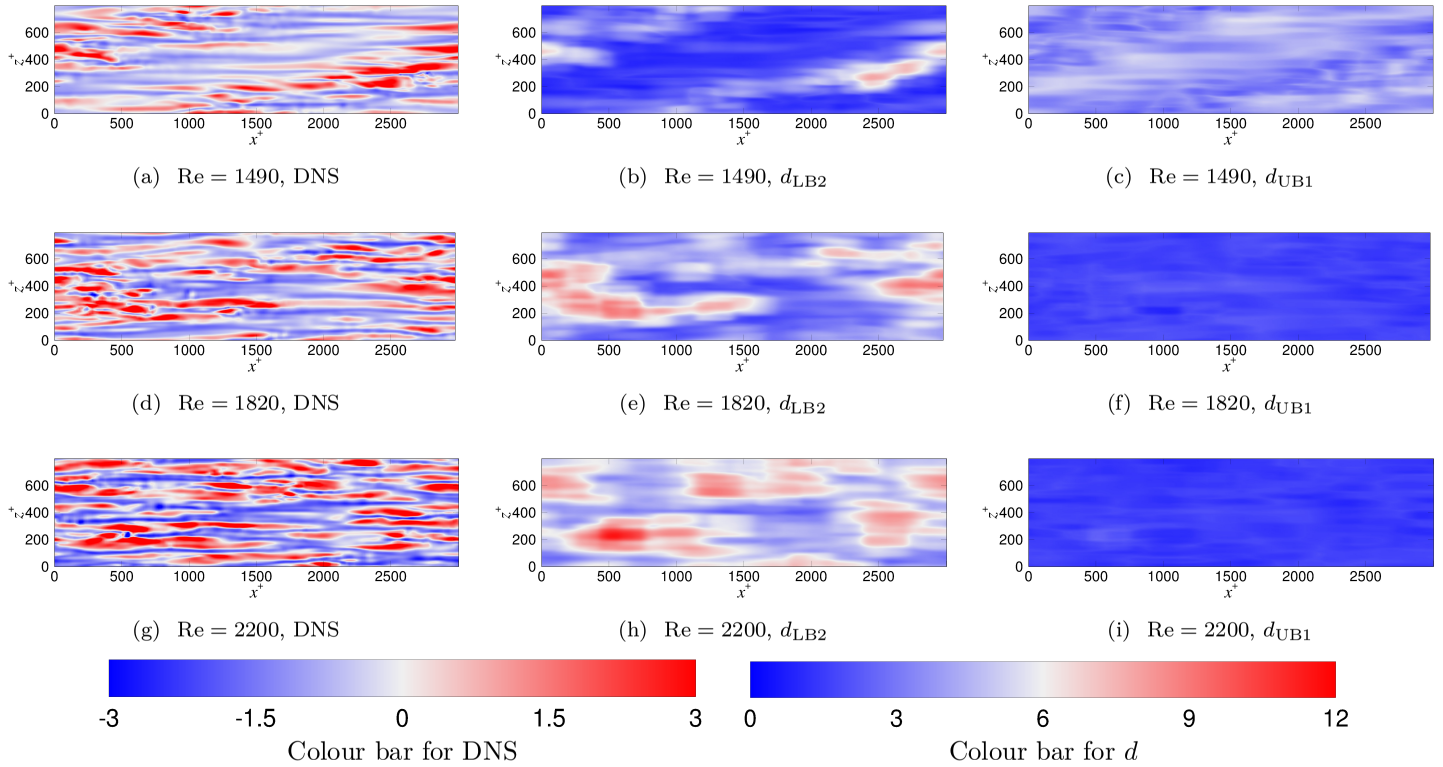

(a) Re = 1490, DNS (b) Re = 1490, d_{LB2} (c) Re = 1490, d_{UB1}

(d) Re = 1820, DNS (e) Re = 1820, d_{LB2} (f) Re = 1820, d_{UB1}

(g) Re = 2200, DNS (h) Re = 2200, d_{LB2} (i) Re = 2200, d_{UB1}

Figure 4.27: (a), (d), (g) Spatial patterns of instantaneous wall shear stress fluctuations from DNS. (b), (e), (h) Distance between DNS and lower branch ECS that lie on LB2. (c), (f), (i) Distance between DNS and upper branch ECS that lie on UB1.

we calculate the following function:

$$d\left(x,z,t\right)=\min_{\phi}\left(\frac{1}{L_x'L_z'}\sqrt{\int_{x-\frac{L_x'}{2}}^{x+\frac{L_x'}{2}}\int_{z-\frac{L_z'}{2}}^{z+\frac{L_z'}{2}}\left\{f\left(x',z',t\right)-g\left(x',z',t,\phi\right)\right\}^2\mathrm{d}x'\mathrm{d}z'}\right) \tag{4.8}$$

Here, d is the "distance" between DNS and ECS, f is a flow property from the DNS and g is the same flow property from the travelling wave or a reference template, x and z are the coordinates in space, ϕ represents the spatial phases in x and z of g relative to f, and $L_x'=\pi$ and $L_z'=\pi/2$ are the streamwise and spanwise periods, respectively, of the ECS we are using for comparison. Since we have chosen to quantify the closeness based on wall shear stresses, here $f=\tau_{w,DNS}\left(x,z,t\right)$ and $g=\tau_{w,TW}\left(x,z\right)$. Shown in Figure 4.26 are wall shear stress fluctuation patterns of the lower (LB2) and upper (UB1) branch travelling wave solutions of the P4 family used as templates for comparison with DNS. Figures 4.27 (b), (e), (h) show instantaneous spatial variation of d when the reference template is wall shear stress of a lower branch travelling wave. It can be observed that bluer regions that have smaller values of d are the ones that are much "closer" to the lower branch travelling wave and thus exhibit low drag. On the other hand, regions that are more red are characteristic of high drag. In Figure 4.27 (c), (f), (i), the distance of DNS from the upper branch travelling wave is shown. A red region in this figure may not necessarily mean low drag, but could also mean a high drag region due to hyperactive or active (normal) turbulence that is just different from the upper branch travelling wave used here for comparison. On the other hand, a blue region on this figure would mean that it is close to the upper branch and will exhibit high drag.

To summarise, a number of separate results, from time-series of wall shear stress to conditional mean velocity profiles to a measure of local similarity between wall shear stress patterns suggest that near-wall features of exact coherent states found in minimal channels appear in a spatiotemporally local manner in extended domains. In summary, the results presented here suggest that spatiotemporal intermittency in transitional channel flow turbulence is related to temporal intermittency, and by extension to the state space structure, in the minimal channel.

Chapter 5

Conclusions of Part I

The present work has quantified, using temporal and spatial sampling and conditional averaging techniques, the intermittent dynamics of transitional channel flow turbulence in an extended domain. In minimal domains, turbulence in this Reynolds number range displays substantial intermittency that is associated with chaotic movement of turbulent trajectories between lower and upper branch invariant solutions known as exact coherent states (ECS). In the present work we address the relationship between temporal dynamics in minimal channels and spatiotemporal dynamics in extended domains. Both temporal and spatial analyses of the turbulent velocity fields are performed, the latter using image analysis methods. These analyses partition the flow characteristics into three classes depending on degree of turbulence activity; we present the differences between flows fields in these classes in terms of simple quantities such as mean velocity, wall shear stress and flow structures. Notably, the temporal and spatial analysis methods, although completely independent of one another, yield very similar results for both low and high drag regions. The conditional mean velocity profiles during low drag events in large domains, both temporal and spatial, closely resemble those found in low drag temporal intervals in the minimal channel. Finally, we present connections between turbulence and exact coherent states by comparing wall shear stress in localised patches the size of minimal channels in large domains with those in actual minimal channel. Conditional mean velocity profiles during low drag intervals occurring temporally and spatially in extended domains were compared with the lower branch ECS profiles from the P4 family of solutions and an excellent

agreement was found in the region $y^+ \lesssim 30$. This analysis shows that, at least with regard to the quantities studied here, the near-wall flow structure in the low drag patches of the large domain resembles that of a lower branch ECS. A clear direction for future work is development of methods to extend the comparison to incorporate more details of the velocity fields.

We believe that these results have the potential to shed light on the structure and dynamics of "laminar" intervals in the laminar-turbulent transition regime, especially as Reynolds number increases toward the uniformly turbulent regime. In particular, our work is consistent with that of Avila et al. [2010], who note that intermittent low-drag excursions persist into the fully turbulent regime. We find that although low-drag "hibernating" events become increasingly rare as Re increases, their structure, especially in terms of conditional mean velocity profile, is insensitive to Re. Finally, the results presented here suggest that spatiotemporal intermittency in transitional channel flow turbulence is related to temporal intermittency, and by extension to the state space structure, in the minimal channel. The similarity in near wall structure, especially wall shear stress and conditional mean velocity profile, suggests that ECS found in a minimal channel continue to play some role in organising the spatiotemporal dynamics in extended domains.

Part II

Implementing wall deformation using immersed boundary methods

Chapter 6

Introduction

We now switch the focus of the dissertation to the development and testing of new flow control strategies. The details of the flow control methods are discussed in Part III of the dissertation. Part II deals with the numerical skeleton behind the implementation of those techniques. At this point, it would suffice to mention that for the flow control methods we have developed to change the dynamics of turbulent flows, they require the domain to change its shape dynamically, specifically the walls of the channel. The deformations are pretty small — they extend only up to a few viscous units, and under such circumstances, the wall can safely be assumed to be hydraulically smooth [Endo et al., 2000]. Satisfying the desired boundary conditions on a wall with a complex shape is not straightforward. Part II presents a detailed literature review of how flows in a domain with complex shapes (both moving and non-moving) can be simulated. It also presents the specific details of the method used in the current work to simulate flows over rigid, complex-shaped, moving walls.

In this work, an immersed boundary method (IBM) is used to facilitate the modelling of deformable wall. Specifically, the IBM is used to achieve a desired velocity distribution over the channel wall of some desired shape. Another common way of simulating flow in domains with complex rigid boundaries is using a boundary-fitted or unstructured grid. However, the boundary (channel wall) may have a complex shape and doing a coordinate transformation by generating a grid that conforms to the shape of the walls at every time step can be computationally expensive. Not only does an unstructured grid require high memory but also the equations resulting from a coordinate

transformation can be complex to solve, more so if the boundaries are deformable. Thus, to address the complex interaction between the fluid and the deformable wall, one would seek to solve the system of equations without having to resort to boundary-conforming methods. A distinguishing feature of immersed boundary methods is that the entire simulation can be carried out on a Cartesian grid without generating an unstructured grid at every time step. The major challenge now is to accurately model the complex walls and satisfy the boundary conditions on the deformable walls. This chapter is intended to introduce different types immersed boundary methods and to describe in detail the method used in this work.

The motion of an incompressible fluid is governed by the momentum equation (A.3) subjected to continuity equation (A.4) (see Appendix A). Equation (A.3) includes the possibility that the fluid is subjected to a body force $\boldsymbol{f}$ which can be included in the right-hand side of the momentum equation, giving it the following form:

$$\frac{\partial \boldsymbol{u}}{\partial t} + \boldsymbol{u} \cdot \boldsymbol{\nabla} \boldsymbol{u} = -\boldsymbol{\nabla} p + \frac{1}{\mathrm{Re}} \nabla^2 \boldsymbol{u} + \boldsymbol{f} \tag{6.1}$$

Gravity is an example of body force. Other body forces, like electromagnetic forces, are produced in the context of flow control. These forces have been used extensively by researchers in both experimental and numerical studies, for example, Mani et al. [2008], Qin et al. [2008], Liu et al. [2009], Choi et al. [2011], Mamori and Fukagata [2014], Whalley and Choi [2014], Hanson et al. [2014], and Fuaad et al. [2016] to name a few. In the context of immersed boundary methods, the body forcing $\boldsymbol{f}$ may be used to mimic a boundary condition. A local force density is introduced to modify the local flow field near the deformable wall while satisfying the proper boundary conditions. The force $\boldsymbol{f}$ is a function of both space and time since the boundary (channel wall) is continuously moving and the fluid velocity field which is the key component in determining the forcing, is unsteady.

Immersed boundary methods can broadly be classified into two categories [Iaccarino and Verzicco, 2003; Mittal and Iaccarino, 2005]: (1) continuous (or feedback) forcing, and (2) discrete (or direct) forcing. In the continuous forcing approach, the forcing term is added to the Navier–Stokes equations before they are discretised whereas in the discrete forcing method, the forcing term is added either explicitly or implicitly to the discretised Navier–Stokes equations [Mittal et al., 2008]. Developed

by Peskin [1972, 1982, 2002], the immersed boundary method was first used to simulate blood flow in heart valves. In his method, he demonstrated the effect of immersed boundary (elastic fibres in this case) on the surrounding fluid by transmitting the fibre stress to the fluid through a localised forcing term $\boldsymbol{f}$ at position $\boldsymbol{x}$ at time t given by:

$$\boldsymbol{f}(\boldsymbol{x},t) = \sum_k \boldsymbol{F}_k(t)\,\delta\left(|\boldsymbol{x}-\boldsymbol{X}_k|\right) \tag{6.2}$$

Here, $\boldsymbol{F}_k$ is the stress at the k^{th} point on the fibre whose coordinates are $\boldsymbol{X}_k$, and δ is the Dirac delta function. In general, the location of fibres does not coincide with grid points on the Cartesian mesh, thus the force $\boldsymbol{f}$ is distributed over a few grid points across the fibre. Thus, the sharp Dirac delta function is replaced by a smooth function d that distributes the force in the surrounding cells. The body forcing is then given as:

$$\boldsymbol{f}(\boldsymbol{x},t) = \sum_k \boldsymbol{F}_k(t)\,d\left(|\boldsymbol{x}-\boldsymbol{X}_k|\right) \tag{6.3}$$

Many forms of the smoothing distribution function d have been used in the past [Peskin, 1972; Saiki and Biringen, 1996; Lai and Peskin, 2000; Taira and Colonius, 2007] depending on the situation. Peskin's method is generally suitable for flows with immersed elastic boundaries.

Researchers like Goldstein et al. [1993, 1995], Saiki and Biringen [1996], Lai and Peskin [2000], Su et al. [2007], Margnat and Morinière [2009] used a modified form of the IBM described above to simulate flow over rigid boundaries. They employed a feedback forcing to represent a solid body and added it to the momentum equation. The analytical expression for the force density $\boldsymbol{f}$ is given as:

$$\boldsymbol{f}(\boldsymbol{x},t) = K_i \int_0^t \left[\boldsymbol{u}(\boldsymbol{x},t') - \boldsymbol{V}(\boldsymbol{x},t')\right] \mathrm{d}t' + K_p\left[\boldsymbol{u}(\boldsymbol{x},t') - \boldsymbol{V}(\boldsymbol{x},t')\right] \tag{6.4}$$

Here, $\boldsymbol{u}$ is the velocity field and $\boldsymbol{V}$ is the desired velocity distribution over a boundary whose position is $\boldsymbol{x}$ at time t. K_i and K_p are negative constants whose dimensions are $1/T^2$ and $1/T$, respectively. The above forcing expression is like a feedback controller where the velocity difference $\boldsymbol{u}(\boldsymbol{x},t) - \boldsymbol{V}(\boldsymbol{x},t)$ is fed as input to the controller with the aim of minimising this difference. In other words, the forcing behaves in a way to enforce $\boldsymbol{u} = \boldsymbol{V}$ on the immersed boundary. As $\boldsymbol{u}$ on

the boundary becomes different from $\boldsymbol{V}$, $\boldsymbol{f}$ brings it back to $\boldsymbol{V}$. Magnitudes of constants K_i and K_p must be big enough so that the force can act with a frequency higher than the highest frequencies present in the flow [Fadlun et al., 2000]. Unfortunately, large values of K_i and K_p make Equation (6.1) stiff which, therefore, requires time integration to take very small time steps — the CFL number typically is $\mathcal{O}\left(10^{-3} - 10^{-2}\right)$ [Goldstein et al., 1993; Saiki and Biringen, 1996]. This increases the total computation time. Another problem associated with the feedback forcing strategy is that the smooth force smears the boundary between the solid and the fluid. This means that the boundary conditions on the immersed surface are not precisely satisfied at its actual location but within a localised region round the boundary. Thus, a sharp representation of the immersed boundary is not possible. This is not acceptable for flows at high Reynolds numbers.

The second category of forcing, the discrete or direct forcing, developed by Mohd-Yusof [1997, 1998] explicitly enforces the boundary conditions at the grid points near the immersed boundary. This form of forcing is obtained by discretising Equation (6.1) in the following way:

$$\frac{\boldsymbol{u}^{n+1} - \boldsymbol{u}^n}{\Delta t} = \mathrm{RHS}^n + \boldsymbol{f}^{n+1} \tag{6.5}$$

where n and $n+1$ are the current and next time steps, and RHS comprises of the advective and diffusive terms and the pressure gradient. Calculation of RHS has been discussed in Appendix A.3. If the desired velocity distribution at the boundary (channel wall) at the next time step is $\boldsymbol{V}$, i.e., $\boldsymbol{u}^{n+1} = \boldsymbol{V}$, then the body force that will yield the desired outcome is simply given by:

$$\boldsymbol{f}^{n+1} = \frac{\boldsymbol{V} - \boldsymbol{u}^n}{\Delta t} - \mathrm{RHS}^n \tag{6.6}$$

The boundary conditions after the forcing described in Equation (6.6) is applied holds at every time step. Moreover, unlike the feedback forcing described in Equation (6.4), there are no free parameters to choose. Another distinguishing feature of the direct forcing schemes is that they are very much dependent on the spatial discretisation, which was not the case for continuous forcing. Many variants of the direct forcing strategy have been tried and tested. In Mohd-Yusof's formulation, the forces are applied only on the surface of the immersed boundary or inside the body. For the tangential velocity components, the velocity of the point immediately interior to the surface is forced to be equal and

opposite to the velocity at the point immediately exterior to the surface. The normal component of the velocity is preserved across the surface. Fadlun et al. [2000] modified Mohd-Yusof's scheme slightly to be able to use it on a staggered grid using finite-differences. They applied the direct forcing at the first Eulerian grid points external to the immersed boundary. The velocity at these points is obtained by a linear interpolation of velocity at the second grid points from the surface in the fluid region, which comes from solving the momentum equation, and the prescribed velocity at the surface.

It is known that direct forcing strategies when applied to moving boundary problems may result in spurious force oscillations on the body. This degrades the quality of solutions and hence should be minimised. These oscillations occur due to the role change of the fluid-solid interface from one time step to the next. For example, if a grid point is located inside a solid body at the current time step and because of the motion of the body, it becomes a part of fluid at the next time step, then force oscillations will arise due to this spatial discontinuity. Same phenomenon will happen when a point in the fluid becomes a point in the solid at the next time step. To tackle this issue, one possibility is to simply filter out the high frequency noise as recommended by Miller and Peskin [2004]. Uhlmann [2005] reduced these spurious oscillations by combining Peskin's smoothing function [Peskin, 2002] and the discrete forcing method of Fadlun et al. [2000]. Yang and Balaras [2006] proposed a field extension approach to reduce the oscillations. They obtained the velocity and pressure data at grid points where solid becomes fluid by extrapolating the velocity and pressure fields from adjacent fluid grid points. These methods proved to be really effective in reducing the force oscillations but did not completely eliminate them. Kim et al. [2001], Huang and Sung [2007], Lee et al. [2011a] and Lee and You [2013] got rid of the pressure discontinuity by adding a mass source/sink term in combination with momentum forcing. The mass source/sink term was added only for the cells containing the immersed boundary to satisfy mass conservation. Lee et al. [2011a] also concluded that the force oscillations can also be reduced by decreasing the grid spacing or increasing the computational time step.

Some of the other researchers who have used direct forcing formulations include Deng et al. [2006], Zhang and Zheng [2007], Kang et al. [2009a], Guy and Hartenstine [2010], Pinelli et al. [2010], Liao et al. [2010], Seo and Mittal [2011], Ji et al. [2012], Chang et al. [2014], Gronskis and

Artana [2016].

We are following the direct forcing scheme proposed by Liao et al. [2010]. The discrete momentum forcing $\boldsymbol{f}(\boldsymbol{x}, t)$ is applied only at nodes adjacent to the immersed boundary (channel wall) on both the fluid and the solid side in order to satisfy the no-slip and no-penetration boundary conditions at the wall. The implementation of the scheme and other problem-specific details are discussed in the following chapters.

Chapter 7

Domain set-up

We consider pressure driven flow of an incompressible Newtonian fluid in a rectangular, wall-bounded domain (channel) maintained at constant mass flux. It is desired to change the shape of the wall dynamically in order to manipulate the near-wall flow. For a Cartesian coordinate system like ours, using immersed boundary methods would be helpful for reasons described in Chapter 6. Conventionally, the deformation of walls in turbulent channel flows has been modelled by transforming the Cartesian coordinates into appropriate boundary-fitted coordinates at each and every time step of the simulation [Carlson et al., 1995; Carlson and Lumley, 1996; Mito and Kasagi, 1998; Kang and Choi, 2000; Endo et al., 2000; Sullivan et al., 2000; Endo and Kasagi, 2001; Kang, 2002; Shen et al., 2003; Sun et al., 2011; Nakanishi et al., 2012; Tomiyama and Fukagata, 2013; Kim and Choi, 2014]. Immersed boundary methods have also been used in the past to simulate turbulent flows over non-flat surfaces for geometries that are of interest to us. For example, Goldstein et al. [1993, 1995] and Mohd-Yusof [1997] have simulated turbulent flows in a channel with riblets on the surface of the wall, Mohd-Yusof [1998] has simulated flows in a turbulent channel with periodic bumps in the wall. Simulations of turbulent flows over a wavy wall have been conducted by Iaccarino and Verzicco [2003] and Kang et al. [2009b], whereas Chang et al. [2014] simulated turbulent flows over periodic hills. Lee et al. [2011b] simulated turbulent boundary layer flows over a rough wall and Ikeno and Kajishima [2007] did turbulent flows over an inclined wall and a pipe. On one hand, in an approach that requires a coordinate transformation, the computational domain includes only

the space occupied by the fluid — the physical Cartesian coordinate system is transformed into a convenient coordinate system on which calculations can be performed easily, e.g., the Cartesian coordinates on a wavy channel wall are transformed to boundary-fitted coordinates that do not change. On the other hand, in an immersed boundary situation, the computational domain consists of both fluid and solid regions, and it is usually a convenient, regular shape on which equations of motion for a fluid can be solved for the regions that contain the fluid as well as for the regions that supposedly contain the solid.

A cartoon depicting the computational domain for our channel flow simulations on deformable walls is shown in Figure 7.1. As was the case in our regular channel (illustrated in Figure 3.1), here too, the x axis is aligned with the streamwise direction, the z axis is aligned with the spanwise direction, and the y axis represents the wall-normal direction. On the whole, the computational domain has a rectangular channel-like shape shown as solid lines. The portion of the domain that is supposed to contain the solid is called virtual solid — there are two virtual solids in the computational domain, one at the top and one at the bottom. The portion between the two virtual solids is the one that contains the actual fluid, and the interface between the fluid and the solid is termed the virtual boundary shown as dashed lines. For clarity, the virtual boundaries, both at top and bottom, are shown as straight dashed lines, but in general they can assume any shape, which may or may not change with time, depending on the flow control algorithm. Either way, both the virtual boundaries, which we will refer to as channel walls from now on, should be periodic in both streamwise and spanwise directions. Both no-slip and no-penetration conditions must be satisfied at both the walls at each and every time step during the simulation.

As mentioned earlier, a local force density $\boldsymbol{f}$ can be applied at or near the walls to satisfy the boundary conditions. A cartoon showing where the forces are applied near the walls in all the three directions is illustrated in Figure 7.2. The dashed line represents the bottom wall (deformable) of the channel while the solid line is the bottom boundary of the computational domain. Above the wall is the physical domain containing the fluid and below it is the virtual solid. If the wall coincides with a grid point, then the forcing is applied at *that* grid point, but in general, this may not be the case. In a more general case when the wall does not coincide with a grid point, which is what is illustrated in Figure 7.2, the forces are *only* applied at grid points located adjacent to the channel wall. These

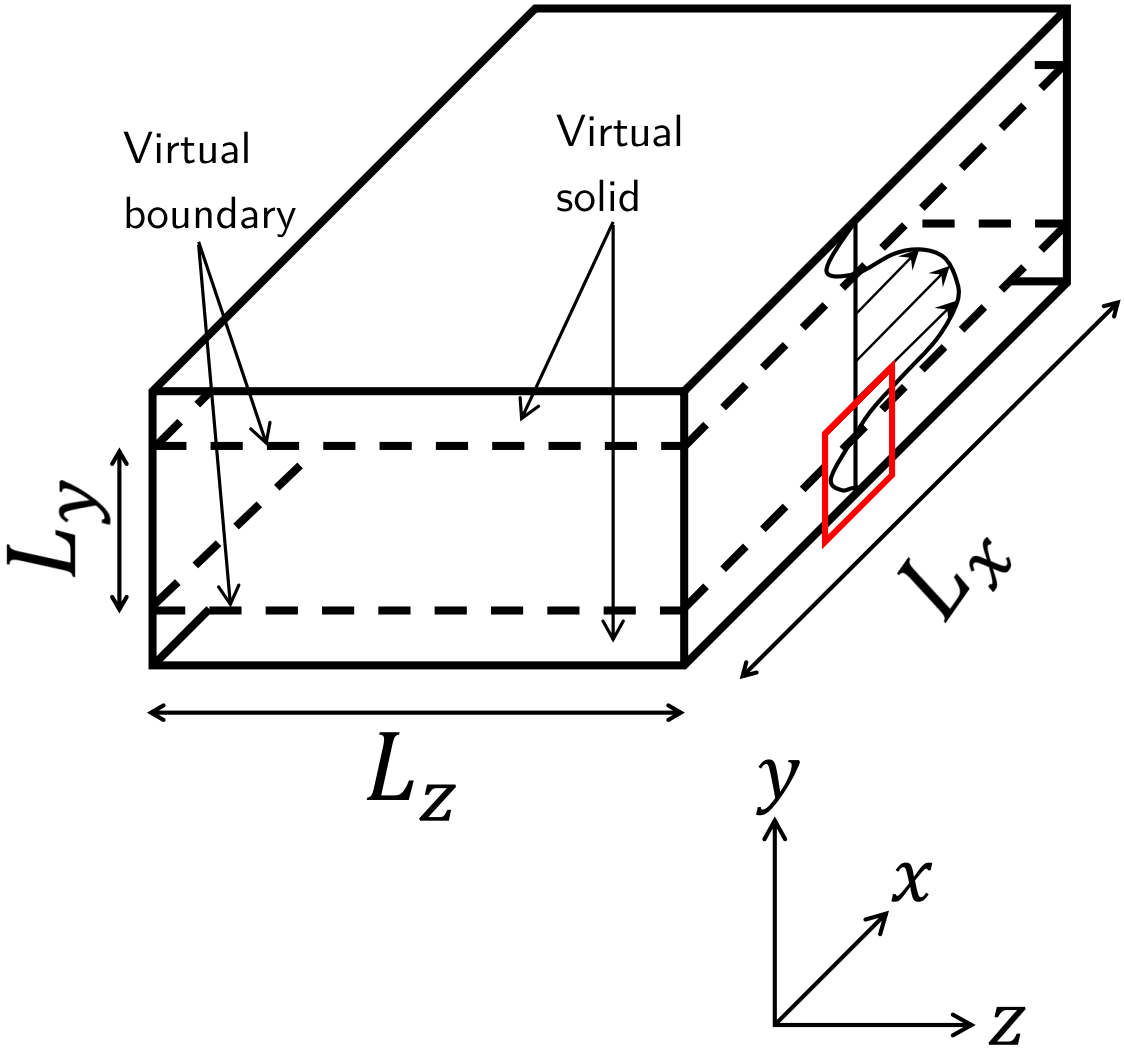

Figure 7.1: Schematic of the flow geometry showing the full computational domain. Computation domain goes from $y = -(l + \delta)$ to $y = l + \delta$, where δ is the height of the virtual solid near the top and bottom walls. The physical fluid flow domain goes from $y = -l$ to $y = l$. Mean locations for the top and bottom walls are set at $\langle y_w \rangle = -l$ and l, respectively. Body forcing is applied across the dashed line (channel wall) — an example region is shown enclosed by red lines near the bottom wall. A magnified representation of this region is illustrated in Figure 7.2.

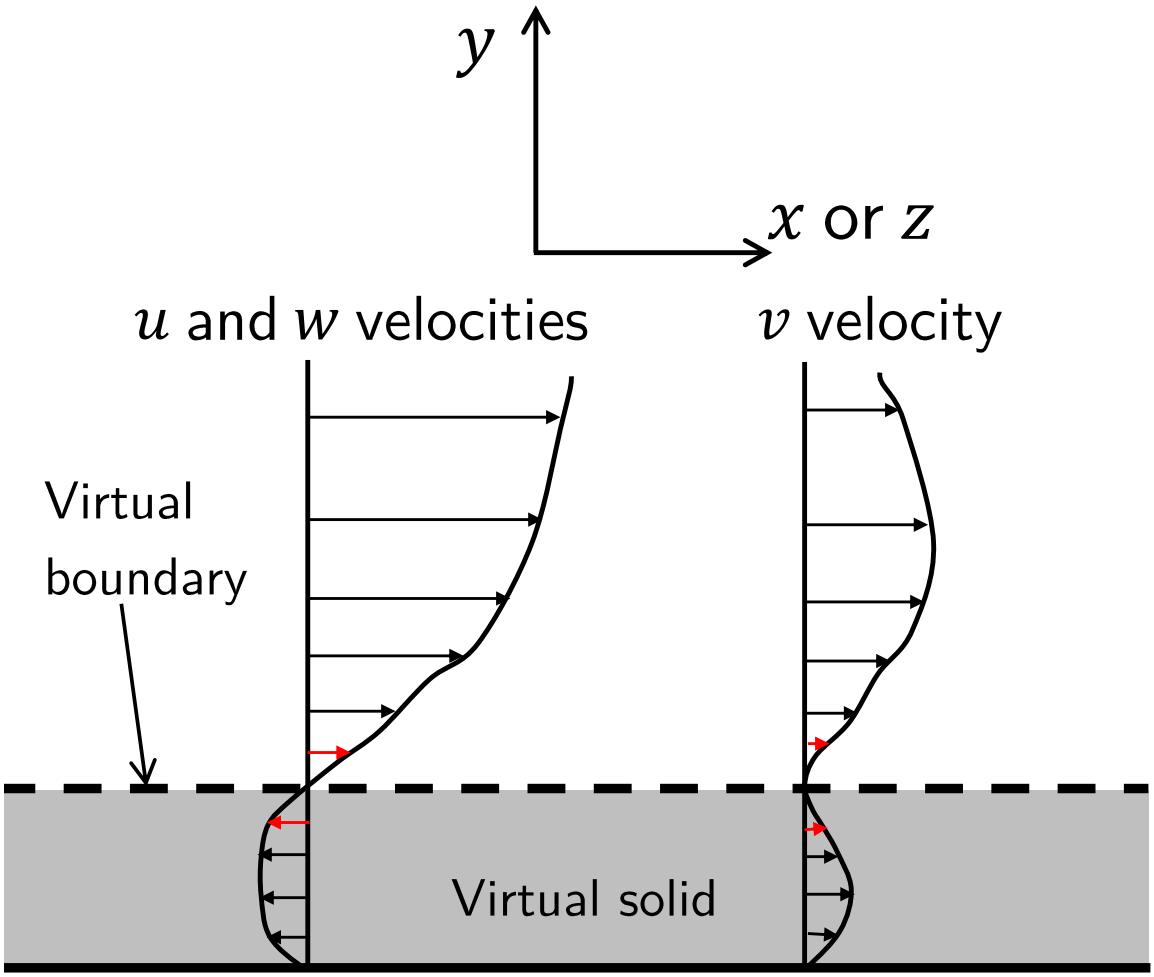

Figure 7.2: Application of body forces in the streamwise, spanwise and wall-normal directions at nodes adjacent to the virtual boundary shown as red arrows.

forces are illustrated as red arrows in the figure. Black arrows simply represent the velocities in the respective direction. The tangential forcing components (f_x and f_z) are such that the corresponding tangential velocity components (u and w, respectively) are reversed across the virtual boundary — this will make the velocity *at* the boundary equal to zero, ensuring the no-slip condition at the wall. The normal forcing component (f_y) is such that the normal velocity component (v) relative to the wall is zero — this ensures the no-penetration condition at the wall. The combined effect of the

three forcing components at grid points adjacent to the boundary is the development of a smooth velocity profile across the boundary. The location of the wall must be known prior to the calculation of $\boldsymbol{f}$. Numerical details about the body forcing $\boldsymbol{f}$ can be found in Chapter 9.

Both the deformable walls (top and bottom) move only in the wall-normal direction. The mean distance between the walls is L_y which is twice the mean half-channel height l, i.e., $L_y = 2l$ (see Figure 7.1). Again, l is chosen as the characteristic length for nondimensionalisation of all the lengths in the geometry. The channel length is L_x and its width is L_z. Thus, the volume of the region occupied by the fluid is $L_x L_y L_z$ and it must be kept constant throughout the simulation, i.e., there must not be any generation or consumption of fluid mass at any given time. The centre of the channel is the plane $y = 0$. The mean location of the two walls of the channel lie at $y = \pm L_y/2 = \pm l$; $+$ for the top wall and $-$ for the bottom wall. The top and bottom boundaries of the computational domain are located at a distance of approximately $0.1l$ from the corresponding virtual boundary, i.e., at $y \approx \pm 1.1l$. The upstream end of the channel corresponds to $x = 0$ whereas the downstream end lies at $x = L_x$. It should be noted that although, the momentum equations are solved for both fluid and solid portions of the computational domain, only the fluid region is of importance to us. The flow inside the virtual solid has no physical meaning and can be safely disregarded.

Chapter 8

Numerical scheme for the immersed boundary method

A finite-volume method with discretisation in Cartesian coordinates is used to solve the Navier–Stokes equations. We adopt a staggered-grid arrangement for flow variables: velocities are calculated at cell faces and pressure at cell centre. This allows for conservation of mass and momentum in every cell/control volume. The three components of the body force $\boldsymbol{f}$, that represent the influence of the immersed boundary on the fluid, are defined at the location of corresponding velocity components. The governing equations for the regions occupied by both the fluid and the solid are given by Equation (6.1), subjected to continuity for incompressible fluids, $\boldsymbol{\nabla} \cdot \boldsymbol{u} = 0$. For incompressible fluids, the advective term in Equation (6.1) can be written in the conservation form, yielding the following form of the momentum equation:

$$\frac{\partial \boldsymbol{u}}{\partial t} + \boldsymbol{\nabla} \cdot \boldsymbol{u}\boldsymbol{u} = -\boldsymbol{\nabla} p + \frac{1}{\mathrm{Re}} \nabla^2 \boldsymbol{u} + \boldsymbol{f} \tag{8.1}$$

The solution of the Navier–Stokes equations is obtained by using the Crank–Nicolson method for the diffusive terms and the second-order Adams–Bashforth method for the convective terms. The discretised momentum and continuity equations are then written as shown below and are solved in

the following sequence:

$$\frac{\hat{\boldsymbol{u}} - \boldsymbol{u}^n}{\Delta t} = -\frac{3}{2}\boldsymbol{\nabla}\cdot(\boldsymbol{uu})^n + \frac{1}{2}\boldsymbol{\nabla}\cdot(\boldsymbol{uu})^{n-1} + \frac{1}{2\mathrm{Re}}\nabla^2\left(\hat{\boldsymbol{u}} + \boldsymbol{u^n}\right) + \boldsymbol{f}^{n+1} \tag{8.2}$$

$$\nabla^2 p^\dagger = \frac{\boldsymbol{\nabla}\cdot\hat{\boldsymbol{u}}}{\Delta t} \tag{8.3}$$

$$\frac{\boldsymbol{u}^{n+1} - \hat{\boldsymbol{u}}}{\Delta t} = -\nabla p^\dagger \tag{8.4}$$

Here, n and $n+1$ are current and next time steps, respectively, $\hat{\boldsymbol{u}}$ is the intermediate velocity, which is a non-divergence-free approximation to $\boldsymbol{u}^{n+1}$, and $p^\dagger$ is the pressure. The fractional-step (projection) method used to integrate the Navier–Stokes equations in time is same as the one discussed in Appendix A.3.1. The body forcing $\boldsymbol{f}^{n+1}$ is direct in that it is imposed directly on the immersed body — the boundary condition holds at every time step. Note that $\boldsymbol{f}^{n+1}$ has to be determined in advance in order to satisfy the no-slip and no-penetration boundary conditions at the immersed boundary at the next time step $n+1$.

Chapter 9

Forcing strategy for the immersed boundary method

The body force ($\boldsymbol{f}$) applied to achieve the desired velocity distribution must be determined before solving for the intermediate velocity $\hat{\boldsymbol{u}}$. We apply the discrete-time momentum forcing only at grid points adjacent to the immersed boundary (channel wall). Specifically, as shown in Figure 7.2, forces are applied at the wall if the wall coincides with a grid point, or at the first grid point above and below the wall if the wall does not coincide with a grid point. The expression for the force density $\boldsymbol{f}$ is given as follows [Liao et al., 2010]:

$$\boldsymbol{f}^{n+1} = \frac{\boldsymbol{u}_s - \boldsymbol{u}^*}{\Delta t} \tag{9.1}$$

where $\boldsymbol{u}^*$ is an approximation for the updated velocity $\boldsymbol{u}^{n+1}$ near the immersed boundary in the absence of any forcing. It is estimated with an explicit Adams–Bashforth scheme using a form similar to Equation (A.46) [Zhang and Zheng, 2007; Kim et al., 2001; Liao et al., 2010; Lee et al., 2011a].

$$\boldsymbol{u}^* = \boldsymbol{u}^n + \Delta t \left\{ -\frac{3}{2}\boldsymbol{\nabla}\cdot(\boldsymbol{uu})^n + \frac{1}{2}\boldsymbol{\nabla}\cdot(\boldsymbol{uu})^{n-1} + \frac{1}{\mathrm{Re}}\nabla^2\boldsymbol{u}^{\boldsymbol{n}} - \boldsymbol{\nabla}p^n \right\} \tag{9.2}$$

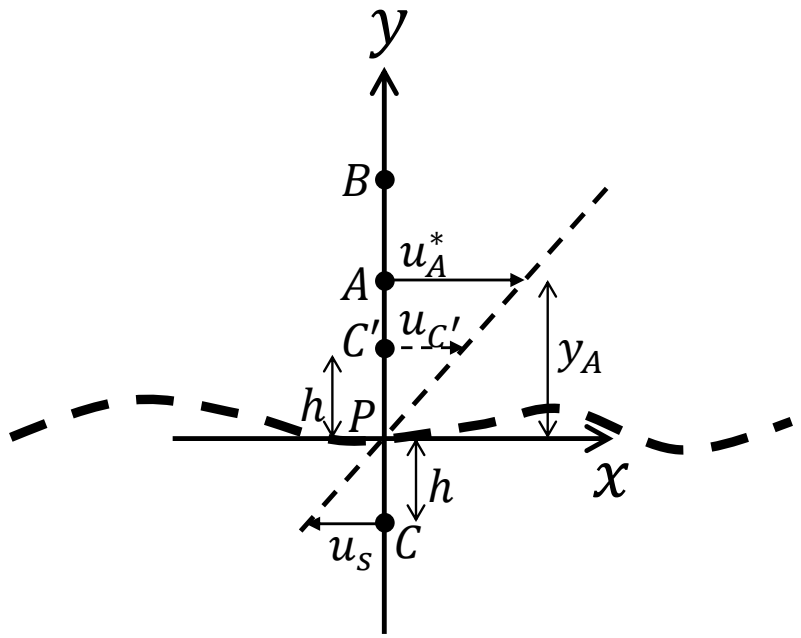

(a) For $0 < h \leq y_A$

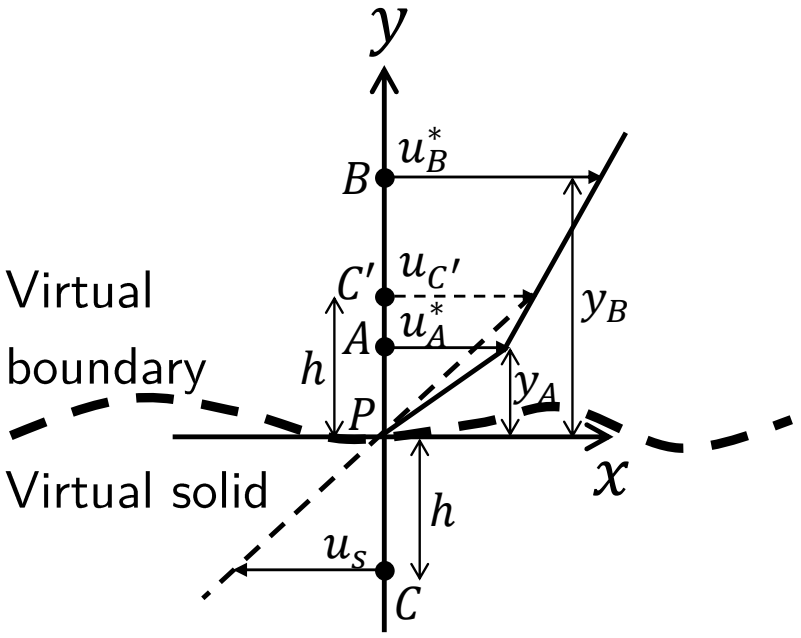

(b) For $y_A < h < y_B$

Figure 9.1: Linear interpolation scheme for the x component of the velocity in the immersed boundary region near the bottom wall. Flow is from left to right. Interpolation for the z component follows the same scheme.

In Equation (9.2), $\boldsymbol{u}_s$ represents the velocity near the immersed boundary region in the presence of forcing. In order to achieve the no-slip boundary condition at the immersed boundary, we seek to reverse the flow across the boundary in the streamwise and spanwise directions — u and w are constrained such that the interpolated velocity field at the immersed boundary is zero. The wall-normal velocity component (v) at grid point adjacent to the immersed boundary is constrained to satisfy the no-penetration condition. This means that if the forcing point (which lies on the immersed boundary interface) coincides with the grid node, then the x and z components of $\boldsymbol{u}_s$ will be set to zero and the y component will be set to the prescribed wall-normal velocity of the wall. The case when forcing points do not coincide with grid locations, and this will be true for most part, is discussed in the following paragraph.

We use linear interpolation to determine the forcing at the grid point inside the immersed boundary adjacent to the interface required to achieve no-slip boundary condition at the moving boundaries. This is illustrated in Figure 9.1 where a linear interpolation scheme for the x component of the velocity in case of the no-slip wall is presented. The region below the dashed line (virtual boundary) denotes the virtual solid. In the figure, C is the forcing point — the point adjacent to the immersed boundary interface. P is the location on the wall directly above C, and C' is the mirror image of C about point P in the fluid region. This means that P lies at the mid-point of the vertical line joining C and C'. If the distance between C and C' is $2h$, then the lengths $|PC| = |PC'| = h$. A and B are, respectively, the first and second velocity points in the fluid region (outside the body surface) lying at a distance of y_A and y_B, respectively, from the point P. Clearly, $y_B > y_A$. We seek that the velocity at C (shown as u_s in the figure) be equal and opposite to the velocity approximation at C' (shown as $u_{C'}$ in the figure). Velocity approximation u_s at C is determined by using the following linear interpolation:

$$u_s = -u_{C'} = \begin{cases} -\frac{h}{y_A} u_A^* & \text{for } 0 < h \leq y_A \\ \\ -\frac{(y_B - h)u_A^* + (h - y_A)u_B^*}{y_B - y_A} & \text{for } y_A < h < y_B \end{cases} \tag{9.3}$$

Velocities u_A^* and u_B^* are determined by solving the x component of Equation (9.2). The same

scheme is applied to the z component of the velocity in order to get w_s. The y component of the velocity at the grid adjacent to the interface in the solid region, v_s, is calculated such that the divergence of the velocity field in the cell cut by the immersed boundary interface is zero. After all the velocities we want to specify at the grid points adjacent to the immersed boundary interface are known, forces are determined using Equation (9.1) which are then substituted in the discretised Equation (8.2) which is then solved to get the updated velocity.

The full numerical procedure at each time step for the above algorithm is summarised below. Let n time steps have been completed and we want the solution at the $(n+1)^{\text{th}}$ time step.

1. Determine the location of the immersed boundary interface at time step $n+1$.
2. Identify the points lying in the fluid and solid regions.
3. Calculate $\boldsymbol{u}^*$ using Equation (9.2).
4. Calculate $\boldsymbol{u}_s$ using Equation (9.3).
5. Calculate the body force using Equation (9.1).
6. Compute the non-divergence-free velocity field $\hat{\boldsymbol{u}}$ using Equation (8.2) and then solve the Poisson equation (8.3) to get the pressure $p^\dagger$.
7. Get the updated, divergence-free velocity $\boldsymbol{u}^{n+1}$ using Equation (8.4).

Chapter 10

Validation of the immersed boundary method

Before using the immersed boundary method to implement wall deformation for conducting drag reduction studies, we apply the method to solve problems with known solutions to establish the accuracy of the method. The advantages of validating the immersed boundary method are many: not only do we gain confidence that the results of the problems that we are trying to solve, drag reduction by wall deformation in our case, are valid but also get to learn more about the method itself, test its limits and develop even better methods. We test our method with the following three problems for which solutions are known, either analytically or experimentally/numerically: (1) unidirectional flow, (2) nearly unidirectional flow, and (3) turbulent flow in a channel.

10.1 Laminar flow in a channel

In this test, we use the immersed boundary method and derive body forcing as described in Chapter 9 to simulate laminar flow in a channel as illustrated in Figure 7.1. We start a simulation with a laminar, parabolic velocity profile in the physical domain, i.e., the region bounded by the two dashed lines, as the initial condition, and see if the laminar profile is maintained. If our immersed boundary condition can maintain the laminar velocity profile in the channel, it is a good indication

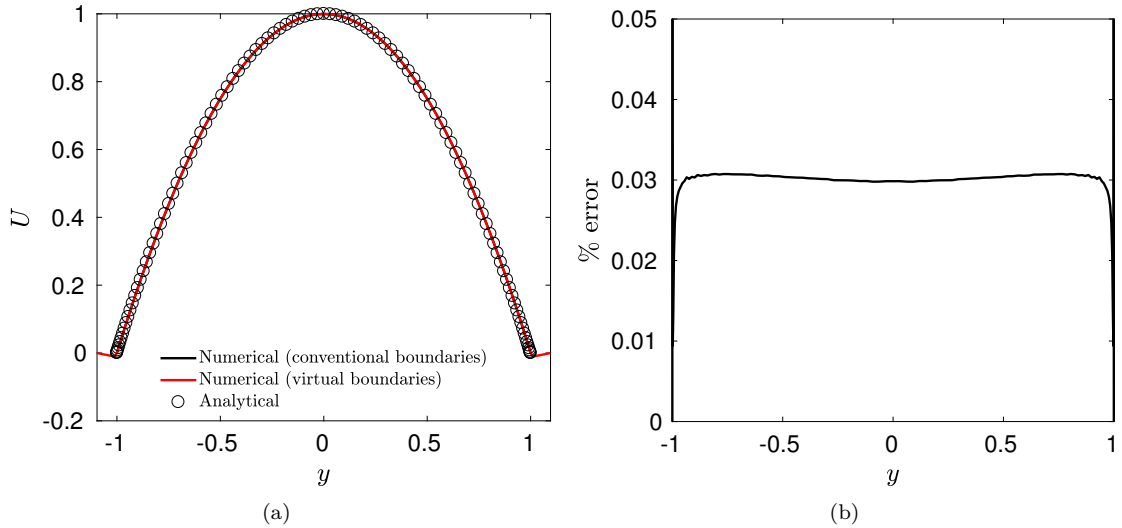

Figure 10.1: (a) Comparison of steady-state velocity profile obtained numerically from the finite-volume code with the analytical solution $u\,(y) = 1 - y^2$. (b) Percent error between the numerical and analytical solutions.

that the forcing strategy and the implementation of IBM are correct.

We initialise the streamwise velocity with a laminar, parabolic profile as described by Equation (A.83); velocity at the centre of the channel is 1. No-slip boundary condition is enforced at the virtual boundary (channel wall). This is achieved by setting the u velocity at the first grid point in the virtual solid such that the interpolated value at the virtual boundary is zero. The flow field in the rest of the virtual solid is arbitrary. The wall-normal and spanwise components are set to zero everywhere (Equations (A.84) and (A.85)). Other simulation parameters for this validation test are the same as discussed in Table A.2. The momentum equations are integrated in time until a steady state is reached. The numerical result is then compared with the analytical solution as well as laminar flow results from a channel with conventional boundaries, that have been discussed in Appendix A.4.2.

Figure 10.1(a) shows the laminar steady state velocity profile across the entire computational domain in red colour. In between the planes $y = -1$ (bottom wall) and $y = 1$ (top wall), it shows an excellent agreement with the analytical solution (shown as black circles) as well as with the numerical solution in a channel with conventional boundaries, i.e., without virtual boundaries (shown as black line). The red line lies exactly on top of the black line, hence the latter is not visible. The region to

the left of $y = -1$ and the region to the right of $y = 1$ correspond to virtual solids: the numerical solution in these regions does not have any physical meaning and hence it can safely be ignored.

Figure 10.1(b) illustrates the percent error in the computation of numerical solution. Specifically, we have plotted $|(U_n - U_a)/U_a| \times 100\%$, where U_n is the numerical solution and U_a is the analytical solution. Error only in the region of interest, i.e., physical domain $-1 \leq y \leq 1$ is shown. Overall, the error across the channel height is extremely small just like what was observed in Appendix A.4.2 — it is less than 0.035%.

For future reference, we would like to mention that showing of numerical results in the non-physical part of the computational domain, i.e., virtual solid, will be restricted to the current chapter only. In all the future chapters, only the results in the physical domain will be presented and discussed.

10.2 Nearly unidirectional flow in a channel

Laminar flow in a channel, as we discussed in Chapter 10.1, is an example of a unidirectional flow. Two velocity components, wall-normal (v) and spanwise (w), were zero, which enabled the determination of exact solution to the Navier–Stokes equations. There can be situations when one of the velocity components is not identically zero, but small. For such problems, inertial effects are unimportant and their solution can be determined in a way similar to unidirectional flows, by exploiting the *lubrication approximation*. Liquid flowing in a long, narrow channel shows characteristics of being nearly unidirectional and the flow is dominated by viscous effects.

In this chapter, we test our immersed boundary forcing strategy in a long and wide, but very narrow channel with a wavy wall. We consider a steady, two-dimensional flow in between the channel walls: the top wall is flat whereas the bottom wall has a sinusoidal shape in the streamwise direction. Both the walls are rigid and stationary. The flow is along x and y axes only; the main flow is along the x axis though. Spanwise velocity (w) is zero everywhere. Due to the sinusoidal shape of the bottom wall, the channel height or the gap between the walls varies with position along

the streamwise direction. Since $w = 0$, the continuity equation (Equation (A.7)) reduces to:

$$\frac{\partial u}{\partial x} + \frac{\partial v}{\partial y} = 0 \tag{10.1}$$

Here, both u and v depend on x and y. Let $\mathcal{L}_x$ and $\mathcal{L}_y$ represent the length scales for velocity variations in the x and y directions, respectively, and let the velocity scales in the corresponding directions be represented by $\mathcal{U}$ and $\mathcal{V}$, then it follows from Equation (10.1) that $\mathcal{U}/\mathcal{L}_x \sim \mathcal{V}/\mathcal{L}_y$, or

$$\frac{\mathcal{V}}{\mathcal{U}} \sim \frac{\mathcal{L}_y}{\mathcal{L}_x} \tag{10.2}$$

For our test case, we have $\mathcal{L}_y \sim 0.15l$ and $\mathcal{L}_x \sim 100l$, therefore, the variation on velocity in the two directions is such that $\mathcal{V}/\mathcal{U} \sim 1.5 \times 10^{-3} \ll 1$. Making use of this information in addition to the fact that the flow is steady, the Navier–Stokes equation reduces to:

$$\frac{\partial^2 u}{\partial y^2} = \mathrm{Re}\frac{\mathrm{d}p}{\mathrm{d}x} \tag{10.3}$$

Equation (10.3) is known as the lubrication approximation. Here, $u = u\,(x, y)$, $p = p\,(x)$ only and $\mathrm{d}p/\mathrm{d}x$ depends on x. Reynolds number, Re, must be small.

The shape and size of the channel and other simulation parameters are discussed below. The length of the channel is $L_x = 100l$ and its width is $L_z = 50l$; both are large compared to the half-height of the computational domain, l. The plane $y = l$ corresponds to the top wall. If the plane $y = 0$ lies at the centre of the computational domain, then the coordinates of the bottom wall are given by $y = -\{l - h\,(x)\}$ where $h\,(x)$ follows from the equation:

$$h\,(x) = 0.15\left\{1 + \sin\left(\frac{2\pi x}{L_x}\right)\right\} l \tag{10.4}$$

A schematic of the long channel (not drawn to scale) indicating in thick black lines the flat top wall and the wavy bottom wall is shown in Figure 10.2. The red circles on the bottom wall indicate the streamwise locations where comparison between numerical and analytical solutions will be presented. Other parameters used in the simulation are listed in Table 10.1. The Navier–Stokes are integrated

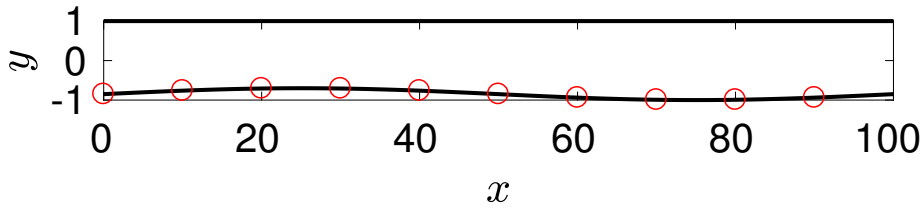

Figure 10.2: A two-dimensional schematic of the plane Poiseuille flow geometry showing the x-y plane. Lengths are scaled with l, the half-height of the computational domain. Both the top and bottom walls are stationary: the top wall is flat and it lies at $y = 1$ while the bottom wall is wavy — it has a sinusoidal shape. The flow is two-dimensional and it is from left to right. Results for comparison between numerical and analytical solutions are presented for streamwise locations indicated by red circles on the bottom wall.

Re (Re_τ)	L_x/l (L_x^+)	L_z/l (L_z^+)	$N_x \times N_y \times N_z$	Δx^+	Δz^+	$\Delta y^+_{min}, \Delta y^+_{max}$
1 (1.54)	100 (153.69)	50 (76.84)	180 × 135 × 200	0.85	0.38	4.22×10^{-4}, 0.04

Table 10.1: Simulation parameters used for simulating a nearly unidirectional flow in a very long and wide channel.

until statistical steadiness is reached. The numerical solution is then compared with the analytical solution at the streamwise locations represented by red circles in Figure 10.2. The analytical solution, which is described by Equation (10.5), is obtained by solving Equation (10.3) for the channel shown in Figure 10.2 and applying appropriate boundary conditions.

$$U_a(y) = \frac{\frac{4}{3}(1-y)(1-h+y)}{(1-h)(2-h) + \frac{h^2}{2}(2-h) - \frac{1}{3}\left\{1+(1-h)^3\right\}} \tag{10.5}$$

Here, the velocity is scaled with the laminar centreline velocity in a channel with both walls flat and stationary, and the lengths are scaled with the half-height of the computational domain, l.

Figures 10.3(a)–10.3(j) show steady-state mean velocity profiles in black lines at the locations represented by red circles in Figure 10.2. Analytical solution at the same locations is also shown in black circles for comparison. The virtual boundary is represented by a dashed vertical line. Although the flow was reversed in the region occupied by virtual solid (left side of the dashed line), velocity in those regions is shown as zero — it is non-physical anyway. In the physical part of the domain (right side of the dashed line), an excellent correspondence is seen at all the locations. Both the numerical and analytical solutions match perfectly.

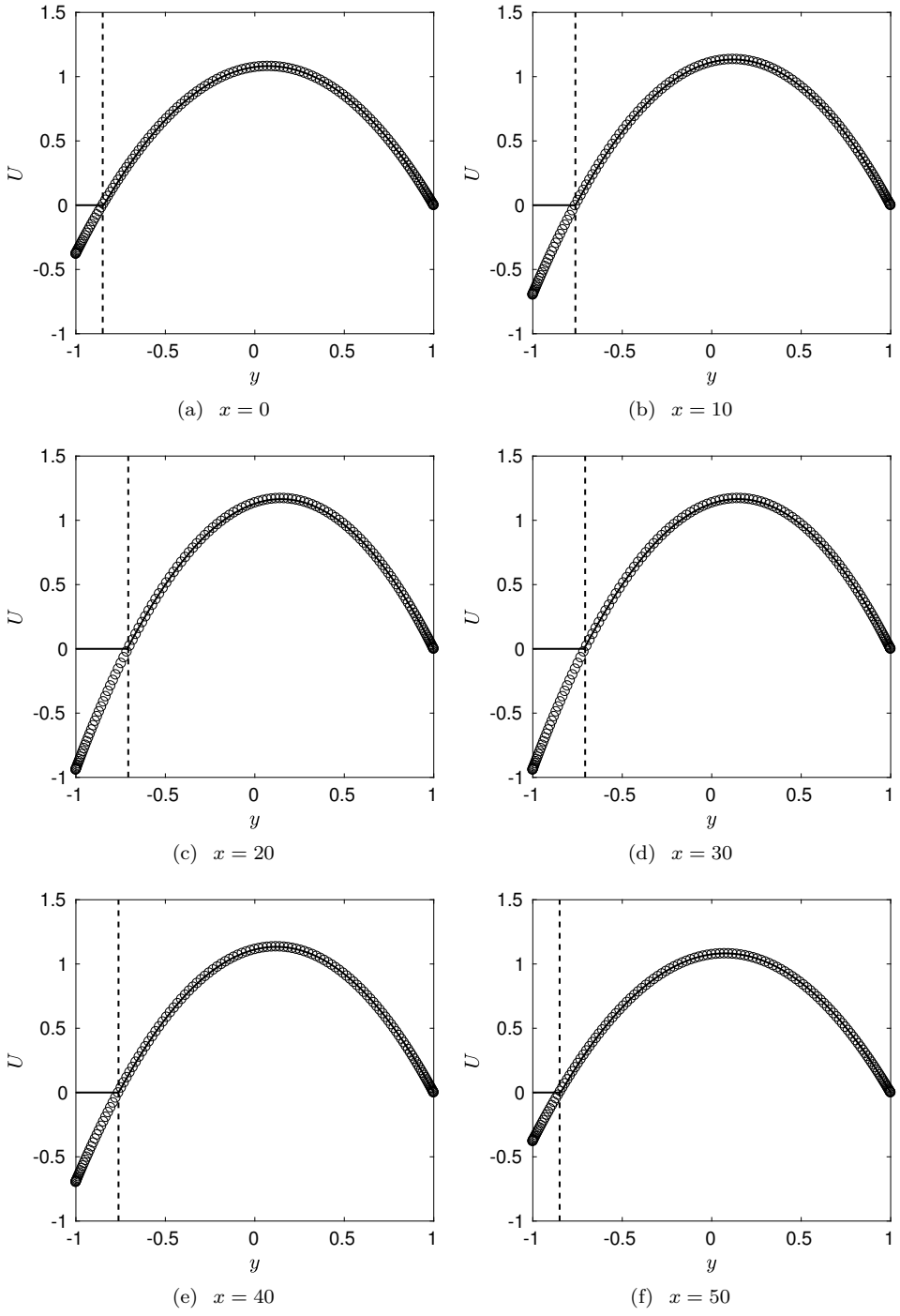

(a) $x = 0$ (b) $x = 10$

(c) $x = 20$ (d) $x = 30$

(e) $x = 40$ (f) $x = 50$

Figure 10.3: For caption see next page.

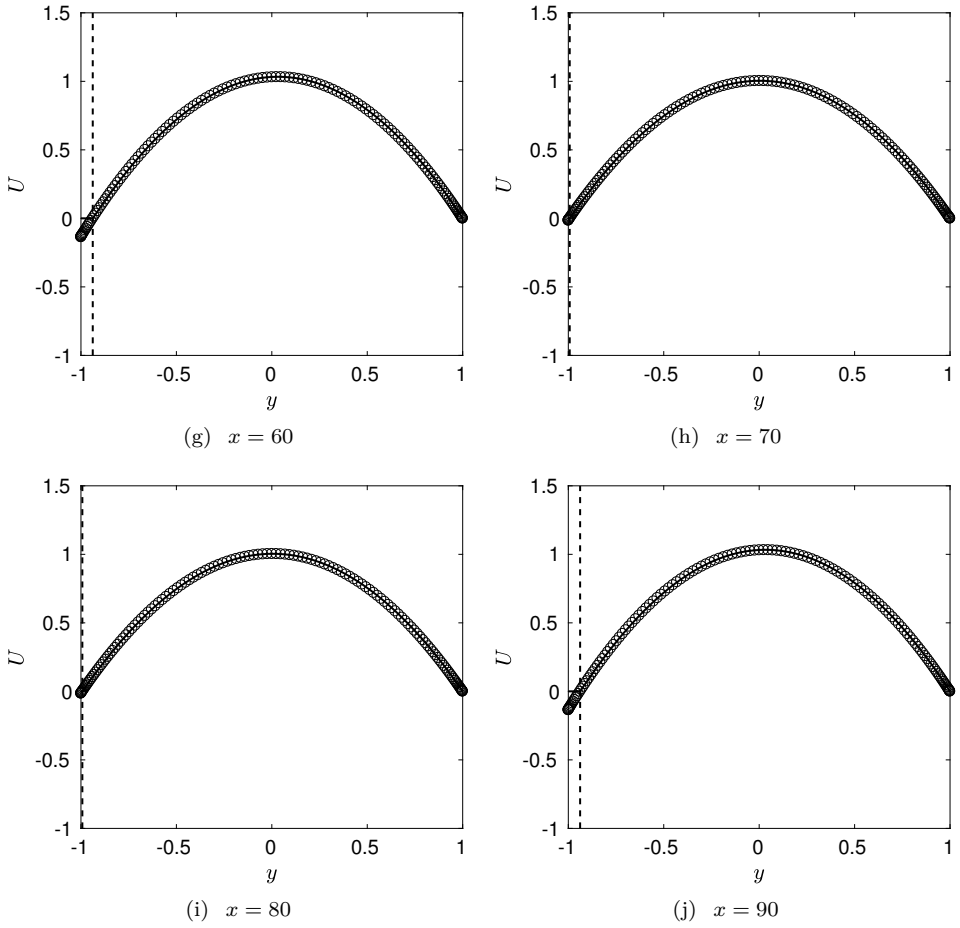

(g) $x = 60$ (h) $x = 70$

(i) $x = 80$ (j) $x = 90$

Figure 10.3: Comparison of steady-state mean velocity profiles at different streamwise locations obtained numerically from the finite-volume code (lines —) with the analytical solution (circles o). The dashed vertical line (——) represents the virtual boundary: both numerical and analytical solutions lying on the left side of this boundary are non-physical and can be safely discarded.

10.3 Turbulent flow in a channel

The primary objective of implementing immersed boundary method in our code is to simulate turbulent flows in a channel with arbitrarily shaped walls. It is, therefore, important that the immersed boundary method is also validated for turbulent flows. The most straightforward way to do it would be to simulate a turbulent channel flow in the physical domain (region bounded by the two dashed lines) with immersed boundary conditions that satisfy the no-slip and no-penetration conditions for non-moving flat walls. There are no analytical solutions for turbulent flows due to their chaotic nature, hence we compare statistics obtained from our code with numerical solutions obtained from ChannelFlow [Gibson, 2009], which has already been validated extensively.

In this validation study, the top and bottom walls of the channel, corresponding to the virtual boundary, remain flat at all times. They lie at $y = 1$ and $y = -1$, respectively, and the plane $y = 0$ corresponds to the centre of the channel. The computational domain extends from $y = -1.0962$ to $y = 1.0962$ — the additional thickness of 0.0962 at the top and the bottom of the computational domain is occupied by virtual solid. The flow is maintained by a pressure gradient in the streamwise (x) direction, and the bulk velocity is kept constant at $U_{bulk} = 2/3$. The pressure gradient is dynamically adjusted to maintain a constant flow rate. Pressure gradients in the wall-normal and spanwise directions are zero. Simulation parameters for this validation test are presented in Table 10.2.

In Figures 10.4(a) and 10.4(b), we have plotted the mean velocity profile (red circles) for Newtonian turbulence the parameters for which are given in Table 10.2, using a linear scale and a semi-log scale, respectively. Note that $y^+ = 0$ represents the location of the channel wall. The region $y^+ < 0$ corresponds to a virtual solid and hence it is non-physical. For comparison, ChannelFlow results (black line) as well as results from the finite volume code with conventional boundaries (black circles) are also presented. The correspondence between the three velocity profiles is commendable near the

Re (Re_τ)	L_x/l (L_x^+)	L_z/l (L_z^+)	$N_x \times N_y \times N_z$	Δx^+	Δz^+	$\Delta y^+_{min}, \Delta y^+_{max}$
1800 (85)	π (267.04)	$\pi/2$ (133.52)	$51 \times 136 \times 41$	5.45	3.42	0.92, 2.18

Table 10.2: Simulation parameters for turbulent flow in a channel with flat walls implemented using the immersed boundary method.

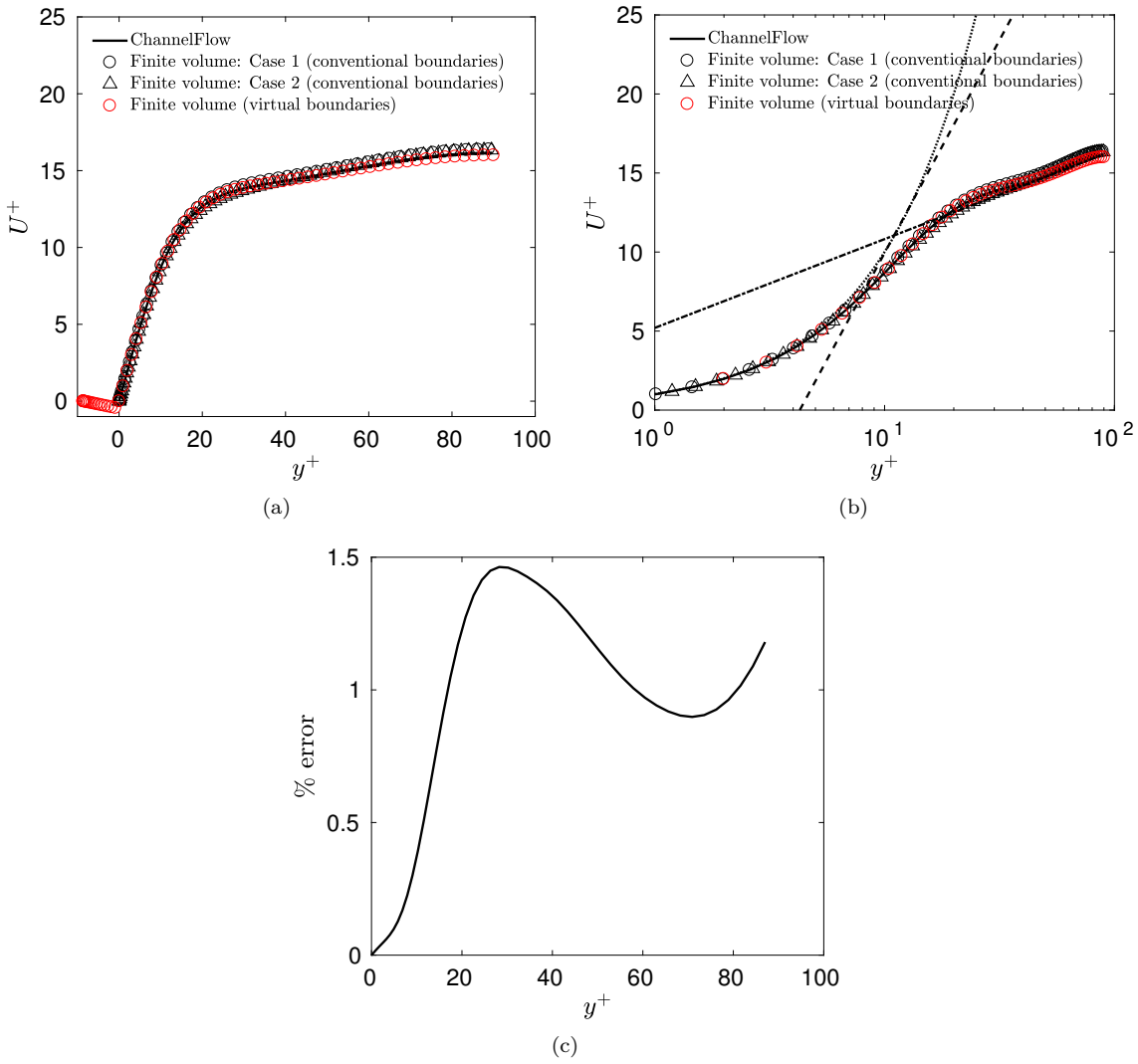

Figure 10.4: Mean velocity profiles in minimal channel Newtonian turbulence at $\mathrm{Re}_\tau = 85$ calculated using ChannelFlow and our finite-volume code plotted using (a) a linear scale, and (b) a semi-log scale. In (b), the black dotted line is the viscous sublayer, $U^+ = y^+$; black dashed-dotted line is the Prandtl-von Kármán log-law, $U^+ = 2.44 \ln y^+ + 5.2$ and the black dashed line is the Virk MDR log-law, $U^+ = 11.7 \ln y^+ - 17.0$. (c) Percent error between the mean velocity profiles obtained from ChannelFlow and finite volume codes.

wall whereas a small discrepancy can be observed away from the wall. Figure 10.4(c) shows the percent error between the finite volume results for the case with virtual boundaries and ChannelFlow results. The error is minimum near the wall and it increases slightly as one moves away from the wall. The maximum percent error across the half-channel is still less than 1.5%.

Chapter 11

Conclusions of Part II

In Part II we discussed immersed boundary methods and their usage to achieve a desired velocity distribution over a smooth rigid surface of an arbitrary shape. Immersed boundary methods are preferred over coordinate transformation as generating a grid that conforms to the shape of the walls at every time step can be computationally expensive. Two broad categories of immersed boundary methods were discussed: continuous forcing and discrete forcing. The continuous forcing approach was found to be more suitable for flows over flexible bodies; for flows over rigid bodies, they made the system stiff. This forces us to take smaller computational time steps, thus increasing the total computation time. The continuous forcing approach also smears the boundary between the solid and the fluid. The situation gets worse at higher Reynolds numbers. Direct forcing approach, on the other hand, suits best for flows over complex, rigid boundaries. This approach does not smear out the interface between the solid and the fluid, and thus, is recommended for flows at higher Reynolds numbers.

A description of the modified computational domain was provided. To allow space for deformable walls, extra solid regions or "virtual solid" regions are included near the top and bottom walls. The thickness of each of these regions is approximately $0.1l$, where l is the half-height of the physical channel. The momentum equations are solved for the entire computational domain, including the virtual solid regions, but the results in the virtual solid regions are ignored as they are not a part of the physical channel.

A step-by-step numerical procedure for the determination and implementation of the direct forcing at each time step is discussed. Body forces are applied at nodes only adjacent to the deformable wall (or the virtual boundary). These nodes are forced in a way such that the the desired boundary conditions at the moving walls are satisfied. No-slip boundary condition in the streamwise and spanwise directions is satisfied by reversing the flow in the virtual solid region. No-penetration boundary condition is satisfied by forcing the wall-normal velocity to a value such that the divergence of the velocity field in the cell cut by the immersed boundary interface is zero.

Finally, a detailed study validating our immersed boundary method in different situations is conducted. It is found that the results — the first and second order statistics in particular — of flows with the immersed boundary conditions match with the known results in a plane channel under the same conditions, or with the analytical solutions. This gave us confidence that the results of the drag-reduction problem we are going to solve using the immersed boundary method will be valid.

Part III

Drag reduction utilising the nonlinear dynamics of near-wall turbulence

Chapter 12

Introduction

Turbulence control is of great importance in fundamentals and applications, and it has been a subject of study for more than a century because of the potential benefits associated with it, particularly with regard to energy savings. Turbulence, characterised by chaotic property changes, results in an increase in skin-friction drag. Each year, ocean shipping consumes more than a billion barrels of oil worldwide. At subsonic cruising speeds, approximately half of the total drag of aircraft is due to skin friction, which results in huge consumption of fuel. Similarly, transportation via road also consumes about a billion barrels of oil per year [Kim, 2011]. Current fuel prices are very high, and may increase further due to increasing demands. Any savings on fuel consumption by reducing skin-friction drag could result in huge gains, ranging from billions of dollars saved in operational costs for transportation industries, to a clean, pollution-free environment. Other examples of turbulence control that are of interest include enhanced heat transfer, control of separation and reattachment, and reduction of energy loses in pipelines.

The necessity and urgency of searching for convenient and efficient methods to conserve energy by flow control has invigorated attempts at designing control strategies and testing them by numerical computations. Studies have shown that flow structures near the wall are responsible for the production of turbulent kinetic energy, and a substantial amount of drag-reduction can be achieved by suppressing these near-wall structures [Choi, 1989]. Most of the attempts at weakening these structures have been based on the physical intuition of the researcher and the physics of the flow.

One of the most widely studied control strategies is the opposition control [Choi et al., 1994; Wang et al., 2016] where blowing and suction is used at the wall based on velocity information inside the flow. This approach results in the suppression of the near-wall structures leading to significant drag reduction (more than 20%). Some control strategies like using riblets or imposing a body force, e.g., Lorentz force, aim at disrupting the fully-developed turbulence near the wall. However, these strategies have their own limitations. The most successful approach to turbulent drag reduction is to add a small amount of polymer molecules to the liquid [Virk, 1975]. This approach was tested on a US Navy submarine (as an external flow) in the 1970s where it was found that hull drag was reduced and speed increased by 10-15%. It is also widely followed by oil industries, e.g., Alaska pipeline [White and Mungal, 2008]. Addition of polymer manipulates the flow in the near-wall region, and drag reduction upwards of 80% can be achieved [White and Mungal, 2008]. This approach, however, can only be used in liquids. We wish to understand and implement turbulent control in situations where addition of polymers is not possible, e.g., flow over the wings of aeroplane.

In the following few paragraphs, a review of existing drag-reduction methods is presented, with their pros and cons wherever required. In the final few paragraphs, some ideas for the development of new control methods are discussed. These ideas come from the fact that some of the invariant solutions to the Navier–Stokes equations form an important part of the intermittent nature of wall turbulence.

Drag reduction techniques are mainly divided into two categories: *passive* and *active*. Passive techniques are the ones that involve no energy expenditure. They include drag reduction by riblets, dimples, usage of outer layer devices (OLDs), boundary layer devices (BLADEs), large eddy breakup devices (LEBUs) and tandem arrayed parallel plate manipulators (TAPPMs) [Abdulbari et al., 2015]. On the other hand, drag reduction techniques that require energy and involve a control system are active techniques. Polymer drag reduction, wall oscillations, travelling wave-like wall movements, blowing and suction, active wall deformations, plasma actuators are some of the examples of active drag reduction techniques. Some of the active techniques require sensing and actuation while some do not. We discuss few of these techniques, the amount of drag reduction they achieve, their feasibility and effectiveness below.

One of the most popular and successful techniques to reduce skin-friction drag is to add a small

amount of long-chain polymer to the liquid flow — concentrations in parts per million (by weight) is often adequate. Also known as the Toms' phenomenon [Toms, 1949, 1977; Virk et al., 1967, 1970; Virk, 1975], it has been shown to occur with many polymers and solvents, e.g., polymethylmethacrylate (PMM) in monochlorobenzene, PMM in toluene, polyisobutylene (PIB) in cyclohexane and in benzene, carboxymethyl cellulose (CMC) in water, guar gum in water, a copolymer of polyacrylamide and polyacrylic acid in water and polyethylene oxide (PEO) in water [Lumley, 1969], and is widely used in the fossil fuel industry [Fink, 2012], in the Alaska pipeline [Burger et al., 1982; White and Mungal, 2008] and in fracking fluids [King, 2012]. It has been shown numerically in minimal channels that stretching of polymer molecules leads to the weakening of three-dimensional coherent structures, which results in the reduction of skin-friction drag [Stone et al., 2002, 2004; Li et al., 2005, 2006; Kim et al., 2007; Li and Graham, 2007; Kim et al., 2008] — a minimal flow unit is the smallest simulation box for a given set of parameters, periodic in streamwise and spanwise directions, with periods corresponding to the smallest length scales containing only the essential self-sustaining turbulent elements for which turbulence persists [Jiménez and Moin, 1991]. Graham and co-workers [Xi and Graham, 2010a, 2012b; Wang et al., 2014; Graham, 2014; Wang et al., 2017] have shown that the flow characteristic of high drag, or *active* turbulence, stretches the polymer chains. The polymer stress that arises due to polymer stretching suppresses the highly turbulent motions and the flow enters a relatively calmer state characteristic of lower drag or *hibernation*. The flow stays near the low-drag state for a time interval during which polymer molecules start relaxing in the weakened flow field. Eventually, polymer chains return to their original, relaxed state: the hibernation period ends and the flow becomes turbulent again. This cycle repeats in a stochastic manner, making the flow behaviour very intermittent with respect to time and space. Drag reduction by polymers is one of the most inexpensive and efficient techniques to reduce skin-friction drag. It can easily be used for all closed geometries and does not require any special boundary conditions. However, it can be used only in liquids, and there are problems associated with polymer breakage — mechanical degradation of polymer molecules occurs under high shear conditions due to interaction with turbulent flows as well as being passed through pumps. The breakdown of polymer chains significantly reduces its relaxation time which then reduces the overall drag reduction capabilities of the polymers [Shanshool et al., 2011; Abubakar et al., 2014]. Some other ways of reducing skin-friction drag that do not

suffer from the problems associated with polymers are discussed in the following paragraphs.

In an attempt to suppress the near-wall vortical structures, Choi et al. [1994] applied opposition control by local blowing/suction at the wall. In their DNS of turbulent flow, they changed the wall-normal velocity at the wall such that it was equal and opposite to the wall-normal velocity of the fluid at a distance of $y^+ = 10$ from the wall. This action prevents the transport of momentum toward and away from the wall [Hammond et al., 1998] by reducing the spin of the vortices. It resulted in a drag-reduction of 25-30% at a Reynolds number of 3300 (corresponding friction Reynolds number, $\mathrm{Re}_\tau = 180$). They examined the resulting flow-fields and found that the strength of the near-wall streamwise vortices was substantially reduced. This approach, however, is difficult to implement, as it requires velocity information within the flow, which is not easily available. However, from the approach, it became clear that near-wall streamwise vorticies can indeed be suppressed and skin-friction drag be reduced by manipulating the turbulent structures near the wall. Chung and Talha [2011] found that the amplitude of blowing/suction as well as the location of the detection plane play an important role in the effectiveness of opposition control. A recent numerical study conducted by Ge et al. [2017] discusses the initial response of turbulent flow to slow and rapid application of opposition control. They show that the application speed of opposition control does not alter the final state of flow but it does have a significant influence on the dynamic evolution during the initial stages after the control is applied.

Many variations of Choi's opposition control have been developed and tested by several researchers. For example, Deng et al. [2014] strengthened the control input by introducing time relaxation into the scheme. The reduction in drag from the updated scheme was enhanced and the maximum drag reduction achieved was 33%. In a different study, Deng et al. [2013] used a linear transient growth model to determine the input for the opposition control using blowing and suction. They show that a detection plane at $y^+ = 15$ can significantly suppress the transient growth of near-wall structures. However, if the detection plane is located in the buffer layer, then the influence of the control on large scale motions is limited and decreases as Reynolds number increases. Pamiès et al. [2007] proposed a blowing-only opposition control — where the suction part was removed — on a spatially developing turbulent boundary layer at high Reynolds numbers. Their method injected fluid into the boundary layer, and the net mass flux across the wall, although non-zero, was very

small. Some studies have stabilised the flow by using a streamwise-travelling wave of blowing and suction in a channel [Min et al., 2006; Lee et al., 2008; Hœpffner and Fukagata, 2009; Moarref and Jovanović, 2010; Lieu et al., 2010], streamwise-varying steady transpiration in a pipe [Gómez et al., 2016], and uniform blowing and suction in a turbulent boundary layer [Kametani and Fukagata, 2011; Kametani et al., 2015].

In order to overcome the problem associated with Choi's opposition control, Lee et al. [1997] designed a neural network that was trained to predict actuation at the wall for a desired output, i.e., flow with reduced drag. The optimal value of the control input was calculated as a function of the weighted sum of spanwise wall shear rate near the point of interest. By actuating the wall using blowing/suction, they were able to reduce the skin-friction drag by as much as 20% at low Reynolds numbers. Upon examining the computed flow-fields, it was found that instantaneous patterns looked very similar to those observed in the opposition-controlled channel of Choi et al. [1994]. Another improvement to Choi's opposition control was provided by Ge et al. [2015]. They developed an opposition control that instead of using information from within the flow, requires flow properties that can be easily measured at the walls. Specifically, they measure the pressure fluctuations (p') and spanwise shear stress fluctuations (τ'_{yz}) at the wall to detect near-wall streamwise vortices, and their opposition control schemes to suppress the near-wall vortices using the above two measurable quantities result in a drag reduction of 16% and 11%, respectively.

In Choi's opposition control, it was observed that blowing and suction increased the spanwise pressure gradient under the streamwise vortex near the wall. Lee et al. [1998] used this result to construct a control scheme that maximised the pressure gradient in the spanwise direction near the wall. Their scheme was suboptimal, i.e., they sought to minimise the objective function over a short time period ($T \to 0$). About 16-22% drag-reduction was obtained in a turbulent channel flow at $\mathrm{Re}_\tau = 110$ (Re_τ is based on the unactuated flow). This control scheme gave results almost identical to the neural network results obtained by Lee et al. [1997] — the two control schemes were derived by totally different approaches, but they resulted into similar feedback control laws. Xu et al. [2002] extended the same strategy to turbulent pipe flows at $\mathrm{Re}_\tau = 150$ and achieved 13-23% drag-reduction. Fukagata and Kasagi [2004] developed a similar scheme which aimed at minimising the near wall Reynolds shear stress, and obtained a drag-reduction of about 12% at $\mathrm{Re}_\tau = 180$ (Re_τ

based on the unactuated flow). Bewley et al. [2001] adopted a control scheme where the objective functions were minimised over a finite time period T, in a turbulent channel at $\mathrm{Re}_\tau = 100$. They achieved flow relaminarisation accompanied by a drag reduction of over 50%, and showed that in order to achieve such high levels of drag reduction, it is necessary to optimise the control schemes over a sufficiently long time, i.e., $T^+ \geq 25$. Their approach, however, is computationally expensive (since it requires solving Navier–Stokes equations iteratively) and impossible to implement in a realistic setting. Choi and Sung [2002] examined the effect of amplitude and timescale of actuation and the size of sensor/actuator and concluded that the optimal timescale is ~ 1 in inner units and that the most effective drag reduction is achieved by using wall-normal velocity at the wall as the control input, determined from the local distributions of the spanwise velocity gradient at the wall.

Among other turbulence control strategies that require energy input by the controller, active wall motion is one of the most practical ways to achieve skin-friction drag reduction. Carlson and Lumley [1996] used a Gaussian shaped actuator, 12 wall units in height, that emerges from one of the walls of minimal turbulent channel flow. They showed that a drag-reduction of 7% can be achieved if the actuator is raised with a maximum velocity of $1u_\tau$ before and under a sweep motion. By doing this, the faster moving fluid is moved away from the wall and the adjacent low-speed region is expanded.

Kang and Choi [2000] implemented local wall-deformation based on two successful control strategies of Choi et al. [1994] and Lee et al. [1998]. At $\mathrm{Re}_\tau = 140$ (based on the unactuated flow), they achieved an overall drag-reduction of 13-17% — lesser than what was achieved by Choi et al. (25-30%) and Lee et al. (16-22%). This was attributed to the fact that the amplitude to wall-deformation was limited to 5 wall units. Opposition control of Choi was also used by Endo et al. [2000], Endo and Kasagi [2001] and Sun et al. [2011] in the form of wall-deformation to attenuate the meandering of low-speed streaks which occurs due to tilted quasi-streamwise vortices in the spanwise direction and contributes to the regeneration mechanism [Jeong et al., 1997]. A drag-reduction of about 10% was obtained at $\mathrm{Re}_\tau = 150$ (based on the unactuated case). Results from DNS of turbulent channel flows with opposition type control indicate that due to the interaction between the wall-normal velocity component accompanied by a vortex and the wall-normal velocity at the wall, a virtual wall is established [Hammond et al., 1998], where the wall-normal velocity component gets nullified and the near-wall momentum transport is reduced.

Pamiès et al. [2011], however, have pointed out that the gains associated with an ideal opposition control are completely annihilated when a realistic actuator description is included in the simulation. In their simulation, they used finite-sized actuators, and for $\mathrm{Re}_\tau = 368$, they showed that form drag, although small, wipes off any reduction in skin-friction drag achieved if it is included in the calculation of overall drag reduction. This is attributed to the fact that the more realistic control is both *confined* and *localised*. In the classical opposition-control scheme, it is assumed that each sensor and actuator is infinitely small and there are infinite number of such actuators, thus the turbulent structures are opposed at every grid point, which is not possible if the actuators have finite spatial dimensions. Therefore, the physical actuators are confined. It is also assumed that the actuators are convected with the turbulent structures whereas in a practical setting, they are fixed to the wall. This imparts a local character to the actuators. Thus, it becomes imperative to develop sensors and actuators to be able to achieve better results in real flows.

Some model predictive active-control algorithms have also been developed and implemented [Joshi et al., 1997; Högberg et al., 2003a,b; Kim and Bewley, 2007; Belson et al., 2013; Semeraro et al., 2013; Dadfar et al., 2014], using the linearised form of the Navier–Stokes equations. It has been identified that important parts in the self-sustaining process of near-wall turbulence are essentially nonlinear, but they are maintained by a linear mechanism [Kim and Lim, 2000; Kim and Bewley, 2007]. However, the linear operator of the linearised Navier–Stokes equations is non-normal, and this non-normality arises due to linear coupling between wall-normal velocity and wall-normal vorticity, which leads to the creation of streaks in the self-sustaining process. That is, disturbances can grow up in time proportional to $\mathcal{O}(\mathrm{Re})$ even below the critical Reynolds number (where laminar flow is linearly stable) before they ultimately die out. Lim [2003] designed a controller with the aim to minimise the linear coupling term L_c ($\omega_x + L_c \Rightarrow$ streaks which lead to more ω_x, where ω_x is the streamwise vorticity). The resultant optimal control input (blowing/suction at the wall) was expressed linearly with the state vector (wall-normal velocity and vorticity as mentioned above) and a drag-reduction of about 20% was achieved. It was also observed that in contrast to opposition control, the control effect in this case was confined to the near-wall region. However, due to nonlinearity of the system, the state vector evolves in time, therefore the linear operator in the linearised Navier–Stokes equations, which depends on the mean flow, does not remain time-

independent [Kim, 2003]. Additionally, the control requires that the entire velocity field be known. Due to these reasons, such approaches seem unrealistic to be experimentally verified, although they do indicate the potential of model-based control for suppression of turbulent skin friction.

Studies have also been conducted to explore the possibility of achieving drag-reduction in a turbulent channel via wall actuation in an open-loop control scheme. Mito and Kasagi [1998] studied drag-reduction in a turbulent channel flow with a wall oscillating like a standing wave. The deformation, comparable with the thickness of the viscous sublayer, is uniform in the streamwise direction and spatiotemporally sinusoidal in the spanwise direction. The skin-friction change is reflected in the vorticity fluctuations, and the receptivity of the induced flow structures changes with the fluctuating skin-friction. Similarly, effects of a streamwise travelling-wave of blowing/suction [Min et al., 2006; Lee et al., 2008; Hœpffner and Fukagata, 2009] as well as wall-deformation in the form of travelling-wave in the streamwise [Shen et al., 2003; Hœpffner and Fukagata, 2009; Nakanishi et al., 2012] and spanwise [Klumpp et al., 2011; Tomiyama and Fukagata, 2013] directions have been studied and it has been found that skin-friction drag can be reduced and even completely eliminated (laminarisation) under certain sets of parameters.

A significant amount of drag-reduction (up to 40%) can be obtained by subjecting a wall flow to high frequency spanwise oscillations [Jung et al., 1992; Akhavan et al., 1993; Pollard, 1998; Choi et al., 1998; Dhanak and Si, 1999; Choi et al., 2001; Choi, 2002; Choi et al., 2002; Lee and Kim, 2002; Iuso et al., 2003; Quadrio and Ricco, 2004; Zhao et al., 2004; Ricco and Quadrio, 2008; Quadrio et al., 2009; Quadrio and Ricco, 2010; Quadrio, 2011; Ricco, 2011; Yudhistira and Skote, 2011; Skote, 2011, 2012; Ricco et al., 2012; Touber and Leschziner, 2012; Duque-Daza et al., 2012; Gatti and Quadrio, 2013; Skote, 2013, 2014]. Baron and Quadrio [1996] suggested that the disruption of the spatial coherence between the longitudinal vortices and the low-speed streaks by oscillating a wall in the spanwise direction causes the vortices to pump the high-speed fluid away from the wall and low-speed fluid toward the wall, thus reducing the turbulent energy production. The most widely accepted mechanism is given by Choi et al. [1998] and Choi [2002] who proposed that the log mean velocity profile is shifted upwards and mean velocity gradient is reduced at the wall due to the creation of a spanwise vorticity near the wall. Bandyopadhyay [2006] analysed experimental and numerical data in the light of Stokes' second problem and proposed a vorticity reorientation hypothesis. He

also found that the mean velocity profile at maximum drag reduction is very similar to that due to polymer.

Results similar to those obtained from spanwise wall oscillations are obtained when an external spanwise body force in the form of oscillations or travelling wave is made to act in the fluid near the wall. This form of force can be achieved by lining permanent magnets and electrodes alternately in the spanwise direction, and the direction of the spanwise force can be altered periodically by switching the polarity of electric current [Huang et al., 2012]. Up to 30% drag-reduction can be obtained from the wavy force [Du et al., 2002], while the oscillatory form can result up to 40% drag-reduction [Berger et al., 2000]. However, the efficiency of this technique is usually very low [Berger et al., 2000; Huang et al., 2010; Breuer et al., 2004] — the energy required to impose the desired force on the flow is more than the energy saved from drag-reduction, and the situation worsens at high Reynolds numbers [Breuer et al., 2004]. This is primarily due to the poor conductivity of the system, e.g., seawater. The open-loop control techniques are attractive in a way that they do not require a large number of sensors and actuators. However, fabricating an actuating device which could induce travelling wave-like blowing and suction is still complicated.

Control techniques that do not require energy expenditure are known as passive control strategies. Many such strategies have been tested in the past, and they are believed to reduce drag in wall-bounded flows by introducing a transverse flow [Karniadakis and Choi, 2003], which disrupts the structures of the equilibrium turbulent flow [Jung et al., 1992]. One such technique which can result in a drag-reduction up to 10% involves microgrooves the size of viscous sublayer, known as riblets [Choi, 1989; Sirovich and Karlsson, 1997; Pollard, 1998; García-Mayoral and Jiménez, 2011a,b]. The concept of riblets gets its inspiration from the skin of a shark which has streamlined V-shaped protrusions [Sagong et al., 2008; Abdulbari et al., 2013] that greatly reduce the drag that a shark experiences while swimming at a speed of up to 50 $\mathrm{km\,h^{-1}}$. These microgrooves are etched into the surface and should be aligned with the local flow direction in order to achieve maximum drag reduction [Karniadakis and Choi, 2003]. Riblets hinder the spanwise movement of the streamwise vortices, preventing their stretching during ejections, thereby weakening the sweep events that follow [Choi et al., 1993]. Experimental and numerical studies conducted by Sagong et al. [2008] and a numerical study conducted by Boomsma and Sotiropoulos [2016] indicate an overall increase in

drag for flows over different arrangements of sharkskin denticles over a channel wall. The three-dimensionality of the denticles causes a secondary flow which results in the overall drag increase. Riblets, on the other hand, decrease Reynolds stresses and overall drag. Thus, the sharkskin denticles must have the correct size and arrangement for them to reduce skin friction drag like riblets. A new application of riblets was tested with the invention of ribbed swimsuits, which helped the swimmers win many gold medals at the 1995 Pan American Games [Jones, 2011].

Other successful passive control strategies include use of dimples [Abdulbari et al., 2013; Sun et al., 2011], compliant walls [Abdulbari et al., 2013; Kim and Choi, 2014], micro-bubbles [McCormick and Bhattacharyya, 1973; Abdulbari et al., 2013] and superhydrophobic surfaces [Min and Kim, 2004; Truesdell et al., 2006; Martell et al., 2009, 2010; Rothstein, 2010; Hasegawa et al., 2011; Busse and Sandham, 2012; Nouri et al., 2012, 2013; Park et al., 2013; Nguyen and Papavassiliou, 2013; Jelly et al., 2014; Lee et al., 2015b; Watanabe et al., 2017].

As noted above, it is extremely important to be able to develop sensors and actuators that can work on frequency and length scales required to directly manipulate near-wall turbulent structures — the spatiotemporal scales of coherent structures for aircraft are in the range of 100 µm and 100 kHz [Kasagi et al., 2009b]. Technology reviews by, for example, Ho and Tai [1998], Löfdahl and Gad-el Hak [1999], Sheplak et al. [2004], Kasagi et al. [2009b] and Cattafesta and Sheplak [2011] to name a few, have shown progresses in the development of micro-electromechanical systems (MEMS) and in the usage of such devices in control applications. Rathnasingham and Breuer [2003] used a spanwise array of synthetic jet actuators in response to shear stress and pressure measurements to introduce pairs of streamwise vortices into the flow — they obtained about 7% drag reduction. Micro hot-film sensors to measure streamwise wall shear stress fluctuations and magnetic actuators to deform the wall were used by Yoshino et al. [2008], who obtained about 6% reduction in drag in channel flow at $\mathrm{Re}_\tau = 300$. Große and Schröder [2009a,b] visualised wall shear stress patterns of coherent structures using micro-pillars with a spatial resolution of 5.33 viscous units. Recently, Hanson et al. [2014] designed a PI control algorithm and used plasma actuators to suppress streaks generated by roughness elements in a boundary layer flow.

Many other successful experimental studies have been conducted based on the control strategies tested numerically. Rebbeck and Choi [2001, 2006] carried out opposition control of the near-wall

turbulence over a flat plate at Re $\approx$ 1000. A piston-type actuator was used to create a jet in the wall-normal direction. They demonstrated that the drag can be reduced by selectively cancelling the downwash of high-momentum fluid during the sweep events. Rathnasingham and Breuer [1997] used a feed-forward control algorithm to investigate turbulence control. Three sensors were located upstream and one sensor was located downstream of the actuator and the aim was to minimise the streamwise-velocity fluctuations at the downstream sensor. A maximum reduction of 31% was obtained. Breuer et al. [2004] studied the effect of spanwise oscillatory Lorentz force in a low-speed salt water channel. A conductive polymer coating was used to reduce the problems associated with electromagnetic flow. They achieved a maximum drag reduction of approximately 10%. Itoh et al. [2006] and Tamano and Itoh [2012] investigated the effect of a spanwise-travelling wave with wall deformation in a wind tunnel. The test plate consisted of a flexible sheet section, where the travelling-wave motion was generated by a rotating eccentric disc connected to a motor. Velocity measurements, obtained by a hot-wire probe, were used to calculate the momentum thickness from which drag-reduction ratio was obtained. Sweep events were reduced and a maximum drag-reduction of 13% was obtained at a time period of 115 and average amplitude of 24 in viscous units. Effects of transversal wall oscillations on the near-wall flow in the buffer layer have been analysed experimentally on a flat plate [Iuso et al., 2003] and in a pipe [Auteri et al., 2010]. Wall oscillations in such experiments are usually produced by a crank-shaft system, which can also be used to create travelling-wave like wall deformations [Itoh et al., 2006; Tamano and Itoh, 2012]. An increase in the streak spacing was observed by Iuso et al. [2003], indicating reduction in turbulence activity, and a maximum of 33% reduction in drag was obtained by Auteri et al. [2010]. Some other successful turbulence control experiments have been performed by a number of researchers like Breuer et al. [1989], Kim et al. [2003] and Bai et al. [2014]. In a recent study, Li et al. [2015] combined the passive and active techniques by using a riblet-structured surface undergoing spanwise transversal wave motion. They observe that the combination yields a better drag reduction compared to the passive means alone. Specifically, while the riblet surface alone gave a drag reduction of 4.7%, the combination of riblets and wave motion resulted in a local drag reduction of up to 9.4%.

Recent advancements in the applications of dynamical systems theory to turbulent flows have shed light on transition to turbulence and the nature of turbulence near the wall [Hof et al., 2004;

Kerswell, 2005; Eckhardt et al., 2007; Willis et al., 2008; Kawahara et al., 2012]. The study of transient nature of wall turbulence and its connections to the near-wall coherent structures have been made possible by the discovery of nontrivial invariant solutions to the Navier–Stokes equations, or the exact coherent states (ECS) [Waleffe, 1998], for the canonical shear flows: plane Couette flow [Nagata, 1990; Clever and Busse, 1997; Nagata, 1997; Viswanath, 2007; Gibson et al., 2008, 2009; Halcrow et al., 2009; Itano and Generalis, 2009; Schneider et al., 2010; Deguchi et al., 2013; Blackburn et al., 2013; Nagata, 2013], plane Poiseuille flow [Waleffe, 1998, 2001, 2003; Toh and Itano, 2003; Nagata and Deguchi, 2013] and pipe flow [Faisst and Eckhardt, 2003; Wedin and Kerswell, 2004; Kerswell, 2005; Kerswell and Tutty, 2007; Pringle and Kerswell, 2007; Eckhardt et al., 2007; Duguet et al., 2008]. Most of these solutions have been found in the minimal flow units. The exact coherent states can be steady state solutions to the Navier–Stokes equations moving with a constant wave speed (nonlinear travelling waves), or relative periodic orbits, or edge states. Some of the exact coherent states display very interesting properties, for example, lying on or very close to the basin boundary between turbulent and laminar states, which is why in addition to understanding transition to turbulence, the nonlinear nature of wall turbulence can also be utilised towards developing effective control strategies. Specifically, the most successful control strategy would be to incorporate the highly nonlinear dynamics of near-wall turbulent flows — which would likely be flow information from the exact solutions — into the control algorithm. We describe this idea below.

Park and Graham [2015] discovered new families of exact coherent states occurring in the form of nonlinear travelling wave solutions for plane Poiseuille flow in a minimal channel. These solutions, also known as the building blocks of turbulence [Avila et al., 2013], arise in pairs as a result of saddle-node bifurcations: the upper branch solution of each pair has larger velocity fluctuations and higher drag compared to the lower branch solution. One family of solutions, which they denoted "P4", showed a particular intriguing behaviour. The mean velocity profile of the upper branch state approaches the Prandtl-von Kármán log-law while that of the lower branch approaches a form generally associated with turbulence in viscoelastic polymer solutions, the so-called Virk profile [Virk, 1975]. This profile is a good approximation of experimental and computational observations in the so-called "maximum drag reduction" (MDR) regime. Their DNS in the minimal channel at Reynolds number near transition exhibited temporal intermittency between high- and low-drag

intervals, a phenomenon that has been observed before by a number of researchers [Jiménez and Moin, 1991; Xi and Graham, 2010a, 2012b]: Xi and Graham [2010a] denoted the high- and low-drag intervals as "active" and "hibernating", respectively. They showed that the turbulent dynamics are organised around the P4 solution family. Specifically, as illustrated in Figure 2.1(a), at friction Reynolds number $\mathrm{Re}_\tau = 85$ the trajectory spends most of its time orbiting in the vicinity of the upper branch solution, displaying relatively high drag and a mean profile near the von Kármán profile, but occasionally takes excursions that approach the lower branch solutions (there are actually two of these because the lower branch turns back on itself) and thus exhibit low drag.

A recent numerical study conducted by Kushwaha et al. [2017] shows that Newtonian turbulence in large channels at Reynolds numbers near transition displays intermittency within turbulence both in time and in space. They did temporal and spatial analyses on their extended-domain data which they classified into low-, intermediate- and high-drag regimes, and showed that the localised flow structures and mean velocities of low-drag intervals show very close resemblance to those observed during low-drag intervals occurring temporally in minimal channels as well as to those of some of the lower branch P4 ECS in the near-wall region. Specifically, the near-wall flow structures and the mean velocity profiles of the low-drag regions resemble those of a lower branch minimal domain ECS, and hence, lie close to the Virk MDR profile. These intermittencies have also been observed experimentally by Whalley et al. [2017]. The similarities in flow properties between turbulence and ECS suggest that intermittenly, the turbulent trajectories approach the lower branch ECS in the state space. These results add to the set of observations in which mean velocity profiles close to the Virk profile are found in Newtonian flows [Kerswell et al., 2003; Bandyopadhyay, 2006; Xi and Graham, 2010a,b; Dubief et al., 2010; Xi and Graham, 2012a,b].

The existence of intermittency described above wherein the flow trajectory moves chaotically and approaches a particular family of exact coherent states has recently been supported experimentally by Suri et al. [2017] and Hof and Budanur [2017]. They studied turbulent flow at transitional Reynolds numbers generated in an electromagnetically forced shallow electrolyte layer and showed that the turbulent trajectory visit the neighbourhood of exact coherent structures repeatedly. Specifically, a trajectory approaches an ECS along its stable manifold, where the fluid dynamics slows down and the trajectory stays in the neighbourhood for a considerable period of time, and finally leaves the

region along the unstable manifold and heads toward another turbulent attractor, which could be a different exact coherent state. This process continues which not only gives rise to the chaotic nature of the flow but also develops into an intermittent phenomenon, and the intermittency is seen in the flow properties, e.g., wall shear stress, velocities, pressure, both temporally and spatially.

We use the idea that turbulent trajectories approach the lower branch ECS in the state space intermittenly to develop turbulence control strategies. As already discussed, many researchers have examined the effect of imposing wall deformations and oscillations in an attempt to manipulate the flow near the wall and achieve reduction in skin-friction drag. Wall deformations have been imposed either as simple opposition or as travelling wave-like perturbations. Travelling wave-like perturbations or wall oscillations have generally taken a sinusoidal form and have been tested for a large set of values of important parameters like wave amplitude, wave length, wave speed, in part because it has not been obvious which wave form might be most effective at reducing skin-friction drag. In the control strategies that we are developing, the idea is to drive the flow toward a low-drag state that is known *a priori*. We manipulate the near-wall flow structures by wall deformations, but instead of using monochromatic planar waves as the shape of the wall, we use information coming directly from the desired low-drag state. Using low-drag ECS solutions that have a particular structure and wave speed and imprinting their patterns on a flow field, it will be interesting to see how the flow responds to such an imposition. In particular, whether the turbulent flow field will move close to the imprinted pattern or not. To begin with, an obvious choice for the desired low-drag state could be a lower branch travelling wave solution. We describe the implementation of the abovementioned ideas in Chapter 13.

Chapter 13

Results and discussion for Part III

In the present study, we use DNS to study the effect of a wave-like wall deformation on the near-wall dynamics and the drag. The shape of the wave in question is derived from a known solution to the Navier–Stokes equations. In particular, we use ideas from dynamical systems theory to develop and test new control strategies. Prior open loop control strategies that implement wall-deformation have used monochromatic planar waves, mostly a sine wave-form, as the shape of the moving wall. Part of the reason is that it was not obvious what non-planar wave-form might be effective at drag-reduction. However, with the knowledge of the existence of naturally appearing low-drag transients in turbulent flows, specifically the lower-branch exact coherent states, more avenues to choosing the wall shape or the rate at which deformations happen are now open. These lower branch ECS are of course travelling waves, but with quite particular structures and wave speeds. Here, we answer the question we raised in Chapter 12 that whether somehow imprinting the features of a particular ECS on a flow field can drive the flow toward that state.

We test this hypothesis by imposing the travelling wave perturbations on wall deformation that mimics the wall shear stress patterns a particular ECS. We choose the "P4" family of lower branch ECS discovered recently by Park and Graham [2015] in the minimal channel. At $\mathrm{Re} = 1800$, the wall shear stress patterns of the P4 lower branch ECS look as shown in Figure 13.1. Note that both the DNS and the P4 lower branch ECS have the same mass flux (same laminar centreline $\mathrm{Re} = 1800$). Since this ECS has a lower drag, its friction Reynolds number (Re_τ) is expected to be smaller than

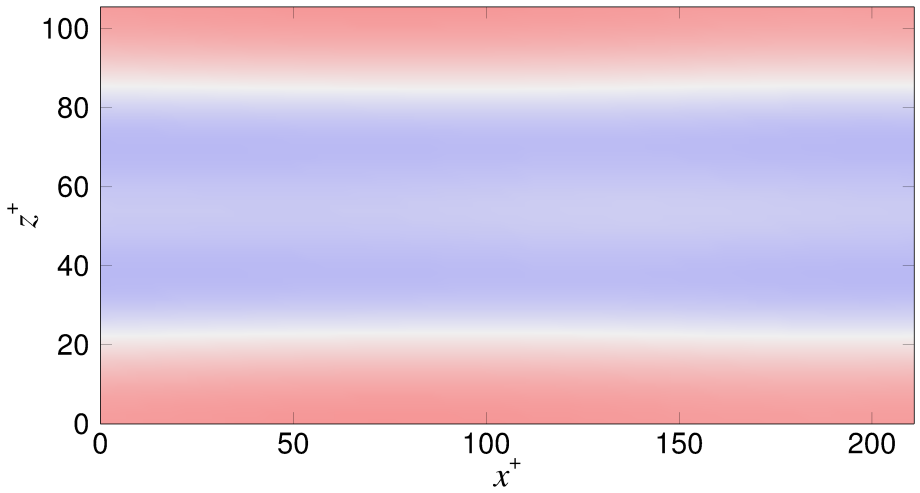

Figure 13.1: Spatial patterns of wall shear stress fluctuations, $g\,(x, z)$, of P4 lower branch travelling wave solution at $\mathrm{Re} = 1800$ ($\mathrm{Re}_\tau = 67.13$) in a minimal channel of size $L_x \times L_y \times L_z = \pi \times 2 \times \pi/2$. The shape of the moving wall in the wall-deformation cases mimics this pattern.

that of the DNS at the same laminar centreline Reynolds number — Re_τ for the ECS is in fact 67.13. In Figure 13.1, the streamwise and spanwise periods are shown in wall units.

As for wall motions, the wall elements are assumed to move up and down in the wall-normal direction only. This can occur in the form of a wave travelling either in the streamwise or in the spanwise direction. The shape of the wall, as illustrated in Figure 13.1, is maintained at all times, only the phase keeps changing with time either in the streamwise or in the spanwise direction, depending on what direction the wave is travelling. The wall-normal displacement of the bottom wall (denoted as 'b') from its mean location is given by:

$$\eta_\mathrm{b} = \alpha g\,(x - c_x t, z - c_z t) \tag{13.1}$$

Here, $g\,(x, z)$ is the wall shear stress fluctuations patterns at time $t = 0$ as shown in Figure 13.1, c_x and c_z are wave speeds in the streamwise and spanwise directions, respectively, and α is the scaling parameter. All the three parameters, α, c_x and c_z, are kept constant for a given simulation. We also keep $\alpha > 0$, $c_x \geq 0$, and $c_z \geq 0$, although negative values will not change the mean statistics — only the instantaneous shape/speed of the moving wall will differ by a phase angle of π. The wave travels in one direction only, i.e., only one of the following two cases holds true: (1) $c_x \neq 0$,

$c_z = 0$ or (2) $c_x = 0$, $c_z \neq 0$. Both of these cases and their results are discussed separately in the following chapters. We consider that both the walls are undergoing motions with the same scaling factor and with the same speed in the same direction and assume that they are in the varicose mode, i.e., moving in the same phase. The wall-normal displacement of the top wall (denoted as 't') from its mean location is then given as:

$$\eta_{\mathrm{t}} = -\eta_{\mathrm{b}} = -\alpha g\left(x - c_x t, z - c_z t\right) \tag{13.2}$$

Thus, if the mean location of the bottom and top walls are represented by $\langle y_w \rangle_{\mathrm{b}}$ and $\langle y_w \rangle_{\mathrm{t}}$, respectively, then any point on these walls will be given by $\langle y_w \rangle_{\mathrm{b}} + \eta_{\mathrm{b}}$ and $\langle y_w \rangle_{\mathrm{t}} + \eta_{\mathrm{t}}$, respectively. The amplitude of wall deformation, i.e., the distance between the highest crest and the lowest trough over the entire area of the wall is given by

$$\eta = \alpha\left\{\max\left(g\right) - \min\left(g\right)\right\} \tag{13.3}$$

where $\max\left(g\right)$ and $\min\left(g\right)$ are the maximum and minimum values of g, respectively. The wall-normal boundary conditions at the bottom and top walls are given as:

$$v_{\mathrm{b}} = \frac{\partial \eta_{\mathrm{b}}}{\partial t} \tag{13.4}$$

$$v_{\mathrm{t}} = \frac{\partial \eta_{\mathrm{t}}}{\partial t} \tag{13.5}$$

At both the walls, no-slip conditions are enforced in the streamwise and spanwise directions, and the no-penetration conditions are enforced by making sure that Equations (13.4) and (13.5) are satisfied. Implementation of the boundary conditions is described in Chapter 9.

The details of the DNS code, spatial discretisation, domain set-up and immersed boundary forcing have been discussed extensively in Appendix A.2. This study focusses on flows for which the laminar centreline Reynolds number, Re, is 1800 (corresponding to friction Reynolds number $\mathrm{Re}_\tau \approx 85$). The streamwise and spanwise periods in outer units are $\pi \times \pi/2$ — they are scaled by the half-height of the channel, l. The reader is referred to Appendix A.2.1 for the meaning of dimensionless symbols. These dimensions correspond to a domain size of $L_x^+ \approx 267, L_z^+ \approx 134$ in wall units.

Here, the superscript '+' indicates normalisation with the viscous length scale, $\delta_\nu = \nu/u_\tau$, for the plane channel, i.e., the controlled or the unactuated case. We use $(N_x, N_y, N_z) = (51, 106, 41)$ grid points for the controlled case in the streamwise, wall-normal and spanwise directions, respectively. The numerical grid spacings in streamwise and spanwise directions are $\delta_x^+ \approx 5.45$ and $\delta_z^+ \approx 3.42$, respectively. Nonuniform Chebyshev spacing in the wall-normal direction gives $\delta_{y,min}^+ \approx 0.04$ at the wall and $\delta_{y,max}^+ \approx 2.57$ at the centre of the channel. A convergence check was also done — spatial resolution was increased and the flow quantities were recalculated, yielding negligible changes from the results reported here (see Appendix A.4.3). Due to the introduction of regions of virtual solid, we increase the number of grid points in the wall-normal direction, N_y, to 136 for all the wall deformation cases. For the values of η, c_x and c_z tested, the streamwise and spanwise spacings are fine enough to resolve the boundary conditions varying in the spanwise or the streamwise direction for the wall deformation cases. A constant time step, $\delta t = 0.01$ (or $\delta t^+ = 0.04$ in wall units based on the controlled channel flow), which satisfies the CFL stability condition, is used in all simulations. The spatial and temporal resolutions for both unactuated and actuated cases are at the same level as those reported in previous studies [Alfonsi, 2011; Tomiyama and Fukagata, 2013]. It should, however, be noted that for large deformations or wave speeds, the spatial and temporal resolutions must be made finer. The computations are performed under a constant flow rate. Thus, the reduction in skin-friction drag is reflected by the reduction in the mean pressure gradient, $-\mathrm{d}P/\mathrm{d}x$. Each simulation run is sufficiently long to ensure meaningful statistical averages; averages are taken only after statistically stationary state is attained. We now discuss various forms of the P4-like travelling wave wall motions.

13.1 P4-LB-like wall moving in the streamwise direction

Figure 13.2 shows an instantaneous snapshot of the deformable bottom wall mimicking the wall shear stress fluctuations patterns of the P4 lower branch ECS shown in Figure 13.1. Since the P4 family of ECS moves in the streamwise direction, and since one of the solutions from that family is being imprinted on the flow, an obvious choice for wall deformation waves would be have them move in the same direction. Therefore, in this case we consider that a streamwise wave is generated due

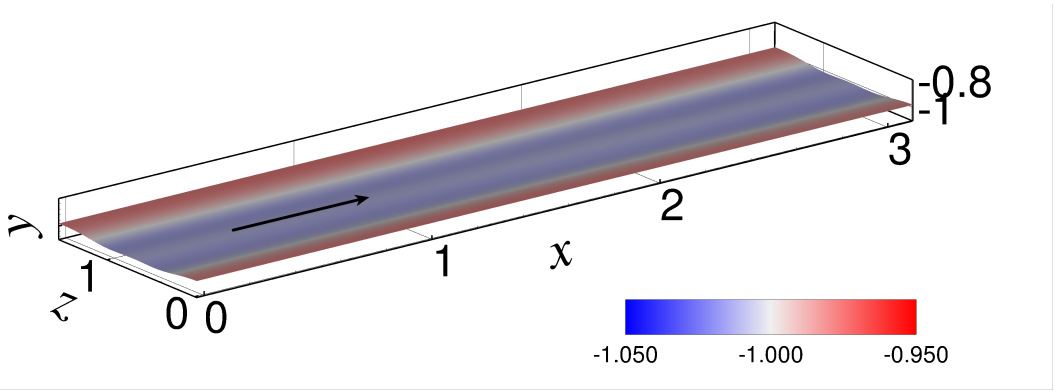

Figure 13.2: Schematic of the streamwise travelling wave-like wall deformation showing the the bottom wall. The wave travels in the streamwise direction with a wave speed c_x. Colour map at the bottom represents the location of the wall in the form of y coordinates. White denotes the mean location of the wall, red means a crest (above the mean) whereas blue means a trough (below the mean).

to the up and down motion of the wall, and it propagates in the direction of increasing x as shown by an arrow in Figure 13.2. The spanwise wave speed, c_z, is zero. The streamwise wave propagation speed chosen for this study is such that the time period of the wall deformation wave propagation in the streamwise direction, T_x, is comparable to that of the P4 lower branch travelling wave in a plane channel ($T_{x,\text{P4-LB2}}$) at the same Reynolds number. Two cases are considered: (1) $T_x = T_{x,\text{P4-LB2}}$, and (2) $T_x = 5T_{x,\text{P4-LB2}}$. Park and Graham [2015] have reported that the propagation speed of the P4 lower branch travelling wave ($c_{x,\text{P4-LB2}}$) at Re = 1800 (the one that is imprinted here) in the streamwise direction is 0.74 (nondimensionalised by the laminar centreline velocity, U_c, at the same mass flux). Therefore, its time period would be $T_{x,\text{P4-LB2}} = L_{x,\text{P4-LB2}}/c_{x,\text{P4-LB2}} = \pi/c_{x,\text{P4-LB2}}$. For the deformable wall travelling wave to have a streamwise time period n times that of the P4 lower branch travelling wave, i.e., for T_x to be equal to $nT_{x,\text{P4-LB2}}$, the wave speed must be $c_x = L_x/\left(n\pi/c_{x,\text{P4-LB2}}\right) = (\pi)/\left(n\pi/c_{x,\text{P4-LB2}}\right) = c_{x,\text{P4-LB2}}/n = 0.74/n$. Thus, for case (1), $T_x^+ = 18.22$, and for case (2), $T_x^+ = 91.08$, scaled with the inner time scale for the plane, unactuated channel. Results for both the frequencies examined are presented below.

In Figure 13.3, we show the mean velocity, Reynolds shear stress and RMS fluctuations for the three velocity components for the plane channel (black solid lines) and the actuated channel (red hollow symbols) for case (1) when $T_x = T_{x,\text{P4-LB2}}$. At this Reynolds number, the velocity profile for the plane channel lies slightly above the Prandtl-von Kármán log law [Patel and Head, 1969; Kasagi

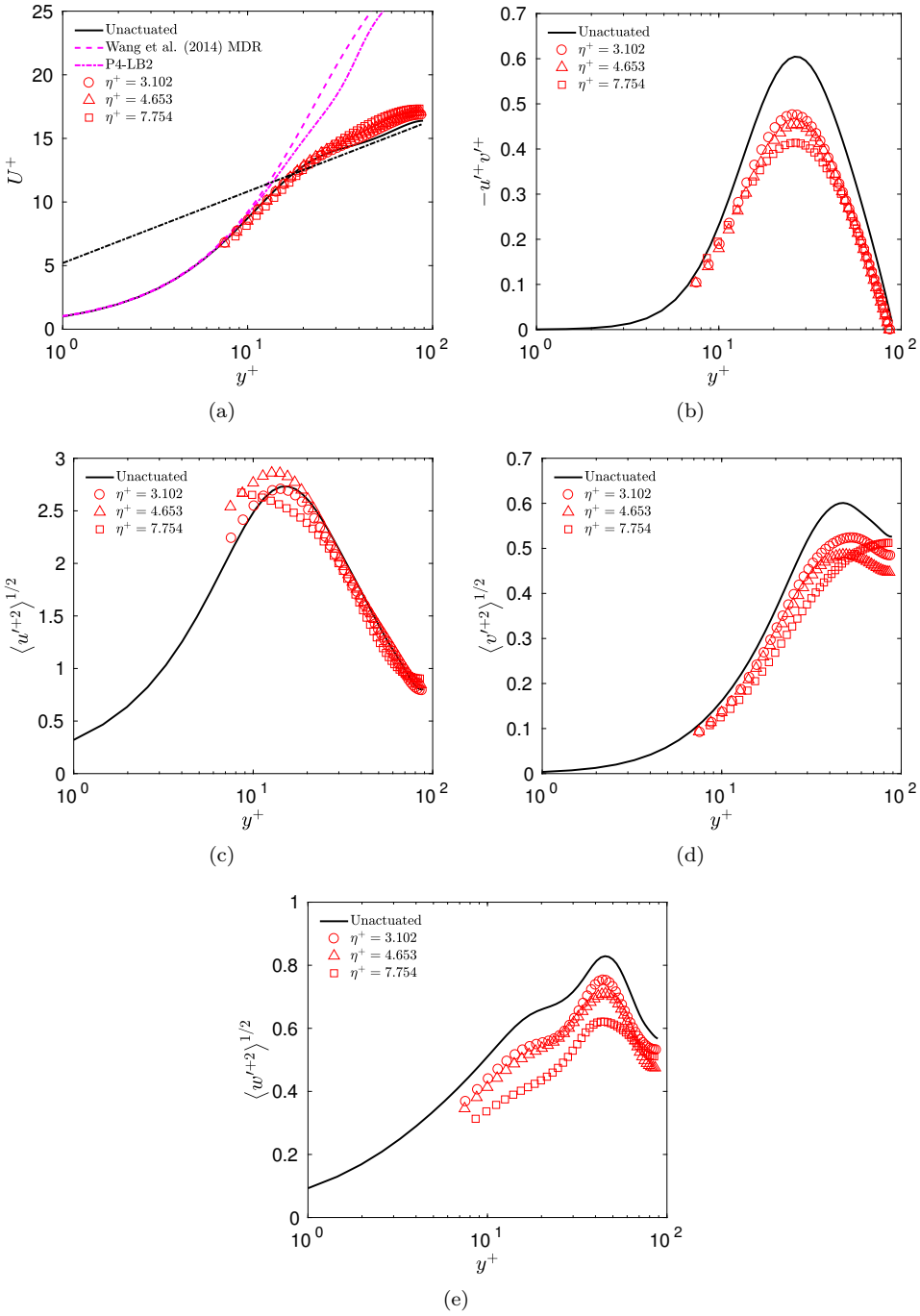

Figure 13.3: (a) Mean velocity profile, (b) Reynolds shear stress, and (c) streamwise, (d) wall-normal and (e) spanwise RMS velocity fluctuations when the P4-LB2 shaped wall moves in the streamwise direction with a time period of $T_x^+ = 18.22$. Corresponding profiles for the unactuated case are shown in black.

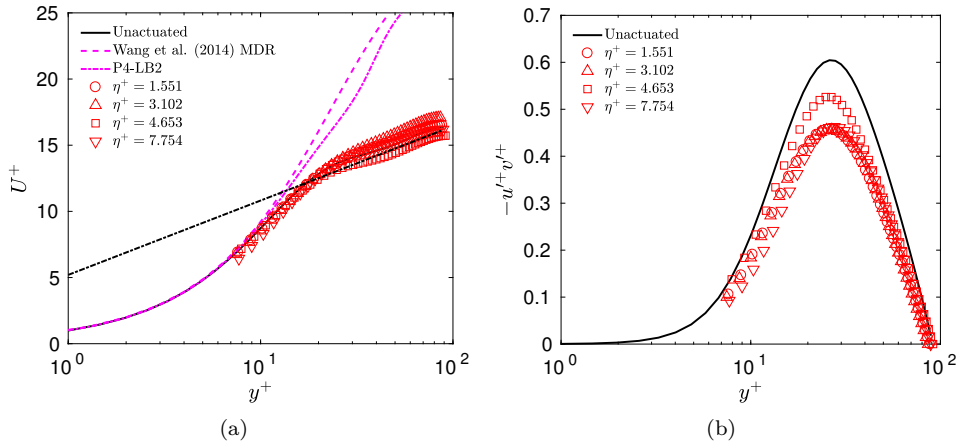

Figure 13.4: (a) Mean velocity profile, and (b) Reynolds shear stress when the P4-LB2 shaped wall moves in the streamwise direction with a time period of $T_x^+ = 91.08$. Corresponding profiles for the unactuated case are shown in black.

and Shikazono, 1995; Tsukahara et al., 2005]. For reference, also shown in Figure 13.3(a) are the viscoelastic maximum drag reduction (MDR) velocity profile from the numerical work of Wang et al. [2014], and the P4 lower branch ECS velocity profile due to Park and Graham [2015]. Statistics for the actuated channel have been obtained by averaging data at each distance from the mean height of the deformable wall. Since the motion of both the bottom and the top walls is congruent, data for both the halves of the channel are considered for better statistics. Note that here, and in all the future chapters, each first and second order statistics is scaled with the corresponding mean wall shear stress, from unactuated or actuated wall as the case may be. Local zones near the deforming walls are excluded from averaging and hence not shown. We observe that the velocity profiles are elevated, they have a slightly higher slope compared to the Prandtl von Kármán log law slope, and the Reynolds shear stresses are reduced. This is indicative of reduction is the skin-friction drag; specifically, the reduction is more for a higher deformation amplitude for the range of amplitudes studied. Overall, wall-normal (Figure 13.3(d)) and spanwise (Figure 13.3(e)) velocity fluctuations follow the same trend. However, the streamwise velocity fluctuations (Figure 13.3(c)) seem to increase in the buffer layer as the deformation amplitude is increased. Moreover, the RMS fluctuations for the wall-normal velocity are very small near the wall due to the small deformation velocity of the wall. For case (2), when $T_x = 5T_{x,\text{P4-LB2}}$, a negligible change in results is observed

(Figure 13.4).

Since we are imprinting a P4 lower branch travelling wave structure (shown in Figure 13.1) on a turbulent flow field, it will be interesting to see how close the flow quantities approach that of the imprinted structure. To visualise the approach of turbulent trajectories to the P4 lower branch ECS in the state space, we project the trajectories onto a three-dimensional space with the following quantities as references: disturbance kinetic energy (KE), energy dissipation rate (D), and area-averaged instantaneous wall shear stress scaled with the mean wall shear stress in the plane channel ($\tau_w/\bar{\tau}_w$). Each of these quantities is calculated only in half of the channel. Without any loss of generality, we choose the lower half for this purpose. The disturbance kinetic energy, KE, for the lower half of the channel is given by the following expression:

$$\mathrm{KE} = \frac{1}{\Gamma}\int_{\Gamma}\int_{\langle y_w\rangle_\mathrm{b}+\eta_\mathrm{b}}^{0} \frac{1}{2}\left(\boldsymbol{u}-\boldsymbol{u}_\mathrm{lam}\right)^2 \mathrm{d}y\mathrm{d}\gamma \tag{13.6}$$

where $\boldsymbol{u}_\mathrm{lam}$ is the laminar flow field, $\mathrm{d}\gamma$ is an area element on the wall whose total area is Γ, and $\langle y_w\rangle_\mathrm{b}+\eta_\mathrm{b}$ denotes a point on the bottom wall. For the plane channel, $\mathrm{d}\gamma = \mathrm{d}x\mathrm{d}z$, $\Gamma = L_xL_z$, and $\langle y_w\rangle_\mathrm{b}+\eta_\mathrm{b}$ is simply -1. The energy dissipation rate for the lower half of the channel is given by the following expression:

$$D = \frac{1}{\mathrm{Re}\Gamma}\int_{\Gamma}\int_{\langle y_w\rangle_\mathrm{b}+\eta_\mathrm{b}}^{0} \left(|\boldsymbol{\nabla}u|^2+|\boldsymbol{\nabla}v|^2+|\boldsymbol{\nabla}w|^2\right)\mathrm{d}y\mathrm{d}\gamma \tag{13.7}$$

The above quantity is multiplied by 3Re/4 before plotting, so that the scaled energy dissipation rate is 1 for the Newtonian laminar flow.

Figure 13.5 shows dynamical trajectories of channel flow turbulence at $\mathrm{Re}_\tau = 85$ (unactuated) in the minimal channel for both unactuated (black lines) and actuated wall (red lines) cases. The deformation amplitude and the time period of the streamwise wave for the actuated wall cases are $\eta^+ = 7.754$ and $T^+ = 18.22$. The P4 lower branch travelling wave and the laminar flow are also projected for reference. It is known that the dynamical trajectories spend most of their time in the region of the state space that is populated with high-drag-exhibiting upper branch solutions, and occasionally pass through the vicinity of low-drag-exhibiting lower branch solutions [Park and Graham, 2015]. Trajectories for the plane channel, shown in black colour, display this behaviour.

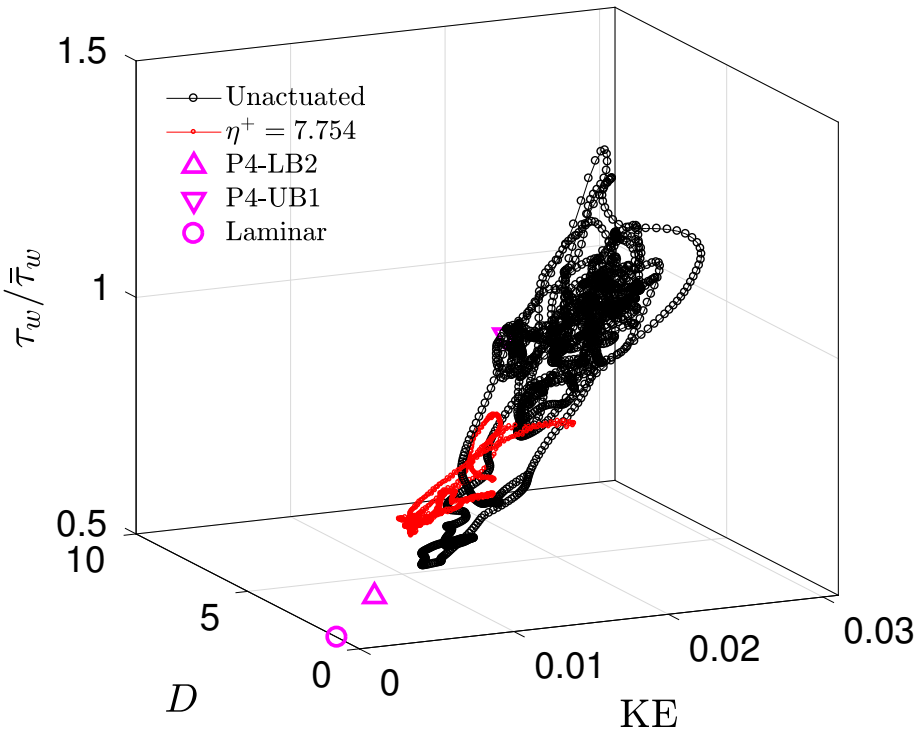

Figure 13.5: State space visualisation of DNS trajectories for plane channel (black) and for a channel with P4-LB-like wall motion in the streamwise direction (red) with $\eta^+ = 7.754$ and $T_x^+ = 18.22$ in a minimal channel turbulent flow at $\mathrm{Re}_\tau = 85$, projected onto three dimensions: disturbance kinetic energy (KE), energy dissipation rate (D), and normalised instantaneous wall shear stress ($\tau_w/\bar{\tau}_w$). Circles are attached to the lines at intervals of 1 l/U_c. P4-LB2, P4-UB1 and laminar solutions are also included for reference. All quantities are calculated only for the bottom half of the channel.

For the actuated wall case, the trajectories start from the same high-drag core and then move closer to the low-drag region where they spend more time compared to the unactuated case. These trajectories are shown in red colour. For both the unactuated and actuated cases, initial transients have been removed and only the statistically stationary trajectories are shown. Clearly, in a state of statistical steadiness, the trajectories for the wall-actuation case stay in the low-drag region of the state space.

Joint probability density functions (PDFs) of KE and D, $\tau_w/\bar{\tau}_w$ and D, and $\tau_w/\bar{\tau}_w$ and KE for both the actuated and the unactuated cases are shown in Figure 13.6. The first thing to notice is that there is a positive correlation between any two quantities: for a plane channel, higher D is more likely to be observed with higher KE and a higher τ_w. High values of these quantities are indicative of higher drag, and vice versa. The PDF for the plane channel (left column) is spread over a larger

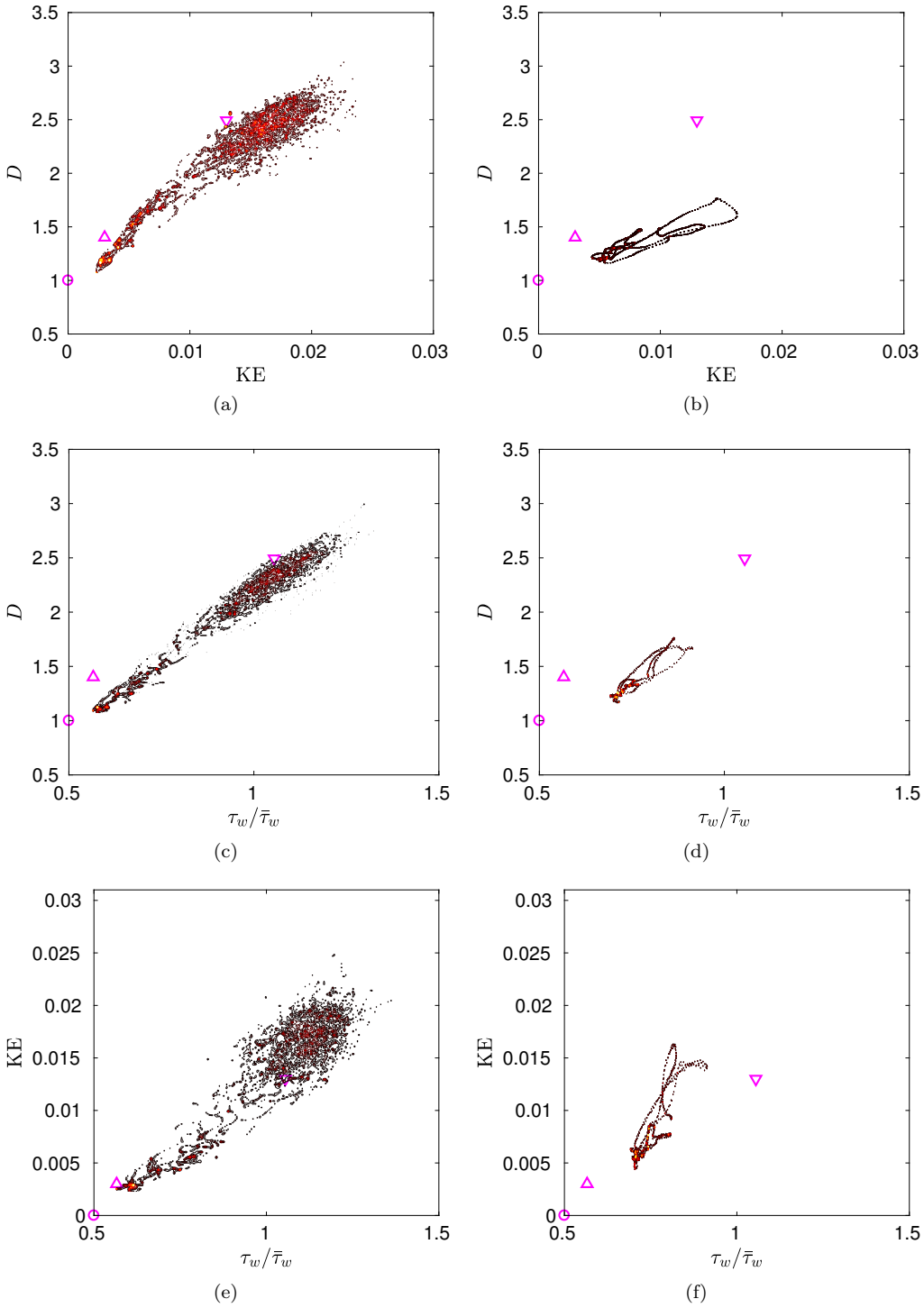

Figure 13.6: Joint probability densities of [(a), (b)] KE and D, [(c), (d)] $\tau_w/\bar{\tau}_w$ and D, and [(e), (f)] $\tau_w/\bar{\tau}_w$ and KE for both the plane channel (left column) and for a channel with P4-LB-like wall motion in the streamwise direction with $\eta^+ = 7.754$ and $T_x^+ = 18.22$ (right column). Hollow symbols have same meaning as before.

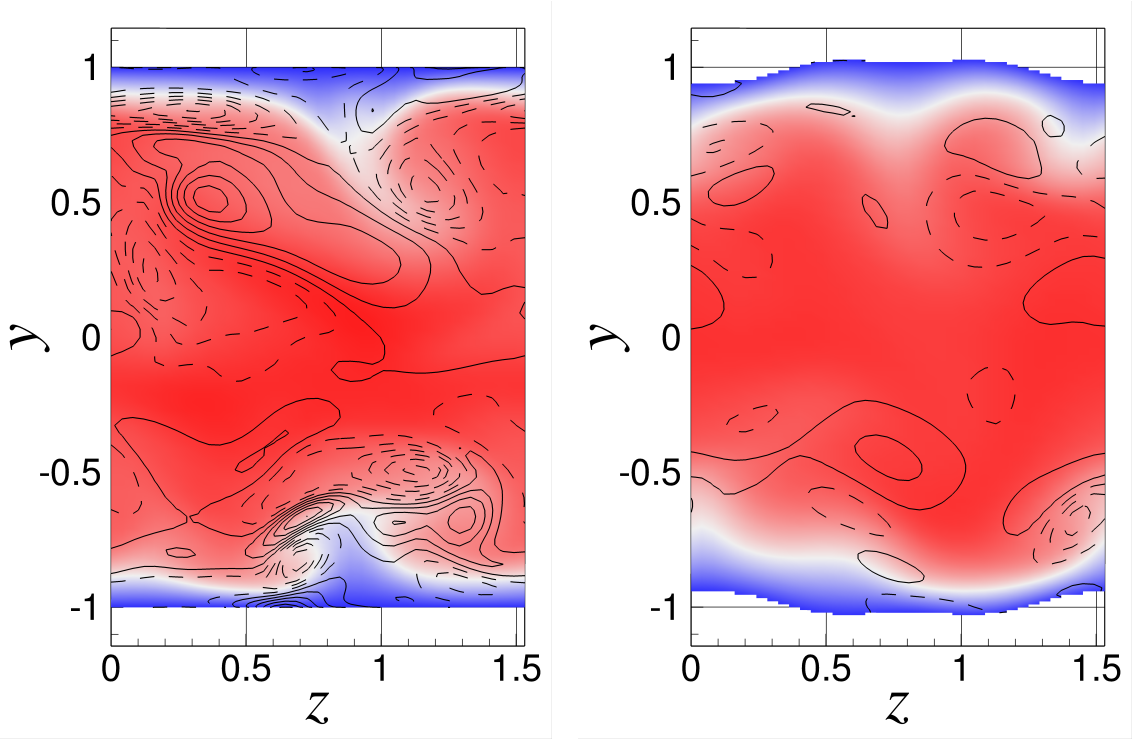

Figure 13.7: Instantaneous snapshots of the full cross-flow plane showing streamwise velocity as colour contours and streamwise vorticity as line contours (positive vorticity as solid lines and negative vorticity as dashed lines) for (a) unactuated case, and (b) actuated case with $\eta^+ = 7.754$ and $T_x^+ = 18.22$. In (b), the wave moves in the direction of increasing x. Note that in (b), both the walls are smooth but they look like sharp steps due to the blanking limitations of `Tecplot 360 EX 2017 R1`.

area, indicating the movement of trajectories between high- and low-drag states in the space space. In contrast, the PDF for the actuated wall case (right column) is not only spread over a smaller area but also lies in the region of low KE, low D and low $\tau_w/\bar{\tau}_w$ indicating low-drag throughout the actuation process after a statistically stationary state has been attained. The positive correlation between the quantities is maintained.

We now look at some instantaneous flow structures. Illustrated in Figure 13.7 are instantaneous snapshots of the cross-flow plane showing the streamwise velocity, U, as colour contours and the streamwise vorticity, ω_x, as line contours. In the unactuated plane channel (Figure 13.7(a)), dense lines of both positive (solid) and negative (dashed) ω_x can be seen indicating strong streamwise vorticity, which is associated with the high skin-friction drag. On the other hand, for the actuated

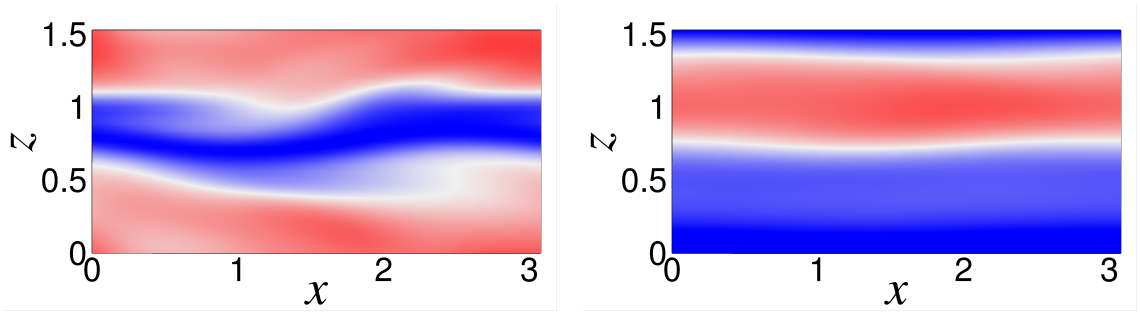

(a) (b)

Figure 13.8: Instantaneous snapshots of streamwise velocity fluctuations, u', at $y^+ \approx 15$ for (a) unactuated case, and (b) actuated case with $\eta^+ = 7.754$ and $T_x^+ = 18.22$. In (b), the wave moves in the direction of increasing x.

channel case (Figure 13.7(b)) in which the wave at both the walls propagates in the increasing x direction (into the plane of paper), the streamwise vorticity is significantly reduced, and on average, they have moved away from the wall. We can also see that the cross-section of streamwise streaks that are more fluctuating and show great degree of disorder in the plane channel have become calm and orderly with actuation and have more or less taken the shape of the wall.

Figure 13.8 shows instantaneous streamwise velocity fluctuations, u', at $y^+ \approx 15$ from the bottom wall corresponding to the snapshots shown in Figure 13.7. In Figure 13.8(a), the unactuated case, the streaks are meandering which is typical of a turbulent channel flow, implying strong three-dimensionality in the flow. In the actuated wall case (Figure 13.8(b)), the three-dimensionality in the flow is significantly reduced and the low-speed streaks appear to be aligned above the crest in the streamwise direction. Thus, in a way, the P4 lower branch ECS has been imprinted on the flow. The alignment of streaks, for a different wave form though, for wall deformation has also been observed by Klumpp et al. [2011] and Tomiyama and Fukagata [2013]. Orderly streaks aligned in the streamwise direction with less fluctuating motions is indicative of weak turbulence and hence drag reduction.

13.2 P4-LB-like wall moving in the spanwise direction

Figure 13.9 shows an instantaneous snapshot of the deformable bottom wall whose shape mimics the wall shear stress fluctuations patterns of a lower branch ECS illustrated in Figure 13.1. In the current set-up, the effect of a spanwise travelling wave that arises due to the up and down motion of the wall on the near-wall dynamics is investigated. The idea of the spanwise motion is, in part, derived from the work of Tomiyama and Fukagata [2013] who used a spanwise-dependent sinusoidal wave form travelling in the spanwise direction. For our case, the wave propagates in the positive z direction only which is shown by a black arrow in Figure 13.9. The streamwise propagation speed, c_x, for this case is zero. The spanwise wave speed, c_z, is not chosen arbitrarily — it is such that the time period of the wave motion of the deformable wall in the spanwise direction (T_z) is comparable to that of the P4 lower branch travelling wave in a plane channel ($T_{x,\text{P4-LB2}}$) at the same Reynolds number. We consider two cases: (1) $T_z = T_{x,\text{P4-LB2}}$, and (2) $T_z = 5T_{x,\text{P4-LB2}}$. The reasoning behind case (1) is straightforward: here the deformable wall wave is made to propagate with the same frequency as that of P4 lower branch ECS. For the deformable wall travelling wave to have a spanwise time period (T_z) same as that of the P4 ECS ($T_{x,\text{P4-LB2}}$), the wave speed should be $c_z = L_z / \left(L_{x,\text{P4-LB2}}/c_{x,\text{P4-LB2}}\right) = (\pi/2) \,/\, (\pi/c_{x,\text{P4-LB2}}) = c_{x,\text{P4-LB2}}/2 = 0.37$. In case (2), the wave moves 5 times slower and the frequency now is comparable to those of other wall-actuation methods, e.g., drag reduction by transverse wall oscillations [Ricco and Quadrio, 2008] or spanwise travelling wave-like wall deformation using a monochromatic planar wave [Tomiyama and Fukagata, 2013]. Results for both the frequencies examined are presented below.

Figure 13.10 shows the first and second order statistics for case (1) when the P4-LB travelling wave-like wall deformation propagates in the spanwise direction such that $T_z = T_{x,\text{P4-LB2}}$. For this case, $T_z^+ = 18.22$. Figure 13.10(a) shows the streamwise time averaged velocity profile for the unactuated channel at $\text{Re}_\tau = 85$ with a black solid line. We also present in red hollow symbols the velocity profiles during wall actuation for different values of deformation amplitude η^+ (or η in outer units; see Equation (13.3)). Velocity profiles for viscoelastic MDR and P4 lower branch ECS are also shown in Figure 13.10(a). It is observed that as the amplitude of deformation increases, the velocity profile gets elevated and displays a higher log law slope just outside the buffer layer compared to the

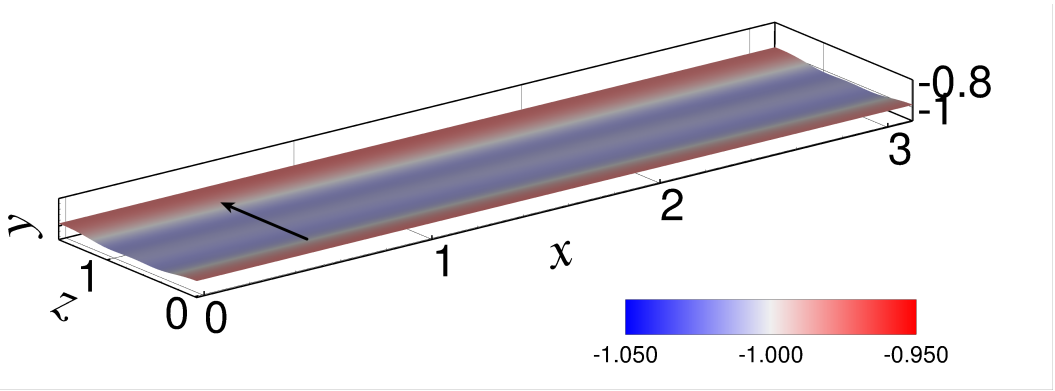

Figure 13.9: Schematic of the spanwise travelling wave-like wall deformation showing the the bottom wall. The wave travels in the spanwise direction with a wave speed c_z. Colour map at the bottom represents the location of the wall in the form of y coordinates. White denotes the mean location of the wall, red means a crest (above the mean) whereas blue means a trough (below the mean).

Prandtl-von Kármán log law. This elevation of the velocity profile above the Prandtl-von Kármán log law indicates deceleration of fluid near the deforming wall resulting in a lower drag.

Figure 13.10(b) shows the variation of mean Reynolds shear stress (stress arising due to fluctuating velocity field) as a function of distance from the wall. It can be clearly seen that compared to the unactuated case, the Reynolds shear stress has reduced with wall actuation and the reduction is more for a higher amplitude. The position of the peak in Reynolds stress remains unaltered though. Figures 13.10(c)–13.10(e) show the distribution of root-mean-squared (RMS) velocity fluctuations for all the three velocity components on the deformed wall. Almost negligible difference is observed in the streamwise velocity fluctuations — the peak and its position compared to the unactuated channel remain unchanged, although a very minor reduction can be seen in the region $y^+ \approx 20 - 40$. Wall-normal and spanwise velocity fluctuations, on the other hand, are considerably reduced for deforming walls. The trend in reduction is consistent with that observed in the mean velocity and the Reynolds shear stress — greater the deformation amplitude, greater the reduction in RMS fluctuations. In the near-wall region though ($y^+ \lesssim 10$), the wall-normal velocity fluctuations are higher than the unactuated case. This is in accordance with the boundary conditions on the wall-normal velocity component due to the wall motion as described by Equations (13.4) and (13.5).

The state space picture for spanwise wall movement is compared with that of a plane channel in Figure 13.11. Both the trajectories are plotted after a state of statistical steadiness has been

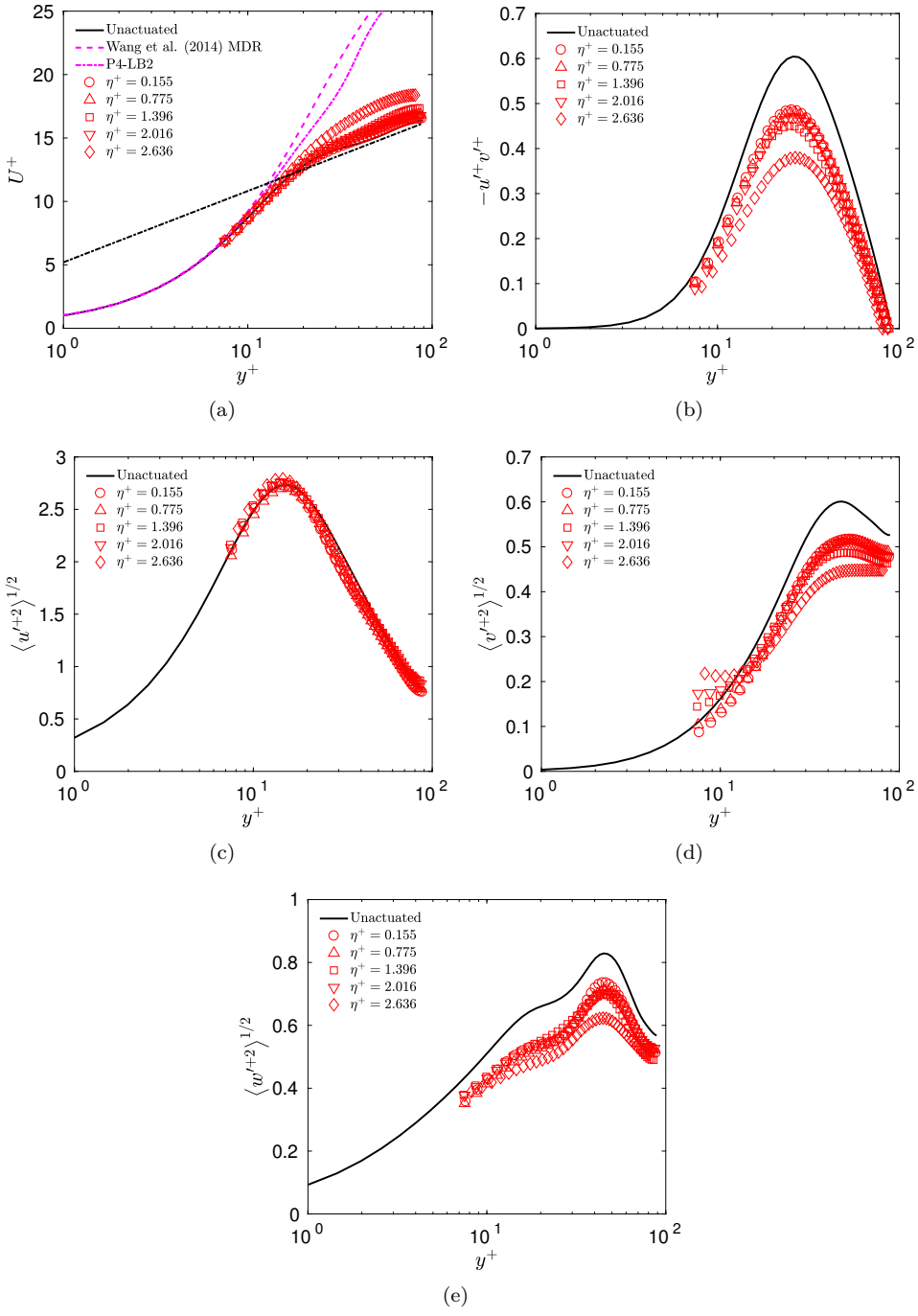

Figure 13.10: (a) Mean velocity profile, (b) Reynolds shear stress, and (c) streamwise, (d) wall-normal and (e) spanwise RMS velocity fluctuations when the P4-LB2 shaped wall moves in the spanwise direction with a time period of $T_z^+ = 18.22$. Corresponding profiles for the unactuated case are shown in black.

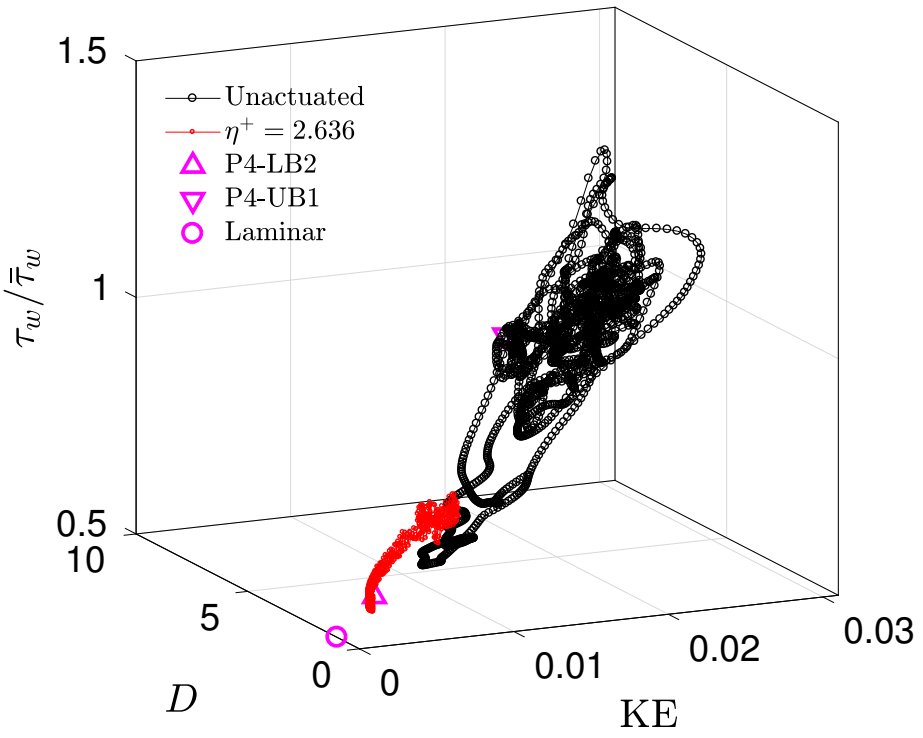

Figure 13.11: State space visualisation of DNS trajectories for plane channel (black) and for a channel with P4-LB-like wall motion in the spanwise direction (red) with $\eta^+ = 2.636$ and $T_z^+ = 18.22$ in a minimal channel turbulent flow at $\mathrm{Re}_\tau = 85$.

attained. The trajectories for the actuated wall case (shown in red colour) stay in the low-drag region of the state space. Interestingly, they also come very close to the P4 lower branch ECS used to determine the shape of the deformable wall. Joint PDFs of disturbance kinetic energy and energy dissipation rate are plotted in Figure 13.12. Observations similar to the streamwise wall movements are made for the spanwise case as well — the PDF for the actuated wall case (right column) is spread over a smaller area and lies in the region of low KE, low D and low $\tau_w/\bar{\tau}_w$.

Instantaneous snapshots of a cross-flow plane and streamwise velocity fluctuations at $y^+ \approx 15$ for both the plane and actuated channels are shown in Figure 13.13 and Figure 13.14, respectively. The actuated channel shows lesser degree of fluctuations in the streamwise velocity structure in the cross-flow plane, streamwise vorticity as well as velocity fluctuations compared to those observed in the plane channel. In Figure 13.13(b), however, some regions of relatively high density of ω_x lines can be observed locally very close to the walls — these are generated due to the spanwise motion of

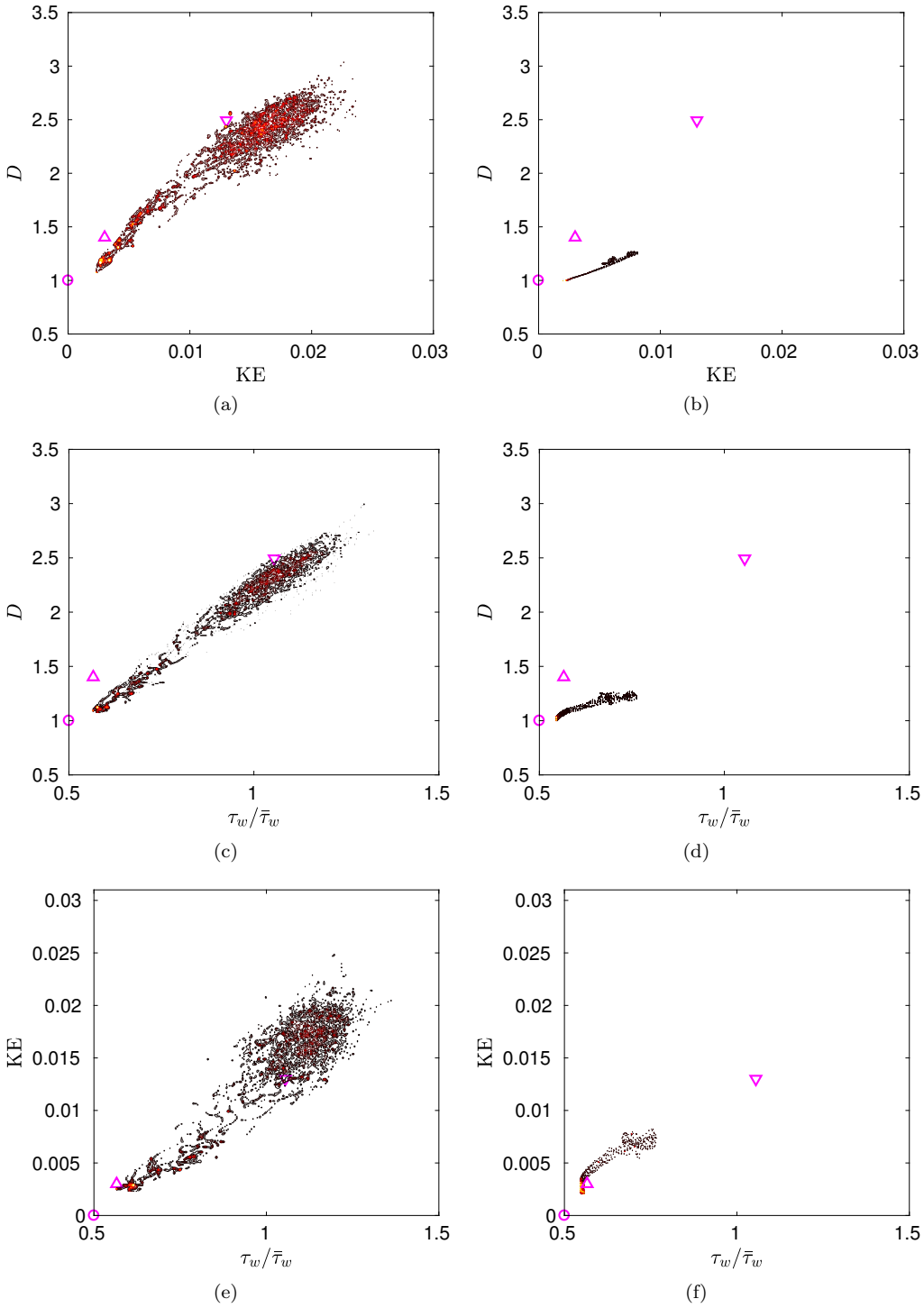

Figure 13.12: Joint probability densities of [(a), (b)] KE and D, [(c), (d)] $\tau_w/\bar{\tau}_w$ and D, and [(e), (f)] $\tau_w/\bar{\tau}_w$ and KE for both the plane channel (left column) and for a channel with P4-LB-like wall motion in the spanwise direction with $\eta^+ = 2.636$ and $T_x^+ = 18.22$ (right column).

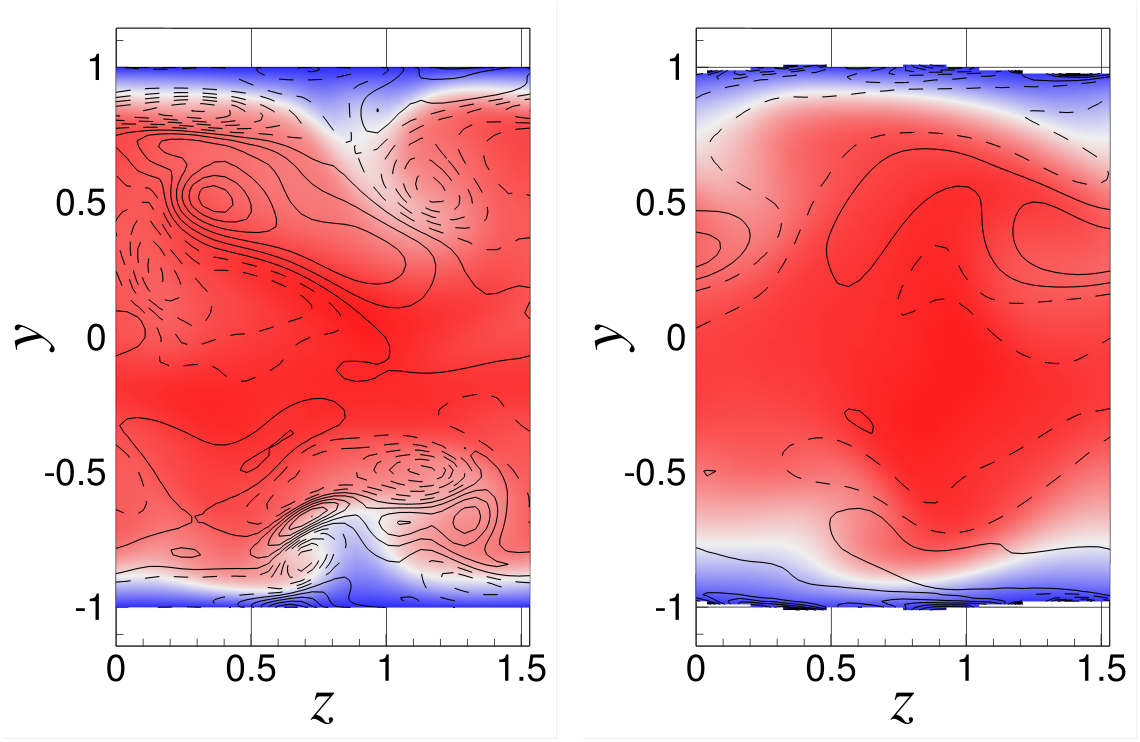

Figure 13.13: Instantaneous snapshots of the full cross-flow plane showing streamwise velocity as colour contours and streamwise vorticity as line contours (positive vorticity as solid lines and negative vorticity as dashed lines) for (a) unactuated case, and (b) actuated case with $\eta^+ = 2.636$ and $T_z^+ = 18.22$. In (b), the wave moves in the direction of increasing z. Note that in (b), both the walls are smooth but they look like sharp steps due to the blanking limitations of `Tecplot 360 EX 2017 R1`.

the wavy wall.

Now we present flow statistics for case (2) when the P4-LB travelling wave-like wall deformation propagates in the spanwise direction such that $T_z = 5T_{x,\text{P4-LB2}}$. For this case, the time period of wall motion is $T_z^+ = 91.08$, which is comparable to those of other wall-actuation methods mentioned before. Figure 13.15 shows the mean velocity and Reynolds shear stress profiles over the deformable wall for this case. The RMS velocity fluctuations are omitted for conciseness. The velocity profiles are slightly elevated and the Reynolds stresses are slightly reduced, with respect to the unactuated case. Qualitatively it appears that there is some level of drag reduction but a quick comparison with case (1) results (Figure 13.10) indicates that the reduction in drag is smaller. A quantitative study on the levels of drag reduction for both the cases is presented in Chapter 13.3.

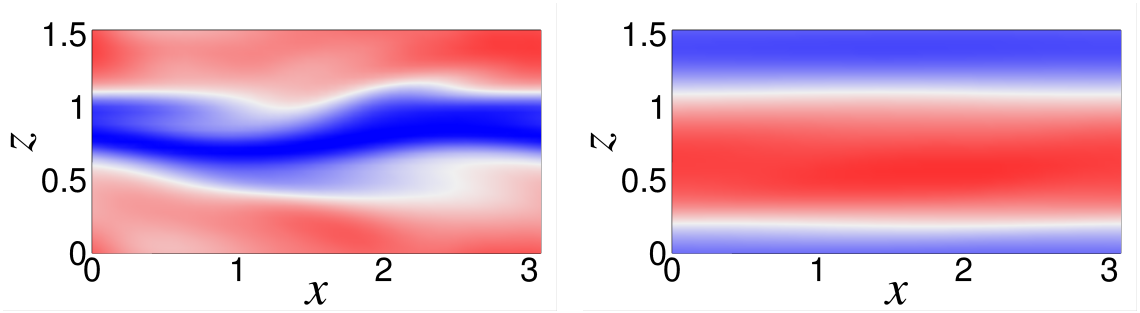

(a) (b)

Figure 13.14: Instantaneous snapshots of streamwise velocity fluctuations, u', at $y^+ \approx 20$ for (a) unactuated case, and (b) actuated case with $\eta^+ = 2.636$ and $T_z^+ = 18.22$. In (b), the wave moves in the direction of increasing z.

13.3 Drag reduction and energy savings

In this chapter, we will quantify the extent of drag reduction achieved by different control strategies described in previous chapters, as well as comment on energy savings and the efficiency of the process. Since the mass flux is maintained constant throughout a given simulation, the resultant percent drag reduction, % DR, or the percent gain in pumping power, can be determined from the reduction in the pressure gradient, $-\mathrm{d}P/\mathrm{d}x$. The power required to pump the fluid, W_p, is given by

$$W_p = \left\{ \frac{1}{T_f - Ti} \int_{T_i}^{T_f} \left\langle -\frac{\mathrm{d}P}{\mathrm{d}x} \right\rangle \mathrm{d}t \right\} U_b \tag{13.8}$$

where T_i and T_f indicate the start and end times of the simulation, excluding the initial transients, $\langle \cdot \rangle$ denotes volume average, and U_b is the constant bulk velocity. Calculations are performed only after a statistical stationary state has been attained. The percent drag reduction can then be calculated as:

$$\%\ \mathrm{DR} = \frac{W_{p0} - W_p}{W_{p0}} \times 100\% \tag{13.9}$$

Here, the "0" in the subscript indicates the unactuated, plane channel case.

Figure 13.16 shows the variation of % DR with the deformation amplitude when the travelling deformable wall propagates in the streamwise (Chapter 13.1) and spanwise (Chapter 13.2) directions at two different frequencies. Drag reduction rates for laminar and P4 lower branch travelling wave

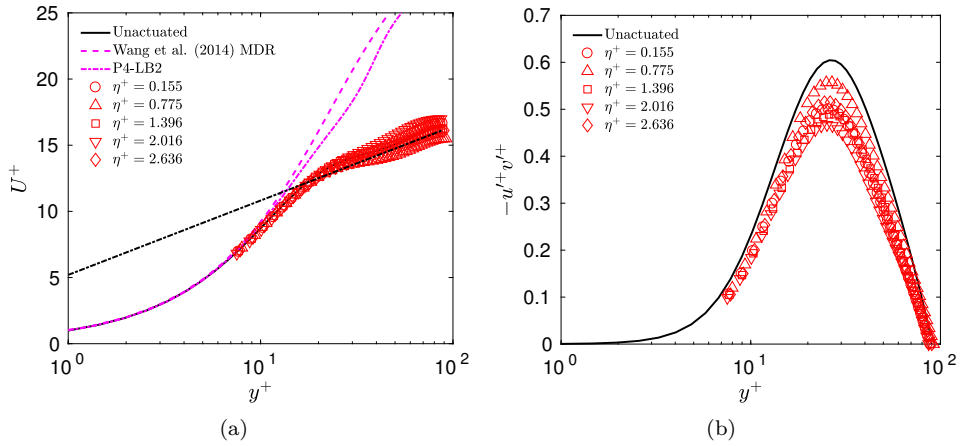

Figure 13.15: (a) Mean velocity profile, and (b) Reynolds shear stress when the P4-LB2 shaped wall moves in the spanwise direction with a time period of $T_z^+ = 91.08$. Corresponding profiles for the unactuated case are shown in black.

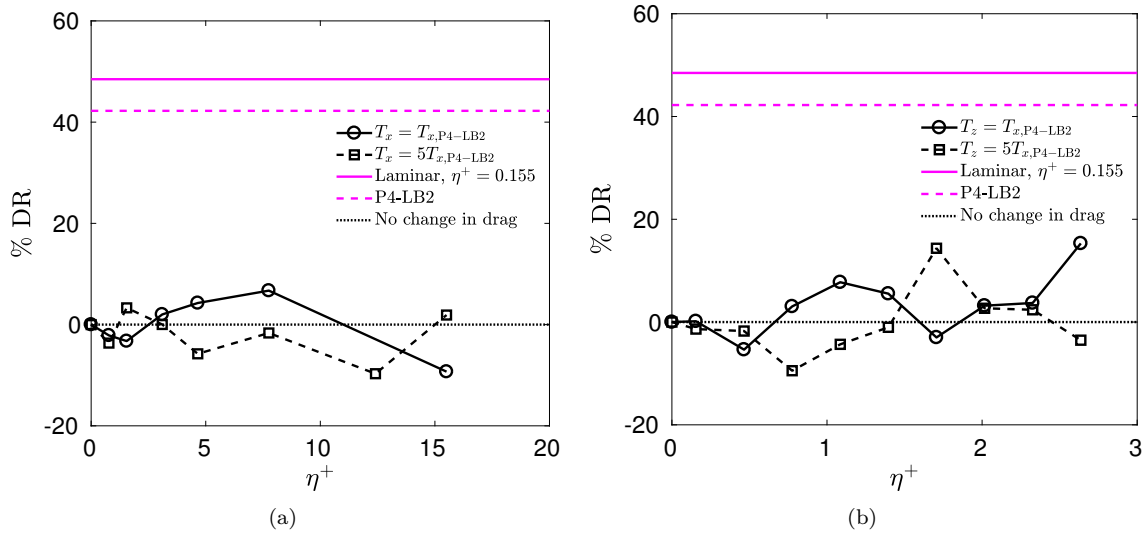

Figure 13.16: Drag reduction rate as a function of deformation amplitude for (a) streamwise and (b) spanwise motion of channel walls the shape of which that mimics the spatial patterns of wall shear stress fluctuations of a P4 lower branch travelling wave. Corresponding values for laminar and P4-LB2 solutions are included for reference.

are also shown for reference. Note that the laminar solution will be different for different deformation amplitudes, hence the solution, among other laminar solutions computed, for which drag reduction rate is minimum is shown here. For extremely small deformations, the drag reduction rate for all the cases approaches zero which is expected for an actuated channel tending to a plane channel. As the

deformation amplitude increases, deviations from the controlled case can be seen. Interestingly, for both the spanwise and streamwise travelling waves of wall deformation, more positive drag reduction cases are observed for case (1), i.e., for the higher frequency case. Case (2), for which the frequency of the wave motion corresponds to the wall oscillation frequency in case of drag reduction by oscillating walls, predominantly results in drag increase. All the drag reduction values due to wall deformation are far off from their laminar or P4-LB2 counterparts.

Even though we do achieve drag reduction in some cases using the strategies described in previous chapters, which result in a gain in pumping power, it comes at the expense of an external energy that is required for actuating the wall. Thus, in order to truly capture the energy savings, we have to take into account the energy we are adding to the system to actuate the walls. At statistically steady state, the total rate of work for pumping the fluid and wall-shape change at constant volume is identical to the dissipation function [Fukagata et al., 2009] given by Equation (13.10) for the full channel.

$$W_{\text{total}} = \frac{1}{2\text{Re}\Gamma\left(T_f - Ti\right)} \int_{T_i}^{T_f} \int_{\Gamma} \int_{\langle y_w \rangle_{\text{b}} + \eta_{\text{b}}}^{\langle y_w \rangle_{\text{t}} + \eta_{\text{t}}} \left(|\boldsymbol{\nabla} u|^2 + |\boldsymbol{\nabla} v|^2 + |\boldsymbol{\nabla} w|^2 \right) \text{d}y\text{d}\gamma\text{d}t \tag{13.10}$$

The net energy savings can be calculated as [Kasagi et al., 2009a]:

$$S = \frac{W_{p0} - W_{\text{total}}}{W_{p0}} \tag{13.11}$$

Therefore, the efficiency of the entire process is given by:

$$\epsilon = \frac{\text{DR}}{\text{DR} - S} \tag{13.12}$$

For any active control strategy to be practically implementable, the net energy savings, S, must be positive, or in other words, the efficiency, ϵ, must be greater than unity. In Figure 13.17, the computed values of ϵ are plotted at different deformation amplitudes for different frequencies. For the sake of completeness, ϵ for cases that resulted in drag increase, or for cases for which $\epsilon < 1$, are also shown. The maximum efficiency observed is ~ 1.7 for the streamwise travelling wave case and ~ 1.5 for the spanwise travelling wave case. These values are very similar to those obtained from other

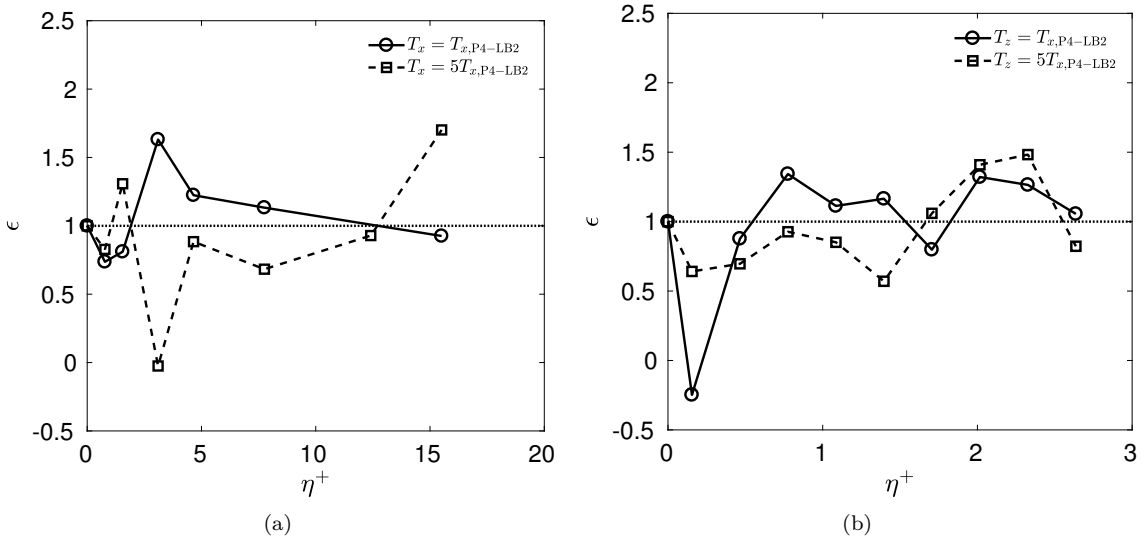

Figure 13.17: Process efficiency as a function of deformation amplitude for (a) streamwise and (b) spanwise motion of channel walls the shape of which that mimics the spatial patterns of wall shear stress fluctuations of a P4 lower branch travelling wave.

control methods, e.g., temporal spanwise wall oscillation [Quadrio and Ricco, 2004] and streamwise-travelling waves of spanwise wall velocity [Quadrio et al., 2009], while they lie on the lower side of the efficiency values obtained from control methods like streamwise oscillation of spanwise wall velocity [Viotti et al., 2009], steady streamwise forcing [Xu et al., 2007] and streamwise travelling wave-like blowing and suction [Min et al., 2006]. This may be attributed to the lower drag reduction rates for our methods — drag reduction of up to 40% can be achieved by spanwise oscillations.

A definitive pattern of the variation of the drag-reduction rate as a function of parameters, e.g., deformation amplitude, wave speed, was not found. Only a single lower branch ECS was imposed on the flow with deformation amplitudes that extended not beyond the viscous sublayer. Even though deformations in this range have been used before both for open loop [Tomiyama and Fukagata, 2013] and closed loop [Kang and Choi, 2000] active control techniques, effects of larger deformations need to be studied with regard to pattern imposition.

13.4 Other forms of wall actuation

13.4.1 P4-UB-like wall moving in the streamwise or spanwise direction

In Chapters 13.1 and 13.2, effects of the imposition of a low-drag state, specifically, a lower branch solution from the P4 family of travelling waves [Park and Graham, 2015], on the near-wall dynamics of a turbulent flow field were discussed. The travelling wave-like wall deformations moved in streamwise and spanwise directions. Quantification of drag-reduction and the efficiency of the process was discussed in Chapter 13.3. We saw that upon the imposition of a low-drag state, the turbulent trajectories approached the vicinity of that state. This provides us motivation to investigate what would happen if instead of a low-drag state, a high-drag state is imposed on the flow. Will the trajectories approach the high-drag state in the state space? Or will they just move chaotically in a general high-drag region? Or will they approach a low-drag region: is the effect of imposing a travelling wave generic? We try to answer some of these questions in the current chapter.

We look at the effects of imprinting a high-drag state on the flow. The most obvious choice for a high-drag state would be an upper branch travelling wave solution. We choose an upper branch travelling wave solution from the same P4 family of solutions at the same laminar centreline Reynolds number, Re = 1800. The upper branch solution is imposed on a turbulent flow in the same manner as was done for lower branch solutions (see Chapters 13.1 and 13.2). Both the streamwise and spanwise motions of wall deformation are considered. The wave speed the chosen upper branch solution in the streamwise direction, $c_{x,\text{P4-UB1}}$, is 0.73 (nondimensionalised by the laminar centreline velocity, U_c, at the same mass flux) [Park and Graham, 2015]. The time period of the travelling wave of wall deformation in the streamwise direction, T_x, and the spanwise direction, T_z, is set to be same as the time period of the P4 upper branch solution, $T_{x,\text{P4-UB1}}$, imprinted on the flow. Thus, for the streamwise propagating wave of wall deformation, $T_x = T_{x,\text{P4-UB1}}$, and for the spanwise propagating wave of wall deformation, $T_z = T_{x,\text{P4-UB1}}$. The results for both the cases are discussed below.

In Figure 13.18, mean velocity profiles above the actuated wall for both the streamwise and spanwise travelling waves are shown in red. Velocity profiles for the plane, unactuated channel are also shown (in black). It is observed that for the actuated wall cases, the velocity profiles lie very close to the velocity profile for the plane channel. Interestingly, these profiles also lie very close to the

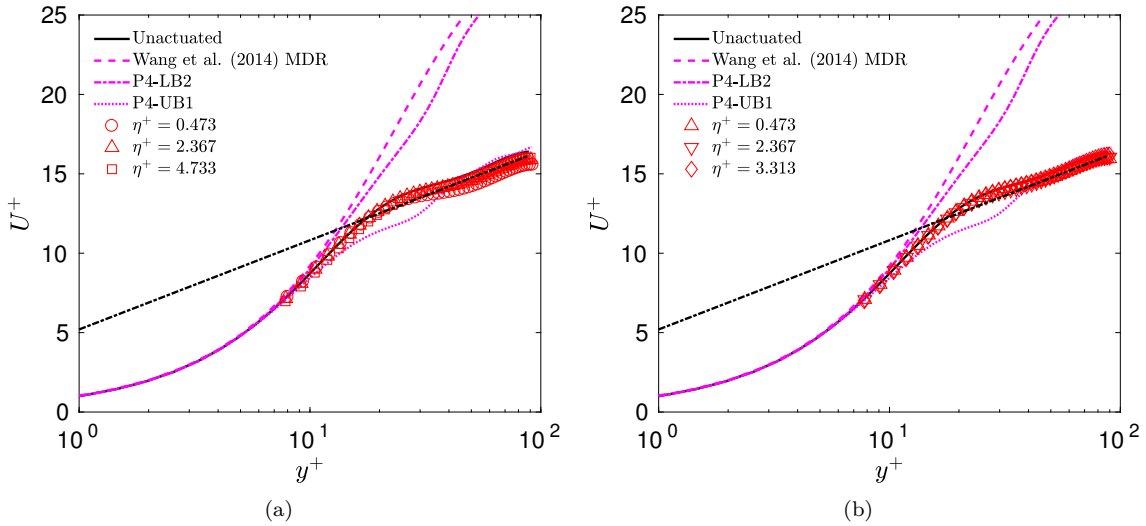

Figure 13.18: Drag reduction rate as a function of deformation amplitude for (a) streamwise and (b) spanwise motion of channel walls the shape of which that mimics the spatial patterns of wall shear stress fluctuations of a P4 upper branch travelling wave. Corresponding values for laminar and P4-UB1 solutions are included for reference.

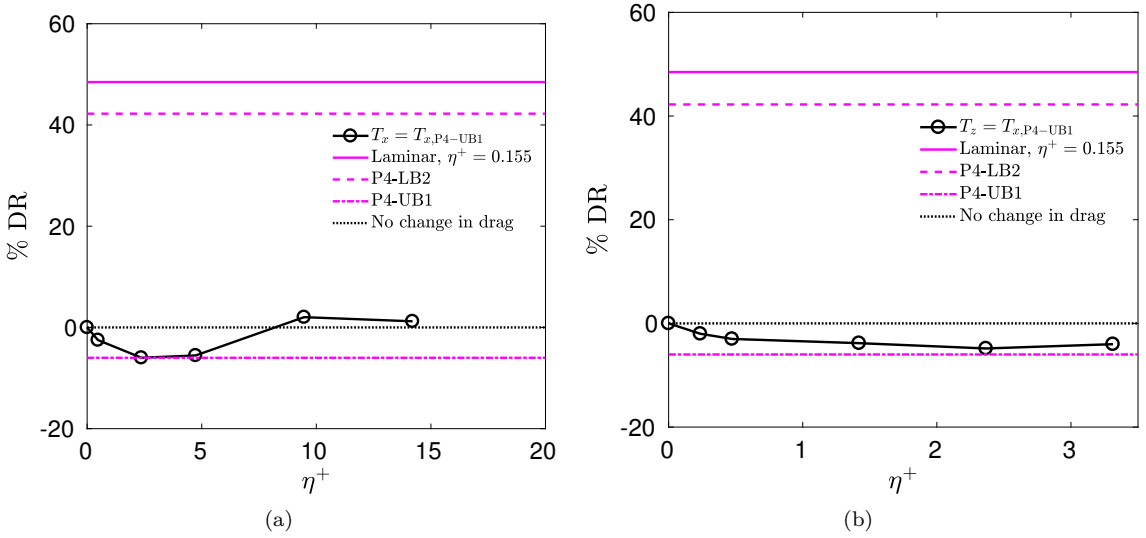

Figure 13.19: Drag reduction rate as a function of deformation amplitude for (a) streamwise and (b) spanwise motion of channel walls the shape of which that mimics the spatial patterns of wall shear stress fluctuations of a P4 upper branch travelling wave. Corresponding values for laminar and P4-UB1 solutions are included for reference.

velocity profile of the upper branch that was imposed on the flow, except in the region $y^+ \approx 15 - 35$ where the upper branch velocity profile shows a deviation.

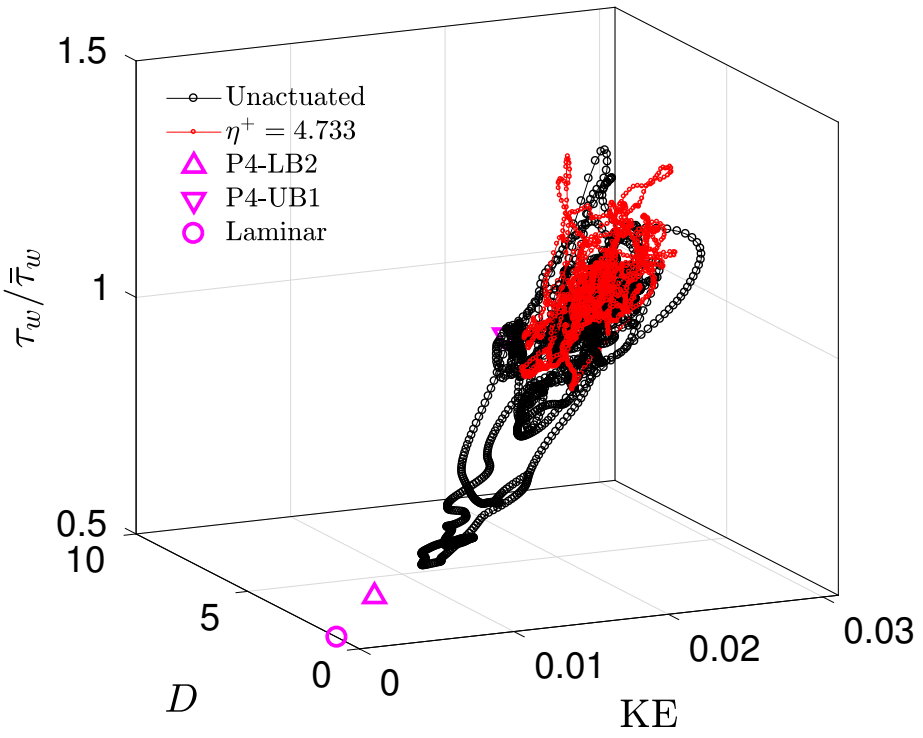

Figure 13.20: State space visualisation of DNS trajectories for plane channel (black) and for a channel with P4-UB-like wall motion in the streamwise direction (red) with $\eta^+ = 4.733$ and $T_x^+ = 18.46$ in a minimal channel turbulent flow at $\mathrm{Re}_\tau = 85$.

The degree to which drag has changed has been quantified in Figure 13.19. Drag reduction rates have been calculated using Equation (13.9). For both the cases, a negative drag-reduction is observed, i.e., an increase in drag. The level of drag-increase is very close to that of the upper branch solution that was imposed on the flow. It is interesting to note that for the streamwise case, minor drag-reduction was observed for two values of deformation amplitude — the reason for this is not known to us.

Figure 13.20 shows state space trajectories in the streamwise actuated channel (red) in comparison with the trajectories in the plane channel (black). The upper branch travelling wave solution (P4-UB1) is also shown for reference. It is observed that the red trajectories remain in the high-drag region of the state space and keep moving chaotically around a high-drag turbulent attractor, not necessarily the upper branch solution that was imposed on the flow. Similar observations are made when the imposed pattern propagate in the spanwise direction (Figure 13.21).

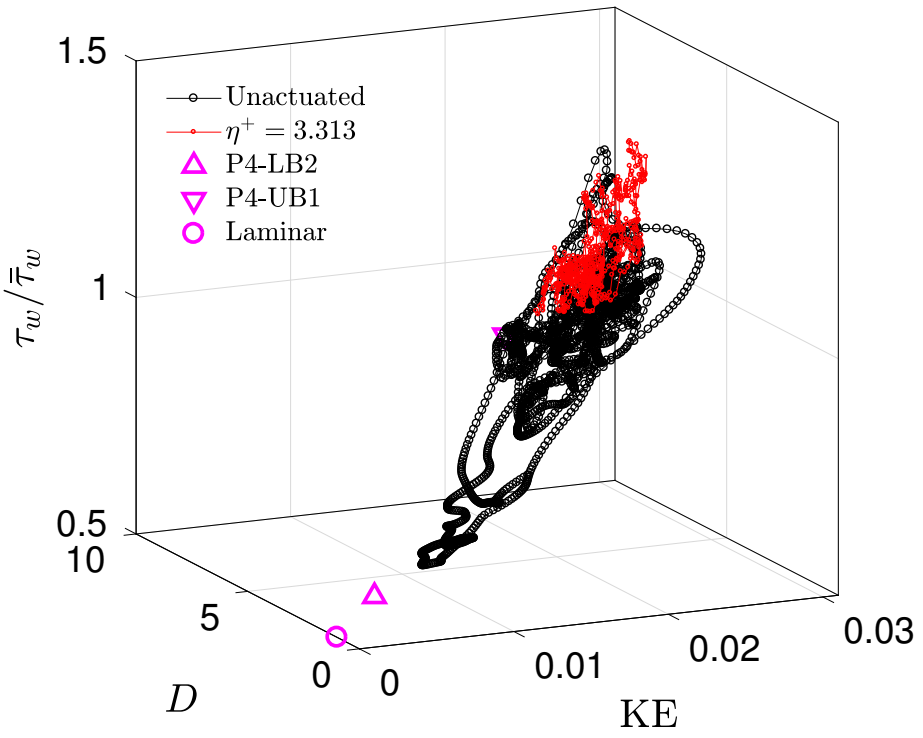

Figure 13.21: State space visualisation of DNS trajectories for plane channel (black) and for a channel with P4-UB-like wall motion in the spanwise direction (red) with $\eta^+ = 3.313$ and $T_z^+ = 18.46$ in a minimal channel turbulent flow at $\mathrm{Re}_\tau = 85$.

Figures 13.22 and 13.23 show the joint probability densities of KE and D, $\tau_w/\bar{\tau}_w$ and D, and $\tau_w/\bar{\tau}_w$ and KE for streamwise and spanwise travelling waves of wall deformation, respectively. Similar plots for the plane channel are also presented for comparison. The joint densities for the wall actuation case with an upper branch solution are concentrated in the regions where the values of all the three quantities are high. The positive correlation between the quantities, which is very strong for the plane channel, still exists for the actuated channel but it appears to have weakened a little bit.

13.4.2 Spanwise wall oscillation of the wall

In this chapter, we visit a drag-reduction technique studied extensively by many researchers: drag reduction via spanwise wall oscillation. An excellent review article by Quadrio [2011] describes many forms in which spanwise wall oscillation has been implemented, why the spanwise motion is particu-

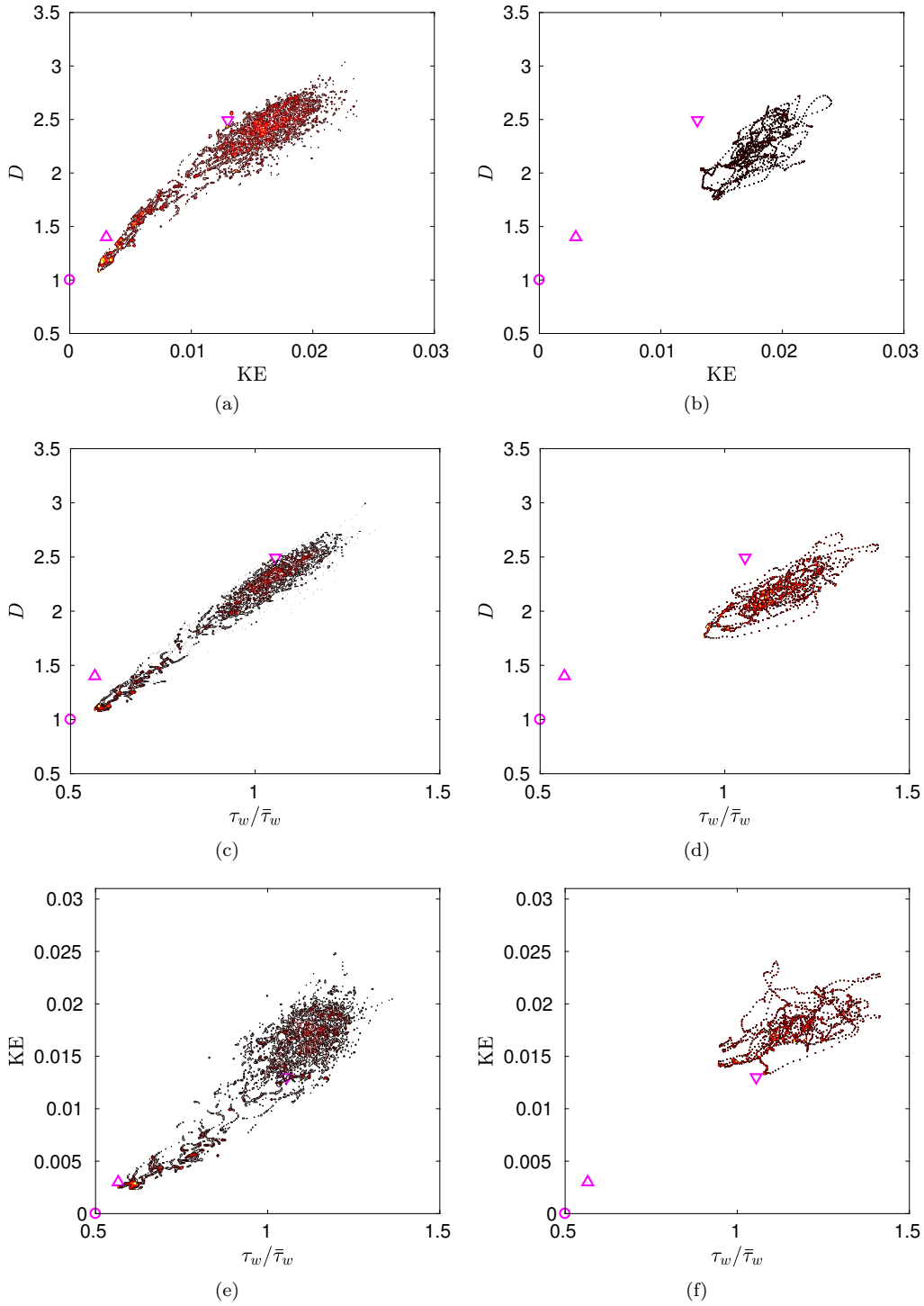

Figure 13.22: Joint probability densities of [(a), (b)] KE and D, [(c), (d)] $\tau_w/\bar{\tau}_w$ and D, and [(e), (f)] $\tau_w/\bar{\tau}_w$ and KE for both the plane channel (left column) and for a channel with P4-UB-like wall motion in the streamwise direction with $\eta^+ = 4.733$ and $T_x^+ = 18.46$ (right column). Hollow symbols have same meaning as before.

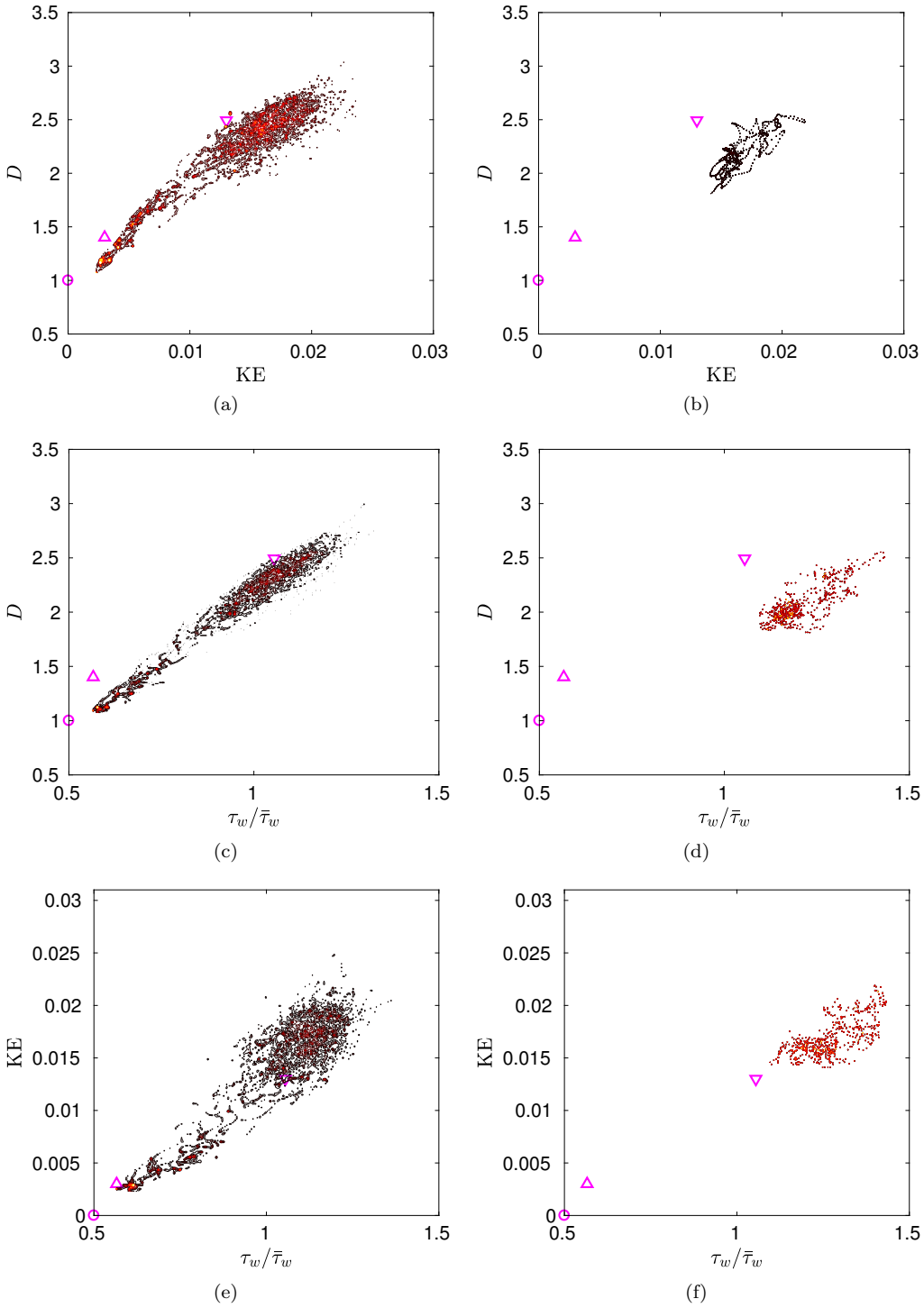

Figure 13.23: Joint probability densities of [(a), (b)] KE and D, [(c), (d)] $\tau_w/\bar{\tau}_w$ and D, and [(e), (f)] $\tau_w/\bar{\tau}_w$ and KE for both the plane channel (left column) and for a channel with P4-UB-like wall motion in the spanwise direction with $\eta^+ = 3.313$ and $T_z^+ = 18.46$ (right column). Hollow symbols have same meaning as before.

larly effective in reducing the drag and the importance of the generalised Stokes layer developed due to the oscillatory motions in determining turbulent drag reduction. The simplest form of spanwise wall oscillation is given by a spatially uniform temporal oscillation of the spanwise velocity of the wall [Jung et al., 1992; Akhavan et al., 1993; Quadrio and Ricco, 2004; Ricco and Quadrio, 2008; Touber and Leschziner, 2012]. It can mathematically be expressed as $W_w = W_m \sin(2\pi t/T)$, where W_w is the spanwise velocity at the wall at any given time t, W_m is the spanwise velocity amplitude, and T is the time period of oscillation. Drag reductions up to 40% can be achieved from this technique at low Reynolds numbers [Jung et al., 1992]. Various other forms of spanwise wall oscillation have also been tried and tested, and they have shown in basically similar effects: streamwise variation of a stationary spanwise velocity, $W_w = W_m \sin(k_x x)$ [Viotti et al., 2009; Skote, 2011], travelling wave-like motion of the spanwise velocity in the streamwise [Quadrio et al., 2009] or the spanwise [Zhao et al., 2004] direction, i.e., $W_w = W_m \sin(k_x x - 2\pi t/T)$ or $W_w = W_m \sin(k_z z - 2\pi t/T)$, respectively. Here, where k_x and k_z are the wave numbers in the streamwise and spanwise directions, respectively.

In this study, we have implemented the simplest form of spanwise wall oscillation, namely, spatially uniform temporal oscillation of the spanwise velocity of the wall, described by $W_w = W_m \sin(2\pi t/T)$. The simulation parameters are same as those for a plane, unactuated channel: laminar centreline Reynolds number, $\mathrm{Re} = 1800$, corresponding friction Reynolds number, $\mathrm{Re}_\tau = 85$, streamwise and spanwise periods equal to π and $\pi/2$, respectively. The domain is discretised using $(N_x, N_y, N_z) = (51, 106, 41)$ grid points in the streamwise, wall-normal and spanwise directions, respectively, and a constant time step, $\delta t = 0.01$, which satisfies the CFL stability condition, is used in all simulations. A constant mass flux is maintained in the channel, thus, the drag-reduction rate is determined by measuring the drop in the mean pressure gradient, $-\mathrm{d}P/\mathrm{d}x$.

A total of 12 different cases have been studied: W_m^+ values corresponding to 6, 12 and 18, and T^+ values corresponding to 25, 50, 100 and 150. The $+$ in the superscript of W_m and T denotes scaling with the friction velocity and the time scale in wall units, respectively, of the plane, unactuated channel. These values of W_m^+ and T^+ have been reported to give high levels of drag reduction at low Reynolds numbers. Only the bottom wall of the channel, i.e., wall at $y = -1$, is oscillating.

First of all, we discuss the effect of spanwise wall oscillation of one of the channel walls on a still

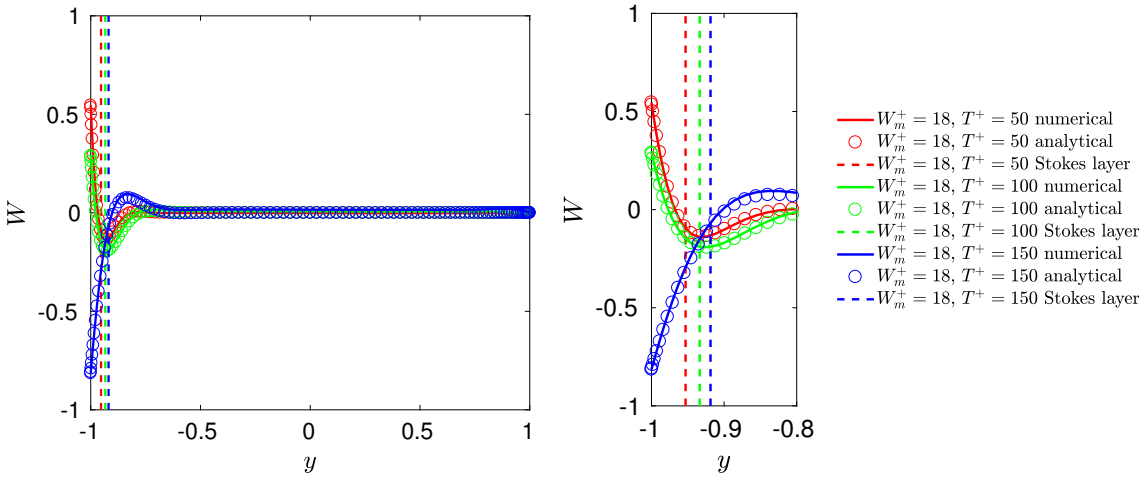

(a) Entire channel height (b) Region close to the oscillating wall

Figure 13.24: Instantaneous spanwise velocity profiles (solid lines) in a channel with still fluid and oscillating bottom wall. Analytical solutions to Stokes layer problem (hollow circles) are also plotted for comparison.

fluid. Figure 13.24 shows instantaneous spanwise velocity profiles over an oscillating bottom wall (at $y = -1$), each with a velocity amplitude $W_m^+ = 18$ and time period $T^+ = 50$ (red), 100 (green) and 150 (blue). Solid lines indicate numerical solution whereas hollow circles indicate analytical solution to the Stokes' second problem, i.e., oscillating flat plate beneath a semi-infinite layer of initially quiescent incompressible fluid. From scaling arguments, it can be derived that the thickness of the effective layer through which momentum can diffuse in one time period is proportional to $\sqrt{\nu T}$, where ν is the kinematic viscosity of the fluid. This thickness is known as the Stokes layer. In Figure 13.24, the location of the Stokes layer relative to the oscillating wall for different time periods of oscillation is shown by vertical dashed lines in their respective colour. In Figure 13.24(a), the entire channel height, from $y = -1$ to $y = 1$ is shown. In Figure 13.24(b), only the region near the oscillating bottom wall, $y = -1$, is emphasised. An extremely good correspondence is observed between the numerical and analytical results at all the oscillation frequencies, especially inside the Stokes layer. Very minor discrepency, which is expected due to the presence of the top wall at $y = 1$, is also observed. An excellent agreement between the numerical results and the analytical solution to the Stokes problem validates our numerical procedure.

We now present mean statistics of drag-reduction results due to spanwise wall oscillation in a

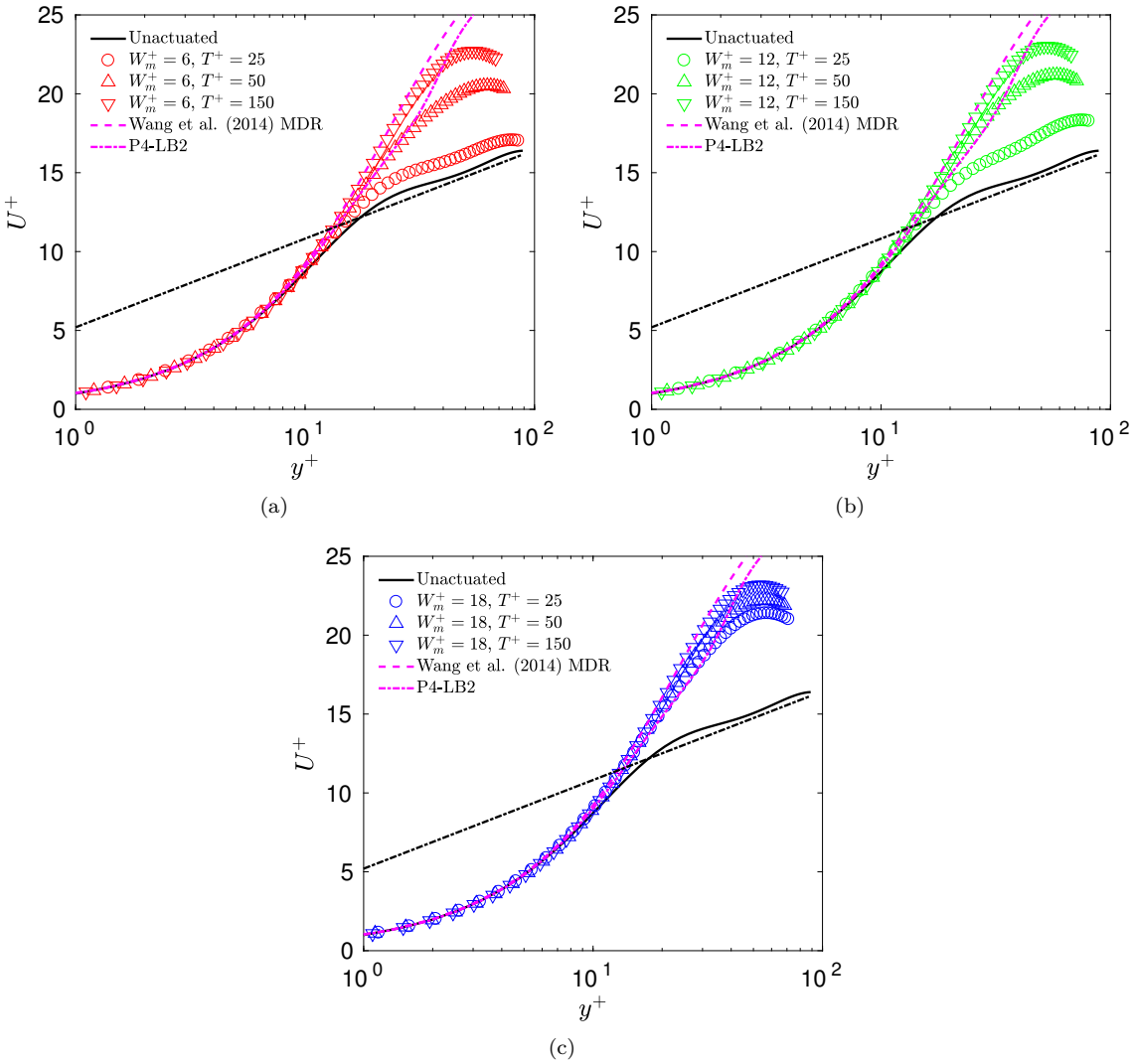

Figure 13.25: Mean velocity profiles above a spanwise oscillating wall for (a) $W_m^+ = 6$, (b) $W_m^+ = 12$ and (c) $W_m^+ = 18$. Plane channel, viscoelastic MDR and P4-LB2 ECS profiles are also shown for comparison. Lines corresponding to $T^+ = 100$ are omitted to avoid overcrowding.

turbulent channel. Note that for all the cases, averages are taken only after a statistical stationary state has been attained. Illustrated in Figure 13.25 are the mean streamwise velocity profiles over the wall oscillating at different velocity amplitudes, and for each velocity amplitude, results corresponding to different frequencies are plotted. The black solid line represents the velocity profile in the plane channel, and at $\mathrm{Re}_\tau = 85$, it lies slightly above the Newtonian log law [Patel and Head,

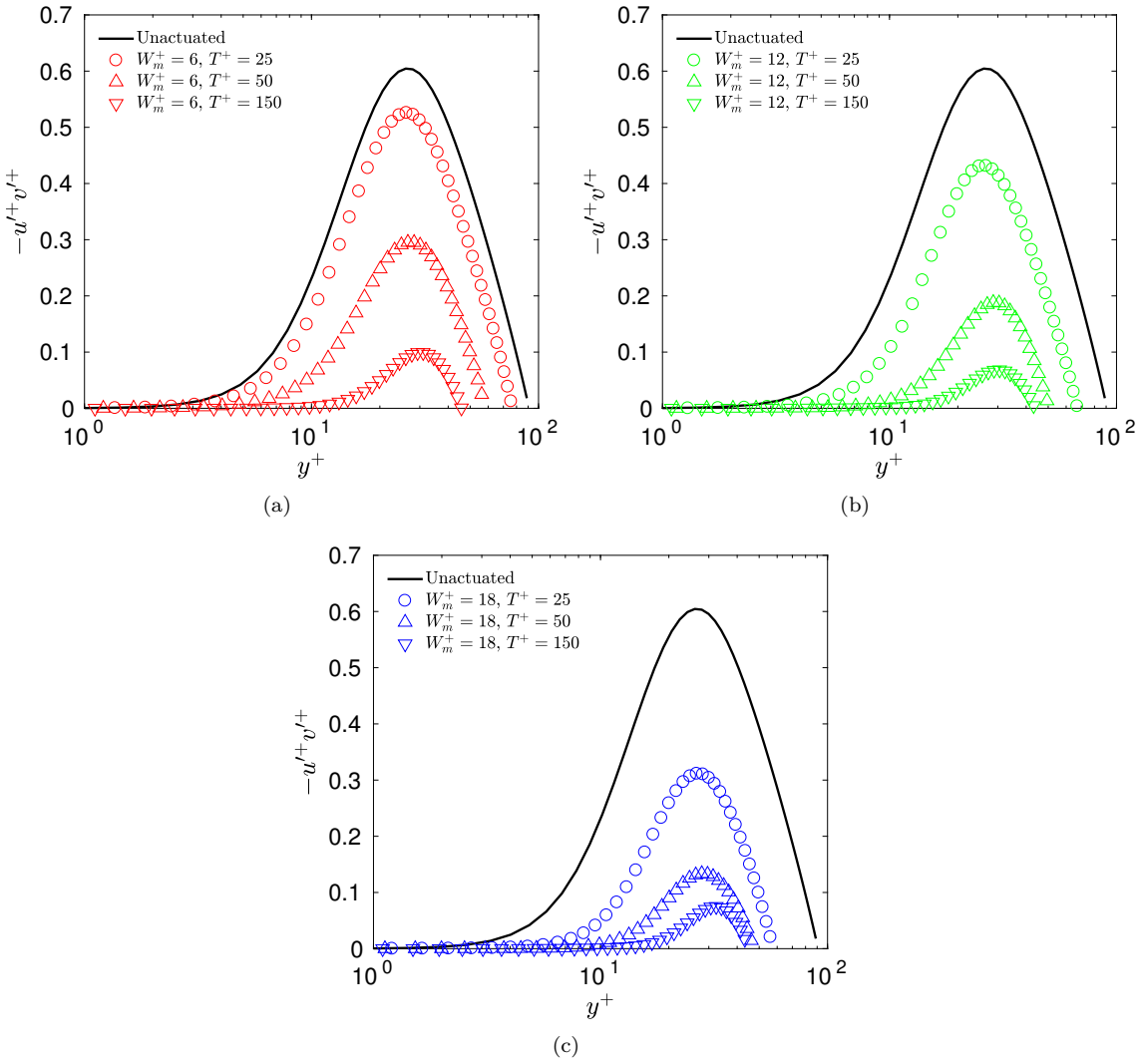

Figure 13.26: Reynolds shear stress above a spanwise oscillating wall for (a) $W_m^+ = 6$, (b) $W_m^+ = 12$ and (c) $W_m^+ = 18$. Plane channel profile is also shown for comparison. Lines corresponding to $T^+ = 100$ are omitted to avoid overcrowding.

1969; Kasagi and Shikazono, 1995; Tsukahara et al., 2005]. Velocity profiles corresponding to the viscoelastic maximum drag reduction (MDR) [Wang et al., 2014] and the P4-LB2 lower branch ECS [Park and Graham, 2015] are also shown for comparison. For all the three cases of velocity amplitudes, it is observed that velocity profiles above the oscillating wall are elevated, i.e., they lie above the Newtonian log law and have a higher slope in the region $y^+ \approx 20 - 30$. For a given velocity amplitude, for example, $W_m^+ = 6$ in Figure 13.25(a), it can be seen that increasing the time period

of spanwise wall oscillation (or decreasing its frequency) elevates the velocity profile approximately up to the viscoelastic MDR profile. Velocity profiles are elevated more for higher time periods for all the three cases, and the viscoelastic MDR profile appears to form the upper bound to the wall oscillation velocity profiles. A related observation, not in a drag-reducing case though, has been made earlier by Park and Graham [2015]: they found that temporally intermittent flow properties in a minimal channel at $\mathrm{Re}_\tau = 85$, e.g., mean velocity, wall shear stress, disturbance kinetic energy, energy dissipation rate, are all bounded on the upper end by a lower branch ECS of the P4 family. Kushwaha et al. [2017] made similar observations for Newtonian turbulence in extended domains where they found that the low-drag velocity profiles (conditionally averaged profiles) lie very close to the same P4 lower branch ECS in the near-wall region, $y^+ \lesssim 30$. Finally, with regard to the spanwise velocity amplitude, it is observed that the velocity profile is elevated more for a higher velocity amplitude at a given time period of oscillation. For example, for $W_m^+ = 18$ in Figure 13.25(c), all the velocity profiles corresponding to the wall actuated at different frequencies are elevated and lie extremely close to the viscoelastic MDR and the P4-LB2 profiles.

Reynolds shear stress profiles for both unactuated and actuated channels are illustrated in Figure 13.26. These profiles follow the trend observed for the velocity profiles: (1) Reynolds shear stresses for the actuated channel are lower compared to that of the unactuated channel, (2) for a given velocity amplitude, the reduction in the stresses increases as the time period of spanwise wall oscillation is increased, and (3) for a given time period, the reduction in the stresses increases as the velocity amplitude of spanwise wall oscillation is increased.

A state space visualisation of DNS trajectories for the plane and actuated channels is presented in Figure 13.27, in black and red colours, respectively. Both the trajectories represent a statistically stationary state for their respective cases. Trajectories for the plane channel follow their usual pattern as seen earlier in the dissertation and in other literature [Park and Graham, 2015; Kushwaha et al., 2017]: they move chaotically between high- and low-drag states in the state space, mostly concentrated in the high-drag region around a high-drag turbulent attractor, and making occasional excursions to very low-drag states, e.g., an exact solution characteristic of low drag. Trajectories corresponding to spanwise wall oscillation look very different from those observed earlier for streamwise (Figure 13.5) or spanwise (Figure 13.11) travelling waves of wall deformation. Due

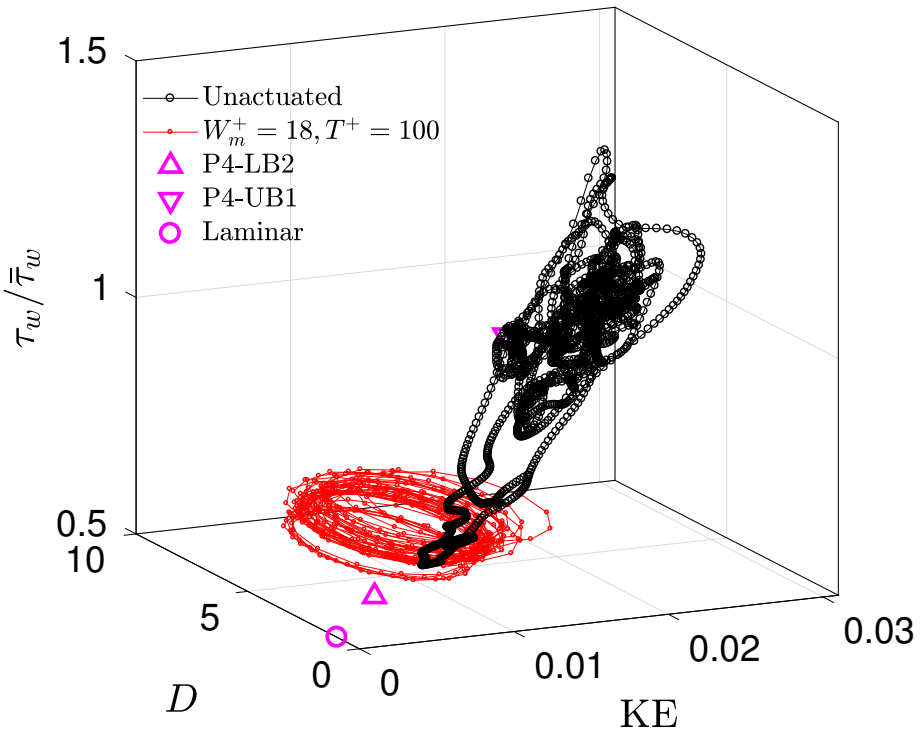

Figure 13.27: State space visualisation of DNS trajectories for plane channel (black) and for a channel with spanwise wall oscillation (red) with $W_m^+ = 18$ and $T^+ = 100$ in a minimal channel turbulent flow at $\mathrm{Re}_\tau = 85$.

to the sinusoidal form of spanwise wall oscillation, the trajectories appear to move continuously in a spiral in the low-drag region (region where $\tau_w/\bar{\tau}_w$ is small) of the state space. In addition, they are restricted to the region they are spiralling in — they never come out of it. A projection of these trajectories on two-dimensional planes is better represented in the form of joint PDFs as illustrated in Figure 13.28. Compared to the joint PDF for the unactuated channel (left column) that shows a positive correlation between the two variables and the high density in the high-D, high-KE and the high-$\tau_w/\bar{\tau}_w$ regions, the joint PDFs for the wall oscillation case (right column) takes an oval shape with high densities only along the thick edge of the oval. In contrast to the joint PDFs for the streamwise (in Figure 13.6) or spanwise (in Figure 13.12) travelling waves of wall deformation, the joint PDF for the current case shows a greater spread across the D-KE plane.

We now look at some instantaneous snapshots of flow structures observed over a spanwise oscillating wall in a turbulent channel flow. Figure 13.29 shows instantaneous cross-flow planes for

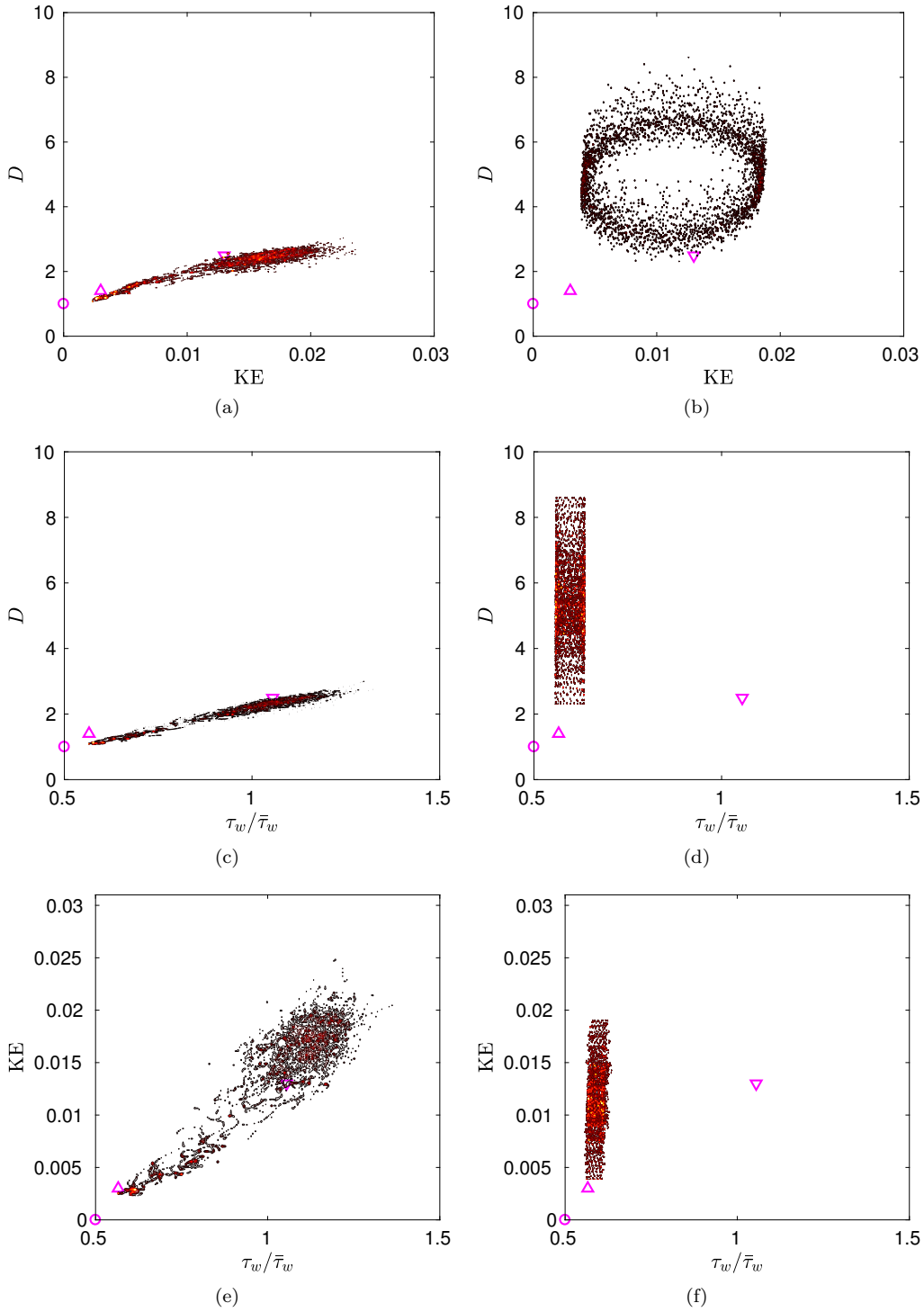

Figure 13.28: Joint probability densities of [(a), (b)] KE and D, [(c), (d)] $\tau_w/\bar{\tau}_w$ and D, and [(e), (f)] $\tau_w/\bar{\tau}_w$ and KE for both the plane channel (left column) and for a channel with spanwise wall oscillation with $W_m^+ = 18$ and $T^+ = 100$ (right column).

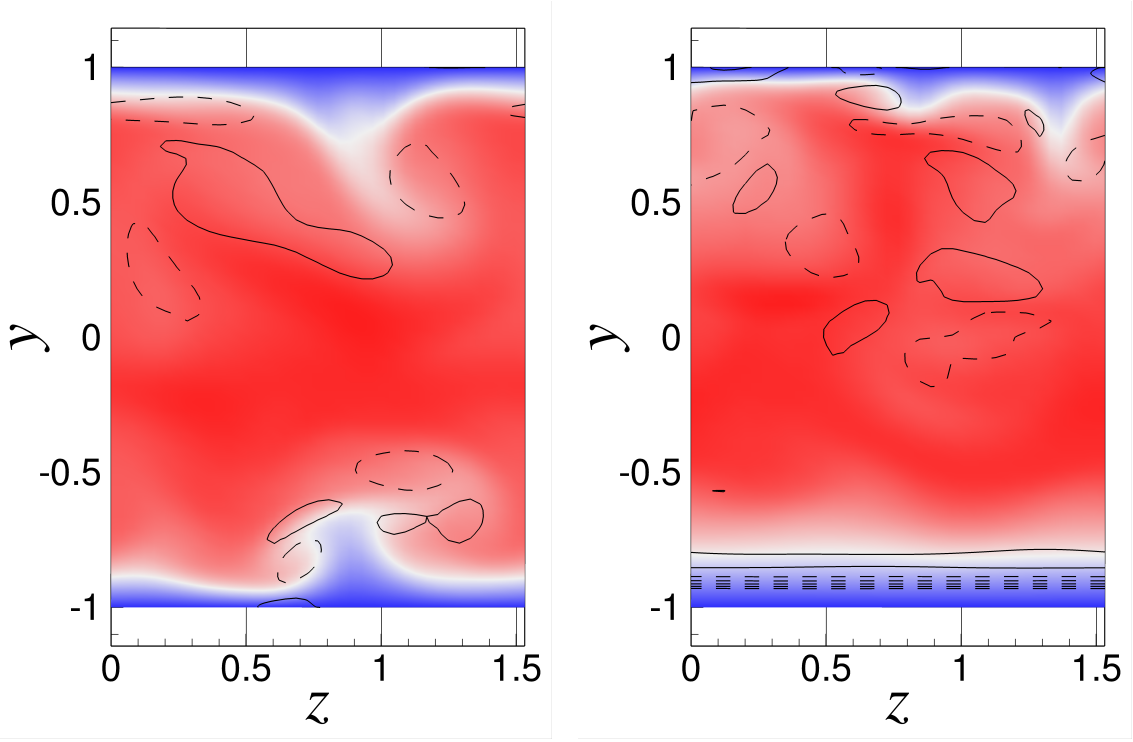

Figure 13.29: Instantaneous snapshots of the full cross-flow plane showing streamwise velocity as colour contours and streamwise vorticity as line contours (positive vorticity as solid lines and negative vorticity as dashed lines) for (a) unactuated case, and (b) oscillating wall case with $W_m^+ = 18$ and $T^+ = 100$. Note that the number of vorticity contour levels has been reduced here for a better visualisation of the induced vorticity near the bottom wall in (b).

the unactuated channel (Figure 13.29(a)) and the actuated channel with the bottom wall oscillating in the spanwise direction (Figure 13.29(b)). Colour contours are the streamwise velocity, U, and line contours represent the streamwise vorticity, ω_x, (solid: positive vorticity, and dashed: negative vorticity). In the unactuated plane channel, dense vorticity lines can be seen indicating strong streamwise vorticity, which is associated with the high skin-friction drag. For the wall oscillation case, vorticity lines are in fact denser near the oscillating wall — this is due to the streamwise vorticity induced by the spanwise wall oscillation. However, just above the oscillating bottom wall (near-wall region), the flow appears to be very orderly: the nearly-flat vorticity-lines indicate that the streaks and vortices have been stabilised, without actually laminarising. Overall, the vortices in the fluid region have moved away from the wall. Interestingly, the near-wall region where the

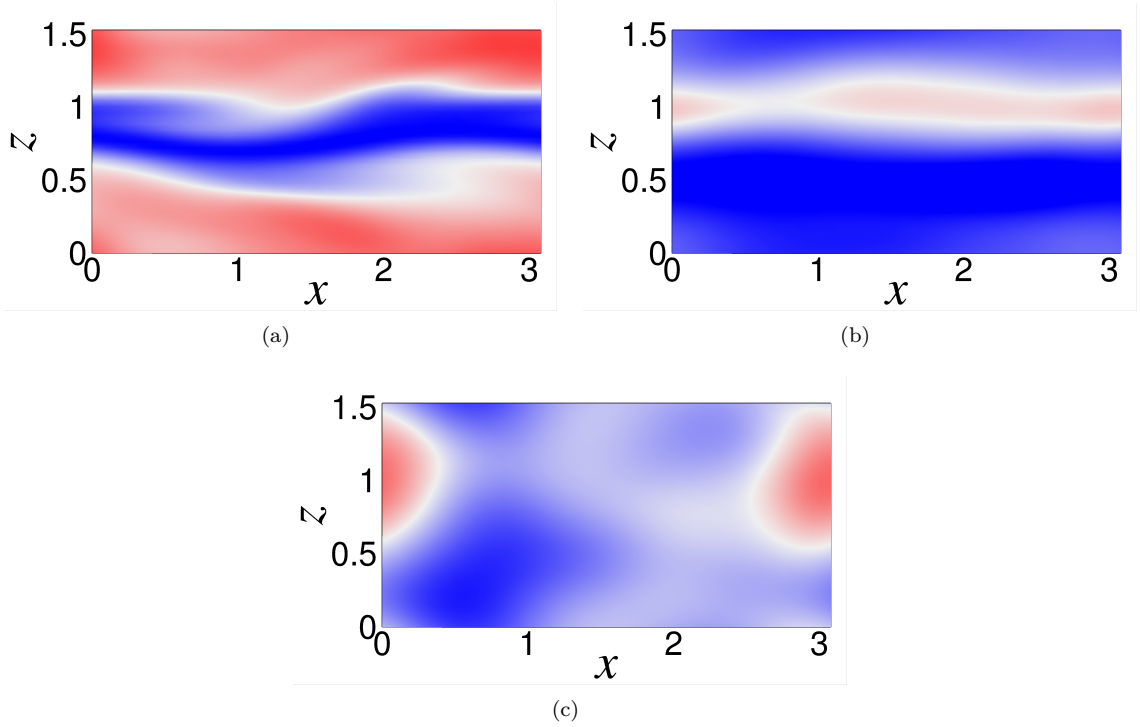

Figure 13.30: Instantaneous snapshots of streamwise velocity fluctuations, u', at $y^+ \approx 15$ for (a) unactuated case, and (b) oscillating wall case with $W_m^+ = 18$ and $T^+ = 100$. (c) u' at $y^+ \approx 3$ for the same oscillating wall case at the same time instant.

flow has been stabilised and fluctuations reduced, lies within the Stokes layer formed due to the oscillation. The Stokes layer thickness when $W_m^+ = 18$ and $T^+ = 100$ is close to 0.8 in outer units (see the blue dashed line in Figure 13.24(b)), which is the thickness in which the turbulent motions have been stabilised in Figure 13.29(b).

Instantaneous snapshots of streamwise velocity fluctuations, u', at the time instants for which Figure 13.29 was plotted, are shown in Figure 13.30. Fluctuations for the unactuated channel are plotted at a distance $y^+ \approx 15$ from the wall (Figure 13.30(a)), whereas for the actuated channel, they have been plotted at two locations: $y^+ \approx 15$ (Figure 13.30(b)) and $y^+ \approx 3$ (Figure 13.30(c)). The former one lies outside the Stokes layer while the latter one lies within the Stokes layer. The unactuated channel shows a typical streamwise dependent streaky behaviour implying strong three-dimensionality in the flow. The velocity fluctuation patterns for the actuated channel at $y^+ \approx 15$ are relatively calmer and show reduced streamwise dependence. Interestingly, the streamwise velocity

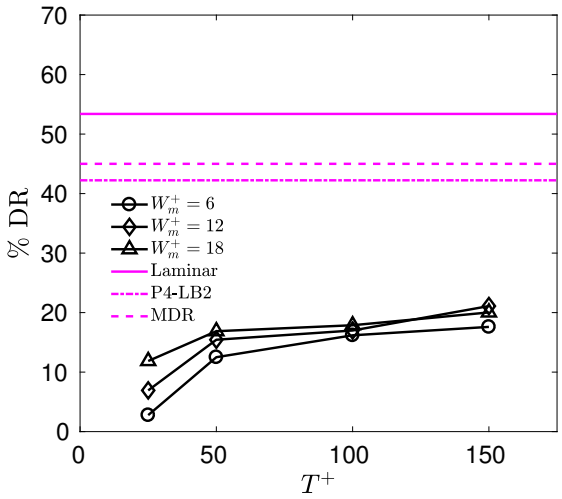

Figure 13.31: Drag reduction rate as a function of time period of spanwise wall oscillation for different velocity amplitudes. The friction Reynolds number for the controlled flow, $\mathrm{Re}_\tau = 85$. Corresponding drag reduction rates for laminar and P4-LB2 solutions are included for reference.

fluctuation patterns within the Stokes layer, at $y^+ \approx 3$, do not look similar to the patterns outside the Stokes layer. The low-speed regions appear to be more or less aligned in the spanwise direction whereas the high-speed regions appear to show some degree of obliqueness. Wall shear stress patterns were also plotted (not shown) and they were found to look like the streamwise velocity fluctuation patterns within the Stokes layer — not aligned in the streamwise direction.

Drag reduction due to spanwise wall oscillation has been quantified in Figure 13.31. The rates have been computed from the drop in the mean pressure gradient, as described by Equation (13.9). Regardless of the parameters of the wall oscillation, a maximum drag-reduction of close to 20% is observed. In addition, for all the parameters studied, none resulted in an increase in overall drag. The overall trend looks like the following: drag reduction increases with increasing time period of wall oscillation, as well as with the velocity amplitude.

13.4.3 Sinusoidal wave-like wall deformation moving in the spanwise direction

In this chapter, we conduct DNS to look at drag reduction in a turbulent channel flow using spanwise sinusoidal travelling wave-like wall deformation. This technique of achieving reduction

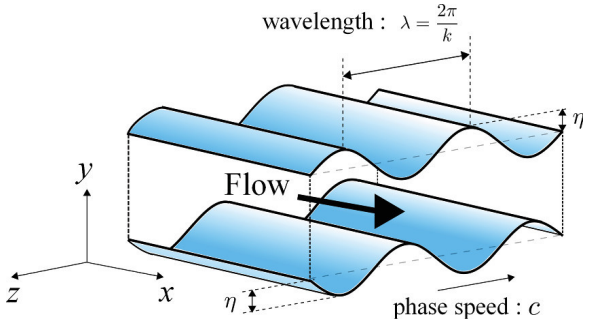

Figure 13.32: Schematic of the spanwise sinusoidal travelling wave-like wall deformation (after Tomiyama and Fukagata [2013]).

in skin-friction drag has been implemented numerically in a turbulent channel flow by Tomiyama and Fukagata [2013]. For their flows at a friction Reynolds number, Re_τ, of 180, they achieved a maximum drag reduction of 13.4%. It should be noted that compared to their Re_τ, ours is in the transitional Reynolds number regime: $\mathrm{Re}_\tau = 85$. The second difference between their set-up and ours is the domain size: the streamwise, wall-normal and spanwise lengths of their computational domain are $2\pi \times 2 \times \pi$ whereas our computational domain is half this size in both streamwise and spanwise directions, i.e., $\pi \times 2 \times \pi/2$.

We ran some simulations to see the effect of spanwise sinusoidal travelling wave-like wall deformation on turbulent channel flows in a minimal channel at $\mathrm{Re}_\tau = 85$ (for the controlled, unactuated channel). A schematic of wall deformation and its propagation is shown in Figure 13.32. Other parameters in the simulation, e.g., deformation amplitude η^+, wave speed c_z^+, wave number k_z, were chosen similar to those used by Tomiyama and Fukagata [2013]. Note that the wave number, k_z, reported here is the angular wave number, i.e., number of waves over a period of 2π. Since the spanwise period of our minimal channel is $\pi/2$, the wave number over this spanwise length would be $k_z/4$. Drag reduction rates as a function of parameters is presented in Figure 13.33. Surprisingly, for all our runs, the flow laminarised — the drag reduction rate approached the laminar value for all deformation amplitudes, wave numbers and wave speeds. This is due to (1) low Re, and (2) high wave number in the spanwise direction, k_z, used. We looked into cases with smaller spanwise wave number, $k_z = 4$, and got a drag-reduction of about 25% at $\eta^+ = 1.7$ without any laminarisation.

Figure 13.34 shows the patterns of streamwise velocity fluctuations, u', at $y^+ \approx 15$ for both

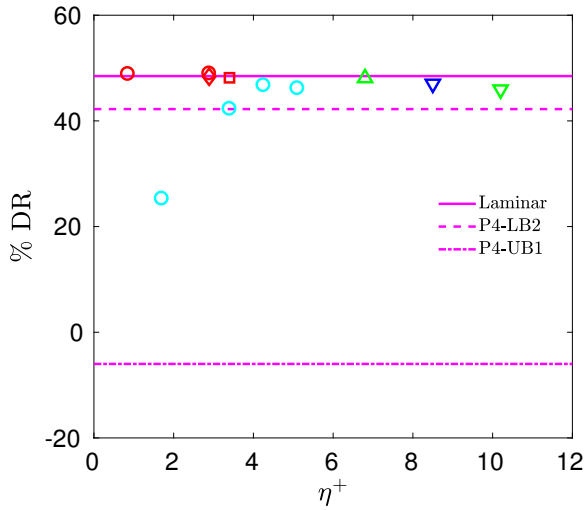

Figure 13.33: Drag reduction rate as a function of deformation amplitude due to spanwise sinusoidal travelling wave-like wall deformation. Cyan: $k_z = 4$, red: $k_z = 8$, green: $k_z = 16$, and blue: $k_z = 32$.

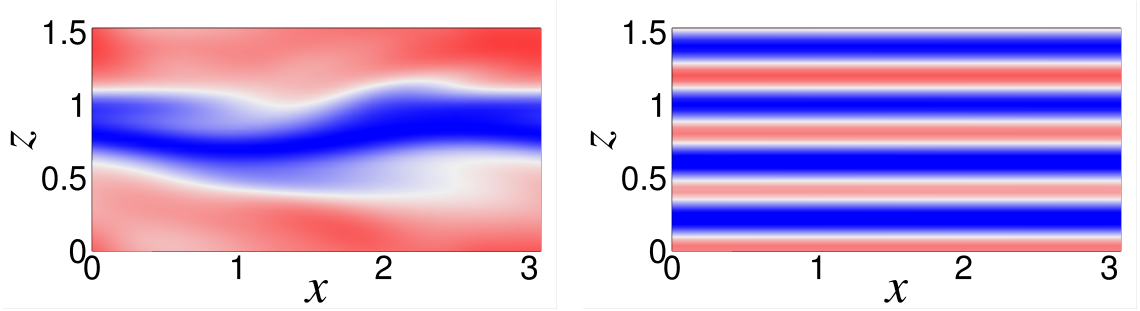

Figure 13.34: Instantaneous snapshots of streamwise velocity fluctuations, u', at $y^+ \approx 15$ for (a) unactuated case, and (b) spanwise sinusoidal travelling wave-like wall deformation with $\eta^+ = 6.8$, $c_z^+ = 0.21$ and $k_z = 16$.

plane and actuated channels. The unactuated channel shows streamwise dependent streaks with fluctuations whereas for the channel with spanwise sinusoidal travelling wave-like wall deformation, due to laminarisation, well-organised streamwise independent streaks are formed. Low-drag regions are formed over the crest whereas high-drag regions are formed over the trough. These patterns move in the spanwise direction with the moving wall.

A list of all wall actuation parameters and the resultant drag reduction rate is presented in Table 13.1.

Table 13.1: Set of wall actuation parameters and resultant drag reduction rate.

	η^+	W_m^+	k_x/k_z	λ^+	c_x^+/c_z^+	T^+	% DR
P4-LB-like wall moving in the streamwise direction with $T_x = T_{x,\text{P4-LB2}}$	0.78	—	—	—	15.67	18.22	-2.14
	1.55	—	—	—	15.67	18.22	-3.26
	3.10	—	—	—	15.67	18.22	2.00
	4.65	—	—	—	15.67	18.22	4.27
	7.75	—	—	—	15.67	18.22	6.71
	15.51	—	—	—	15.67	18.22	-9.30
P4-LB-like wall moving in the streamwise direction with $T_x = 5T_{x,\text{P4-LB2}}$	0.78	—	—	—	3.13	91.08	-3.65
	1.55	—	—	—	3.13	91.08	3.31
	3.10	—	—	—	3.13	91.08	0.02
	4.65	—	—	—	3.13	91.08	-5.77
	7.75	—	—	—	3.13	91.08	-1.66
	12.41	—	—	—	3.13	91.08	-9.70
	15.51	—	—	—	3.13	91.08	1.89
P4-LB-like wall moving in the spanwise direction with $T_z = T_{x,\text{P4-LB2}}$	0.16	—	—	—	7.84	18.22	0.15
	0.47	—	—	—	7.84	18.22	-5.37
	0.78	—	—	—	7.84	18.22	3.04
	1.09	—	—	—	7.84	18.22	7.75
	1.40	—	—	—	7.84	18.22	5.52
	1.71	—	—	—	7.84	18.22	-3.00
	2.02	—	—	—	7.84	18.22	3.18
	2.33	—	—	—	7.84	18.22	3.71
	2.64	—	—	—	7.84	18.22	15.30

Table 13.1: Set of wall actuation parameters and resultant drag reduction rate (continued).

	η^+	W_m^+	k_x/k_z	λ^+	c_x^+/c_z^+	T^+	% DR
	0.16	—	—	—	1.57	91.08	-1.37
	0.47	—	—	—	1.57	91.08	-1.75
	0.78	—	—	—	1.57	91.08	-9.47
P4-LB-like wall moving in the	1.09	—	—	—	1.57	91.08	-4.34
spanwise direction with T_z =	1.40	—	—	—	1.57	91.08	-1.02
$5T_{x,\text{P4-LB2}}$	1.71	—	—	—	1.57	91.08	14.36
	2.02	—	—	—	1.57	91.08	2.68
	2.33	—	—	—	1.57	91.08	2.39
	2.64	—	—	—	1.57	91.08	-3.53
	0.47	—	—	—	15.46	18.22	-2.50
P4-UB-like wall moving in the	2.37	—	—	—	15.46	18.22	-5.99
streamwise direction with T_x =	4.73	—	—	—	15.46	18.22	-5.54
$T_{x,\text{P4-UB1}}$	9.47	—	—	—	15.46	18.22	2.03
	14.20	—	—	—	15.46	18.22	1.21
	0.24	—	—	—	7.73	18.22	-2.00
P4-UB-like wall moving in the	0.47	—	—	—	7.73	18.22	-3.00
spanwise direction with T_z =	1.42	—	—	—	7.73	18.22	-3.81
$T_{x,\text{P4-UB1}}$	2.37	—	—	—	7.73	18.22	-4.84
	3.31	—	—	—	7.73	18.22	-4.01
Sinusoidal stationary riblets	0.85	—	32	16.69	0.00	∞	5.88
Note: these are short runs and	3.40	—	32	16.69	0.00	∞	9.47
may not be statistically con-	6.80	—	32	16.69	0.00	∞	-4.14
verged	10.20	—	32	16.69	0.00	∞	1.78

Table 13.1: Set of wall actuation parameters and resultant drag reduction rate (continued).

	η^+	W_m^+	k_x/k_z	λ^+	c_x^+/c_z^+	T^+	% DR
	1.70	—	4	133.52	7.84	18.22	25.31
	3.40	—	4	133.52	7.84	18.22	42.30
	4.25	—	4	133.52	7.84	18.22	46.77
	5.10	—	4	133.52	7.84	18.22	46.20
Sinusoidal travelling wave moving in the spanwise direction	2.89	—	8	66.76	0.78	182.15	48.37
	2.89	—	8	66.76	7.84	18.22	49.00
	3.40	—	8	66.76	0.74	192.56	48.16
	6.80	—	16	33.38	0.21	673.96	48.11
	8.50	—	32	16.69	0.42	336.98	47.02
	10.20	—	16	33.38	0.42	336.98	45.93
	—	6	—	—	—	25	2.77
	—	6	—	—	—	50	12.50
	—	6	—	—	—	100	16.19
	—	6	—	—	—	150	17.60
	—	12	—	—	—	25	6.93
Spanwise wall oscillation $W_w = W_m \sin(2\pi t/T)$	—	12	—	—	—	50	15.44
	—	12	—	—	—	100	16.99
	—	12	—	—	—	150	21.10
	—	18	—	—	—	25	11.86
	—	18	—	—	—	50	16.87
	—	18	—	—	—	100	17.88
	—	18	—	—	—	150	20.03

Chapter 14

Conclusions of Part III

For the first time in the turbulent channel flow control literature, knowledge from the dynamical systems theory has been used to develop and test active control methods for achieving drag reduction in turbulent channel flows at Reynolds number near transition. In minimal domains, turbulence in this Reynolds number range displays substantial intermittency that is associated with chaotic movement of turbulent trajectories between lower and upper branch invariant solutions known as exact coherent states (ECS). In this work we have attempted to "imprint" some of these exact solutions on the turbulent flow field and looked at the effects of the imposition in terms of quantities like mean velocity, Reynolds shear stress, velocity fluctuations, instantaneous flow structures and the amount of drag reduction.

First, information from a low-drag ECS, specifically, a lower branch travelling wave solution found in transitional channel flow turbulence by Park and Graham [2015], was used as a template. Both the walls of the turbulent channel were dynamically deformed; their shape mimicking the wall shear stress fluctuations of the said travelling wave solution. The up and down motion of wall elements results in a travelling wave of deformations, and the wave propagates in either streamwise or spanwise direction. This affects the near-wall dynamics, and some of the flow quantities, for example, wall shear stress, energy dissipation rate, disturbance kinetic energy, tend to approach those of the set target. Immersed boundary methods (IBM) with direct forcing were used to satisfy the boundary conditions at the deforming wall.

A maximum drag reduction of just above 15% was achieved when the wave of wall deformations moved in the spanwise direction with a time period same as that of the chosen lower branch ECS, and the deformation amplitude of 2.636 wall units. A maximum process efficiency of approximately 1.7 was obtained for a streamwise travelling wave. Few cases also resulted in drag increase, predominantly the ones for which the wave of wall deformation moved at a lower frequency. For the drag reduction cases, the mean velocity profile was found to lie above the Newtonian von Kármán log law, the Reynolds stress as well as the velocity fluctuations were reduced. Streamwise vorticity was also reduced compared to a plane channel, although a slight increase was observed very close to the wall due to wall motions. The low-drag streaks showed significantly reduced fluctuations and they were aligned above the crest of the deformed wall in the streamwise direction. The orderly, streamwise aligned streaks with reduced fluctuating motions is indicative of weak turbulence and hence drag reduction.

A definitive pattern of the variation of the drag-reduction rate as a function of parameters, e.g., deformation amplitude, wave speed, was not found. All the drag-reduction results presented are obtained by imposition of a single lower-branch travelling wave solution with small deformation amplitudes. Thus, a more comprehensive study with more exact solutions as the template and with a wider range of deformation amplitude needs to be conducted to be able to get a better understanding of how drag-reduction rate scales with physical parameters.

Upper branch ECS were also imposed on the turbulent flow. An increase in skin-friction drag was observed for almost all the cases, except a couple. For the cases for which an increase in drag was observed, the turbulent trajectories were found to stay in the high-drag region of the state space, moving chaotically in that region, not necessarily near the imposed upper branch solution.

We also studied drag reduction by uniform spanwise wall oscillation. The wall velocity in the spanwise direction, described by $W_w = W_m \sin(2\pi t/T)$, resulted in drag reduction for all the cases considered. The mean velocity profiles, for the wall oscillation cases, were elevated and they lied very close to the viscoelastic MDR velocity profile as well as the P4 lower branch ECS velocity profile. Reynolds shear stresses were significantly reduced. Spanwise oscillation of the wall induces streamwise vorticity in the near-wall region. The general trend for the parameters studied was that increasing the velocity amplitude or the time period of oscillation resulted in higher drag reduction.

Effect of sinusoidal wave-like wall deformation moving in the spanwise direction was also looked into. Surprisingly, for most of the parameters studied, the flow entered into a laminar state.

Chapter 15

Future directions: extending the scope of the current drag-reduction technique

A major portion of Part III was devoted to getting an understanding of how imprinting a known solution to the Navier–Stokes equations on the turbulent flow field impacts the near-wall flow dynamics. In particular, the goal was to imprint features of a lower branch travelling wave solution that shows characteristics of low-drag, in the form of waves of wall deformations in streamwise and spanwise directions, and see if the flow approaches the imprinted pattern, and if the skin-friction drag due to the flow reduces.

In this chapter, I have tried to present a critical analysis of my work described in Part III, specifically, its limitations and shortcomings, and I have described possible ways of improvement to the physical process as well as the numerical tools that help us in simulating the process.

The idea of imprinting the features of a lower branch travelling-wave, specifically, its spatial wall shear stress patterns and wave speed, on the turbulent flow field is a novel one and it did give promising results. Regardless of the parameters of the wall deformation, a maximum drag reduction of just over 15% was achieved and the process was found to be efficient, i.e., energy savings in the

form of reduction in pumping power were more than the energy spent on actuation. When an upper branch travelling wave solution was imposed, the net drag was found to increase.

Even with some of these positive outcomes, this study raises more questions than it answers, partly because it was conducted for only a few set of parameters:

1. Reynolds number was in the transitional regime: $\mathrm{Re}_\tau = 85$ for the plane, unactuated channel.
2. Flow domain was a minimal channel: $L_x \times L_z = \pi \times \pi/2$.
3. Only two single exact solutions were worked with on the turbulent flow, a lower branch and an upper branch solution, each from the P4 family travelling waves.
4. Deformation amplitudes were small: they lied within the viscous sublayer.

In addition, although the effect of deformation amplitude and wave speed on the drag reduction rate, % DR and efficiency, ϵ, is presented, an in-depth study on the scaling of these quantities has not been done, in part because it requires data from a range of parameters enumerated above. For example, in the work of Tomiyama and Fukagata [2013] in which a spanwise sinusoidal travelling wave-like wall deformation was implemented, the drag reduction rate was found to be reasonably scaled with $a^+\delta^+$, where a^+ is the magnitude of wall deformation velocity and δ^+ is the thickness of its effective layer. Similarly, in the case of stationary riblets, drag-reduction scales nicely with a length scale equivalent to $\sqrt{A_g^+}$, derived from the cross-sectional area of the groove, A_g^+ [García-Mayoral and Jiménez, 2011a,b]. At the moment, the lower and upper branch solutions we have are restricted to minimal channels, and are for flows at transitional Reynolds numbers. Their spatial patterns in this Reynolds number regime do not vary by a lot. Thus, an obvious choice for drag-reduction scaling is not available. Therefore, for our drag-reduction methods, a more comprehensive study using known solutions as potential targets should be done, not only for scaling reasons but also for assessing the generality and effectiveness of our method over a broad parameter range.

Another interesting thing to look into is the effect of imposition lower/upper branch ECS on a turbulent flow field in an extended domain. As discussed in Part I, the temporal intermittency observed in minimal channel flows translates to spatiotemporal intermittency in large domains — high and low drag events happen at the same time at different locations. Quantitatively, we have

shown that the intermittency factors for hibernation (low drag) events, i.e., fraction of time/space the slow spends under hibernation, are nearly same for both temporal and spatial sampling. We also showed that both the local near-wall flow structures in the low-drag patches of the large domain and the conditional mean profiles in the region $y^+ \lesssim 30$ resemble those of a lower branch minimal domain ECS. Thus, it is hypothesised that, with regard to drag reduction, imposing a lower branch solution might have a positive impact. Since all the ECS solutions we have at the moment are in the minimal channel, imprinting these small structures in a large domain can be done in two ways: (1) locally — the pattern can be imposed at an arbitrarily chosen location in the large domain and the resulting effects can be studied and compared with those from imposition in the minimal channel, and (2) globally — exploiting the fact that the solutions are periodic in both streamwise and spanwise directions, the minimal channel ECS can be tiled multiple times in these directions so as to form a bigger pattern the size of large domain. The effect of the imposed solution on the spatiotemporal dynamics in the extended domain can then be studied.

In the current work, we have basically designed an open loop control strategy that uses information from a lower branch travelling wave which acts like a target flow field. The strength of actuation is same throughout the control process irrespective of the instantaneous drag. For example, in the current formulation, the walls continue to move at the same rate even after the flow with reduced drag has attained a statistically stationary state. This may result in more energy consumption than ideally required which would decrease the efficiency of the process. In the longer run, it would be desirable to have a closed loop, feedback control scheme that in addition to using information from known solution, keeps taking measurements of the key components, e.g., wall shear stress or flow velocity, from the flow field. The controller input will be based on some form of difference between the measured quantity and the known solution that was set as the desired state. One may take ideas from the suboptimal control schemes of Lee et al. [1998] and Xu et al. [2002] that aim at minimising the pressure gradient, or of Fukagata and Kasagi [2004] that minimises the near-wall Reynolds shear stress to develop a closed loop control scheme that minimises, for example, the difference between the wall shear stresses of the current state and the desired state.

Another important issue that requires attention is related to our computational methodology: the ability to perform numerical experiments more quickly. All the computational results presented

in this dissertation have been obtained from a serial code that can run only on a single processor. Compared to Gibson's pseudo-spectral ChannelFlow [Gibson, 2009] code, a serial version of which was used to obtain results of Part I of the dissertation, the finite-volume code used to implement wall deformation in Part III is much slower. For example, for the same set of parameters, the finite-volume code could do about 200 time units in a 24 hour period (wall time) compared to about 1000 time units with ChannelFlow on a similar node, i.e., a node with similar technical specifications. Thus, it is imperative that a parallel version of the current finite-volume code be developed and utilise the computing power of our parallel machines. One should also note that computations become prohibitively expensive with increasing Reynolds number and/or domain size, especially if one wants to simulate flow in full-sized channels. This limits the range of control strategies that can be explored [Jiménez, 2003]. A faster code will help deal with situations like this.

In order to achieve parallel computing and improve the speed of our code, we can utilise the Message Passing Interface (MPI) support which is provided by the Portable, Extensible Toolkit for Scientific Computation (PETSc) [Balay et al., 2011] libraries we are using to solve the linear system in the finite-volume code. One way of running the code on multiple processors is to use domain decomposition. As the name suggests, the domain decomposition method decomposes the full three-dimensional domain, which is rectangular in our case, into many sub-domains. Calculations in each sub-domain can be performed by an independent processor; thus, there will be multiple processors performing calculations for multiple sub-domains simultaneously, each working independent of every other processor. Data can be communicated between processors as and when required. PETSc uses distributed arrays to carry out domain decomposition. These arrays contain information pertaining the layout of the sub-domains and the communication information between them, i.e., which sub-domain is connected with which other sub-domains. The actual data are stored in variables that are specific to the data types supported by PETSc. The fact that PETSc has its own data types that support the usage of variables containing data for different sub-domains in a very straightforward manner eliminates coding at the MPI level. The reader is referred to PETSc Users Manual [Balay et al., 2011] for more information on distributed arrays and their usage.

Appendix A

A finite-volume Navier–Stokes solver for direct numerical simulation of incompressible flows

A.1 Introduction

In Part I of the dissertation, all the results that were presented, were obtained using the ChannelFlow code [Gibson, 2009]. The code uses spectral discretisation in spatial directions — Fourier in the streamwise and spanwise directions and Chebyshev in the wall-normal direction, and finite-differencing in time. Problem arises when we try to implement wall actuation via wall deformation using ChannelFlow: the incompressibility condition that can be enforced on each (x, z) Fourier mode independently in a rectangular domain, is no longer valid. Moreover, the influence-matrix approach implemented in ChannelFlow is not flexible enough to be applied to complex boundary conditions or domains. Hence, we switch to a non-spectral code that uses a finite-volume approach on a Cartesian mesh. The system of equations are solved using a fractional-step method, in which a non-solenoidal velocity field is calculated, which is then projected onto a divergence-free vector field.

We use a Newtonian code provided by Prof Sang Lee from the University of New Mexico and

Prof Jae Sung Park from the University of Nebraska–Lincoln. The code was originally written for boundary layer flows over a flat surface, which was modified by us to be used for simulating flows in a wall-bounded channel. In Appendix A, numerical details about the code — system formulation, boundary conditions, flow solver — are provided in great details. Finally, validation of the code is done by comparing its results with known results in the literature.

A.2 Formulation

A.2.1 Governing equations

We consider pressure driven flow of an incompressible Newtonian fluid in a rectangular, wall-bounded domain (channel) maintained at constant mass flux, a schematic of which is shown in Figure A.1. The x, y and z axes correspond to the streamwise, wall-normal and spanwise directions, respectively. Velocities in these directions in the frame of reference of the channel are represented as u, v and w, respectively; the velocity vector is denoted by $\boldsymbol{u}$ as a column vector, i.e., $\boldsymbol{u} = (u\ v\ w)^{\mathrm{T}}$. No-slip boundary conditions are applied at the top and bottom walls and periodic boundary conditions are adopted in the streamwise and spanwise directions. The periods are L_x and L_z in these directions, respectively. More on the grid set-up and implementation of boundary conditions is discussed in Appendix A.2.2 and Appendix A.2.3, respectively. The momentum and continuity equations for an incompressible fluid with constant density (ρ) and viscosity (μ) are given as:

$$\rho\frac{\partial \boldsymbol{u}}{\partial t} + \rho\boldsymbol{u}\cdot\boldsymbol{\nabla}\boldsymbol{u} = -\boldsymbol{\nabla}p + \mu\nabla^2\boldsymbol{u} \tag{A.1}$$

$$\boldsymbol{\nabla}\cdot\boldsymbol{u} = 0 \tag{A.2}$$

The half-channel height, $l = L_y/2$ is chosen as the characteristic length scale for nondimensionalisation of all the lengths in the geometry. Velocities are scaled with the laminar centreline velocity U_c for the given mass flux. Time t is scaled with l/U_c and pressure p with ρU_c^2, where ρ is the fluid density. Replacing $\boldsymbol{u}$ with $\boldsymbol{u}U_c$, t with tl/U_c, p with $p\rho U_c^2$ and $\boldsymbol{\nabla}$ with $\boldsymbol{\nabla}/l$ in Equation (A.1) and

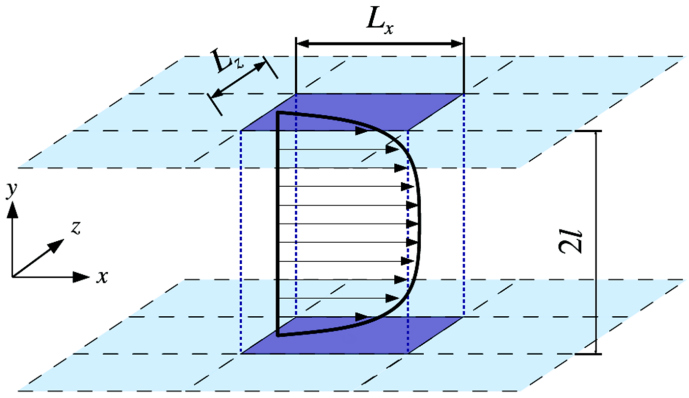

Figure A.1: Schematic of the plane Poiseuille flow geometry: the actual simulation box is highlighted with dark-coloured walls in the centre, surrounded by its periodic images.

Equation (A.2), the nondimensionalised Navier–Stokes equations are then given as:

$$\frac{\partial \boldsymbol{u}}{\partial t} + \boldsymbol{u} \cdot \boldsymbol{\nabla} \boldsymbol{u} = -\boldsymbol{\nabla} p + \frac{1}{\mathrm{Re}} \nabla^2 \boldsymbol{u} \tag{A.3}$$

$$\boldsymbol{\nabla} \cdot \boldsymbol{u} = 0 \tag{A.4}$$

The Reynolds number is given as $\mathrm{Re} \equiv l U_c / \nu$, where ν is the kinematic viscosity of the fluid. The friction Reynolds number is defined as $\mathrm{Re}_\tau \equiv l u_\tau / \nu$, where $u_\tau \equiv \sqrt{\bar{\tau}_w / \rho}$ is the friction velocity; $\bar{\tau}_w$ is the time- and area-averaged (mean) wall shear stress.

The advection term (second term on the left-hand side) in Equation (A.1) and Equation (A.2) is written in the *nonconservation form*. It is easy to show that for incompressible flows,

$$\boldsymbol{u} \cdot \boldsymbol{\nabla} \boldsymbol{u} = \boldsymbol{\nabla} \cdot \boldsymbol{u} \boldsymbol{u} \tag{A.5}$$

In Equation (A.5), the expression on the right-hand side is said to be written in the *conservation form* — we will work with this form in our numerical scheme, i.e., we will be discretising the following momentum equation:

$$\frac{\partial \boldsymbol{u}}{\partial t} + \boldsymbol{\nabla} \cdot \boldsymbol{u} \boldsymbol{u} = -\boldsymbol{\nabla} p + \frac{1}{\mathrm{Re}} \nabla^2 \boldsymbol{u} \tag{A.6}$$

The continuity equation can be written using the three velocity components, u, v and w as:

$$\frac{\partial u}{\partial x} + \frac{\partial v}{\partial y} + \frac{\partial w}{\partial z} = 0 \tag{A.7}$$

A.2.2 Grid

We adopt a staggered grid arrangement for flow variables: velocities are calculated at cell faces and pressure at cell centre. This allows for conservation of mass and momentum in every cell/control volume. The streamwise and spanwise velocity components, u and w, respectively, are located at the vertical boundaries, each aligned in their respective directions, and the wall-normal velocity component, v, is located at the horizontal boundaries. Each of the velocity components is defined at the centre of cell faces, i.e., where the diagonals of a given rectangular face intersect, and the pressure is defined where the space diagonals of a cell (cuboid) intersect. We also define control volumes for pressure (p) and the three velocity components (u, v, w) such that a control volume for a quantity α contains the quantity α at the centre of the control volume (cell centre). For example, a control volume for p has p located at the centre and u-, v-, w-velocity components located at its boundaries. A control volume for the u-velocity component has its centre located at the middle of the vertical boundary of the p control volume and a control volume for the v-velocity component has its centre located at the middle of the horizontal boundary of the p control volume. Similarly, one can imagine the formation of a w control volume. In addition to these control volumes, an additional row of ghost cells is provided outside the domain to facilitate the implementation of no-slip and periodic boundary conditions. Two-dimensional representation of control volumes for p, u, v and w is depicted in Figure A.3. The nodes of the four flow quantities are identified in the following way: p-nodes by indices (i, j, k), u-nodes by indices $(i + 1/2, j, k)$, v-nodes by indices $(i, j + 1/2, k)$ and w-nodes by indices $(i, j, k + 1/2)$. In the code, the grids are shifted and each component is referenced by a positive integer. The advective and diffusive terms of the Navier–Stokes equations are stored at the corresponding velocity nodes. A cartoon of the computational domain, which includes the physical domain and ghost cells, is illustrated In Figure A.2. The z dimension is omitted for a better representation. The boundaries of the channel are depicted as thick black lines. Pressure nodes are located at the centre of the cell whereas velocity nodes are located at the centre of cell faces. The

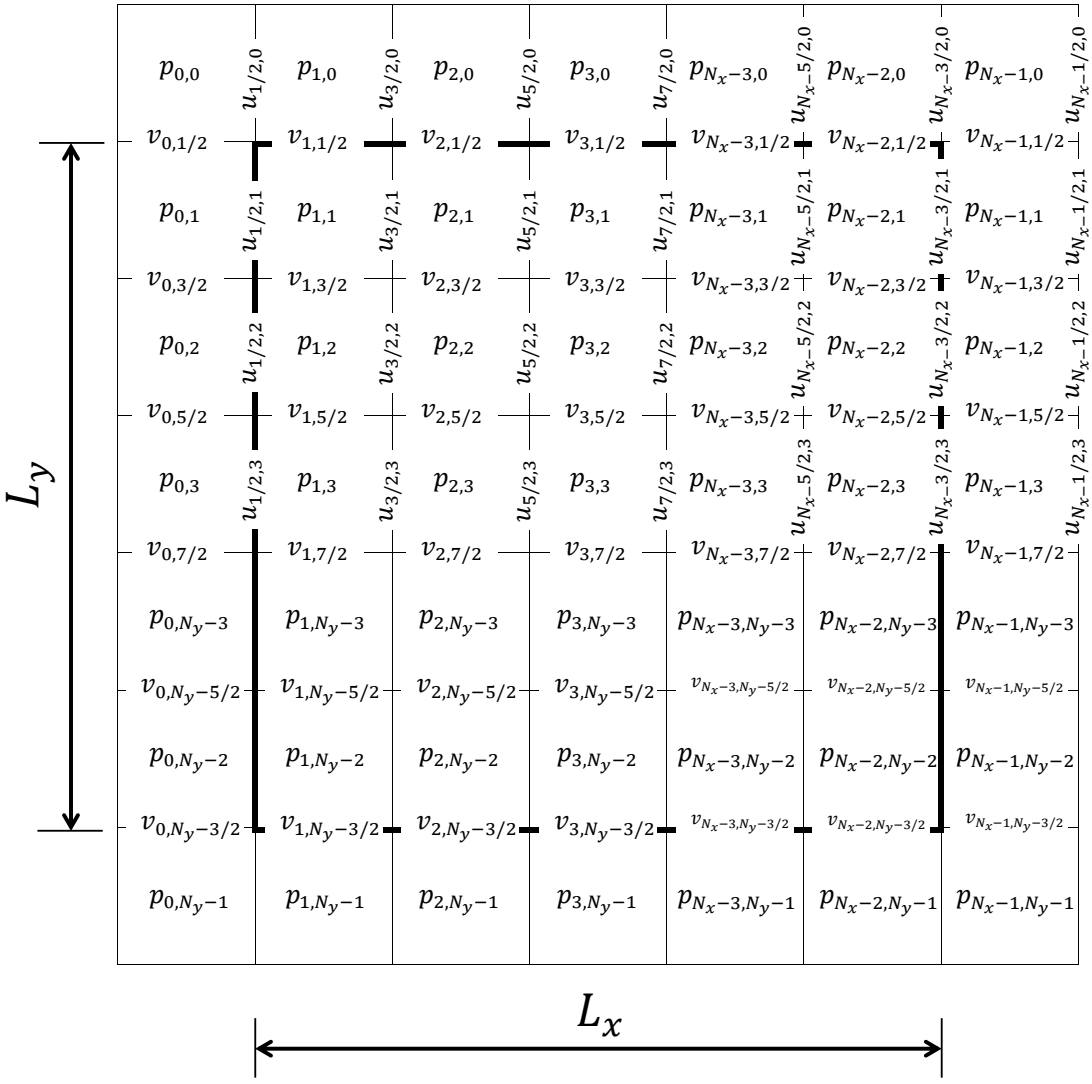

Figure A.2: The staggered grid arrangement used for flow variables. Pressure nodes are located at the centre of the cell whereas velocity nodes are located at the centre of cell faces. Only the x and y dimensions are shown for clarity — the z dimension is into the plane of the sheet. The boundaries of the channel are represented by thick black lines: the thick black horizontal lines near the top and bottom represent the top ($y = l$) and bottom ($y = -l$) walls, respectively, and the thick black vertical lines at the left and the right represent the channel inlet ($x = 0$) and outlet ($x = L_x$), respectively. Cells lying outside the thick black lines are ghost cells. Some u velocity nodes in the bottom half of the channel have not been labelled to avoid overcrowding. The indices (i, j, k) start at $(0, 0, 0)$; k is not shown here though.

thick horizontal line near the top represents the top wall, $y = l$, whereas the thick horizontal line near the bottom represents the bottom wall, $y = -l$. Similarly, thick vertical lines near the left and the right represent channel inlet ($x = 0$) and outlet ($x = L_x$), respectively. Although not shown, one can imagine the existence of two more vertical planes at $z = 0$ and $z = L_z$, and the corresponding ghost cells.

As mentioned earlier, L_x, L_y and L_z are the box dimensions in the streamwise, wall-normal and spanwise directions, respectively. L_y is always twice the channel half-height, l, i.e., $L_y = 2l$. The periodic dimensions, L_x and L_z, are specified in *outer* units, i.e., in real-number multiples of l. The spatial resolution of the numerical discretisation in the three directions is given by positive integers N_x, N_y and N_z — they are the number of grid points in the physical space in the three dimensions. In the y direction, only $N_y - 1$ points are in the physical domain, thus in order to have v-nodes at channel centre, it is advisable to have an *even* N_y. The numerical grid spacings in streamwise (x) and spanwise (z) directions are uniform while a nonuniform Chebyshev spacing is used in the wall-normal (y) direction. In the x direction, the first grid point is located at $x = 0$ and the last one is located at $x = L_x + \Delta x$, where Δx is the uniform grid spacing in the x direction. The last but one grid point corresponds to $x = L_x$. Similarly, in the z direction, the first and last grid points are located at $z = 0$ and $z = L_z + \Delta z$, respectively, where Δz is the uniform grid spacing in the z direction. Not considering the nodes that are repeated due to periodicity in the streamwise and spanwise directions, we can write the uniform streamwise and spanwise grid spacings as:

$$\Delta x = \frac{L_x}{N_x - 2} \tag{A.8}$$

$$\Delta z = \frac{L_z}{N_z - 2} \tag{A.9}$$

Thus, the computational domain in the x dimension spans from 0 to $\left(\frac{N_x-1}{N_x-2}\right) L_x$, with grid points at regular intervals of width Δx. Same is applicable to the computational domain in the z direction. This can be represented mathematically as:

$$x_{i+1/2} = (i + 1/2)\,\Delta x \qquad i = 0, 1, 2, \ldots, (N_x - 1) \tag{A.10}$$

$$z_{k+1/2} = (k + 1/2)\,\Delta z \qquad k = 0, 1, 2, \ldots, (N_z - 1) \tag{A.11}$$

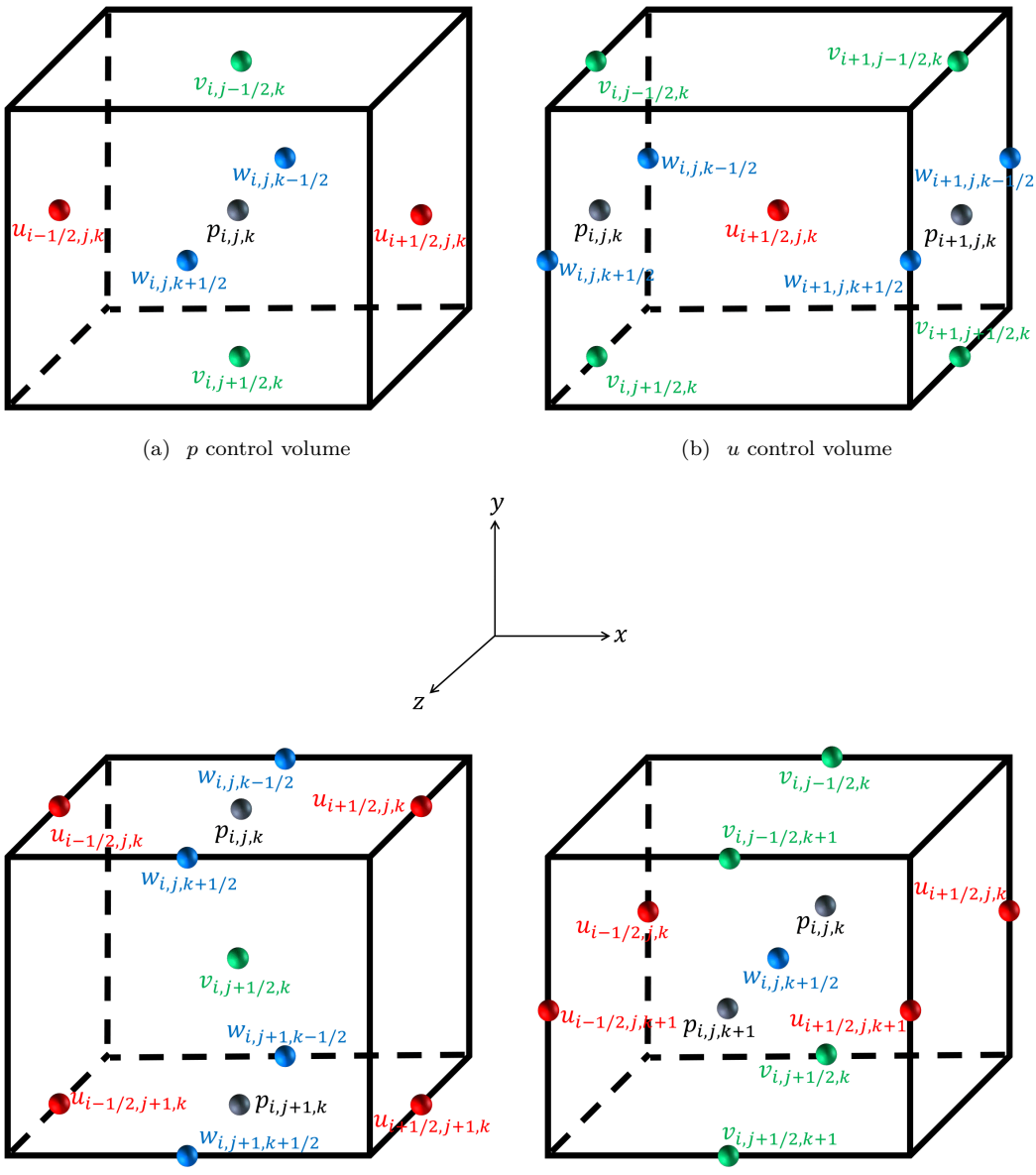

(a) p control volume

(b) u control volume

(d) v control volume

(e) w control volume

Figure A.3: Placement of pressure and velocity nodes in a staggered-grid arrangement. The control volume (a) shows pressure location at the cell centre of the control volume while velocities are located at the cell faces. Control volumes for each velocity component are shifted by half a cell in the corresponding direction as shown in (b), (c), and (d).

The Chebyshev nodes in the wall-normal direction span from $y = -1$ (bottom wall) to $y = 1$ (top wall), with the channel-centre at $y = 0$. These nodes are given by:

$$y_{j+1/2} = \cos\left(\frac{\{j + 1/2\}\,\pi}{N_y - 2}\right) \qquad j = 0, 1, 2, \ldots, (N_y - 1) \tag{A.12}$$

Note again that the point $y = \cos\left(\frac{N_y-1}{N_y-2}\right)\pi$ lies outside of the channel (and hence computational domain).

Since pressure is stored at cell centres denoted by indices (i, j, k), and velocities at cell faces (half a grid spacing from the pressure point), we can define grid spacing at the pressure points as:

$$\Delta x_i = x_{i+1/2} - x_{i-1/2} \tag{A.13}$$

$$\Delta y_j = y_{j+1/2} - y_{j-1/2} \tag{A.14}$$

$$\Delta z_k = z_{k+1/2} - z_{k-1/2} \tag{A.15}$$

and at the velocity points as:

$$\Delta x_{i+1/2} = x_{i+1} - x_i \tag{A.16}$$

$$\Delta y_{j+1/2} = y_{j+1} - y_j \tag{A.17}$$

$$\Delta z_{k+1/2} = z_{k+1} - z_k \tag{A.18}$$

Clearly, $\Delta x_i = \Delta x_{i+1/2}$ and $\Delta z_k = \Delta z_{k+1/2}$ due to uniform grid spacing in the x and z directions whereas due to nonuniform Chebyshev discretisation in the y direction, $\Delta y_j \neq \Delta y_{j+1/2}$. Notations for grid spacing at pressure and velocity points will come handy while discretising advective and diffusive terms.

Finally, we define linear interpolation factors that are used to determine velocities at locations where they are not defined. They are given as:

$$\alpha_i = \frac{x_{i+1/2} - x_{i-1/2}}{x_{i+3/2} - x_{i-1/2}} \qquad i = 1, 2, 3, \ldots, (N_x - 3) \tag{A.19}$$

$$\beta_j = \frac{y_{j+1/2} - y_{j-1/2}}{y_{j+3/2} - y_{j-1/2}} \qquad j = 1, 2, 3, \ldots, (N_y - 3) \tag{A.20}$$

$$\gamma_k = \frac{z_{k+1/2} - z_{k-1/2}}{z_{k+3/2} - z_{k-1/2}} \qquad k = 1, 2, 3, \ldots, (N_z - 3) \tag{A.21}$$

Interpolation factors at the edges of the domain are all assigned a constant value of 0.5, i.e., $\alpha_0 = \alpha_{N_x-2} = \beta_0 = \beta_{N_y-2} = \gamma_0 = \gamma_{N_z-2} = 0.5$. It should also be noted that due to uniform grid spacing in the streamwise and spanwise directions, we have $\alpha_i = \gamma_k = 0.5$ for all possible values of i and k.

A.2.3 Boundary conditions

Implementation of desired boundary conditions is pretty straightforward on a staggered mesh. Refer to Figure A.2. Both the tangential velocities, u and w are not stored at the rigid boundaries (channel walls), but we do have them specified at half a grid spacing inside the flow. In particular, we know the values of $u_{i+1/2,1,k}$, $u_{i+1/2,N_y-2,k}$, $w_{i,1,k+1/2}$ and $w_{i,N_y-2,k+1/2}$. We can use them in combination with the velocities at the walls, u_{wall} and w_{wall} to specify the velocity at the face-centre of ghost cells outside the boundary. Assuming that the velocity at the wall is given by a linear interpolation between the ghost velocity and the velocity just inside the domain, we can write, for the streamwise velocity component at the top wall:

$$u_{wall} = \beta_1 u_{i+1/2,0,k} + \beta_0 u_{i+1/2,1,k} \tag{A.22}$$

Here, the first term on the right-hand side is the ghost velocity and the second term is the velocity just inside the domain. For the no-slip boundary condition to hold, u_{wall} must be zero. This gives us:

$$u_{i+1/2,0,k} = -\frac{\beta_0}{\beta_1} u_{i+1/2,1,k} \tag{A.23}$$

Similarly, boundary conditions can be written for u at the bottom wall and for the spanwise velocity component, w, at both the walls:

$$u_{i+1/2,N_y-1,k} = -\frac{\beta_{N_y-1}}{\beta_{N_y-2}} u_{i+1/2,N_y-2,k} \tag{A.24}$$

$$w_{i,0,k+1/2} = -\frac{\beta_0}{\beta_1} w_{i,1,k+1/2} \tag{A.25}$$

$$w_{i,N_y-1,k+1/2} = -\frac{\beta_{N_y-1}}{\beta_{N_y-2}} w_{i,N_y-2,k+1/2} \tag{A.26}$$

The wall-normal velocity, v, is specified at the walls. Thus, the boundary conditions for v at the walls are straightforward:

$$v_{i,1/2,k} = 0 \tag{A.27}$$

$$v_{i,N_y-3/2,k} = 0 \tag{A.28}$$

The inlet and outlet boundary conditions for all the three velocity components are dictated by the fact that the system is periodic in streamwise and spanwise directions. The periodic boundary conditions are implemented as follows:

$$u_{1/2,j,k} = u_{N_x-3/2,j,k} \tag{A.29}$$

$$u_{N_x-1/2,j,k} = u_{3/2,j,k} \tag{A.30}$$

$$u_{i+1/2,j,0} = u_{i+1/2,j,N_z-2} \tag{A.31}$$

$$u_{i+1/2,j,N_z-1} = u_{i+1/2,j,1} \tag{A.32}$$

$$v_{0,j+1/2,k} = v_{N_x-2,j+1/2,k} \tag{A.33}$$

$$v_{N_x-1,j+1/2,k} = v_{1,j+1/2,k} \tag{A.34}$$

$$v_{i,j+1/2,0} = v_{i,j+1/2,N_z-2} \tag{A.35}$$

$$v_{i,j+1/2,N_z-1} = v_{i,j+1/2,1} \tag{A.36}$$

$$w_{0,j,k+1/2} = w_{N_x-2,j,k+1/2} \tag{A.37}$$

$$w_{N_x-1,j,k+1/2} = w_{1,j,k+1/2} \tag{A.38}$$

$$w_{i,j,1/2} = w_{i,j,N_z-3/2} \tag{A.39}$$

$$w_{i,j,N_z-1/2} = w_{i,j,3/2} \tag{A.40}$$

On a staggered mesh, pressure does not require any special treatment at boundaries as it is stored at the cell centre. Simply using incompressibility yields correct boundary conditions for pressure.

A.3 Flow solver

We introduce simplified notations for the advective and diffusive terms in the momentum equation (Equation (A.6)) and decompose the pressure field into the base and perturbation components:

$$\boldsymbol{A} \equiv \boldsymbol{\nabla} \cdot \boldsymbol{u}\boldsymbol{u} \tag{A.41}$$

$$\boldsymbol{D} \equiv \frac{1}{\mathrm{Re}} \nabla^2 \boldsymbol{u} \tag{A.42}$$

$$\boldsymbol{\nabla} p = \Pi_x \boldsymbol{e}_x + \Pi_y \boldsymbol{e}_y + \Pi_z \boldsymbol{e}_z + \boldsymbol{\nabla} p^\dagger \tag{A.43}$$

Here, $\boldsymbol{A}$ is the advection term, $\boldsymbol{D}$ is the diffusive term, Π_x, Π_y and Π_z are the instantaneous mean pressure gradients in the streamwise, wall-normal and spanwise directions, respectively, and $p^\dagger$ indicates the perturbation component of pressure. $\boldsymbol{e}_x$, $\boldsymbol{e}_y$ and $\boldsymbol{e}_z$ are the unit vectors in the streamwise, wall-normal and spanwise directions, respectively. Note that for an incompressible flow in a channel with periodic boundary conditions in the spanwise direction, $\Pi_y = \Pi_z = 0$ at all times; the streamwise component, $\Pi_x \neq 0$, is balanced by the shear stress experienced at the channel walls. Hence, the simplified pressure decomposition equation looks like:

$$\boldsymbol{\nabla} p = \Pi_x \boldsymbol{e}_x + \boldsymbol{\nabla} p^\dagger \tag{A.44}$$

The momentum equation can now be written as:

$$\frac{\partial \boldsymbol{u}}{\partial t} = -\boldsymbol{A} - \boldsymbol{\nabla} p^\dagger + \boldsymbol{D} + \Pi_x \boldsymbol{e}_x \tag{A.45}$$

with continuity (Equation (A.4)) being the constraint.

A.3.1 Time integration

A fractional-step (projection) method is used to integrate the Navier–Stokes equations in time. We split the momentum equation (Equation (A.45)) and compute an intermediate velocity field, which is not divergence-free, without considering the pressure perturbations, and then project the intermediate velocity on to a divergence-free field and determine the pressure. The projection method

is used in combination with a second-order Adams–Bashforth and Crank–Nicolson methods for advective and diffusive terms, respectively. The intermediate velocity field, $\hat{\boldsymbol{u}}$, is determined by solving the implicit system:

$$\frac{\hat{\boldsymbol{u}} - \boldsymbol{u}^n}{\Delta t} = -\left(\frac{3}{2}\boldsymbol{A}^n - \frac{1}{2}\boldsymbol{A}^{n-1}\right) + \frac{1}{2}\left(\hat{\boldsymbol{D}} + \boldsymbol{D}^n\right) - \Pi_x^n \boldsymbol{e}_x \tag{A.46}$$

Here, n and $n-1$ indicate the current time and the previous time, respectively, and Δt indicates the numerical time step. Velocity at the next time, $n+1$, can be determined as:

$$\frac{\boldsymbol{u}^{n+1} - \hat{\boldsymbol{u}}}{\Delta t} = -\boldsymbol{\nabla}\left(p^\dagger\right)^{n+1} \tag{A.47}$$

The intermediate velocity, $\hat{\boldsymbol{u}}$, does not satisfy continuity but the updated velocity, $\boldsymbol{u}^{n+1}$, does, i.e., $\boldsymbol{\nabla} \cdot \boldsymbol{u}^{n+1} = 0$. This information can be used to determine pressure prior to solving Equation (A.47) — taking divergence of both the sides of Equation (A.47) gives us:

$$\nabla^2\left(p^\dagger\right)^{n+1} = \frac{\boldsymbol{\nabla} \cdot \hat{\boldsymbol{u}}}{\Delta t} \tag{A.48}$$

Equation (A.48) is the Poisson equation for pressure.

A.3.2 Spatial discretisation

We use the finite-volume approach to discretise the momentum equations. In this approach, a small control volume V is chosen where the conservation principles for mass and momentum are applied.

The continuity equation becomes:

$$\frac{u^{n+1}_{i+1/2,j,k} - u^{n+1}_{i-1/2,j,k}}{x_{i+1/2} - x_{i-1/2}} + \frac{v^{n+1}_{i,j+1/2,k} - v^{n+1}_{i,j-1/2,k}}{y_{j+1/2} - y_{j-1/2}} + \frac{w^{n+1}_{i,j,k+1/2} - w^{n+1}_{i,j,k-1/2}}{z_{k+1/2} - z_{k-1/2}} = 0 \tag{A.49}$$

The three components of the intermediate velocity $\hat{\boldsymbol{u}}$ can be determined by solving the following

equations:

$$\hat{u}_{i+1/2,j,k} = u^n_{i+1/2,j,k} + \Delta t \left\{ -\left(\frac{3}{2} \left(A_x\right)^n_{i+1/2,j,k} - \frac{1}{2} \left(A_x\right)^{n-1}_{i+1/2,j,k} \right) + \frac{1}{2} \left(\left(\hat{D}_x \right)_{i+1/2,j,k} + \left(D_x\right)^n_{i+1/2,j,k} \right) - \Pi^n_x \right\} \tag{A.50}$$

$$\hat{v}_{i,j+1/2,k} = v^n_{i,j+1/2,k} + \Delta t \left\{ -\left(\frac{3}{2} \left(A_y\right)^n_{i,j+1/2,k} - \frac{1}{2} \left(A_y\right)^{n-1}_{i,j+1/2,k} \right) + \frac{1}{2} \left(\left(\hat{D}_y \right)_{i,j+1/2,k} + \left(D_y\right)^n_{i,j+1/2,k} \right) - \Pi^n_y \right\} \tag{A.51}$$

$$\hat{w}_{i,j,k+1/2} = w^n_{i,j,k+1/2} + \Delta t \left\{ -\left(\frac{3}{2} \left(A_z\right)^n_{i,j,k+1/2} - \frac{1}{2} \left(A_z\right)^{n-1}_{i,j,k+1/2} \right) + \frac{1}{2} \left(\left(\hat{D}_z \right)_{i,j,k+1/2} + \left(D_z\right)^n_{i,j,k+1/2} \right) - \Pi^n_z \right\} \tag{A.52}$$

Note that for our system, there is no net flow in the wall-normal and spanwise directions, therefore the pressure gradients in these directions vanish, i.e., $\Pi_y = \Pi_z = 0$, and the pressure gradient in the streamwise direction, Π_x, can be calculated by integrating the x-momentum equation over the control volume V:

$$\Pi_x = \frac{1}{V} \int_V \frac{\partial p}{\partial x} \mathrm{d}V \tag{A.53}$$

$$= \frac{1}{V} \int_V \frac{1}{\mathrm{Re}} \nabla^2 u \mathrm{d}V \tag{A.54}$$

The velocity at the next time, $\boldsymbol{u}^{n+1}$, step can be determined as follows:

$$u^{n+1}_{i+1/2,j,k} = \hat{u}_{i+1/2,j,k} - \Delta t \left\{ \frac{\left(p^\dagger\right)^{n+1}_{i+1,j,k} - \left(p^\dagger\right)^{n+1}_{i,j,k}}{x_{i+1/2} - x_{i-1/2}} \right\} \tag{A.55}$$

$$v^{n+1}_{i,j+1/2,k} = \hat{v}_{i,j+1/2,k} - \Delta t \left\{ \frac{\left(p^\dagger\right)^{n+1}_{i,j+1,k} - \left(p^\dagger\right)^{n+1}_{i,j,k}}{y_{j+1/2} - y_{j-1/2}} \right\} \tag{A.56}$$

$$w^{n+1}_{i,j,k+1/2} = \hat{w}_{i,j,k+1/2} - \Delta t \left\{ \frac{\left(p^\dagger\right)^{n+1}_{i,j,k+1} - \left(p^\dagger\right)^{n+1}_{i,j,k}}{z_{k+1/2} - z_{k-1/2}} \right\} \tag{A.57}$$

A.3.3 Discretisation of the advective term

The advective terms, $\boldsymbol{A} = (A_x\ A_y\ A_z)^{\mathrm{T}}$, at a cell face is approximated by their value at the centre of the face:

$$\begin{aligned}
(A_x)_{i+1/2,j,k} &= \frac{1}{\Delta x_{i+1/2}}\left[(uu)_{i+1,j,k} - (uu)_{i,j,k}\right] \\
&+ \frac{1}{\Delta y_j}\left[(vu)_{i+1/2,j+1/2,k} - (vu)_{i+1/2,j-1/2,k}\right] \\
&+ \frac{1}{\Delta z_k}\left[(wu)_{i+1/2,j,k+1/2} - (wu)_{i+1/2,j,k-1/2}\right] \qquad \text{(A.58)} \\
(A_y)_{i,j+1/2,k} &= \frac{1}{\Delta x_i}\left[(uv)_{i+1/2,j+1/2,k} - (uv)_{i-1/2,j+1/2,k}\right] \\
&+ \frac{1}{\Delta y_{j+1/2}}\left[(vv)_{i,j+1,k} - (vv)_{i,j,k}\right] \\
&+ \frac{1}{\Delta z_k}\left[(wv)_{i,j+1/2,k+1/2} - (wv)_{i,j+1/2,k-1/2}\right] \qquad \text{(A.59)} \\
(A_z)_{i,j,k+1/2} &= \frac{1}{\Delta x_i}\left[(uw)_{i+1/2,j,k+1/2} - (uw)_{i-1/2,j,k+1/2}\right] \\
&+ \frac{1}{\Delta y_j}\left[(vw)_{i,j+1/2,k+1/2} - (vw)_{i,j-1/2,k+1/2}\right] \\
&+ \frac{1}{\Delta z_{k+1/2}}\left[(ww)_{i,j,k+1} - (ww)_{i,j,k}\right] \qquad \text{(A.60)}
\end{aligned}$$

Spatial derivatives are approximated using second-order centred differencing. At low Reynolds numbers, central schemes for convection are stabilised by viscosity [Versteeg and Malalasekera, 2007]. Velocities at locations where they are not defined, for example, u velocity at the boundary of the u-velocity control volume, are determined using linear interpolation, i.e.,

$$u_{i+1,j,k} = \alpha_{i+1/2} u_{i+3/2,j,k} + \left\{1 - \alpha_{i+1/2}\right\} u_{i+1/2,j,k} \qquad \text{(A.61)}$$

Similarly, v and w velocities can be determined at locations where they are not defined. Now, the advective terms using these interpolated values can be written as:

$$(A_x)_{i+1/2,j,k} = \left(\frac{1}{x_{i+1} - x_i}\right)\left[\left(\frac{u_{i+3/2,j,k} + u_{i+1/2,j,k}}{2}\right)^2 - \left(\frac{u_{i+1/2,j,k} + u_{i-1/2,j,k}}{2}\right)^2\right]$$

$$
\begin{aligned}
&+\left(\frac{1}{y_{j+1/2}-y_{j-1/2}}\right)\left[\left(\frac{v_{i+1,j+1/2,k}+v_{i,j+1/2,k}}{2}\right)\left(\beta_j u_{i+1/2,j+1,k}+\{1-\beta_j\}\,u_{i+1/2,j,k}\right)\right.\\
&\left.-\left(\frac{v_{i+1,j-1/2,k}+v_{i,j-1/2,k}}{2}\right)\left(\beta_{j-1} u_{i+1/2,j,k}+\{1-\beta_{j-1}\}\,u_{i+1/2,j-1,k}\right)\right]\\
&+\left(\frac{1}{z_{k+1/2}-z_{k-1/2}}\right)\left[\left(\frac{w_{i+1,j,k+1/2}+w_{i,j,k+1/2}}{2}\right)\left(\gamma_k u_{i+1/2,j,k+1}+\{1-\gamma_k\}\,u_{i+1/2,j,k}\right)\right.\\
&\left.-\left(\frac{w_{i+1,j,k-1/2}+w_{i,j,k-1/2}}{2}\right)\left(\gamma_{k-1} u_{i+1/2,j,k}+\{1-\gamma_{k-1}\}\,u_{i+1/2,j,k-1}\right)\right] \qquad \text{(A.62)}\\
(A_y)_{i,j+1/2,k} &= \left(\frac{1}{x_{i+1/2}-x_{i-1/2}}\right)\left[\left(\frac{u_{i+1/2,j+1,k}+u_{i+1/2,j,k}}{2}\right)\left(\alpha_i v_{i+1,j+1/2,k}+\{1-\alpha_i\}\,v_{i,j+1/2,k}\right)\right.\\
&\left.-\left(\frac{u_{i-1/2,j+1,k}+u_{i-1/2,j,k}}{2}\right)\left(\alpha_{i-1} v_{i,j+1/2,k}+\{1-\alpha_{i-1}\}\,v_{i-1,j+1/2,k}\right)\right]\\
&+\left(\frac{1}{y_{j+1}-y_j}\right)\left[\left(\frac{v_{i,j+3/2,k}+v_{i,j+1/2,k}}{2}\right)^2-\left(\frac{v_{i,j+1/2,k}+v_{i,j-1/2,k}}{2}\right)^2\right]\\
&+\left(\frac{1}{z_{k+1/2}-z_{k-1/2}}\right)\left[\left(\frac{w_{i,j+1,k+1/2}+w_{i,j,k+1/2}}{2}\right)\left(\gamma_k v_{i,j+1/2,k+1}+\{1-\gamma_k\}\,v_{i,j+1/2,k}\right)\right.\\
&\left.-\left(\frac{w_{i,j+1,k-1/2}+w_{i,j,k-1/2}}{2}\right)\left(\gamma_{k-1} v_{i,j+1/2,k}+\{1-\gamma_{k-1}\}\,v_{i,j+1/2,k-1}\right)\right] \qquad \text{(A.63)}\\
(A_z)_{i,j,k+1/2} &= \left(\frac{1}{x_{i+1/2}-x_{i-1/2}}\right)\left[\left(\frac{u_{i+1/2,j,k+1}+u_{i+1/2,j,k}}{2}\right)\left(\alpha_i w_{i+1,j,k+1/2}+\{1-\alpha_i\}\,w_{i,j,k+1/2}\right)\right.\\
&\left.-\left(\frac{u_{i-1/2,j,k+1}+u_{i-1/2,j,k}}{2}\right)\left(\alpha_{i-1} w_{i,j,k+1/2}+\{1-\alpha_{i-1}\}\,w_{i-1,j,k+1/2}\right)\right]\\
&+\left(\frac{1}{y_{j+1/2}-y_{j-1/2}}\right)\left[\left(\frac{v_{i,j+1/2,k+1}+v_{i,j+1/2,k}}{2}\right)\left(\beta_j w_{i,j+1,k+1/2}+\{1-\beta_j\}\,w_{i,j,k+1/2}\right)\right.\\
&\left.-\left(\frac{v_{i,j-1/2,k+1}+v_{i,j-1/2,k}}{2}\right)\left(\beta_{j-1} w_{i,j,k+1/2}+\{1-\beta_{j-1}\}\,w_{i,j-1,k+1/2}\right)\right]\\
&+\left(\frac{1}{z_{k+1}-z_k}\right)\left[\left(\frac{w_{i,j,k+3/2}+w_{i,j,k+1/2}}{2}\right)^2-\left(\frac{w_{i,j,k+1/2}+w_{i,j,k-1/2}}{2}\right)^2\right] \qquad \text{(A.64)}
\end{aligned}
$$

A.3.4 Discretisation of the diffusive term

The diffusive terms, $\boldsymbol{D} = (D_x \; D_y \; D_z)^{\mathrm{T}}$, are approximated at the centre of cell faces in a similar fashion:

$$\begin{aligned}
(D_x)_{i+1/2,j,k} = {} & \frac{1}{\Delta x_{i+1/2}} \left[2 \left(\frac{\partial u}{\partial x} \right)_{i+1,j,k} - 2 \left(\frac{\partial u}{\partial x} \right)_{i,j,k} \right] \\
& + \frac{1}{\Delta y_j} \left[\left(\frac{\partial u}{\partial y} + \frac{\partial v}{\partial x} \right)_{i+1/2,j+1/2,k} - \left(\frac{\partial u}{\partial y} + \frac{\partial v}{\partial x} \right)_{i+1/2,j-1/2,k} \right] \\
& + \frac{1}{\Delta z_k} \left[\left(\frac{\partial u}{\partial z} + \frac{\partial w}{\partial x} \right)_{i+1/2,j,k+1/2} - \left(\frac{\partial u}{\partial z} + \frac{\partial w}{\partial x} \right)_{i+1/2,j,k-1/2} \right] \qquad \text{(A.65)} \\
(D_y)_{i,j+1/2,k} = {} & \frac{1}{\Delta x_i} \left[\left(\frac{\partial v}{\partial x} + \frac{\partial u}{\partial y} \right)_{i+1/2,j+1/2,k} - \left(\frac{\partial v}{\partial x} + \frac{\partial u}{\partial y} \right)_{i-1/2,j+1/2,k} \right] \\
& + \frac{1}{\Delta y_{j+1/2}} \left[2 \left(\frac{\partial v}{\partial y} \right)_{i,j+1,k} - 2 \left(\frac{\partial v}{\partial y} \right)_{i,j,k} \right] \\
& + \frac{1}{\Delta z_k} \left[\left(\frac{\partial v}{\partial z} + \frac{\partial w}{\partial y} \right)_{i,j+1/2,k+1/2} - \left(\frac{\partial v}{\partial z} + \frac{\partial w}{\partial y} \right)_{i,j+1/2,k-1/2} \right] \qquad \text{(A.66)} \\
(D_z)_{i,j,k+1/2} = {} & \frac{1}{\Delta x_i} \left[\left(\frac{\partial w}{\partial x} + \frac{\partial u}{\partial z} \right)_{i+1/2,j,k+1/2} - \left(\frac{\partial w}{\partial x} + \frac{\partial u}{\partial z} \right)_{i-1/2,j,k+1/2} \right] \\
& + \frac{1}{\Delta y_j} \left[\left(\frac{\partial w}{\partial y} + \frac{\partial v}{\partial z} \right)_{i,j+1/2,k+1/2} - \left(\frac{\partial w}{\partial y} + \frac{\partial v}{\partial z} \right)_{i,j-1/2,k+1/2} \right] \\
& + \frac{1}{\Delta z_{k+1/2}} \left[2 \left(\frac{\partial w}{\partial z} \right)_{i,j,k+1} - 2 \left(\frac{\partial w}{\partial z} \right)_{i,j,k} \right] \qquad \text{(A.67)}
\end{aligned}$$

Using the second-order central differencing scheme for calculating the derivatives, we get:

$$\begin{aligned}
(D_x)_{i+1/2,j,k} = {} & \left(\frac{1}{x_{i+1} - x_i} \right) \left[2 \left(\frac{u_{i+3/2,j,k} - u_{i+1/2,j,k}}{x_{i+3/2} - x_{i+1/2}} \right) - 2 \left(\frac{u_{i+1/2,j,k} - u_{i-1/2,j,k}}{x_{i+1/2} - x_{i-1/2}} \right) \right] \\
& + \left(\frac{1}{y_{j+1/2} - y_{j-1/2}} \right) \left[\left(\frac{u_{i+1/2,j+1,k} - u_{i+1/2,j,k}}{y_{j+1} - y_j} + \frac{v_{i+1,j+1/2,k} - v_{i,j+1/2,k}}{x_{i+1} - x_i} \right) \right. \\
& \left. - \left(\frac{u_{i+1/2,j,k} - u_{i+1/2,j-1,k}}{y_j - y_{j-1}} + \frac{v_{i+1,j-1/2,k} - v_{i,j-1/2,k}}{x_{i+1} - x_i} \right) \right] \\
& + \left(\frac{1}{z_{k+1/2} - z_{k-1/2}} \right) \left[\left(\frac{u_{i+1/2,j,k+1} - u_{i+1/2,j,k}}{z_{k+1} - z_k} + \frac{w_{i+1,j,k+1/2} - w_{i,j,k+1/2}}{x_{i+1} - x_i} \right) \right.
\end{aligned}$$

$$- \left(\frac{u_{i+1/2,j,k} - u_{i+1/2,j,k-1}}{z_k - z_{k-1}} + \frac{w_{i+1,j,k-1/2} - w_{i,j,k-1/2}}{x_{i+1} - x_i} \right) \Bigg] \tag{A.68}$$

$$\begin{aligned}
(D_y)_{i,j+1/2,k} = & \left(\frac{1}{x_{i+1/2} - x_{i-1/2}} \right) \left[\left(\frac{v_{i+1,j+1/2,k} - v_{i,j+1/2,k}}{x_{i+1} - x_i} + \frac{u_{i+1/2,j+1,k} - u_{i+1/2,j,k}}{y_{j+1} - y_j} \right) \right. \\
& \left. - \left(\frac{v_{i,j+1/2,k} - v_{i-1,j+1/2,k}}{x_i - x_{i-1}} + \frac{u_{i-1/2,j+1,k} - u_{i-1/2,j,k}}{y_{j+1} - y_j} \right) \right] \\
& + \left(\frac{1}{y_{j+1} - y_j} \right) \left[2 \left(\frac{v_{i,j+3/2,k} - v_{i,j+1/2,k}}{y_{j+3/2} - y_{j+1/2}} \right) - 2 \left(\frac{v_{i,j+1/2,k} - v_{i,j-1/2,k}}{y_{j+1/2} - y_{j-1/2}} \right) \right] \\
& + \left(\frac{1}{z_{k+1/2} - z_{k-1/2}} \right) \left[\left(\frac{v_{i,j+1/2,k+1} - v_{i,j+1/2,k}}{z_{k+1} - z_k} + \frac{w_{i,j+1,k+1/2} - w_{i,j,k+1/2}}{y_{j+1} - y_j} \right) \right. \\
& \left. - \left(\frac{v_{i,j+1/2,k} - v_{i,j+1/2,k-1}}{z_k - z_{k-1}} + \frac{w_{i,j+1,k-1/2} - w_{i,j,k-1/2}}{y_{j+1} - y_j} \right) \right]
\end{aligned} \tag{A.69}$$

$$\begin{aligned}
(D_z)_{i,j,k+1/2} = & \left(\frac{1}{x_{i+1/2} - x_{i-1/2}} \right) \left[\left(\frac{w_{i+1,j,k+1/2} - w_{i,j,k+1/2}}{x_{i+1} - x_i} + \frac{u_{i+1/2,j,k+1} - u_{i+1/2,j,k}}{z_{k+1} - z_k} \right) \right. \\
& \left. - \left(\frac{w_{i,j,k+1/2} - w_{i-1,j,k+1/2}}{x_i - x_{i-1}} + \frac{u_{i-1/2,j,k+1} - u_{i-1/2,j,k}}{z_{k+1} - z_k} \right) \right] \\
& + \left(\frac{1}{y_{j+1/2} - y_{j-1/2}} \right) \left[\left(\frac{w_{i,j+1,k+1/2} - w_{i,j,k+1/2}}{y_{j+1} - y_j} + \frac{v_{i,j+1/2,k+1} - v_{i,j+1/2,k}}{z_{k+1} - z_k} \right) \right. \\
& \left. - \left(\frac{w_{i,j,k+1/2} - w_{i,j-1,k+1/2}}{y_j - y_{j-1}} + \frac{v_{i,j-1/2,k+1} - v_{i,j-1/2,k}}{z_{k+1} - z_k} \right) \right] \\
& + \left(\frac{1}{z_{k+1} - z_k} \right) \left[2 \left(\frac{w_{i,j,k+3/2} - w_{i,j,k+1/2}}{z_{k+3/2} - z_{k+1/2}} \right) - 2 \left(\frac{w_{i,j,k+1/2} - w_{i,j,k-1/2}}{z_{k+1/2} - z_{k-1/2}} \right) \right]
\end{aligned} \tag{A.70}$$

A.3.5 Determining intermediate velocity

The intermediate velocity, $\hat{\boldsymbol{u}}$, is determined by solving Equation (A.46). Plugging in the meaning of $\boldsymbol{D}$ and adding and subtracting $\frac{1}{2\mathrm{Re}}\nabla^2 (2\boldsymbol{u}^n)$ to the right-hand side of Equation (A.46), it can be rewritten as:

$$\frac{\hat{\boldsymbol{u}} - \boldsymbol{u}^n}{\Delta t} = - \left(\frac{3}{2}\boldsymbol{A}^n - \frac{1}{2}\boldsymbol{A}^{n-1} \right) + \frac{1}{2\mathrm{Re}} \left(\nabla^2 \hat{\boldsymbol{u}} - \nabla^2 \boldsymbol{u}^n \right) + \frac{1}{\mathrm{Re}} \nabla^2 \boldsymbol{u}^n - \Pi_x^n \boldsymbol{e}_x \tag{A.71}$$

Introducing $\boldsymbol{u}_d = \hat{\boldsymbol{u}} - \boldsymbol{u}^n$, the above equation can be written as:

$$\boldsymbol{u}_d - \frac{\Delta t}{2\mathrm{Re}}\nabla^2 \boldsymbol{u}_d = \Delta t \left\{ -\left(\frac{3}{2}\boldsymbol{A}^n - \frac{1}{2}\boldsymbol{A}^{n-1}\right) + \frac{1}{\mathrm{Re}}\nabla^2 \boldsymbol{u}^n - \Pi_x^n \boldsymbol{e}_x \right\} \tag{A.72}$$

The right-hand side of Equation (A.72) is known as it depends on the current time n and the previous time $n-1$; let's call it $\boldsymbol{R}$. The equation can then simply be written as:

$$\left(1 - \frac{\Delta t}{2\mathrm{Re}}\nabla^2\right)\boldsymbol{u}_d = \boldsymbol{R} \tag{A.73}$$

or:

$$L\boldsymbol{u}_d = \boldsymbol{R} \tag{A.74}$$

where operator $L = 1 - \frac{\Delta t}{2\mathrm{Re}}\nabla^2$. Equation (A.74) is solved using the Alternating Direction Implicit (ADI) method. It is a three-step process where a one-dimensional problem is solved in each step. The method is second-order accurate in both time and space and is unconditionally stable . Neglecting the higher order terms, the operator L can be approximated as:

$$L \approx L_x L_y L_z \tag{A.75}$$

where

$$L_x = 1 - \frac{\Delta t}{2\mathrm{Re}}\frac{\partial^2}{\partial x^2} \tag{A.76}$$

$$L_y = 1 - \frac{\Delta t}{2\mathrm{Re}}\frac{\partial^2}{\partial y^2} \tag{A.77}$$

$$L_z = 1 - \frac{\Delta t}{2\mathrm{Re}}\frac{\partial^2}{\partial z^2} \tag{A.78}$$

The system that needs to be solved now becomes:

$$L_x L_y L_z \boldsymbol{u}_d = \boldsymbol{R} \tag{A.79}$$

which is solved in the following three steps:

1. Solve $L_x \boldsymbol{u}^{\ddagger} = \boldsymbol{R}$ for $\boldsymbol{u}^{\ddagger}$, where $\boldsymbol{u}^{\ddagger} = L_y L_z \boldsymbol{u}_d$.

2. Solve $L_y \boldsymbol{u}^{\dagger} = \boldsymbol{u}^{\ddagger}$ for $\boldsymbol{u}^{\dagger}$, where $\boldsymbol{u}^{\dagger} = L_z \boldsymbol{u}_d$.

3. Solve $L_z \boldsymbol{u}_d = \boldsymbol{u}^{\dagger}$ for $\boldsymbol{u}_d$.

The abovementioned steps follow the sequence C/T/C for u_d, T/C/C for v_d and C/C/T for w_d where T and C denote solving a tridiagonal and a cyclic tridiagonal system, respectively. The tridiagonal system (T) of equations is solved using the Thomas algorithm [Thomas, 1949] while to solve the cyclic tridiagonal system (C), we use the Sherman–Morrison formula [Sherman and Morrison, 1950] in combination with the Thomas algorithm.

The intermediate velocity, $\hat{\boldsymbol{u}}$, can now be calculated:

$$\hat{\boldsymbol{u}} = \boldsymbol{u}_d + \boldsymbol{u}^n \tag{A.80}$$

A.3.6 Pressure equation

Expanding the right-hand side of the pressure Poisson equation, Equation (A.48) can be written as:

$$\nabla^2 \left(p^{\dagger}\right)^{n+1} = \frac{1}{\Delta t}\left(\frac{\hat{u}_{i+1/2,j,k} - \hat{u}_{i-1/2,j,k}}{x_{i+1/2} - x_{i-1/2}} + \frac{\hat{v}_{i,j+1/2,k} - \hat{v}_{i,j-1/2,k}}{y_{j+1/2} - y_{j-1/2}} + \frac{\hat{w}_{i,j,k+1/2} - \hat{w}_{i,j,k-1/2}}{z_{k+1/2} - z_{k-1/2}}\right) \tag{A.81}$$

Discretising the left-hand side, we get the final form of the Poisson equation for pressure as the following:

$$\begin{aligned}
&\left(\frac{1}{x_{i+1/2} - x_{i-1/2}}\right)\left\{\frac{p^{\dagger}_{i+1,j,k} - p^{\dagger}_{i,j,k}}{x_{i+1} - x_i} - \frac{p^{\dagger}_{i,j,k} - p^{\dagger}_{i-1,j,k}}{x_i - x_{i-1}}\right\} \\
&\qquad + \left(\frac{1}{y_{j+1/2} - y_{j-1/2}}\right)\left\{\frac{p^{\dagger}_{i,j+1,k} - p^{\dagger}_{i,j,k}}{y_{j+1} - y_j} - \frac{p^{\dagger}_{i,j,k} - p^{\dagger}_{i,j-1,k}}{y_j - y_{j-1}}\right\} \\
&\qquad + \left(\frac{1}{z_{k+1/2} - z_{k-1/2}}\right)\left\{\frac{p^{\dagger}_{i,j,k+1} - p^{\dagger}_{i,j,k}}{z_{k+1} - z_k} - \frac{p^{\dagger}_{i,j,k} - p^{\dagger}_{i,j,k-1}}{z_k - z_{k-1}}\right\} \\
&\qquad = \frac{1}{\Delta t}\left(\frac{\hat{u}_{i+1/2,j,k} - \hat{u}_{i-1/2,j,k}}{x_{i+1/2} - x_{i-1/2}} + \frac{\hat{v}_{i,j+1/2,k} - \hat{v}_{i,j-1/2,k}}{y_{j+1/2} - y_{j-1/2}} + \frac{\hat{w}_{i,j,k+1/2} - \hat{w}_{i,j,k-1/2}}{z_{k+1/2} - z_{k-1/2}}\right)
\end{aligned} \tag{A.82}$$

Equation (A.82) is the full discretised form of Equation (A.48) and a linear system that is solved using the conjugate gradient method. Several linear system solvers are available in the `KSP` object of PETSc.

A.4 Validation of the DNS code

We conduct a few tests to validate our finite-volume DNS code: (1) test the spatial discretisation of the code, and (2) compare the results of laminar and turbulent flows obtained from our code with either analytical results or results from other popular DNS codes, e.g., ChannelFlow [Gibson, 2009], as well as with experiments. Each of the abovementioned tests is described in the following paragraphs.

A.4.1 Validating the spatial discretisation

As already mentioned in Appendix A.2.1, the mean flow in the channel (or the streamwise direction) is aligned with the x axis and the spanwise direction is aligned with the z axis. Since the boundary conditions in both streamwise and spanwise directions are the same, the solution to the Navier–Stokes equations should remain unchanged if keeping everything else the same, the fluid is made to flow along the z axis, i.e., the mean pressure gradient is applied along the z axis. In other words, DNS results should remain unchanged if the z axis corresponds to the streamwise direction and the x axis corresponds to the spanwise direction. This is what we are testing in our code, and if the results for both the DNS runs come out to be the same, it would mean that the spatial discretisation in the x and z directions is the same. Its correctness and accuracy are discussed in further tests.

The results of the spatial discretisation validation test are presented in Figure A.4. We consider two cases for a plane Poiseuille flow in a minimal channel maintained at a constant mass flux: Case

Case	Re (Re_τ)	L_x/l (L_x^+)	L_z/l (L_z^+)	$N_x \times N_y \times N_z$	Δx^+	Δz^+	$\Delta y^+_{min}, \Delta y^+_{max}$
1	2000 (91)	2π (571.77)	π (285.88)	$81 \times 166 \times 71$	7.24	4.14	0.02, 1.74
2	2000 (91)	π (285.88)	2π (571.77)	$71 \times 166 \times 81$	4.14	7.24	0.02, 1.74

Table A.1: Simulation parameters used for validating the spatial discretisation of the finite-volume code.

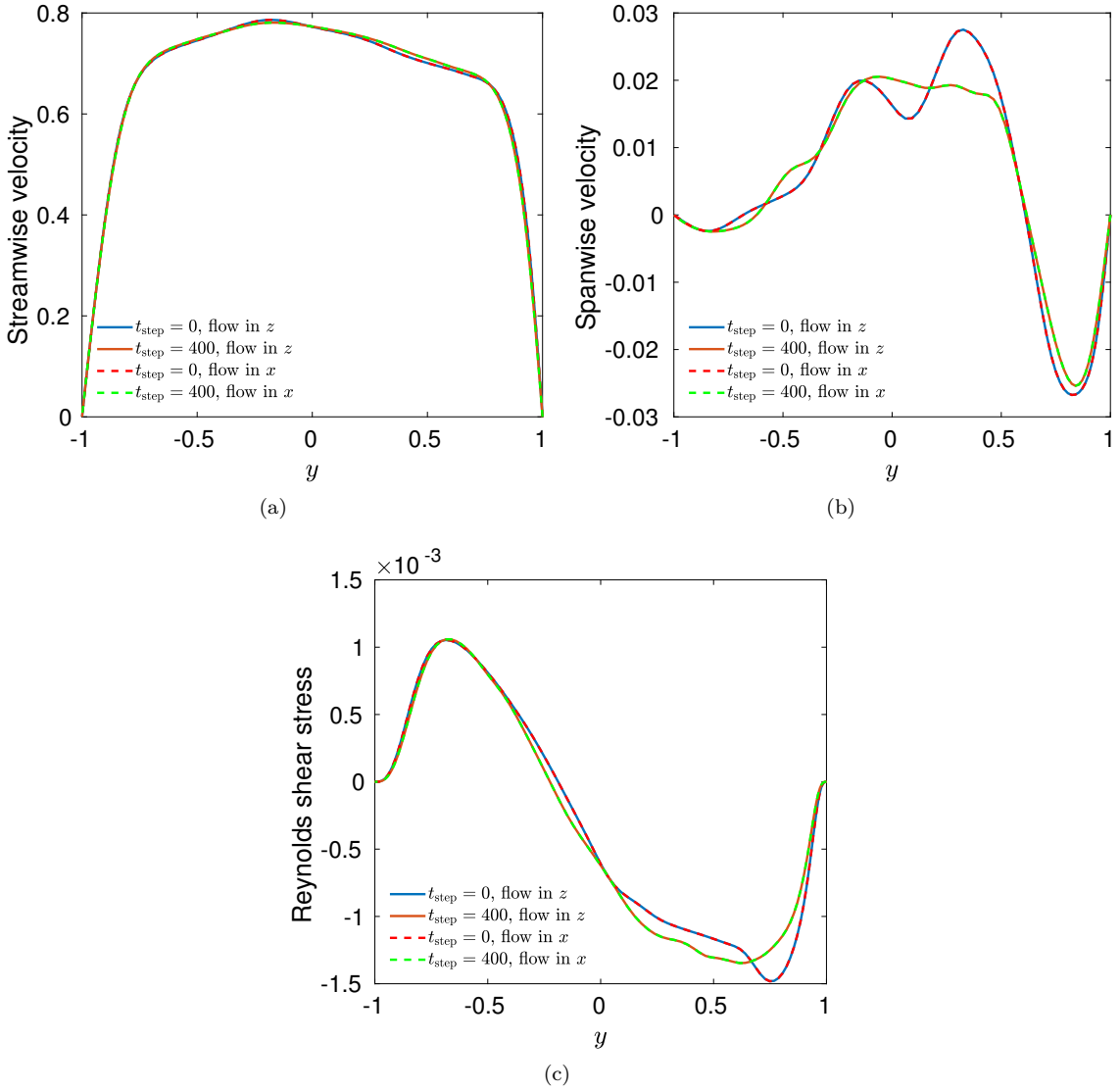

Figure A.4: Instantaneous profiles for (a) streamwise velocity, (b) spanwise velocity, and (c) Reynolds shear stress at 0^{th} and 400^{th} time step for flows in x and z directions.

1 when the flow is in x direction, and Case 2 when the flow is in z direction. Case 2 is nothing but Case 1 rotated by an angle of 90 degrees about the y axis. For both the cases, the bulk velocity is maintained at $U_{bulk} = 2/3$. The simulation parameters for the two cases are presented in Table A.1. Runs for both cases 1 and 2 (flow along x and z, respectively) are started with the same initial condition. The momentum equations need not be time integrated for a very long duration since

the goal here is not to validate the accuracy of the code but to make sure that if we start from the same initial flow field and maintain a given mass flux, we get *exactly* same results irrespective of the direction of application of the pressure gradient. The equations were marched forward 500 time steps and results for flow along x and z were compared at arbitrarily chosen times. In Figure A.4, we are showing instantaneous profiles for three flow properties, streamwise velocity, spanwise velocity, and Reynolds shear stress, at 0^{th} and 400^{th} time step for both the cases. It is observed that at both the time instants, a flow property when the flow is along the x axis matches exactly with itself when the flow is along the z axis. We did the comparisons at other time instants as well (not shown to avoid overcrowding), and each comparison resulted in a perfect match. Hence, it is concluded that the spatial discretisation used in the code is consistent along both the x and z axes.

A.4.2 Laminar flow in a channel

We start a simulation with a laminar, parabolic velocity profile in the domain as the initial condition, and see if the laminar profile is maintained. If our numerical scheme can maintain the laminar velocity profile in the channel, it is a good indication that the implementation of the Navier–Stokes solver is correct. All velocities are nondimensionalised with the laminar centreline velocity, U_c, and all lengths are nondimensionalised with the half-height of the channel, l. The three velocity components, streamwise (u), wall-normal (v) and spanwise (w), for a laminar flow are then given as:

$$u\,(y) = 1 - y^2 \tag{A.83}$$

$$v = 0 \tag{A.84}$$

$$w = 0 \tag{A.85}$$

The plane $y = 0$ corresponds to the centre of the channel. The top and bottom walls lie at $y = 1$ and $y = -1$, respectively. The flow is maintained by a constant pressure gradient in the streamwise (x) direction, $\mathrm{d}P/\mathrm{d}x = -2/\mathrm{Re}$, where Re is the Reynolds number as defined in Appendix A.2.1, and the bulk velocity is maintained at $U_{bulk} = 2/3$. Pressure gradients in the wall-normal and spanwise directions are zero, i.e., $\mathrm{d}P/\mathrm{d}y = \mathrm{d}P/\mathrm{d}z = 0$ since there is no net flow in the y and z directions. For a laminar flow, the wall shear rate in the streamwise direction, which is also the drag, is always 2.

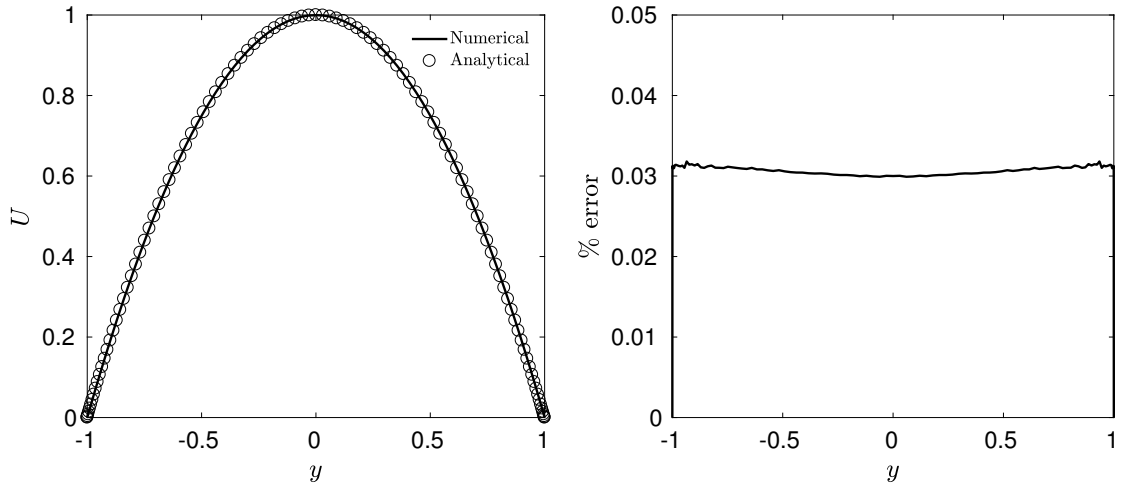

(a) (b)

Figure A.5: (a) Comparison of steady-state velocity profile obtained numerically from the finite-volume code with the analytical solution $u\left(y\right) = 1 - y^2$. (b) Percent error between the numerical and analytical solutions.

Hence, the friction Reynolds number, Re_τ, for a laminar flow at $\mathrm{Re} = 1800$ turns out to be $\mathrm{Re}_\tau = 60$. Other simulation parameters for this validation test are presented in Table A.2:

We initialise the streamwise velocity with a laminar, parabolic profile as described by Equation (A.83). The velocity at the centre of the channel is 1. The wall-normal and spanwise components are set to zero everywhere (Equations (A.84) and (A.85)). The momentum equations are integrated in time until a steady state is reached. The numerical result is then compared with the analytical solution.

Figure A.5(a) shows a comparison between the steady-state solution obtained by integrating the momentum equations and the analytical solution. Streamwise velocity profiles across the channel are plotted and it can be observed that there is an excellent agreement between the numerical and analytical solutions — both the profiles nearly collapse on each other. In Figure A.5(b), we have shown the percent error, i.e., $\left|\left(U_n - U_a\right)/U_a\right| \times 100\%$, where U_n is the numerical solution and U_a is

$\mathrm{Re}\ (\mathrm{Re}_\tau)$	$L_x/l\ (L_x^+)$	$L_z/l\ (L_z^+)$	$N_x \times N_y \times N_z$	Δx^+	Δz^+	$\Delta y^+_{min}, \Delta y^+_{max}$
1800 (60)	π (188.50)	$\pi/2$ (94.25)	$51 \times 106 \times 41$	3.85	2.42	0.03, 1.81

Table A.2: Simulation parameters used for validating a laminar flow in a plane channel.

the analytical solution. Overall, the error across the channel height is extremely small and is less than 0.035%.

A.4.3 Turbulent flow in a channel

Channel flow Newtonian turbulence results from the finite-volume code are compared with Gibson's ChannelFlow [Gibson, 2009] at similar Reynolds numbers for validation. Gibson's code is a popular Navier–Stokes simulator; it is used by many researchers worldwide and has been validated extensively. We compare wall shear stresses, mean velocity profiles, Reynolds shear stresses, velocity fluctuations obtained from the finite-volume code with those obtained from ChannelFlow. Parameters used in the simulation for the current validation test are very similar to those used in Appendix A.4.2, except that the friction Reynolds number in this case would be higher due to turbulence. A complete list of the parameters used in this validation test is given in Table A.3.

Turbulence statistics are presented in 'inner' units, after normalisation with length or velocity scales in the viscosity-dominated region very close to the wall. The friction Reynolds number, as defined in Appendix A.2.1, is given as $\mathrm{Re}_\tau \equiv l u_\tau/\nu$, where $u_\tau \equiv \sqrt{\bar{\tau}_w/\rho}$ is the friction velocity; $\bar{\tau}_w$ is the time- and area-averaged (mean) wall shear stress, ν and ρ are the kinematic viscosity and density of the fluid, respectively. The viscous length scale or 'wall unit' is given as $\delta_\nu \equiv \nu/u_\tau$. Most of the turbulence statistics presented below are a function of distance from the wall. Quantities enclosed within angular brackets, e.g., $\langle u \rangle$, are area averaged quantities, and quantities with an overbar, e.g., $\bar{\tau}_w$ above, represent area and time averaged quantities. In the case of velocities, we will represent the area and time averaged value of a velocity component by the corresponding capital letter, e.g., $\bar{u}$ is represented as U. An apostrophe is used to define fluctuations of a quantity, deviations from the mean, e.g., $u' = u - \langle u \rangle$ or $u' = u - U$ as the case may be. Unless or otherwise stated, a fluctuation would mean deviation from the area and time averaged quantity.

In Figure A.6, we show the probability density functions of wall shear stress fluctuations from

Case	Re (Re_τ)	L_x/l (L_x^+)	L_z/l (L_z^+)	$N_x \times N_y \times N_z$	Δx^+	Δz^+	$\Delta y^+_{min}, \Delta y^+_{max}$
1	1800 (85)	π (267.04)	$\pi/2$ (133.52)	$51 \times 106 \times 41$	5.45	3.42	0.04, 2.57
2	1800 (85)	π (267.04)	$\pi/2$ (133.52)	$71 \times 156 \times 61$	3.87	2.26	0.02, 1.73

Table A.3: Simulation parameters used for validating a turbulent flow in a plane channel.

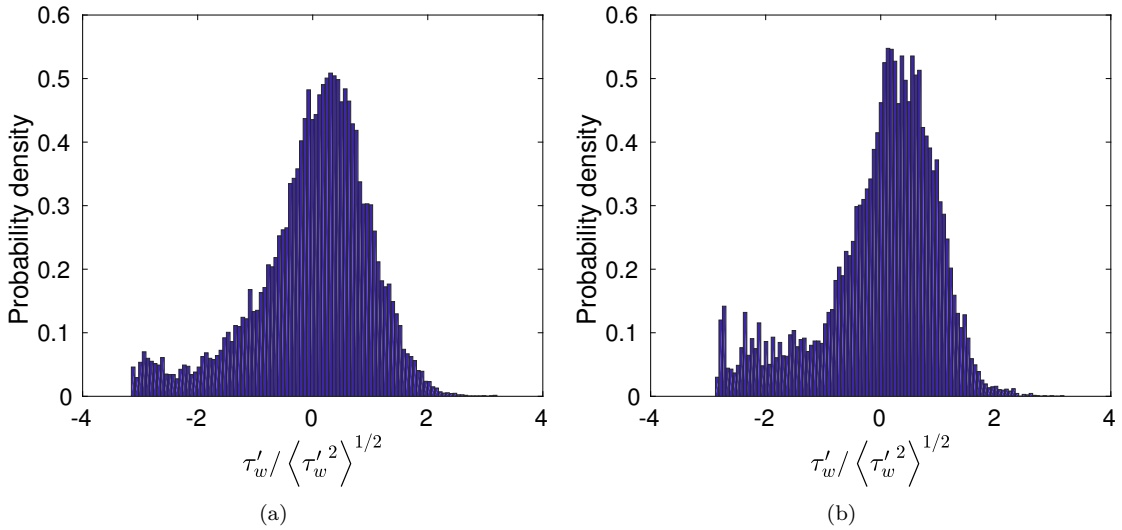

Figure A.6: Probability density functions of wall shear stress fluctuations in minimal channel Newtonian turbulence calculated using (a) ChannelFlow, and (b) our finite-volume code. The $\left\langle \tau_w'^{\,2} \right\rangle^{1/2}$ in the denominator of the x-axis label indicates the root-mean-squared value of the wall shear stress fluctuations.

our code and from ChannelFlow. These were obtained from a very long time series of area averaged wall shear stress in the minimal channel. The mean of these fluctuations is zero. Not only do the two probability density functions are in a very nice agreement but they also very similar to those reported by Xi and Graham [2012b] for Newtonian flows at a constant pressure drop in minimal channels — they are nearly symmetric with respect to the mean value, except for a shoulder on the left side. The existence of this shoulder is attributed to the presence of a low-drag attractor in the state space. Park and Graham [2015] have shown that Newtonian turbulence trajectories in a minimal channel that spend most of the time near a high-drag attractor, make close visits near this low-drag attractor, thus imparting an intermittent nature to turbulence.

Figures A.7(a)–A.7(b) show the mean velocity profiles from both finite-volume code and ChannelFlow at $\mathrm{Re} = 1800$ ($\mathrm{Re}_\tau = 85$), one using a linear scale and the other using a semi-log scale. For flows at low Reynolds numbers (near transition), the mean velocity profile lies slightly above the Prandtl-von Kármán log-law [Patel and Head, 1969; Kasagi and Shikazono, 1995; Tsukahara et al., 2005]. Velocity profiles from the two codes show a very good correspondence — they almost collapse on each other near the wall whereas away from the wall, very minute discrepancy can be noticed.

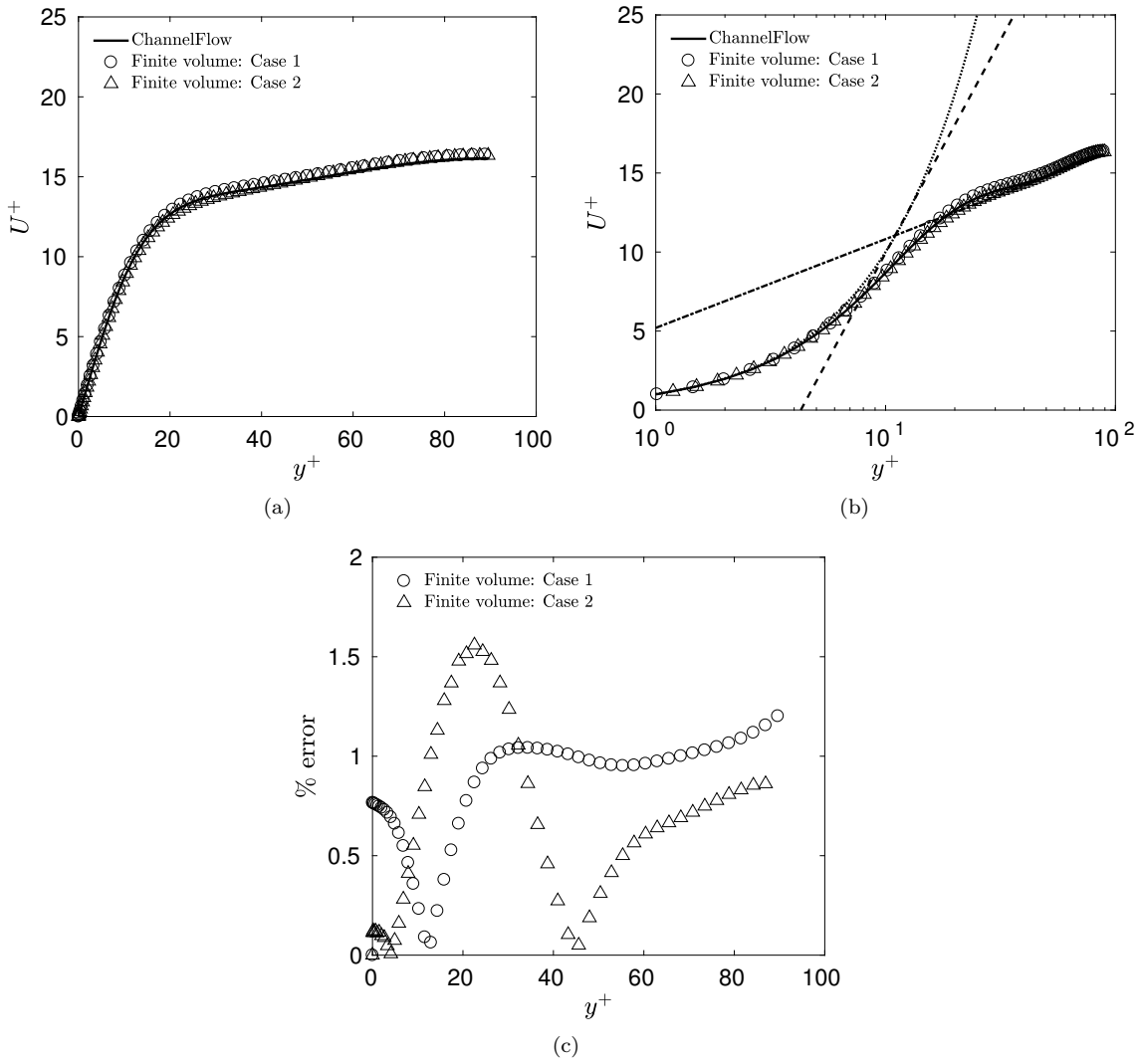

Figure A.7: Mean velocity profiles in minimal channel Newtonian turbulence at $\mathrm{Re}_\tau = 85$ calculated using ChannelFlow and our finite-volume code plotted using (a) a linear scale, and (b) a semi-log scale. In (b), the black dotted line is the viscous sublayer, $U^+ = y^+$; black dashed-dotted line is the Prandtl-von Kármán log-law, $U^+ = 2.44 \ln y^+ + 5.2$ and the black dashed line is the Virk MDR log-law, $U^+ = 11.7 \ln y^+ - 17.0$. (c) Percent error between the mean velocity profiles obtained from ChannelFlow and finite volume codes.

Percent error between velocity profiles from the two codes is plotted in Figure A.7(c). The error across the half-channel is very small and the maximum percent error is approximately 1.5%. The reason for the occurrence of discrepancy between ChannelFlow results and finite volume results is explained in the following paragraph.

Reynolds shear stress from both the codes at $\mathrm{Re} = 1800$ ($\mathrm{Re}_\tau = 85$) are presented in Figure A.8(a)

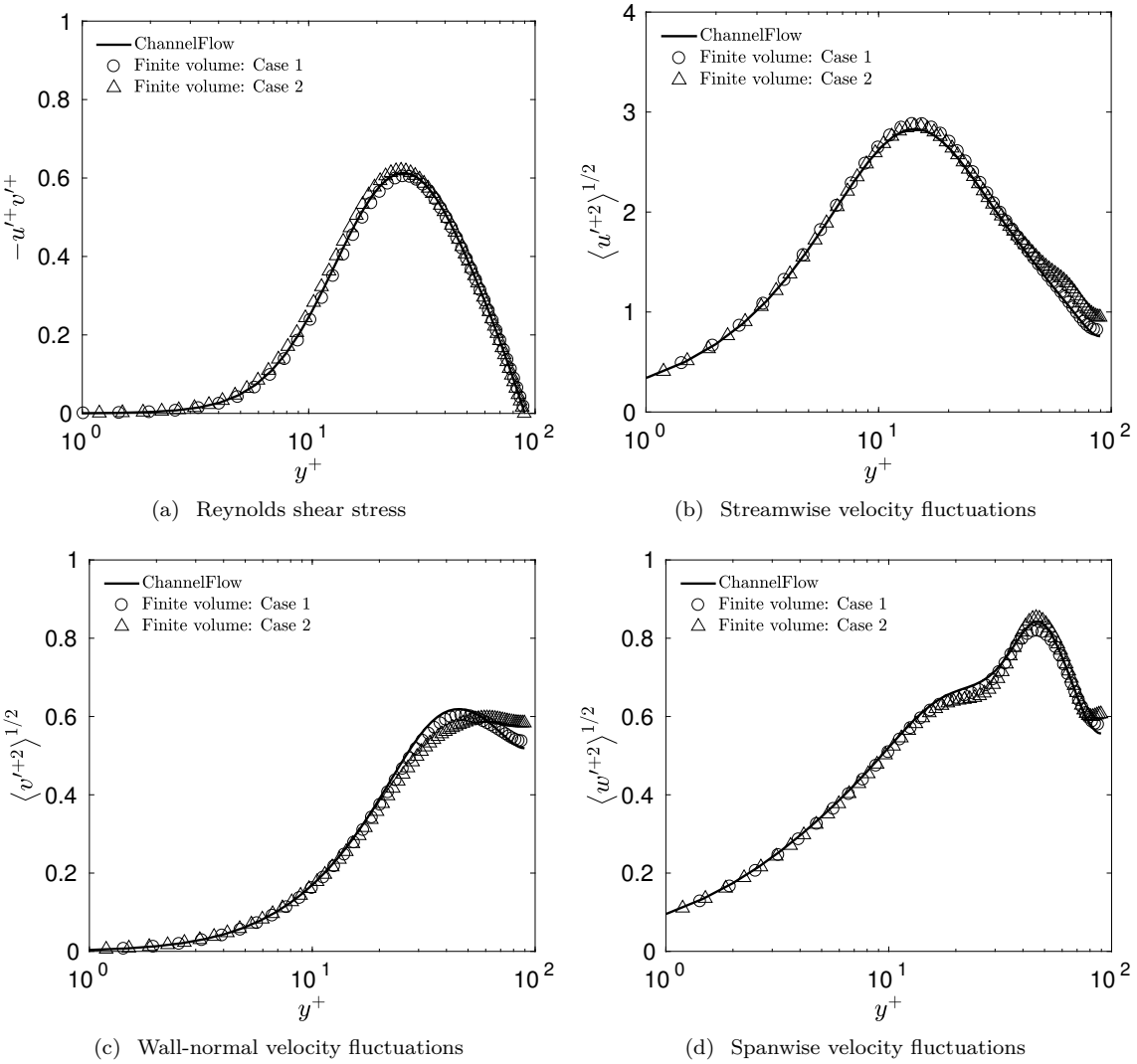

(a) Reynolds shear stress

(b) Streamwise velocity fluctuations

(c) Wall-normal velocity fluctuations

(d) Spanwise velocity fluctuations

Figure A.8: Reynolds shear stress and root-mean-squared velocity fluctuations for all the three components in minimal channel Newtonian turbulence at $\mathrm{Re}_\tau = 85$ calculated using ChannelFlow and our finite-volume code.

and root-mean-squared fluctuations of the three velocity components are plotted in Figures A.8(b)–A.8(d). A commendable correspondence can be seen between ChannelFlow results and results from our finite-volume code. All the quantities match very well near the wall whereas some discrepancy occurs near the centre of the channel. This discrepancy is due to different orders of time integration in the two codes. In ChannelFlow, the whole equation system is advanced in time with a third-order semi-implicit Adams–Bashforth scheme whereas in the finite volume code, the time advancement is

second order. Hence, large structures near the centre of the channel take the longest to evolve in time and average out. This was verified by running a simulation with smaller time step. In any case, it is worth mentioning that we are interested in the flow dynamics near the wall, more so when discussing flow manipulation by wall actuation, and in the near-wall region, the statistics are converged.

Bibliography

Abdulbari, H. A., Mahammed, H. D., and Hassan, Z. B. Y. (2015). Bio-Inspired Passive Drag Reduction Techniques: A Review. *ChemBioEng Rev.*, 2(3):185–203.

Abdulbari, H. A., Yunus, R. M., Abdurahman, N. H., and Charles, A. (2013). Going against the flow—A review of non-additive means of drag reduction. *J. Ind. Eng. Chem.*, 19(1):27–36.

Abubakar, A., Al-Wahaibi, T., Al-Wahaibi, Y., Al-Hashmi, A., and Al-Ajmi, A. (2014). Roles of drag reducing polymers in single- and multi-phase flows. *Chem. Eng. Res. Des.*, 92(11):2153–2181.

Akhavan, R., Jung, W. J., and Mangiavacchi, N. (1993). Turbulence control in wall-bounded flows by spanwise oscillations. *Appl. Sci. Res.*, 51(1):299–303.

Alfonsi, G. (2011). On Direct Numerical Simulation of Turbulent Flows. *Appl. Mech. Rev.*, 64(2):020802.

Auteri, F., Baron, A., Belan, M., Campanardi, G., and Quadrio, M. (2010). Experimental assessment of drag reduction by traveling waves in a turbulent pipe flow. *Phys. Fluids*, 22(11):115103.

Avila, K., Moxey, D., de Lozar, A., Avila, M., Barkley, D., and Hof, B. (2011). The onset of turbulence in pipe flow. *Science*, 333(6039):192–196.

Avila, M. and Hof, B. (2013). Nature of laminar-turbulence intermittency in shear flows. *Phys. Rev. E*, 87(6):063012.

Avila, M., Mellibovsky, F., Roland, N., and Hof, B. (2013). Streamwise-localized solutions at the onset of turbulence in pipe flow. *Phys. Rev. Lett.*, 110(22):224502.

Avila, M., Willis, A. P., and Hof, B. (2010). On the transient nature of localized pipe flow turbulence. *J. Fluid Mech.*, 646:127–136.

Bai, H. L., Zhou, Y., Zhang, W. G., Xu, S. J., Wang, Y., and Antonia, R. A. (2014). Active control of a turbulent boundary layer based on local surface perturbation. *J. Fluid Mech.*, 750:316–354.

Balay, S., Gropp, W. D., McInnes, L. C., and Smith, B. F. (2011). PETSc Users Manual. Technical Report ANL-95/11–Revision 3.2, Argonne National Laboratory.

Baltzer, J. R., Adrian, R. J., and Wu, X. (2013). Structural organization of large and very large scales in turbulent pipe flow simulation. *J. Fluid Mech.*, 720:236–279.

Bandyopadhyay, P. R. (2006). Stokes Mechanism of Drag Reduction. *J. Appl. Mech.*, 73(3):483–489.

Barkley, D. (2011). Simplifying the complexity of pipe flow. *Phys. Rev. E*, 84(1):016309.

Barkley, D., Song, B., Mukund, V., Lemoult, G., Avila, M., and Hof, B. (2015). The rise of fully turbulent flow. *Nature*, 526(7574):550–553.

Barkley, D. and Tuckerman, L. S. (2005). Computational study of turbulent laminar patterns in Couette flow. *Phys. Rev. Lett.*, 94(1):014502.

Baron, A. and Quadrio, M. (1996). Turbulent drag reduction by spanwise wall oscillations. *Appl. Sci. Res.*, 55(4):311–326.

Belson, B. A., Semeraro, O., Rowley, C. W., and Henningson, D. S. (2013). Feedback control of instabilities in the two-dimensional Blasius boundary layer: The role of sensors and actuators. *Phys. Fluids*, 25(5):054106.

Berger, T. W., Kim, J., Lee, C., and Lim, J. (2000). Turbulent boundary layer control utilizing the Lorentz force. *Phys. Fluids*, 12(3):631.

Bewley, T. R., Moin, P., and Temam, R. (2001). DNS-based predictive control of turbulence: an optimal benchmark for feedback algorithms. *J. Fluid Mech.*, 447:179–225.

Bird, R. B., Stewart, W. E., and Lightfoot, E. N. (2007). *Transport Phenomena*. John Wiley & Sons, Inc., 2nd edition.

Blackburn, H. M., Hall, P., and Sherwin, S. J. (2013). Lower branch equilibria in Couette flow: the emergence of canonical states for arbitrary shear flows. *J. Fluid Mech.*, 726:R2.

Boomsma, A. and Sotiropoulos, F. (2016). Direct numerical simulation of sharkskin denticles in turbulent channel flow. *Phys. Fluids*, 28(3):035106.

Brand, E. and Gibson, J. F. (2014). A doubly localized equilibrium solution of plane Couette flow. *J. Fluid Mech.*, 750:R3.

Breuer, K. S., Haritonidis, J. H., and Landahl, M. T. (1989). The control of transient disturbances in a flat plate boundary layer through active wall motion. *Phys. Fluids A Fluid Dyn.*, 1(3):574.

Breuer, K. S., Park, J., and Henoch, C. (2004). Actuation and control of a turbulent channel flow using Lorentz forces. *Phys. Fluids*, 16(4):897.

Burger, E. D., Munk, W. R., and Wahl, H. A. (1982). Flow Increase in the Trans Alaska Pipeline Through Use of a Polymeric Drag-Reducing Additive. *J. Pet. Technol.*, 34(02):377–386.

Busse, A. and Sandham, N. D. (2012). Influence of an anisotropic slip-length boundary condition on turbulent channel flow. *Phys. Fluids*, 24(5):055111.

Carlson, D. R., Widnall, S. E., and Peeters, M. F. (1982). A flow-visualization study of transition in plane Poiseuille flow. *J. Fluid Mech.*, 121:487–505.

Carlson, H. A., Berkooz, G., and Lumley, J. L. (1995). Direct Numerical Simulation of Flow in a Channel with Complex, Time-Dependent Wall Geometries: A Pseudospectral Method. *J. Comput. Phys.*, 121(1):155–175.

Carlson, H. A. and Lumley, J. L. (1996). Active control in the turbulent wall layer of a minimal flow unit. *J. Fluid Mech.*, 329:341–371.

Cattafesta, L. N. and Sheplak, M. (2011). Actuators for Active Flow Control. *Annu. Rev. Fluid Mech.*, 43(1):247–272.

Chang, P.-H., Liao, C.-C., Hsu, H.-W., Liu, S.-H., and Lin, C.-A. (2014). Simulations of laminar and turbulent flows over periodic hills with immersed boundary method. *Comput. Fluids*, 92:233–243.

Chantry, M., Willis, A. P., and Kerswell, R. R. (2014). Genesis of streamwise-localized solutions from globally periodic traveling waves in pipe flow. *Phys. Rev. Lett.*, 112(16):164501.

Choi, H., Moin, P., and Kim, J. (1993). Direct numerical simulation of turbulent flow over riblets. *J. Fluid Mech.*, 255:503–539.

Choi, H., Moin, P., and Kim, J. (1994). Active turbulence control for drag reduction in wall-bounded flows. *J. Fluid Mech.*, 262:75–110.

Choi, J.-I. and Sung, H. J. (2002). Assessment of suboptimal control for drag reduction in turbulent channel flow. *J. Turbul.*, 3:N29.

Choi, J.-I., Xu, C.-X., and Sung, H. J. (2001). Turbulent drag reduction by spanwise wall oscillations. In *Proc. 14th Australas. Fluid Mech. Conf.*, volume 1, pages 187–190, Adelaide, Australia. Australasian Fluid Mechanics Society.

Choi, J.-I., Xu, C.-X., and Sung, H. J. (2002). Drag Reduction by Spanwise Wall Oscillation in Wall-Bounded Turbulent Flows. *AIAA J.*, 40(5):842–850.

Choi, K.-S. (1989). Near-wall structure of a turbulent boundary layer with riblets. *J. Fluid Mech.*, 208:417–458.

Choi, K.-S. (2002). Near-wall structure of turbulent boundary layer with spanwise-wall oscillation. *Phys. Fluids*, 14(7):2530.

Choi, K.-S., Debisschop, J.-R., and Clayton, B. R. (1998). Turbulent Boundary-Layer Control by Means of Spanwise-Wall Oscillation. *AIAA J.*, 36(7):1157–1163.

Choi, K.-S., Jukes, T., and Whalley, R. D. (2011). Turbulent boundary-layer control with plasma actuators. *Philos. Trans. R. Soc. London A Math. Phys. Eng. Sci.*, 369(1940):1443–1458.

Chung, Y. M. and Talha, T. (2011). Effectiveness of active flow control for turbulent skin friction drag reduction. *Phys. Fluids*, 23(2):025102.

Clever, R. M. and Busse, F. H. (1997). Tertiary and quaternary solutions for plane Couette flow. *J. Fluid Mech.*, 344:137–153.

Dadfar, R., Fabbiane, N., Bagheri, S., and Henningson, D. S. (2014). Centralised versus decentralised active control of boundary layer instabilities. *Flow, Turbul. Combust.*, 93(4):537–553.

Deguchi, K., Hall, P., and Walton, A. (2013). The emergence of localized vortex–wave interaction states in plane Couette flow. *J. Fluid Mech.*, 721:58–85.

del Álamo, J. C., Jiménez, J., Zandonade, P., and Moser, R. D. (2006). Self-similar vortex clusters in the turbulent logarithmic region. *J. Fluid Mech.*, 561:329–358.

Deng, B., Xu, C., Huang, W., and Cui, G. (2013). Effect of active control on optimal structures in wall turbulence. *Sci. China Physics, Mech. Astron.*, 56(2):290–297.

Deng, B.-Q., Xu, C.-X., Huang, W.-X., and Cui, G.-X. (2014). Strengthened opposition control for skin-friction reduction in wall-bounded turbulent flows. *J. Turbul.*, 15(2):122–143.

Deng, J., Shao, X.-M., and Ren, A.-L. (2006). A new modification of the immersed-boundary method for simulating flows with complex moving boundaries. *Int. J. Numer. Methods Fluids*, 52:1195–1213.

Dennis, D. J. C. and Nickels, T. B. (2011). Experimental measurement of large-scale three-dimensional structures in a turbulent boundary layer. Part 2. Long structures. *J. Fluid Mech.*, 673:218–244.

Dhanak, M. R. and Si, C. (1999). On reduction of turbulent wall friction through spanwise wall oscillations. *J. Fluid Mech.*, 383:175–195.

Du, Y., Symeonidis, V., and Karniadakis, G. E. (2002). Drag reduction in wall-bounded turbulence via a transverse travelling wave. *J. Fluid Mech.*, 457:1–34.

Dubief, Y., White, C. M., Shaqfeh, E. S. G., and Terrapon, V. E. (2010). Polymer maximum drag reduction: A unique transitional state. *Cent. Turbul. Res. Annu. Res. Briefs*, pages 47–56.

Duguet, Y., Pringle, C. C. T., and Kerswell, R. R. (2008). Relative periodic orbits in transitional pipe flow. *Phys. Fluids*, 20(11):114102.

Duguet, Y. and Schlatter, P. (2013). Oblique Laminar-Turbulent Interfaces in Plane Shear Flows. *Phys. Rev. Lett.*, 110(3):034502.

Duque-Daza, C. A., Baig, M. F., Lockerby, D. A., Chernyshenko, S. I., and Davies, C. (2012). Modelling turbulent skin-friction control using linearized Navier–Stokes equations. *J. Fluid Mech.*, 702:403–414.

Eckhardt, B., Schneider, T. M., Hof, B., and Westerweel, J. (2007). Turbulence transition in pipe flow. *Annu. Rev. Fluid Mech.*, 39(1):447–468.

Emmons, H. W. (1951). The Laminar-Turbulent Transition in a Boundary Layer-Part I. *J. Aeronaut. Sci.*, 18(7):490–498.

Endo, T. and Kasagi, N. (2001). Active control of wall turbulence with wall deformation. *JSME Int. J. Ser. B*, 44(2):195–203.

Endo, T., Kasagi, N., and Suzuki, Y. (2000). Feedback control of wall turbulence with wall deformation. *Int. J. Heat Fluid Flow*, 21(5):568–575.

Fadlun, E. A., Verzicco, R., Orlandi, P., and Mohd-Yusof, J. (2000). Combined Immersed-Boundary Finite-Difference Methods for Three-Dimensional Complex Flow Simulations. *J. Comput. Phys.*, 161(1):35–60.

Faisst, H. and Eckhardt, B. (2003). Traveling waves in pipe flow. *Phys. Rev. Lett.*, 91(22):224502.

Fink, J. K. (2012). *Petroleum Engineer's Guide to Oil Field Chemicals and Fluids*. Gulf Professional Publishing, Boston.

Flores, O. and Jiménez, J. (2010). Hierarchy of minimal flow units in the logarithmic layer. *Phys. Fluids*, 22(7):071704.

Fuaad, P. A., Baig, M. F., and Khan, B. A. (2016). Turbulent drag reduction using active control of buoyancy forces. *Int. J. Heat Fluid Flow*, 61(B):585–598.

Fukagata, K. and Kasagi, N. (2004). Suboptimal control for drag reduction via suppression of near-wall Reynolds shear stress. *Int. J. Heat Fluid Flow*, 25(3):341–350.

Fukagata, K., Sugiyama, K., and Kasagi, N. (2009). On the lower bound of net driving power in controlled duct flows. *Phys. D Nonlinear Phenom.*, 238(13):1082–1086.

Gad-El-Hak, M., Blackwelder, R. F., and Riley, J. J. (1984). On the interaction of compliant coatings with boundary-layer flows. *J. Fluid Mech.*, 140:257–280.

García-Mayoral, R. and Jiménez, J. (2011a). Drag reduction by riblets. *Philos. Trans. R. Soc. London A Math. Phys. Eng. Sci.*, 369(1940):1412–1427.

García-Mayoral, R. and Jiménez, J. (2011b). Hydrodynamic stability and breakdown of the viscous regime over riblets. *J. Fluid Mech.*, 678:317–347.

Gatti, D. and Quadrio, M. (2013). Performance losses of drag-reducing spanwise forcing at moderate values of the Reynolds number. *Phys. Fluids*, 25(12):125109.

Ge, M., Tian, D., and Yongqian, L. (2017). Dynamic evolution process of turbulent channel flow after opposition control. *Fluid Dyn. Res.*, 49(1):015505.

Ge, M., Xu, C., and Cui, G.-X. (2015). Active control of turbulence for drag reduction based on the detection of near-wall streamwise vortices by wall information. *Acta Mech. Sin.*, 31(4):512–522.

Gibson, J. F. (2009). Channelflow: A spectral Navier–Stokes simulator in C++. Technical report, University of New Hampshire.

Gibson, J. F., Halcrow, J., and Cvitanović, P. (2008). Visualizing the geometry of state space in plane Couette flow. *J. Fluid Mech.*, 611:107–130.

Gibson, J. F., Halcrow, J., and Cvitanović, P. (2009). Equilibrium and travelling-wave solutions of plane Couette flow. *J. Fluid Mech.*, 638:243–266.

Goldstein, D., Handler, R., and Sirovich, L. (1993). Modeling a No-Slip Flow Boundary with an External Force Field. *J. Comput. Phys.*, 105(2):354–366.

Goldstein, D., Handler, R., and Sirovich, L. (1995). Direct numerical simulation of turbulent flow over a modeled riblet covered surface. *J. Fluid Mech.*, 302:333–376.

Gómez, F., Blackburn, H. M., Rudman, M., Sharma, A. S., and McKeon, B. J. (2016). Streamwise-varying steady transpiration control in turbulent pipe flow. *J. Fluid Mech.*, 796:588–616.

Graham, M. D. (2014). Drag reduction and the dynamics of turbulence in simple and complex fluids. *Phys. Fluids*, 26(10):101301.

Graham, M. D. (2015). Fluid dynamics: Turbulence spreads like wildfire. *Nature*, 526(7574):508–509.

Gronskis, A. and Artana, G. (2016). A simple and efficient direct forcing immersed boundary method combined with a high order compact scheme for simulating flows with moving rigid boundaries. *Comput. Fluids*, 124:86–104.

Große, S. and Schröder, W. (2009a). Two-Dimensional Visualization of Turbulent Wall Shear Stress Using Micropillars. *AIAA J.*, 47(2):314–321.

Große, S. and Schröder, W. (2009b). Wall-shear stress patterns of coherent structures in turbulent duct flow. *J. Fluid Mech.*, 633:147–158.

Guy, R. D. and Hartenstine, D. A. (2010). On the accuracy of direct forcing immersed boundary methods with projection methods. *J. Comput. Phys.*, 229(7):2479–2496.

Halcrow, J., Gibson, J. F., Cvitanović, P., and Viswanath, D. (2009). Heteroclinic connections in plane Couette flow. *J. Fluid Mech.*, 621:365–376.

Hammond, E. P., Bewley, T. R., and Moin, P. (1998). Observed mechanisms for turbulence attenuation and enhancement in opposition-controlled wall-bounded flows. *Phys. Fluids*, 10(9):2421.

Hanson, R. E., Bade, K. M., Belson, B. A., Lavoie, P., Naguib, A. M., and Rowley, C. W. (2014). Feedback control of slowly-varying transient growth by an array of plasma actuators. *Phys. Fluids*, 26(2):024102.

Hasegawa, Y., Frohnapfel, B., and Kasagi, N. (2011). Effects of spatially varying slip length on friction drag reduction in wall turbulence. *J. Phys. Conf. Ser.*, 318(2):022028.

Hashimoto, S., Hasobe, A., Tsukahara, T., Kawaguchi, Y., and Kawamura, H. (2009). An experimental study on turbulent-stripe structure in transitional channel flow. In *Proc. Sixth Int. Symp. Turbul. Heat Mass Transf.*, pages 193–196, Rome, Italy. Begell House Inc.

Ho, C.-M. and Tai, Y.-C. (1998). Micro-electro-mechanical-systems (MEMS) and fluid flows. *Annu. Rev. Fluid Mech.*, 30(1):579–612.

Hœpffner, J. and Fukagata, K. (2009). Pumping or drag reduction? *J. Fluid Mech.*, 635:171–187.

Hof, B. and Budanur, N. B. (2017). Searching for Order in Turbulent Flow. *Physics (College. Park. Md).*, 10(25):25.

Hof, B., van Doorne, C. W. H., Westerweel, J., Nieuwstadt, F. T. M., Faisst, H., Eckhardt, B., Wedin, H., Kerswell, R. R., and Waleffe, F. (2004). Experimental observation of nonlinear traveling waves in turbulent pipe flow. *Science*, 305(5690):1594–1598.

Högberg, M., Bewley, T. R., and Henningson, D. S. (2003a). Linear feedback control and estimation of transition in plane channel flow. *J. Fluid Mech.*, 481:149–175.

Högberg, M., Bewley, T. R., and Henningson, D. S. (2003b). Relaminarization of Re_τ=100 turbulence using gain scheduling and linear state-feedback control. *Phys. Fluids*, 15(11):3572–3575.

Huang, L., Fan, B., and Dong, G. (2010). Turbulent drag reduction via a transverse wave traveling along streamwise direction induced by Lorentz force. *Phys. Fluids*, 22(1):015103.

Huang, L., Fan, B., and Mei, D. (2012). Mechanism of drag reduction by spanwise oscillating Lorentz force in turbulent channel flow. *Theor. Appl. Mech. Lett.*, 2(1):012005.

Huang, W.-X. and Sung, H. J. (2007). Improvement of mass source/sink for an immersed boundary method. *Int. J. Numer. Methods Fluids*, 53(11):1659–1671.

Hutchins, N. and Marusic, I. (2007). Large-scale influences in near-wall turbulence. *Philos. Trans. A. Math. Phys. Eng. Sci.*, 365(1852):647–64.

Hutchins, N., Monty, J. P., Ganapathisubramani, B., Ng, H. C. H., and Marusic, I. (2011). Three-dimensional conditional structure of a high-Reynolds-number turbulent boundary layer. *J. Fluid Mech.*, 673:255–285.

Hwang, Y., Willis, A. P., and Cossu, C. (2016). Invariant solutions of minimal large-scale structures in turbulent channel flow for Reτ up to 1000. *J. Fluid Mech.*, 802:R1.

Iaccarino, G. and Verzicco, R. (2003). Immersed boundary technique for turbulent flow simulations. *Appl. Mech. Rev.*, 56(3):331.

Ikeno, T. and Kajishima, T. (2007). Finite-difference immersed boundary method consistent with wall conditions for incompressible turbulent flow simulations. *J. Comput. Phys.*, 226(2):1485–1508.

Itano, T. and Generalis, S. C. (2009). Hairpin vortex solution in planar Couette flow: A tapestry of knotted vortices. *Phys. Rev. Lett.*, 102(11):114501.

Itano, T. and Toh, S. (2001). The dynamics of bursting process in wall turbulence. *J. Phys. Soc. Japan*, 70(3):703–716.

Itoh, M., Tamano, S., Yokota, K., and Taniguchi, S. (2006). Drag reduction in a turbulent boundary layer on a flexible sheet undergoing a spanwise traveling wave motion. *J. Turbul.*, 7:N27.

Iuso, G., Cicca, G. M. D., Onorato, M., Spazzini, P. G., and Malvano, R. (2003). Velocity streak structure modifications induced by flow manipulation. *Phys. Fluids*, 15(9):2602.

Jelly, T. O., Jung, S. Y., and Zaki, T. A. (2014). Turbulence and skin friction modification in channel flow with streamwise-aligned superhydrophobic surface texture. *Phys. Fluids*, 26(9):095102.

Jeong, J., Hussain, F., Schoppa, W., and Kim, J. (1997). Coherent structures near the wall in a turbulent channel flow. *J. Fluid Mech.*, 332:185–214.

Ji, C., Munjiza, A., and Williams, J. J. R. (2012). A novel iterative direct-forcing immersed boundary method and its finite volume applications. *J. Comput. Phys.*, 231(4):1797–1821.

Jiménez, J. (2003). Computing high-Reynolds-number turbulence: will simulations ever replace experiments? *J. Turbul.*, 4:N22.

Jiménez, J. (2013). Near-wall turbulence. *Phys. Fluids*, 25(10):101302.

Jiménez, J., Kawahara, G., Simens, M. P., Nagata, M., and Shiba, M. (2005). Characterization of near-wall turbulence in terms of equilibrium and "bursting" solutions. *Phys. Fluids*, 17(1):015105.

Jiménez, J. and Moin, P. (1991). The minimal flow unit in near-wall turbulence. *J. Fluid Mech.*, 225:213–240.

Jiménez, J. and Pinelli, A. (1999). The autonomous cycle of near-wall turbulence. *J. Fluid Mech.*, 389:335–359.

Johansson, A. V., Alfredsson, P. H., and Kim, J. (1991). Evolution and dynamics of shear-layer structures in near-wall turbulence. *J. Fluid Mech.*, 224:579–599.

Jones, J. (2011). Ribbed Swimsuit. `https://spinoff.nasa.gov/spinoff1996/45.html`. Last accessed on 8 June 2017.

Joshi, S. S., Speyer, J. L., and Kim, J. (1997). A systems theory approach to the feedback stabilization of infinitesimal and finite-amplitude disturbances in plane Poiseuille flow. *J. Fluid Mech.*, 332:157–184.

Jung, W. J., Mangiavacchi, N., and Akhavan, R. (1992). Suppression of turbulence in wall-bounded flows by high-frequency spanwise oscillations. *Phys. Fluids A Fluid Dyn.*, 4(8):1605.

Kaiser, E., Noack, B. R., Cordier, L., Spohn, A., Segond, M., Abel, M., Daviller, G., Östh, J., Krajnović, S., and Niven, R. K. (2014). Cluster-based reduced-order modelling of a mixing layer. *J. Fluid Mech.*, 754:365–414.

Kametani, Y. and Fukagata, K. (2011). Direct numerical simulation of spatially developing turbulent boundary layers with uniform blowing or suction. *J. Fluid Mech.*, 681:154–172.

Kametani, Y., Fukagata, K., Örlü, R., and Schlatter, P. (2015). Effect of uniform blowing/suction in a turbulent boundary layer at moderate Reynolds number. *Int. J. Heat Fluid Flow*, 55:132–142.

Kang, S. (2002). Approximate coordinate transformations for simulation of turbulent flows with wall deformation. *J. Mech. Sci. Technol.*, 16(5):703–709.

Kang, S. and Choi, H. (2000). Active wall motions for skin-friction drag reduction. *Phys. Fluids*, 12(12):3301–3304.

Kang, S., Iaccarino, G., Ham, F., and Moin, P. (2009a). Prediction of wall-pressure fluctuation in turbulent flows with an immersed boundary method. *J. Comput. Phys.*, 228(18):6753–6772.

Kang, S., Iaccarino, G., and Moin, P. (2009b). Accurate Immersed-Boundary Reconstructions for Viscous Flow Simulations. *AIAA J.*, 47(7):1750–1760.

Karniadakis, G. E. and Choi, K.-S. (2003). Mechanisms on Transverse Motions in Turbulent Wall Flows. *Annu. Rev. Fluid Mech.*, 35(1):45–62.

Kasagi, N., Hasegawa, Y., and Fukagata, K. (2009a). Toward Cost-effective Control of Wall Turbulence for Skin Friction Drag Reduction. In Eckhardt, B., editor, *Adv. Turbul. XII Proc. 12th EUROMECH Eur. Turbul. Conf. Sept. 7-10, 2009, Marburg, Ger.*, volume 132, pages 189–200. Springer Berlin Heidelberg, Berlin, Heidelberg.

Kasagi, N. and Shikazono, N. (1995). Contribution of Direct Numerical Simulation to Understanding and Modelling Turbulent Transport. *Proc. Math. Phys. Sci.*, 451(1941):257–292.

Kasagi, N., Suzuki, Y., and Fukagata, K. (2009b). Microelectromechanical Systems–Based Feedback Control of Turbulence for Skin Friction Reduction. *Annu. Rev. Fluid Mech.*, 41(1):231–251.

Kawahara, G., Uhlmann, M., and van Veen, L. (2012). The significance of simple invariant solutions in turbulent flows. *Annu. Rev. Fluid Mech.*, 44(1):203–225.

Kerswell, R. R. (2005). Recent progress in understanding the transition to turbulence in a pipe. *Nonlinearity*, 18(6):R17–R44.

Kerswell, R. R., Obrist, D., and Schmid, P. J. (2003). On smoothed turbulent shear flows: Bounds, numerics and stress-reducing additives. *Phys. Fluids*, 15(1):78.

Kerswell, R. R. and Tutty, O. R. (2007). Recurrence of travelling waves in transitional pipe flow. *J. Fluid Mech.*, 584:69–102.

Kim, C., Jeon, W.-P., Park, J., and Choi, H. (2003). Effect of a localized time-periodic wall motion on a turbulent boundary layer flow. *Phys. Fluids*, 15(1):265.

Kim, E. and Choi, H. (2014). Space–time characteristics of a compliant wall in a turbulent channel flow. *J. Fluid Mech.*, 756:30–53.

Kim, J. (2003). Control of turbulent boundary layers. *Phys. Fluids*, 15(5):1093.

Kim, J. (2011). Physics and control of wall turbulence for drag reduction. *Philos. Trans. R. Soc. London A Math. Phys. Eng. Sci.*, 369(1940):1396–1411.

Kim, J. and Bewley, T. R. (2007). A Linear Systems Approach to Flow Control. *Annu. Rev. Fluid Mech.*, 39(1):383–417.

Kim, J., Kim, D., and Choi, H. (2001). An Immersed-Boundary Finite-Volume Method for Simulations of Flow in Complex Geometries. *J. Comput. Phys.*, 171(1):132–150.

Kim, J. and Lim, J. (2000). A linear process in wall-bounded turbulent shear flows. *Phys. Fluids*, 12(8):1885.

Kim, K., Adrian, R. J., Balachandar, S., and Sureshkumar, R. (2008). Dynamics of Hairpin Vortices and Polymer-Induced Turbulent Drag Reduction. *Phys. Rev. Lett.*, 100(13):134504.

Kim, K., Li, C.-F., Sureshkumar, R., Balachandar, S., and Adrian, R. J. (2007). Effects of polymer stresses on eddy structures in drag-reduced turbulent channel flow. *J. Fluid Mech.*, 584:281–299.

King, G. E. (2012). Hydraulic Fracturing 101: What Every Representative, Environmentalist, Regulator, Reporter, Investor, University Researcher, Neighbor and Engineer Should Know About Estimating Frac Risk and Improving Frac Performance in Unconventional Gas and Oil Wells. In *SPE (Society Pet. Eng. Hydraul. Fract. Technol. Conf.*, page SPE 152596, The Woodlands, TX. Society for Petroleum Engineers.

Klumpp, S., Meinke, M., and Schröder, W. (2011). Friction Drag Variation via Spanwise Transversal Surface Waves. *Flow, Turbul. Combust.*, 87(1):33–53.

Kushwaha, A., Park, J. S., and Graham, M. D. (2017). Temporal and spatial intermittencies within channel flow turbulence near transition. *Phys. Rev. Fluids*, 2(2):024603.

Lai, M.-C. and Peskin, C. S. (2000). An Immersed Boundary Method with Formal Second-Order Accuracy and Reduced Numerical Viscosity. *J. Comput. Phys.*, 160(2):705–719.

Lee, C. and Kim, J. (2002). Control of the viscous sublayer for drag reduction. *Phys. Fluids*, 14(7):2523.

Lee, C., Kim, J., Babcock, D., and Goodman, R. (1997). Application of neural networks to turbulence control for drag reduction. *Phys. Fluids*, 9(6):1740.

Lee, C., Kim, J., and Choi, H. (1998). Suboptimal control of turbulent channel flow for drag reduction. *J. Fluid Mech.*, 358:245–258.

Lee, C., Min, T., and Kim, J. (2008). Stability of a channel flow subject to wall blowing and suction in the form of a traveling wave. *Phys. Fluids*, 20(10):101513.

Lee, J., Ahn, J., and Sung, H. J. (2015a). Comparison of large- and very-large-scale motions in turbulent pipe and channel flows. *Phys. Fluids*, 27(2):025101.

Lee, J., Jelly, T. O., and Zaki, T. A. (2015b). Effect of Reynolds Number on Turbulent Drag Reduction by Superhydrophobic Surface Textures. *Flow, Turbul. Combust.*, 95(2):277–300.

Lee, J., Kim, J., Choi, H., and Yang, K.-S. (2011a). Sources of spurious force oscillations from an immersed boundary method for moving-body problems. *J. Comput. Phys.*, 230(7):2677–2695.

Lee, J., Lee, J. H., Choi, J.-I., and Sung, H. J. (2014). Spatial organization of large- and very-large-scale motions in a turbulent channel flow. *J. Fluid Mech.*, 749:818–840.

Lee, J. and You, D. (2013). An implicit ghost-cell immersed boundary method for simulations of moving body problems with control of spurious force oscillations. *J. Comput. Phys.*, 233:295–314.

Lee, J. H. and Sung, H. J. (2011). Very-large-scale motions in a turbulent boundary layer. *J. Fluid Mech.*, 673:80–120.

Lee, J. H., Sung, H. J., and Krogstad, P.-Å. (2011b). Direct numerical simulation of the turbulent boundary layer over a cube-roughened wall. *J. Fluid Mech.*, 669(2011):397–431.

Lemoult, G., Aider, J.-L., and Wesfreid, J. E. (2012). Experimental scaling law for the subcritical transition to turbulence in plane Poiseuille flow. *Phys. Rev. E*, 85(2):025303.

Lemoult, G., Aider, J.-L., and Wesfreid, J. E. (2013). Turbulent spots in a channel: large-scale flow and self-sustainability. *J. Fluid Mech.*, 731:R1.

Lemoult, G., Gumowski, K., Aider, J.-L., and Wesfreid, J. E. (2014). Turbulent spots in channel flow: An experimental study. *Eur. Phys. J. E*, 37(4):25.

Li, W. and Graham, M. D. (2007). Polymer induced drag reduction in exact coherent structures of plane Poiseuille flow. *Phys. Fluids*, 19(8):083101.

Li, W., Jessen, W., Roggenkamp, D., Klaas, M., Silex, W., Schiek, M., and Schröder, W. (2015). Turbulent drag reduction by spanwise traveling ribbed surface waves. *Eur. J. Mech. - B/Fluids*, 53:101–112.

Li, W., Stone, P. A., and Graham, M. D. (2005). Viscoelastic nonlinear travelling waves and drag reduction in plane Poiseuille flow. In Mullin, T. and Kerswell, R. R., editors, *IUTAM Symp. Laminar-Turbulent Transit. Finite Amplitude Solut.*, pages 289–312. Springer-Verlag, Dordrecht, The Netherlands.

Li, W., Xi, L., and Graham, M. D. (2006). Nonlinear travelling waves as a framework for understanding turbulent drag reduction. *J. Fluid Mech.*, 565:353–362.

Liao, C.-C., Chang, Y.-W., Lin, C.-A., and McDonough, J. (2010). Simulating flows with moving rigid boundary using immersed-boundary method. *Comput. Fluids*, 39(1):152–167.

Lieu, B. K., Moarref, R., and Jovanović, M. R. (2010). Controlling the onset of turbulence by streamwise travelling waves. Part 2. Direct numerical simulation. *J. Fluid Mech.*, 663:100–119.

Lim, J. (2003). *Control of wall-bounded turbulent shear flows using modern control theory.* PhD thesis, University of California, Los Angeles.

Liu, D. and Yu, J. (2009). Otsu method and K-means. In *Proc. Ninth Int. Conf. Hybrid Intell. Syst.*, volume 1, pages 344–349, Shenyang, China. IEEE.

Liu, N.-s., Wang, L., and Lu, X.-y. (2009). Turbulent Open Channel Flow Subjected to the Control of a Spanwise Traveling Wave. *J. Hydrodyn. Ser. B*, 21(1):65–70.

Löfdahl, L. and Gad-el Hak, M. (1999). MEMS applications in turbulence and flow control. *Prog. Aerosp. Sci.*, 35(2):101–203.

Lumley, J. and Blossey, P. (1998). Control of Turbulence. *Annu. Rev. Fluid Mech.*, 30(1):311–327.

Lumley, J. L. (1969). Drag Reduction by Additives. *Annu. Rev. Fluid Mech.*, 1(33):367–384.

Mamori, H. and Fukagata, K. (2014). Drag reduction effect by a wave-like wall-normal body force in a turbulent channel flow. *Phys. Fluids*, 26(11):115104.

Mani, R., Lagoudas, D. C., and Rediniotis, O. K. (2008). Active skin for turbulent drag reduction. *Smart Mater. Struct.*, 17(3):035004.

Manneville, P. (2015). On the transition to turbulence of wall-bounded flows in general, and plane Couette flow in particular. *Eur. J. Mech. - B/Fluids*, 49(Part B):345–362.

Margnat, F. and Morinière, V. (2009). Behaviour of an immersed boundary method in unsteady flows over sharp-edged bodies. *Comput. Fluids*, 38(6):1065–1079.

Martell, M. B., Perot, J. B., and Rothstein, J. P. (2009). Direct numerical simulations of turbulent flows over superhydrophobic surfaces. *J. Fluid Mech.*, 620:31–41.

Martell, M. B., Rothstein, J. P., and Perot, J. B. (2010). An analysis of superhydrophobic turbulent drag reduction mechanisms using direct numerical simulation. *Phys. Fluids*, 22(6):065102.

McCormick, M. E. and Bhattacharyya, R. (1973). Drag reduction of a submersible hull by electrolysis. *Nav. Eng. J.*, 85(2):11–16.

Miller, L. A. and Peskin, C. S. (2004). When vortices stick: an aerodynamic transition in tiny insect flight. *J. Exp. Biol.*, 207(17):3073–3088.

Min, T., Kang, S. M., Speyer, J. L., and Kim, J. (2006). Sustained sub-laminar drag in a fully developed channel flow. *J. Fluid Mech.*, 558:309–318.

Min, T. and Kim, J. (2004). Effects of hydrophobic surface on skin-friction drag. *Phys. Fluids*, 16(7):L55.

Mito, Y. and Kasagi, N. (1998). DNS study of turbulence modification with streamwise-uniform sinusoidal wall-oscillation. *Int. J. Heat Fluid Flow*, 19(5):470–481.

Mittal, R., Dong, H., Bozkurttas, M., Najjar, F. M., Vargas, A., and von Loebbecke, A. (2008). A versatile sharp interface immersed boundary method for incompressible flows with complex boundaries. *J. Comput. Phys.*, 227(10):4825–4852.

Mittal, R. and Iaccarino, G. (2005). Immersed Boundary Methods. *Annu. Rev. Fluid Mech.*, 37(1):239–261.

Moarref, R. and Jovanović, M. R. (2010). Controlling the onset of turbulence by streamwise travelling waves. Part 1. Receptivity analysis. *J. Fluid Mech.*, 663:70–99.

Mohd-Yusof, J. (1997). Combined immersed-boundary/B-spline methods for simulations of flow in complex geometries. *Cent. Turbul. Res. Annu. Res. Briefs*, pages 317–327.

Mohd-Yusof, J. (1998). Development of immersed boundary methods for complex geometries. *Cent. Turbul. Res. Annu. Res. Briefs*, pages 325–336.

Nagata, M. (1990). Three-dimensional finite-amplitude solutions in plane Couette flow: bifurcation from infinity. *J. Fluid Mech.*, 217:519–527.

Nagata, M. (1997). Three-dimensional traveling-wave solutions in plane Couette flow. *Phys. Rev. E*, 55(2):2023–2025.

Nagata, M. (2013). A note on the mirror-symmetric coherent structure in plane Couette flow. *J. Fluid Mech.*, 727:R1.

Nagata, M. and Deguchi, K. (2013). Mirror-symmetric exact coherent states in plane Poiseuille flow. *J. Fluid Mech.*, 735:R4.

Nakanishi, R., Mamori, H., and Fukagata, K. (2012). Relaminarization of turbulent channel flow using traveling wave-like wall deformation. *Int. J. Heat Fluid Flow*, 35:152–159.

Nguyen, Q. T. and Papavassiliou, D. V. (2013). Turbulent plane Poiseuille-Couette flow as a model for fluid slip over superhydrophobic surfaces. *Phys. Rev. E*, 88(6):063015.

Nolan, K. P. and Zaki, T. A. (2013). Conditional sampling of transitional boundary layers in pressure gradients. *J. Fluid Mech.*, 728:306–339.

Nouri, N. M., Bakhsh, M. S., and Sekhavat, S. (2013). Analysis of shear rate effects on drag reduction in turbulent channel flow with superhydrophobic wall. *J. Hydrodyn. Ser. B*, 25(6):944–953.

Nouri, N. M., Sekhavat, S., and Mofidi, A. (2012). Drag reduction in a turbulent channel flow with hydrophobic wall. *J. Hydrodyn. Ser. B*, 24(3):458–466.

Otsu, N. (1979). A Threshold Selection Method from Gray-Level Histograms. *IEEE Trans. Syst. Man. Cybern.*, 9(1):62–66.

Pamiès, M., Garnier, É., Merlen, A., and Sagaut, P. (2007). Response of a spatially developing turbulent boundary layer to active control strategies in the framework of opposition control. *Phys. Fluids*, 19(10):108102.

Pamiès, M., Garnier, É., Merlen, A., and Sagaut, P. (2011). Opposition control with arrayed actuators in the near-wall region of a spatially developing turbulent boundary layer. *Int. J. Heat Fluid Flow*, 32(3):621–630.

Park, H., Park, H., and Kim, J. (2013). A numerical study of the effects of superhydrophobic surface on skin-friction drag in turbulent channel flow. *Phys. Fluids*, 25(11):110815.

Park, J. S. and Graham, M. D. (2015). Exact coherent states and connections to turbulent dynamics in minimal channel flow. *J. Fluid Mech.*, 782:430–454.

Patel, V. C. and Head, M. R. (1969). Some observations on skin friction and velocity profiles in fully developed pipe and channel flows. *J. Fluid Mech.*, 38(01):181–201.

Peskin, C. S. (1972). Flow patterns around heart valves: A numerical method. *J. Comput. Phys.*, 10(2):252–271.

Peskin, C. S. (1982). The Fluid Dynamics of Heart Valves: Experimental, Theoretical, and Computational Methods. *Annu. Rev. Fluid Mech.*, 14:235–259.

Peskin, C. S. (2002). The immersed boundary method. *Acta Numer.*, 11:479–517.

Peyret, R. (2002). *Spectral methods for incompressible viscous flow*. Springer-Verlag, New York.

Pinelli, A., Naqavi, I., Piomelli, U., and Favier, J. (2010). Immersed-boundary methods for general finite-difference and finite-volume Navier–Stokes solvers. *J. Comput. Phys.*, 229(24):9073–9091.

Pollard, A. (1998). Passive and active control of near-wall turbulence. *Prog. Aerosp. Sci.*, 33(11-12):689–708.

Pope, S. B. (2000). *Turbulent Flows*. Cambridge University Press.

Pringle, C. C. T. and Kerswell, R. R. (2007). Asymmetric, Helical, and Mirror-Symmetric Traveling Waves in Pipe Flow. *Phys. Rev. Lett.*, 99(7):074502.

Qin, T., Gao, P., Liu, N.-S., and Lu, X.-Y. (2008). Turbulent Boundary Layer Control via a Streamwise Travelling Wave Induced by an External Force. *Chinese Phys. Lett.*, 25(10):3700–3703.

Quadrio, M. (2011). Drag reduction in turbulent boundary layers by in-plane wall motion. *Philos. Trans. R. Soc. London A Math. Phys. Eng. Sci.*, 369(1940):1428–1442.

Quadrio, M. and Ricco, P. (2004). Critical assessment of turbulent drag reduction through spanwise wall oscillations. *J. Fluid Mech.*, 521:251–271.

Quadrio, M. and Ricco, P. (2010). The laminar generalized Stokes layer and turbulent drag reduction. *J. Fluid Mech.*, 667:135–157.

Quadrio, M., Ricco, P., and Viotti, C. (2009). Streamwise-travelling waves of spanwise wall velocity for turbulent drag reduction. *J. Fluid Mech.*, 627:161–178.

Rathnasingham, R. and Breuer, K. S. (1997). System identification and control of a turbulent boundary layer. *Phys. Fluids*, 9(7):1867.

Rathnasingham, R. and Breuer, K. S. (2003). Active control of turbulent boundary layers. *J. Fluid Mech.*, 495:209–233.

Rawat, S., Cossu, C., and Rincon, F. (2016). Travelling-wave solutions bifurcating from relative periodic orbits in plane Poiseuille flow. *Comptes Rendus Mécanique*, 344(6):448–455.

Rebbeck, H. and Choi, K.-S. (2001). Opposition control of near-wall turbulence with a piston-type actuator. *Phys. Fluids*, 13(8):2142.

Rebbeck, H. and Choi, K.-S. (2006). A wind-tunnel experiment on real-time opposition control of turbulence. *Phys. Fluids*, 18(3):035103.

Rehill, B., Walsh, E. J., Brandt, L., Schlatter, P., Zaki, T. A., and McEligot, D. M. (2012). Identifying Turbulent Spots in Transitional Boundary Layers. *J. Turbomach.*, 135(1):011019.

Reynolds, O. (1883). An experimental investigation of the circumstances which determine whether the motion of water shall be direct or sinuous, and of the law of resistance in parallel channels. *Philos. Trans. R. Soc. London*, 174:935–982.

Ricco, P. (2011). Laminar streaks with spanwise wall forcing. *Phys. Fluids*, 23(6):064103.

Ricco, P., Ottonelli, C., Hasegawa, Y., and Quadrio, M. (2012). Changes in turbulent dissipation in a channel flow with oscillating walls. *J. Fluid Mech.*, 700:77–104.

Ricco, P. and Quadrio, M. (2008). Wall-oscillation conditions for drag reduction in turbulent channel flow. *Int. J. Heat Fluid Flow*, 29(4):601–612.

Rolland, J. (2015). Stochastic analysis of the time evolution of laminar-turbulent bands of plane Couette flow. *Eur. Phys. J. E*, 38(11):121.

Rothstein, J. P. (2010). Slip on Superhydrophobic Surfaces. *Annu. Rev. Fluid Mech.*, 42(1):89–109.

Sagong, W., Kim, C., Choi, S., Jeon, W.-P., and Choi, H. (2008). Does the sailfish skin reduce the skin friction like the shark skin? *Phys. Fluids*, 20(10):101510.

Saiki, E. M. and Biringen, S. (1996). Numerical simulation of a cylinder in uniform flow: application of a virtual boundary method. *J. Comput. Phys.*, 123(2):450–465.

Schneider, T. M., Gibson, J. F., and Burke, J. (2010). Snakes and ladders: localized solutions of plane Couette flow. *Phys. Rev. Lett.*, 104(10):104501.

Semeraro, O., Bagheri, S., Brandt, L., and Henningson, D. S. (2013). Transition delay in a boundary layer flow using active control. *J. Fluid Mech.*, 731:288–311.

Seo, J. H. and Mittal, R. (2011). A sharp-interface immersed boundary method with improved mass conservation and reduced spurious pressure oscillations. *J. Comput. Phys.*, 230(19):7347–7363.

Shanshool, J., Abdul Jabbar, M. F., and Slaiman, I. N. (2011). The influence of mechanical effects on degradation of polyisobutylenes as drag reducing agents. *Pet. Coal*, 53(3):218–222.

Shen, L., Zhang, X., Yue, D. K. P., and Triantafyllou, M. S. (2003). Turbulent flow over a flexible wall undergoing a streamwise travelling wave motion. *J. Fluid Mech.*, 484:197–221.

Sheplak, M., Cattafesta, L., Nishida, T., and McGinley, C. B. (2004). MEMS Shear Stress Sensors: Promise and Progress. In *24th AIAA Aerodyn. Meas. Technol. Gr. Test. Conf.*, Portland, OR. American Institute of Aeronautics and Astronautics.

Sherman, J. and Morrison, W. J. (1950). Adjustment of an Inverse Matrix Corresponding to a Change in One Element of a Given Matrix. *Ann. Math. Stat.*, 21(1):124–127.

Sirovich, L. and Karlsson, S. (1997). Turbulent drag reduction by passive mechanisms. *Nature*, 388(6644):753–755.

Skote, M. (2011). Turbulent boundary layer flow subject to streamwise oscillation of spanwise wall-velocity. *Phys. Fluids*, 23(8):081703.

Skote, M. (2012). Temporal and spatial transients in turbulent boundary layer flow over an oscillating wall. *Int. J. Heat Fluid Flow*, 38:1–12.

Skote, M. (2013). Comparison between spatial and temporal wall oscillations in turbulent boundary layer flows. *J. Fluid Mech.*, 730:273–294.

Skote, M. (2014). Scaling of the velocity profile in strongly drag reduced turbulent flows over an oscillating wall. *Int. J. Heat Fluid Flow*, 50:352–358.

Stone, P. A., Roy, A., Larson, R. G., Waleffe, F., and Graham, M. D. (2004). Polymer drag reduction in exact coherent structures of plane shear flow. *Phys. Fluids*, 16(9):3470–3482.

Stone, P. A., Waleffe, F., and Graham, M. D. (2002). Toward a Structural Understanding of Turbulent Drag Reduction: Nonlinear Coherent States in Viscoelastic Shear Flows. *Phys. Rev. Lett.*, 89(20):208301.

Su, S. W., Lai, M. C., and Lin, C. A. (2007). An immersed boundary technique for simulating complex flows with rigid boundary. *Comput. Fluids*, 36:313–324.

Sullivan, P. P., McWilliams, J. C., and Moeng, C.-H. (2000). Simulation of turbulent flow over idealized water waves. *J. Fluid Mech.*, 404:47–85.

Sun, Z., Ren, Y., and Larricq, C. (2011). Drag reduction of compressible wall turbulence with active dimples. *Sci. China Physics, Mech. Astron.*, 54(2):329–337.

Suri, B., Tithof, J., Grigoriev, R. O., and Schatz, M. F. (2017). Forecasting Fluid Flows Using the Geometry of Turbulence. *Phys. Rev. Lett.*, 118(11):114501.

Taira, K. and Colonius, T. (2007). The immersed boundary method: A projection approach. *J. Comput. Phys.*, 225(2):2118–2137.

Tamano, S. and Itoh, M. (2012). Drag reduction in turbulent boundary layers by spanwise traveling waves with wall deformation. *J. Turbul.*, 13(9):1–26.

Thomas, L. H. (1949). Elliptic Problems in Linear Differential Equations over a Network: The Watson Scientific Computing Laboratory. Technical report, Columbia University, New York.

Toh, S. and Itano, T. (2003). A periodic-like solution in channel flow. *J. Fluid Mech.*, 481:67–76.

Tomiyama, N. and Fukagata, K. (2013). Direct numerical simulation of drag reduction in a turbulent channel flow using spanwise traveling wave-like wall deformation. *Phys. Fluids*, 25(10):105115.

Toms, B. A. (1949). Some observations on the flow of linear polymer solutions through straight tubes at large Reynolds numbers. In *Proc. First Int. Congr. Rheol.*, pages 135–141, Scheveningen. North-Holland.

Toms, B. A. (1977). On the early experiments on drag reduction by polymers. *Phys. Fluids*, 20(10):S3.

Touber, E. and Leschziner, M. A. (2012). Near-wall streak modification by spanwise oscillatory wall motion and drag-reduction mechanisms. *J. Fluid Mech.*, 693:150–200.

Truesdell, R., Mammoli, A., Vorobieff, P., van Swol, F., and Brinker, C. J. (2006). Drag Reduction on a Patterned Superhydrophobic Surface. *Phys. Rev. Lett.*, 97(4):044504.

Tsukahara, T., Seki, Y., Kawamura, H., and Tochio, D. (2005). DNS of turbulent channel flow at very low Reynolds numbers. In *Proc. Fourth Int. Symp. Turbul. Shear Flow Phenom. TSFP-4*, pages 935–940, Williamsburg, VA, USA. Begell House Inc.

Tuckerman, L. S., Kreilos, T., Schrobsdorff, H., Schneider, T. M., and Gibson, J. F. (2014). Turbulent-laminar patterns in plane Poiseuille flow. *Phys. Fluids*, 26(11):114103.

Uhlmann, M. (2005). An immersed boundary method with direct forcing for the simulation of particulate flows. *J. Comput. Phys.*, 209(2):448–476.

Versteeg, H. K. and Malalasekera, W. (2007). *An Introduction to Computational Fluid Dynamics: The Finite Volume Method*. Pearson Education Limited, 2nd edition.

Viotti, C., Quadrio, M., and Luchini, P. (2009). Streamwise oscillation of spanwise velocity at the wall of a channel for turbulent drag reduction. *Phys. Fluids*, 21(11):115109.

Virk, P. S. (1975). Drag reduction fundamentals. *AIChE J.*, 21(4):625–656.

Virk, P. S., Merrill, E. W., Mickley, H. S., Smith, K. A., and Mollo-Christensen, E. L. (1967). The Toms phenomenon: turbulent pipe flow of dilute polymer solutions. *J. Fluid Mech.*, 30(2):305–328.

Virk, P. S., Mickley, H. S., and Smith, K. A. (1970). The Ultimate Asymptote and Mean Flow Structure in Toms' Phenomenon. *J. Appl. Mech.*, 37(2):488–493.

Viswanath, D. (2007). Recurrent motions within plane Couette turbulence. *J. Fluid Mech.*, 580:339–358.

Volino, R. J., Schultz, M. P., and Pratt, C. M. (2003). Conditional Sampling in a Transitional Boundary Layer Under High Freestream Turbulence Conditions. *J. Fluids Eng.*, 125(1):28–37.

Waleffe, F. (1997). On a self-sustaining process in shear flows. *Phys. Fluids*, 9(4):883.

Waleffe, F. (1998). Three-Dimensional Coherent States in Plane Shear Flows. *Phys. Rev. Lett.*, 81(19):4140–4143.

Waleffe, F. (2001). Exact coherent structures in channel flow. *J. Fluid Mech.*, 435:93–102.

Waleffe, F. (2003). Homotopy of exact coherent structures in plane shear flows. *Phys. Fluids*, 15(6):1517.

Wang, S.-N., Graham, M. D., Hahn, F. J., and Xi, L. (2014). Time-series and extended Karhunen–Loève analysis of turbulent drag reduction in polymer solutions. *AIChE J.*, 60(4):1460–1475.

Wang, S.-N., Shekar, A., and Graham, M. D. (2017). Spatiotemporal dynamics of viscoelastic turbulence in transitional channel flow. *J. Non-Newtonian Fluid Mech.*, 244:104–122.

Wang, Y.-S., Huang, W.-X., and Xu, C.-X. (2016). Active control for drag reduction in turbulent channel flow: the opposition control schemes revisited. *Fluid Dyn. Res.*, 48(5):055501.

Watanabe, S., Mamori, H., and Fukagata, K. (2017). Drag-reducing performance of obliquely aligned superhydrophobic surface in turbulent channel flow. *Fluid Dyn. Res.*, 49(2):025501.

Webber, G. A., Handler, R. A., and Sirovich, L. (1997). The Karhunen–Loéve decomposition of minimal channel flow. *Phys. Fluids*, 9(4):1054.

Wedin, H. and Kerswell, R. R. (2004). Exact coherent structures in pipe flow: travelling wave solutions. *J. Fluid Mech.*, 508(23):333–371.

Whalley, R. D. and Choi, K.-S. (2014). Turbulent boundary-layer control with plasma spanwise travelling waves. *Exp. Fluids*, 55(8):1796.

Whalley, R. D., Park, J. S., Kushwaha, A., Dennis, D. J. C., Graham, M. D., and Poole, R. J. (2017). Low-drag events in transitional wall-bounded turbulence. *Phys. Rev. Fluids*, 2(3):034602.

White, C. M. and Mungal, M. G. (2008). Mechanics and Prediction of Turbulent Drag Reduction with Polymer Additives. *Annu. Rev. Fluid Mech.*, 40(1):235–256.

Willis, A. P., Peixinho, J., Kerswell, R. R., and Mullin, T. (2008). Experimental and theoretical progress in pipe flow transition. *Philos. Trans. R. Soc. A Math. Phys. Eng. Sci.*, 366(1876):2671–2684.

Wygnanski, I., Sokolov, M., and Friedman, D. (1975). On transition in a pipe. Part 2. The equilibrium puff. *J. Fluid Mech.*, 69(02):283–304.

Wygnanski, I., Sokolov, M., and Friedman, D. (1976). On a turbulent 'spot' in a laminar boundary layer. *J. Fluid Mech.*, 78(04):785–819.

Wygnanski, I. J. and Champagne, F. H. (1973). On transition in a pipe. Part 1. The origin of puffs and slugs and the flow in a turbulent slug. *J. Fluid Mech.*, 59(02):281–335.

Xi, L. and Graham, M. D. (2010a). Active and Hibernating Turbulence in Minimal Channel Flow of Newtonian and Polymeric Fluids. *Phys. Rev. Lett.*, 104(21):218301.

Xi, L. and Graham, M. D. (2010b). Turbulent drag reduction and multistage transitions in viscoelastic minimal flow units. *J. Fluid Mech.*, 647:421–452.

Xi, L. and Graham, M. D. (2012a). Dynamics on the laminar-turbulent boundary and the origin of the maximum drag reduction asymptote. *Phys. Rev. Lett.*, 108(2):028301.

Xi, L. and Graham, M. D. (2012b). Intermittent dynamics of turbulence hibernation in Newtonian and viscoelastic minimal channel flows. *J. Fluid Mech.*, 693:433–472.

Xu, C.-X., Choi, J.-I., and Sung, H. J. (2002). Suboptimal control for drag reduction in turbulent pipe flow. *Fluid Dyn. Res.*, 30:217–231.

Xu, J., Dong, S., Maxey, M. R., and Karniadakis, G. E. (2007). Turbulent drag reduction by constant near-wall forcing. *J. Fluid Mech.*, 582:79–101.

Yang, J. and Balaras, E. (2006). An embedded-boundary formulation for large-eddy simulation of turbulent flows interacting with moving boundaries. *J. Comput. Phys.*, 215(1):12–40.

Yoshino, T., Suzuki, Y., and Kasagi, N. (2008). Drag Reduction of Turbulence Air Channel Flow with Distributed Micro Sensors and Actuators. *J. Fluid Sci. Technol.*, 3(1):137–148.

Yudhistira, I. and Skote, M. (2011). Direct numerical simulation of a turbulent boundary layer over an oscillating wall. *J. Turbul.*, 12(9):1–17.

Zammert, S. and Eckhardt, B. (2014). Streamwise and doubly-localised periodic orbits in plane Poiseuille flow. *J. Fluid Mech.*, 761:348–359.

Zhang, N. and Zheng, Z. C. (2007). An improved direct-forcing immersed-boundary method for finite difference applications. *J. Comput. Phys.*, 221(1):250–268.

Zhao, H., Wu, J.-Z., and Luo, J.-S. (2004). Turbulent drag reduction by traveling wave of flexible wall. *Fluid Dyn. Res.*, 34(3):175–198.